



ISSN 1580-3155

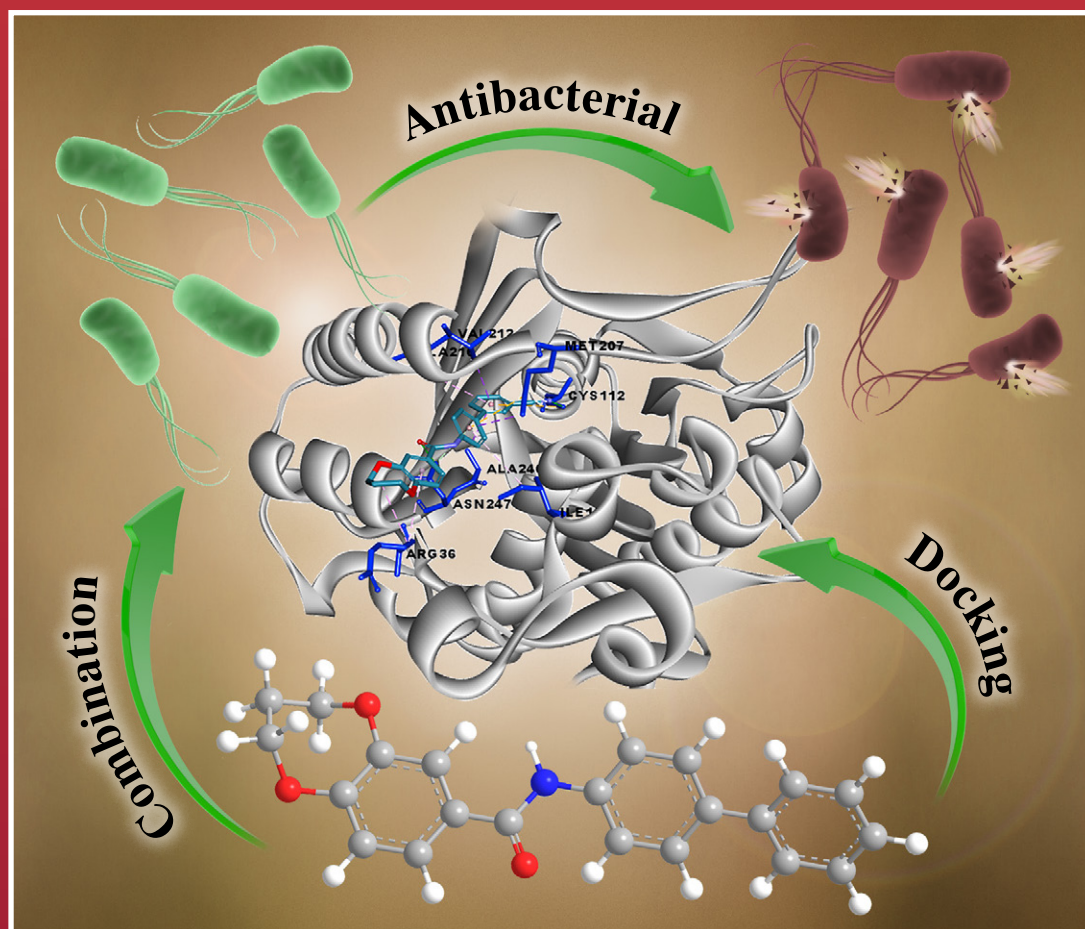
Pages 437–539 ■ Year 2024, Vol. 71, No. 3

Slovensko kemijsko društvo
Slovenian Chemical Society



ActaChimicaSlo ActaChimicaSlo SlovenicaActaC 3

71/2024



EDITOR-IN-CHIEF

FRANC PERDIH

University of Ljubljana, Faculty of Chemistry and Chemical Technology, Večna pot 113, SI-1000 Ljubljana, Slovenija
E-mail: ACSi@fkk.uni-lj.si, Telephone: (+386)-1-479-8514

ASSOCIATE EDITORS

Alen Albreht, National Institute of Chemistry, Slovenia
Aleš Berlec, Jožef Stefan Institute, Slovenia
Janez Cerkovnik, University of Ljubljana, Slovenia
Mirela Dragomir, Jožef Stefan Institute, Slovenia
Krištof Kranjc, University of Ljubljana, Slovenia
Matjaž Kristl, University of Maribor, Slovenia
Maja Leitgeb, University of Maribor, Slovenia

Helena Prosen, University of Ljubljana, Slovenia
Jernej Stare, National Institute of Chemistry, Slovenia
Irena Vovk, National Institute of Chemistry, Slovenia

ADMINISTRATIVE ASSISTANT

Eva Mihalinec, Slovenian Chemical society, Slovenia

EDITORIAL BOARD

Wolfgang Buchberger, Johannes Kepler University, Austria
Alojz Demšar, University of Ljubljana, Slovenia
Stanislav Gobec, University of Ljubljana, Slovenia
Marko Goličnik, University of Ljubljana, Slovenia
Günter Grampp, Graz University of Technology, Austria
Wojciech Grochala, University of Warsaw, Poland
Danijel Kikelj, University of Ljubljana
Janez Košmrlj, University of Ljubljana, Slovenia
Mahesh K. Lakshman, The City College and
The City University of New York, USA
Blaž Likozar, National Institute of Chemistry, Slovenia

Janez Mavri, National Institute of Chemistry, Slovenia
Jiří Pinkas, Masaryk University Brno, Czech Republic
Friedrich Sreenc, University of Minnesota, USA
Walter Steiner, Graz University of Technology, Austria
Jurij Svete, University of Ljubljana, Slovenia
David Šarlah, University of Illinois at Urbana-Champaign, USA;
Università degli Studi di Pavia, Italy
Ivan Švancara, University of Pardubice, Czech Republic
Gašper Tavčar, Jožef Stefan Institute, Slovenia
Ennio Zangrando, University of Trieste, Italy
Polona Žnidaršič Plazl, University of Ljubljana, Slovenia

ADVISORY EDITORIAL BOARD

Chairman

Branko Stanovnik, Slovenia

Members

Udo A. Th. Brinkman, The Netherlands
Attilio Cesaro, Italy
Vida Hudnik, Slovenia
Venčeslav Kaučič, Slovenia

Željko Knez, Slovenia
Radovan Komel, Slovenia
Stane Pejovnik, Slovenia
Anton Perdih, Slovenia
Slavko Pečar, Slovenia
Andrej Petrič, Slovenia
Boris Pihlar, Slovenia
Milan Randić, Des Moines, USA

Jože Škerjanc, Slovenia
Đurđa Vasić-Rački, Croatia
Marjan Veber, Slovenia
Gorazd Vesnaver, Slovenia
Jure Zupan, Slovenia
Majda Žigon, Slovenia

Acta Chimica Slovenica is indexed in: Academic Search Complete, Central & Eastern European Academic Source, Chemical Abstracts Plus, Chemical Engineering Collection (India), Chemistry Citation Index Expanded, Current Contents (Physical, Chemical and Earth Sciences), Digitalna knjižnica Slovenije (dLib.si), DOAJ, ISI Alerting Services, PubMed, Science Citation Index Expanded, SciFinder (CAS), Scopus, Web of Science and Portico. Impact factor for 2022 is IF = 1.20.



Articles in this journal are published under the
Creative Commons Attribution 4.0 International License

Izdaja – Published by:

SLOVENSKO KEMIJSKO DRUŠTVO – SLOVENIAN CHEMICAL SOCIETY
Naslov redakcije in uprave – Address of the Editorial Board and Administration
Hajdrihova 19, SI-1000 Ljubljana, Slovenija
Tel.: (+386)-1-476-0252; Fax: (+386)-1-476-0300; E-mail: chem.soc@ki.si

Izdajanje sfinancirajo – Financially supported by:

National Institute of Chemistry, Ljubljana, Slovenia
Jožef Stefan Institute, Ljubljana, Slovenia
Faculty of Chemistry and Chemical Technology, University of Ljubljana, Slovenia
Faculty of Chemistry and Chemical Engineering, University of Maribor, Slovenia
University of Nova Gorica, Slovenia

Slovensko kemijsko društvo
Slovenian Chemical Society

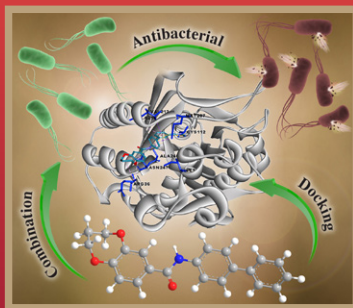


Acta Chimica Slovenica izhaja štirikrat letno v elektronski obliki na spletni strani <http://acta.chem-soc.si>. V primeru posvečenih številk izhaja revija tudi v tiskani obliki v omejenem številu izvodov.

Acta Chimica Slovenica appears quarterly in electronic form on the web site <http://acta.chem-soc.si>. In case of dedicated issues, a limited number of printed copies are issued as well.

Transakcijski račun: 02053-0013322846 Bank Account No.: SI56020530013322846-Nova Ljubljanska banka d. d., Trg republike 2, SI-1520 Ljubljana, Slovenia, SWIFT Code: LJBA SI 2X

Oblikovanje ovitka – Design cover: KULT, oblikovalski studio, Simon KAJTNA, s. p. Grafična priprava za tisk: OSITO, Laura Jankovič, s.p.

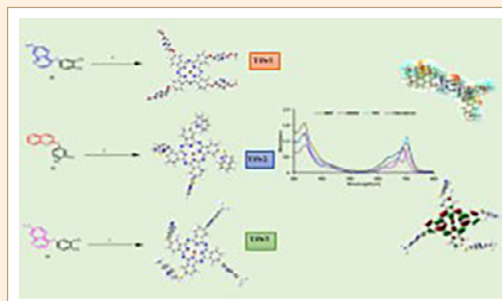


SCIENTIFIC PAPER

437–450 Organic chemistry

Synthesis, Characterization and DFT Study of Ti(IV) Phthalocyanines with Quinoline Groups

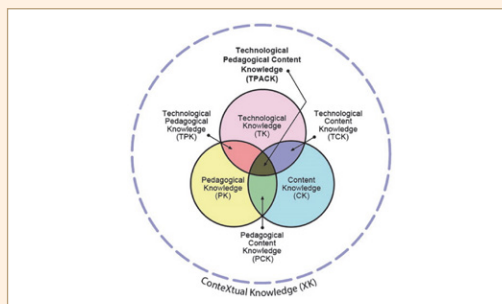
Seyda Aydogdu, Oznur Dulger Kutlu, Ali Erdogmus and Arzu Hatipoglu



451–461 Chemical education

Exploring Teachers' Technological Pedagogical Content Knowledge as an Indicator for the Planning of In-service Teacher Training in Chemistry Education

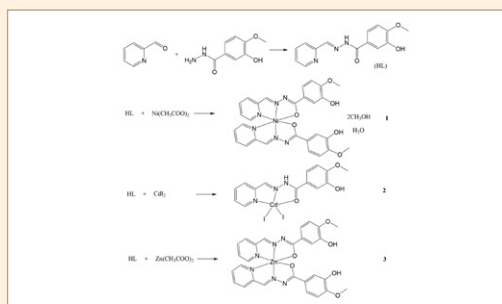
Mojca Orel, Cirila Peklaj and Vesna Ferk Savec



462–470 Inorganic chemistry

Synthesis, Crystal Structures and Antibacterial Activity of Nickel(II), Cadmium(II) and Zinc(II) Complexes with Hydrazone Ligands

Wei-Guang Zhang

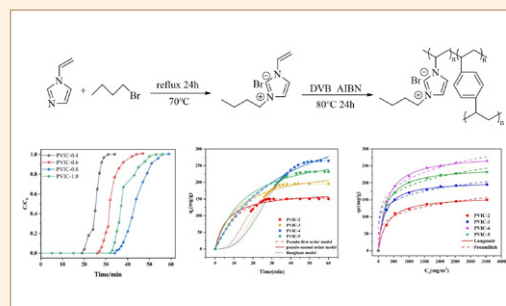


471–481

Chemical, biochemical and environmental engineering

Preparation of Porous Imidazole-based Poly(ionic liquid) Adsorbents and Their Toluene Adsorption Performance

Fangwen Luo, Xujiao Tian, Xian Dong, Longchao Liang and Zhuo Chen

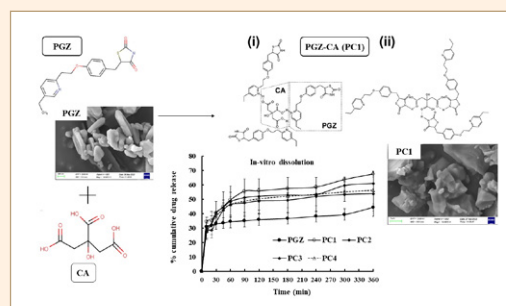


482–491

Physical chemistry

Development of Eutectics of Pioglitazone with Citric Acid and its Effect on Crystallite Properties and Dissolution

Mouli Das, Shibashis Panigrahy, Rasmita Dash, Rudra Narayan Sahoo, Rakesh Swain, Souvik Nandi, Sk Habibullah, Tanisha Das and Subrata Mallick

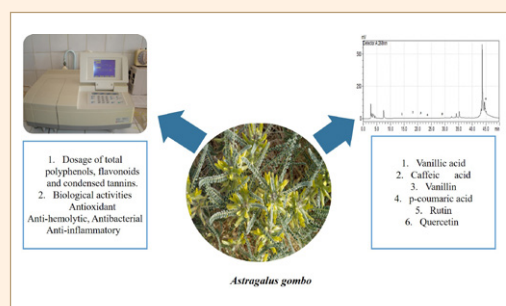


492–499

Biochemistry and molecular biology

Phytochemical Analysis and Evaluation of the Antioxidant, Anti-Inflammatory, Hemolytic, and Antibacterial Effects of *Astragalus gombo* (L.) Leaves

Mohammed Laid Tlili, Ibtissam Laib, Khadidja Salemi, Imane Chetehouna, Ines BenMoussa and Elhafnaoui Lanez

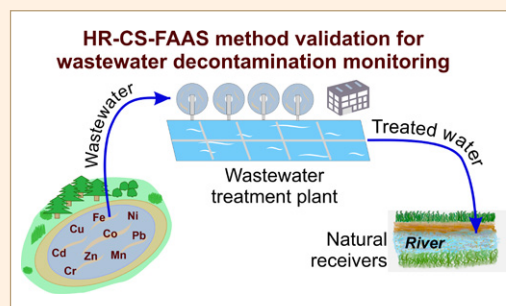


500–508

Analytical chemistry

Validation of High-Resolution Continuum Source Flame Atomic Absorption Spectrometry for Determination of Selected Toxic Metals in the Decontamination Process of Wastewater Discharged in Natural Receivers

Bame Sanah Senna, Wellington Masamba, Veronica Obuseng, Tiberiu Frentiu, Bogdan Simion Angyus and Eniko Covaci

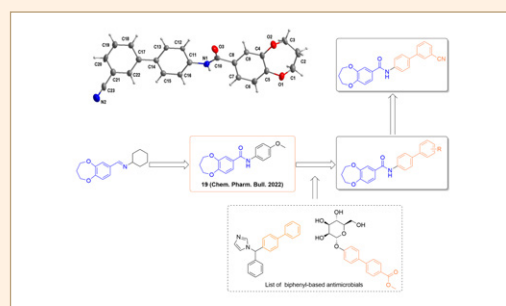


509–518

Biomedical applications

Synthetic Optimization and Antibacterial Activity of Novel Benzodioxepine-Biphenyl Amide Derivatives

Shao-Peng Yan, Zhi-Yu Zhu, Qi-Ke Jia, Rui-Ying Ji, Ya-Pin Wang, Dan He, Rong Wang, Xiao-Jun Xu and Yang Zhou

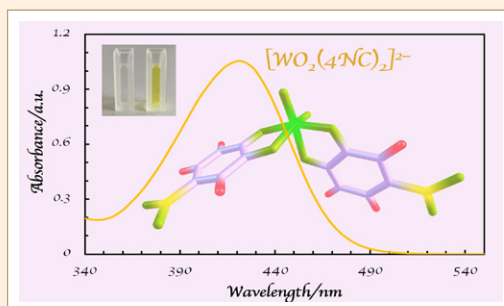


519–527

Inorganic chemistry

Extraction System for the Spectrophotometric Determination of Tungsten(VI) with 4-Nitrocatechol and Benzalkonium Chloride

Vidka V. Divarova, Kirila T. Stojnova, Ivelina D. Radkovska, Antoaneta D. Saravanska, Galya K. Toncheva, Vassil B. Delchev and Kiril B. Gavazov

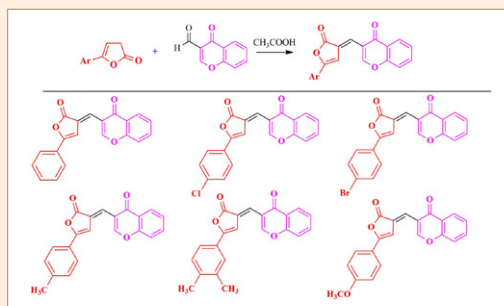


527–539


Organic chemistry

Synthesis of (*E*)-3-[[2-Oxo-5-arylfuran-3(2*H*)-ylidene]methyl]-4*H*-1-benzopyran-4-ones, Crystal Structure, Quantum Chemical Substantiation

Ekaterina M. Arzyamova, Olga A. Mazhukina and Alevtina Yu. Yegorova



Synthesis, Characterization and DFT Study of Ti(IV) Phthalocyanines with Quinoline Groups

Seyda Aydogdu, Oznur Dulger Kutlu, Ali Erdoganmus and Arzu Hatipoglu* 

Department of Chemistry, Yildiz Technical University, 34220, Istanbul, Turkey

* Corresponding author: E-mail: hatiparzu@yahoo.com

Received: 05-18-2024

Abstract

The synthesis, characterization, and electronic properties of 4-((7-methoxyquinolin-4-yl)oxy), 4-(quinolin-2-ylthio), and 4-((7-(trifluoromethyl)quinolin-4-yl)thio) peripherally substituted oxo-titanium phthalocyanines are described for the first time. The structures of the compounds were determined by UV-Vis, FTIR, ^1H NMR, and MALDI-TOF mass spectrometry. Electronic spectra and molecular and electronic properties of compounds were calculated by Density Functional Theory (DFT) and Time-Dependent Density Functional Theory (TD-DFT) methods. Solvent effects on the electronic, geometric, and reactivity properties of the compounds were also investigated. Global and local reactivity indices and Molecular Electrostatic Potential surfaces of compounds were calculated. The reactivities and electronic structures of molecules vary depending on the solvent and substituents. It has been found that the synthesized compounds can be used for different purposes such as dye-sensitized solar cells and photodynamic therapy applications.

Keywords: Oxo-titanium phthalocyanine, synthesis, Density Functional Theory, solvent effect.

1. Introduction

Phthalocyanines (Pcs) are 18 π electron ring systems that are composed of four isoindole units bridged with aza nitrogen atoms.¹ It has 18 delocalized electrons that are responsible for its strong absorption in the visible spectrum domain and also they have the high thermal and chemical stability.² Thus, Pcs with their tunable chemical properties can be good candidates for use in photodynamic therapy, gas sensors, organic field transistors, or dye sensitized solar cells.^{3,4} These in turn, lead to high interest to Pc compounds and studies about variation in the chemical structure of Pcs have been reported in the last years. In the literature, there are lots of Pc papers about different synthesizing method and their applications.^{5–13} With the increasing popularity of theoretical methods there are also some studies that performed by using DFT to understand electronic properties of Pcs.^{14–17} Although, knowledge and understanding of different substituent and solvents effects on the Pcs properties are still not sufficient.

There is a need for experimental and theoretical studies on new types of Pcs for finding desired properties. One of the most desired properties of a compound is to have a red-shifted absorption spectrum. Because these types of compounds can be used in photodynamic therapy and dye sensitized solar cell areas.^{18,19} The shift is more

prominent with electron-donating substituents such as –OR and –SR, etc. A closely related practical method of obtaining a red-shift is by introduction of special metal ions such as TiO^{2+} .²⁰ Quinoline is a heterocyclic compound containing aromatic nitrogen and water-soluble compounds are obtained by methylation of nitrogen atoms in its structure using appropriate agents.²⁰ It is also known that trifluoromethyl group is prominent for medicinal chemistry applications.²¹ Owing to the importance of different groups on the reactivity of compounds, a comprehensive research for quinolin and trifluoromethyl group containing compounds is desired.

The properties of compounds depend on their electronic structures. Various properties of compounds can be calculated with quantum chemical methods. Quantum chemical methods allow experimental results to be explained and information can be obtained in cases where some experimental data are not available. The usage of experimental and theoretical methods together lead to obtain more robust scientific datas and new discoveries.^{22,23} In recent years, Density Functional Theory (DFT) has been widely used to effectively find the optimum electronic structure, structural parameters and various properties.^{24,25} It is very important to know the structural and electronic properties of newly synthesized compounds so that they can be used in different areas.

The main purpose of this study is to determine the electronic, geometric and reactivity properties of Pcs containing different quinoline-derived substituents. For this purpose, 4-((7-methoxyquinolin-4-yl)oxy), 4-(quinolin-2-ylthio) and 4-((7-(trifluoromethyl)quinolin-4-yl)thio) phthalonitriles and their oxo-titanium phthalocyanine derivatives were synthesized and characterized. The effects of substituent and solvents on the spectral performance properties of newly synthesized complexes were investigated. DFT and TD-DFT studies were used to understand the electronic transitions nature of compounds. We also conducted local reactivity descriptor analysis for deeper understanding prominent reactive sites of the compounds. At the same time, the calculation results were used to interpret their possible usage areas.

2. Experimental

2. 1. Materials and Equipment in the Experiments

All reagents and solvents were of reagent grade quality and were obtained from commercial suppliers. Absorption spectra in the UV-visible region were recorded with a Shimadzu 2001 UV spectrophotometer. FT-IR spectra were measured with a Perkin Elmer Spectrum One Spectrometer. The mass spectra were acquired on a Bruker Daltonics (Bremen, Germany) Microflex mass spectrometer equipped with an electron spray ionization (ESI) source. ¹H-NMR spectra were recorded on a Varian 500 MHz spectrometer.

2. 2. Synthesis

2. 2. 1. General Procedure for the Aynthesis of Phthalonitrile Derivatives (1-3)

Substituted quinoline derivatives 7-methoxyquinolin-4-ol (0.9 mmol), quinoline-2-thiol (1.24 mmol) and 7-(trifluoromethyl)quinoline-4-thiol (0.8 mmol) were dissolved in dry DMF. To this reaction mixture 4-nitrophthalonitrile (1.25 mmol) and anhydrous K₂CO₃ (6.0 mmol) were added under Ar atmosphere. The resulting reaction mixture was stirred at room temperature for 24h. The reaction was monitored by TLC and then allowed to cool to room temperature. The reaction mixture was poured into cold water (100 mL) and filtered. The precipitate washed with H₂O and diethyl ether, then dried. The residue was recrystallized from ethanol to obtain pure phthalonitrile derivatives.

4-(7-methoxyquinolin-4-yl)oxy)phthalonitrile (1)

Yield: 0.31 g (85%). FT-IR (ATR) (cm⁻¹): 3073–3031 (Ar. C–H), 2965–2831 (Aliph. C–H), 2239 (C≡N), 1272 (C–O–C). ¹H NMR (500 MHz, DMSO-d₆) (δ: ppm): 8.76 (s, 1H, Ar-H), 8.22–8.06 (m, 3H, Ar-H), 7.74 (s, 1H, Ar-H),

7.48 (s, 1H, Ar-H), 7.33 (s, 1H, Ar-H), 6.91 (s, 1H, Ar-H), 3.95 (s, 3H). MALDI-TOF-MS (*m/z*): calcd. 301.298 for C₁₈H₁₁N₃O₂; found 301.687 [M]⁺.

4-(quinolin-2-ylthio)phthalonitrile (2)

Yield: 0.35 g (85%). FT-IR (ATR) (cm⁻¹): 3114–3073 (Ar. C–H), 2229 (C≡N), 1498, 1421, 1292, 1137 (C–S–C). ¹H NMR (500 MHz, Chloroformd) (δ: ppm): 8.18–8.16 (m, 2H, Ar-H), 8.01–7.97 (m, 2H, Ar-H), 7.89–7.84 (m, 2H, Ar-H), 7.81–7.78 (m, 1H, Ar-H), 7.65–7.61 (m, 1H, Ar-H), 7.42–7.41 (d, 1H, Ar-H). MALDI-TOF-MS (*m/z*): calcd. 287.338 for C₁₇H₉N₃S; found 286.00 [M]⁺.

4-((7-(trifluoromethyl)quinolin-4-yl)thio)phthalonitrile (3)

Yield: 0.26 g (88%). FT-IR (ATR) (cm⁻¹): 3099–3027 (Ar. C–H), 2235 (C≡N), 1500, 1477, 1284, 1150 (C–S–C). ¹H NMR (500 MHz, Chloroformd) (δ: ppm): 9.02 (s, 1H, Ar-H), 8.55 (s, 1H, Ar-H), 8.30 (d, 1H, Ar-H), 7.83 (d, 1H, Ar-H), 7.74 (d, 1H, Ar-H), 7.63 (s, 1H, Ar-H), 7.57 (s, 1H, Ar-H), 7.53 (d, 1H, Ar-H). MALDI-TOF-MS (*m/z*): calcd. 355.336 for C₁₈H₈F₃N₃S; found 355.341 [M]⁺.

2. 2. 2. General Synthesis Procedure for Phthalocyanine Derivatives (TiPc1-3)

A mixture of the related phthalonitrile derivative (1–3) (0.28 mmol), DBU (0.50 mmol, 0.3 mL), and Ti(O–Bu)₄ (0.6 mmol, 0.2 mL) in *n*-pentanol (3 mL) were stirred at 110°C under Ar for 12 h. The dark-green product was cooled to room temperature, precipitated by the addition of *n*-hexane, collected by using a centrifuge and then washed with *n*-hexane, methanol and ethanol. The dark-green product was purified performing column chromatography on silica gel with CHCl₃ as the eluent. The pure compounds were obtained as a mixture of four structural isomers. The obtained pure dark green crystal products (TiPc1–3) were characterized by applying different spectroscopic techniques (FT-IR, ¹H-NMR and MS spectroscopy).

{2,(3) 9(10),16(17),23(24)-tetrakis-(4-(7-methoxyquinolin-4-yl)oxy)- phthalocyaninato}oxo-titanium (IV) (TiPc1)

Yield: 0.025 g (44%). FT-IR (ATR) (cm⁻¹): 3070 (Ar. C–H), 2930–2928 (Aliph. C–H), 1272–1018 (C–O–C), 923 (Ti=O). ¹H NMR (500 MHz, Chloroformd) (δ: ppm): 8.88–8.40 (b, 13H, Ar-H), 8.26–8.08 (b, 6H, Ar-H), 8.00–7.77 (b, 5H, Ar-H), 7.60–7.48 (b, 2H, Ar-H), 7.00–6.74 (b, 6H, Ar-H), 4.07 (s, 12H). MALDI-TOF-MS (*m/z*): calcd. 1269.061 for C₇₂H₄₄N₁₂O₉Ti; found 1269.767 [M]⁺.

{2,(3)9(10),16(17),23(24)-tetrakis-(4-(quinolin-2-ylthio))-phthalocyaninato}oxo-titanium(IV) (TiPc2)

Yield: 0.05 g (58%). FT-IR (ATR) (cm⁻¹): 3070 (Ar. C–H), 1497–1336 (C–S–C), 940 (Ti=O). ¹H NMR (500

MHz, Chloroform-*d*) (δ : ppm): 9.73–9.12 (b, 8H, Ar-H), 8.47–8.19 (b, 2H, Ar-H), 8.13–7.32 (b, 26H, Ar-H). MALDI-TOF-MS (*m/z*): calcd. 1212.220 for $C_{72}H_{44}N_{12}O_9Ti$; found 1212.570 [M]⁺.

{2,(3)9(10),16(17),23(24)-tetrakis-(4-(7-(trifluoromethyl)quinolin-4-yl)thio))-phthalocyaninato oxo-titanium(IV) (TiPc3)

Yield: 0.025 g (50%). FT-IR (ATR) (cm^{-1}): 3050 (Ar-C-H), 1368–1284 (C–S–C), 894 (Ti=O). ¹H NMR (500 MHz, Chloroform-*d*) (δ : ppm): 9.00–8.60 (b, 10H, Ar-H), 8.65–8.17 (b, 12H, Ar-H), 7.95–7.69 (b, 3H, Ar-H), 7.76–7.42 (b, 6H, Ar-H), 7.06 (s, 12H) MALDI-TOF-MS (*m/z*): calcd. 1485.212 for $C_{72}H_{32}F_{12}N_{12}OS_4Ti$; found 1421.762 [M-(CF₃)+5H]⁺.

2. 3. Computational Details

Density Functional Theory (DFT) and Time Dependent- Density Functional Theory (TD-DFT) methods are used for through of the study with Gaussian09 software.²⁶ Conformational analyses and geometry optimizations of all the structures are performed to determine the most stable structures. Geometry optimizations of the most stable conformers are done using B3LYP/LANL2DZ basis set. Single point energies are calculated using Becke's three-parameter Lee-Yang-Parr functional (B3LYP) effective core potential calculation where 6-31g(d) basis set for C, H, N, O, S, F and LANL2DZ basis set are used for Ti. Stationary points verification of the molecular structures as a global minimum are performed by frequency calculation with no imaginary frequencies. The ¹H NMR calculations are performed by gauge-independent atomic orbital (GIAO) approach. The Frontier Molecular Orbital (FMO) visualitions and Molecular Electrostatic potential (MEP) surfaces are also obtained with mentioned method by using Gausview.²⁷

Conductor like Polarizable Continuum Model (CPCM), an implicit solvent model, is used with the intention of understanding solvent effect. Solvents are DMSO, DMF, THF, CHCl₃ with the dielectric constants values 46.83, 37.22, 7.43 and 4.71 respectively.²⁸

The global reactivity indices of molecules are calculated with using of Koopman's Theorem. With this theorem it is stated that ionization potential and electron affinity are related to negative values of energies of Highest Occupied Molecular Orbital (E_{HOMO}) and Lowest Unoccupied Molecular Orbital (E_{LUMO}) respectively. Then, chemical potential (μ), hardness (η), electrophilicity index (ω) and softness (S) are calculated with equations 1–4.²⁹

$$\mu = \frac{E_{LUMO} - E_{HOMO}}{2} \quad (1)$$

$$\eta = \frac{E_{LUMO} + E_{HOMO}}{2} \quad (2)$$

$$\omega = \frac{\mu^2}{2 \times \eta} \quad (3)$$

$$S = \frac{1}{2 \times \eta} \quad (4)$$

The local reactivity indices, fukui functions are obtained by using finite difference method which proposed Yang and Mortier. The equations that given below are fukui functions for nucleophilic ($f_{(r)}^+$), electrophilic ($f_{(r)}^-$) and radicalic ($f_{(r)}^0$) attack.^{30,31}

$$f_{(r)}^+ = p_{N+1}(r) - p_N(r) \quad (5)$$

$$f_{(r)}^- = p_N(r) - p_{N-1}(r) \quad (6)$$

$$f_{(r)}^0 = \frac{p_{N+1}(r) - p_{N-1}(r)}{2} = \frac{f_{(r)}^+ - f_{(r)}^-}{2} \quad (7)$$

In these equations $p_N(r)$, $p_{N+1}(r)$, $p_{N-1}(r)$ are the calculated electron density of neutral, anionic and cationic molecule by using Mulliken Population Analysis. Local softness values are calculated by using the values of fukui functions as given below.³¹

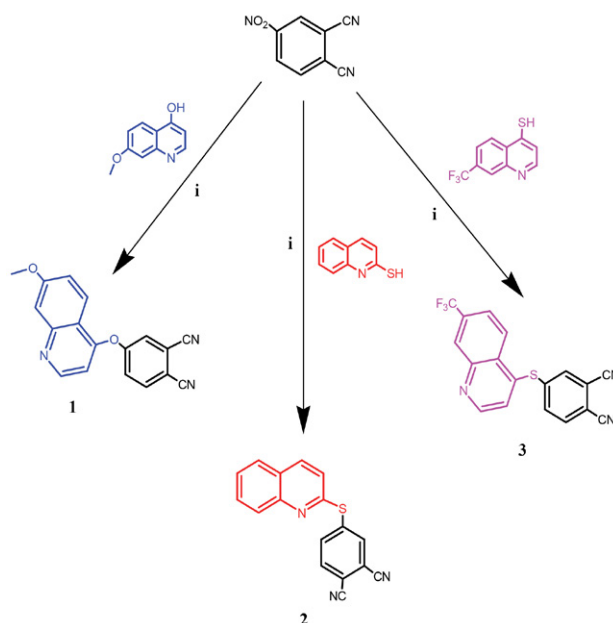
$$S_{(r)} = S \times f_{(r)} \quad (8)$$

3. Results and Discussion

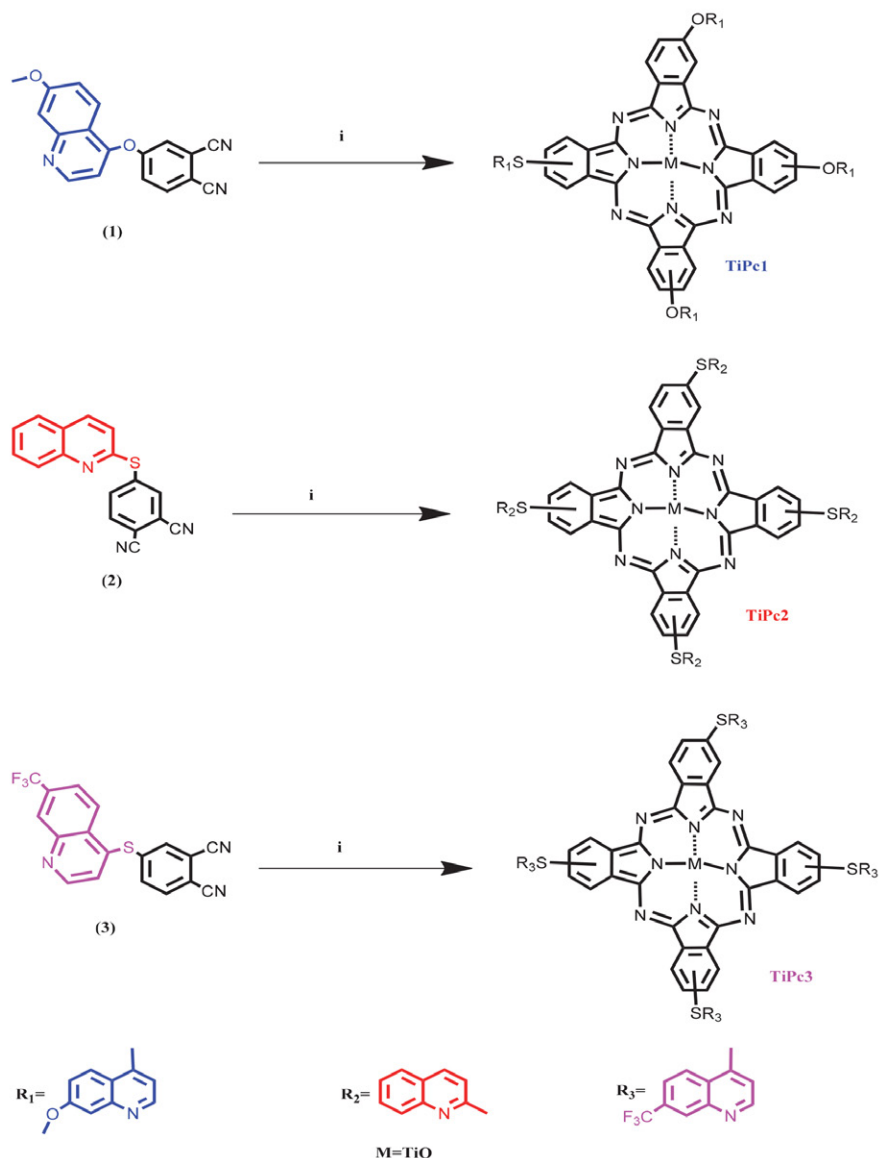
3. 1. Synthesis and Characterization

As shown in Scheme 1, by adding 4-nitrophthalonitrile to 7-methoxyquinolin-4-ol, quinoline-2-thiol, and 7-(trifluoromethyl)quinoline-4-thiol, phthalonitrile derivatives (**1**, **2** and **3**) are achieved by the nucleophilic aromatic substitution reaction in anhydrous K₂CO₃ and dry DMF medium.

The pure product resulting from the reaction to obtain tetra-substituted Pc is predicted to be a mixture of



Scheme 1. Synthesis pathway of phthalonitrile derivatives (**1**, **2** and **3**). Reaction conditions: i) i) K₂CO₃, DMF, rt, 24 h.



Scheme 2. The synthesis pathways of Ti(IV) phthalocyanines (**TiPc1-3**) used phthalonitrile derivatives (**1-3**). Reaction conditions: i) $\text{Ti}(\text{OBu})_4$, *n*-pentanol, 110 °C, 12 h.

four structural isomers of this tetra-substituted phthalocyanine, differing in symmetry.^{32–35}

Scheme 2 presents the synthesis route of the pure products **TiPc1**, **TiPc2**, and **TiPc3**, each obtained as a mixture of its four structural isomers via cyclotramerization of compounds the compounds 4-(7-methoxyquinolin-4-yl)oxyphthalonitrile (**1**), 4-(quinolin-2-ylthio)phthalonitrile (**2**) and 4-((7-(trifluoromethyl)quinolin-4-yl)thio)phthalonitrile (**3**). As seen in Scheme 2, the reaction of starting compounds **1**, **2** and **3** with $\text{Ti}(\text{OBu})_4$ in the presence of DBU in *n*-pentanol produced **TiPc1**, **TiPc2** and **TiPc3**. The main synthesis products peripherally tetra-substituted **TiPc1**, **TiPc2** and **TiPc3** were isolated from the crude product mixture by column chromatography using CHCl_3 as the eluent.

TiPc1, **TiPc2** and **TiPc3** are characterized by FT-IR, ^1H -NMR, MALDI-TOF and UV-Vis spectroscopic meth-

ods. The obtained results with these techniques are compatible with the expected structures for all prepared Pcs.

Experimental and calculated results of the most characteristic corresponding assignments of compounds are listed in Table 1. The given FT-IR values, those in parentheses show the calculated results. The characteristic $\text{C}\equiv\text{N}$ vibrations for phthalonitriles **1**, **2**, and **3** are observed at 2239 cm^{-1} , 2229 cm^{-1} , and 2235 cm^{-1} respectively. When the FT-IR spectrum of the **TiPc1** compound is examined (Figure S1), the characteristic $\text{C}\equiv\text{N}$ vibration observed in phthalonitrile compounds disappears and peaks belonging to aliphatic C-H groups appear in the range of $2928\text{--}2930\text{ cm}^{-1}$ (approximately 2911.91 cm^{-1}). C–O–C vibration is observed at $1018\text{--}1227\text{ cm}^{-1}$ (approximately 1387.38 cm^{-1}) for the **TiPc1** compound. In addition, the formation of the characteristic Ti–O stretch peak around 923 cm^{-1}

(1031.57 cm^{-1}), as well as the sharp peaks observed in the 555–630 cm^{-1} range are indicative of **TiPc1** formation. In the FT-IR spectra of **TiPc2** and **TiPc3** (Figure S1), the vibrations of the C–S–C groups at 1497–1336 cm^{-1} (1355.01 cm^{-1}) for **TiPc2** and for **TiPc3** at 1368–1284 cm^{-1} (1254.81 cm^{-1}).²⁰ The vibrations of the characteristic C–F bond for **TiPc2** are determined at 1150–1115 cm^{-1} (1173.12 cm^{-1}). Experimental and calculated frequencies are in good agreement with each other and the literature.³⁶ The sharp peaks of characteristic Ti–O stretching are observed around 940 cm^{-1} and 894 cm^{-1} for **TiPc2** and **TiPc3**, respectively. The corresponding Ti–O frequencies in the DFT calculations are to be 1032.22 cm^{-1} and 1034.75 cm^{-1} for **TiPc2** and **TiPc3** respectively. These results are indicative of the formation of **TiPc2** and **TiPc3**.

In this study, the unharmonic corrections to calculated IR results are done by multiplying the calculated wave number value with scaling factors 0.983 and 0.958 for be-

In addition to ^1H NMR spectrum results, the MALDI-TOF MS data for the phthalonitrile derivatives (**1**, **2**, and **3**) and their titanium (IV) phthalocyanine derivatives (**TiPc1**, **TiPc2**, and **TiPc3**) are available for the formulations given. The molecular ion peaks of synthesized compounds show parent ions at m/z : 301.687 as $[\text{M}]^+$ for **1**, 286.00 $[\text{M}]^+$ for **2**, 355.341 $[\text{M}]^+$ for **3**, 1269.767 $[\text{M}+\text{H}]^+$ for **TiPc1**, 1212.570 $[\text{M}]^+$ for **TiPc2**, 1661.878 $[\text{M}+5\text{K}+6\text{H}]^+$ for **TiPc3**, respectively. The molecular ion peak values of the fragmentation products of the obtained complexes are also indicated in the supplementary file (Fig. S4a–f).

3. 2. Ground State Electronic Absorption Spectras

The phthalocyanine macrocyclic system is characterized by quite strong absorption bands the Soret and Q bands corresponding to the $\pi \rightarrow \pi^*$ transitions. The former

Table 1. Comparison of experimental and calculated FTIR results (in cm^{-1}).

	TiPc1		TiPc2		TiPc3	
	Exp.	Calc.	Exp.	Calc.	Exp.	Calc.
$\nu_{\text{stretchingC-H(aliphatic)}}$	2930–2928	2911.91	–	–	–	–
$\nu_{\text{stretchingC-H(aromatic)}}$	3070	3087.44	3070	3059.36	3050	3106.59
$\delta_{\text{bendingC-O-C}}$	1227–1018	1387.38	–	–	–	–
$\nu_{\text{stretchingTi-O}}$	923	1031.57	940	1032.22	894	1034.75
$\delta_{\text{bendingC-S-C}}$	–	–	1497–1336	1355.01	1368–1284	1254.81
$\nu_{\text{stretchingC-F}}$	–	–	–	–	1150–1115	1173.12

low and greater than 1700 cm^{-1} .³⁷ All the stretching and bending vibrations are anticipated range and Table 1 demonstrates the agreement between experimental and calculated wavenumbers. The convergence of experimental and theoretical results reinforces the reliability of the identification of compounds.

The ^1H NMR results provide acceptable data about the suggested configurations of the designed complexes. ^1H NMR results together with computationally obtained ones are given in the supplementary material with Table S1. The ^1H -NMR spectrums of the phthalonitrile compounds **1**, **2**, and **3** indicate signals with δ ranging from 3.95 to 9.91 (for **1**, integrating for 8H aromatic–CH protons and 3H aliphatic– CH_3 protons), 7.20 to 8.18 (for **2**, integrating for 9H aromatic–CH protons), 7.0 to 8.5 (for **3**, integrating for 8H aromatic–CH protons) as expected (Fig. S2a–c). The signals with integrating for 12H aliphatic– CH_3 and 32H aromatic–CH protons of **TiPc1** are observed at 3.83 ppm and 6.95–9.06 ppm (Fig. S3a–c), respectively and these results indicate the formation of this complex. In the ^1H NMR spectrum of **TiPc2** and **TiPc3**, the signals of the aromatic–CH are detected at the range of 9.73–7.32 ppm (integrating for 36H) and 9.10–7.18 ppm (integrating for 32H), respectively, and confirming the formation of **TiPc2** and **TiPc3** (Fig. S3).

is at 300–350 nm and the latter is observed in the visible region at 600–700 nm in the UV–Vis spectrum.³⁸ With the central metal ion effect, metallophthalocyanines with D_{4h} symmetry give a single Q band in the visible region, while non-metallic phthalocyanines with D_{2h} symmetry show two bands with equal intensity in the same range in the visible region. The ground state electronic absorption spectra of Ti(IV) phthalocyanines for DMSO, DMF, THF, and chloroform solutions are recorded and the characteristic Soret and single Q bands of newly synthesized phthalocyanines **TiPc1**, **TiPc2** and **TiPc3** are detected in their electronic spectra. Hence, the obtained results are one of the principal pieces of evidence for their formation. The obtained spectral datas confirm the structures of the targeted Pcs are convenient with the electronic absorption spectra of other MPcs.³⁹

The electronic spectra of **TiPc1** bearing 4-(7-methoxyquinolin-4-yl)oxy isoindole moieties (Fig. 1) shows the characteristic absorption bands at around 690, 694 and 697 nm for the Q band region which is characteristic of metallophthalocyanines in DMF, THF, and chloroform, respectively.^{20,39,40} Although **TiPc1** has a high solubility in the previously mentioned organic solvents, its solubility in DMSO is very low, and no appreciable absorption spectrum is observed.

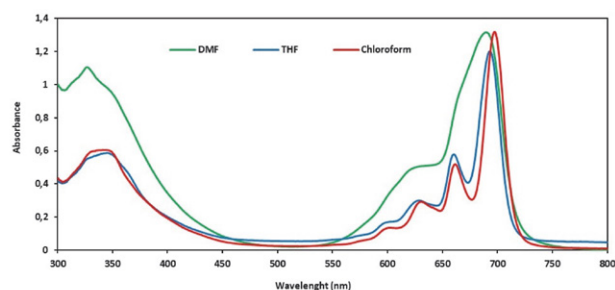


Figure 1. Electronic absorption spectrum of **TiPc1** in DMF, THF and chloroform.

Fig. 2 presents the absorption spectra of **TiPc2** bearing 4-(quinolin-2-ylthio) isoindole moieties in the mentioned solvents. The Q band of **TiPc2** in DMSO, DMF, THF, and chloroform are observed at 689, 700, 703 ve 708 nm, respectively.

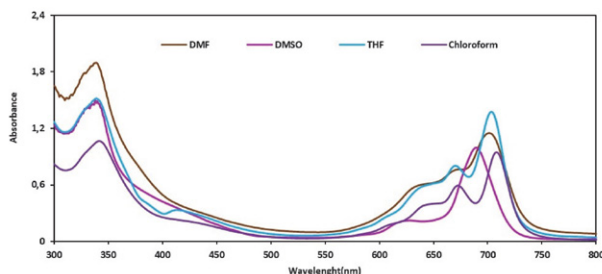


Figure 2. Electronic absorption spectrum of **TiPc2** in DMSO, DMF, THF and chloroform.

Fig. 3 shows the Q bands of **TiPc3** bearing 4-((7-(trifluoromethyl) quinoline-4-yl)thio) isoindole in DMF, THF, and chloroform. The solubility of **TiPc3** in the previously mentioned organic solvents is very high; however, its solubility in DMSO is very low, and an appreciable spectrum of absorption is not recorded. The Q band characteristic for metalized phthalocyanine is observed at 683 nm in DMF solution. The Q-bands of the obtained **TiPc3** are split into two components, Q_x and Q_y, which could result from the solvent effect decreasing symmetry.⁴¹

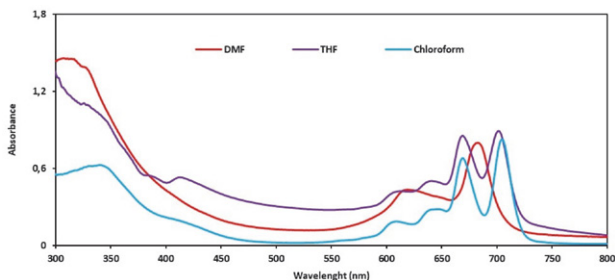


Figure 3. Electronic absorption spectrum of **TiPc3** in DMF, THF and chloroform.

3. 3. TD-DFT Results and FMOs

TD-DFT calculations are used to interpret experimental results. The comparison of experimental UV-Vis results with TD-DFT ones is done and given in Table 2. It is understood that the resulting wavelengths correspond with experimentally obtained maximum absorption wavelengths (λ_{exp}) results. The percentage of errors for calculations ranges between 1.44 % and 5.04 %. For **TiPc2** compound the calculated (experimental) maximum wavelength value is 672.33 (708) nm for chloroform phase (Fig S5). The small discrepancies between the experimental and calculated are the results of environmental factors of experimental conditions and quantum mechanical effect in a chosen computational model.

All the Q absorption bands of newly synthesized compounds are red-shifted. Red shifted absorption is a needed property to use them effectively as photosensitizers and dye-sensitized solar cells.^{18,19} Photochromic behavior that is seen in the absorption spectrums can lead to these compound's usage in photodynamic therapy. **TiPc2** has the most red-shifted absorption peak. This result does not differ with the changing of solvents. Red-shift values of compounds differ from each other and differ with the changing of solvent medium. Thus, the polarity of the solvent, metal atom in the Pc ring, and substituent can affect the red-shifted wavelength absorption of the Q band as stated in the literature.⁴² From Table 2, it is also understood that the dominant transition occurs from the Highest Occupied Molecular Orbital (HOMO) to the Lowest Unoccupied Molecular Orbital (LUMO) which is a π - π^* transition. As seen in Table 2, the π - π^* transition of molecules occurs with approximately the same energy (1.85 eV) in all solvents. However, only in **TiPc1**, the energy is 0.02 eV higher than in other solvents except THF. In all molecules, transitions from HOMO to LUMO occur with a probability of 96%.

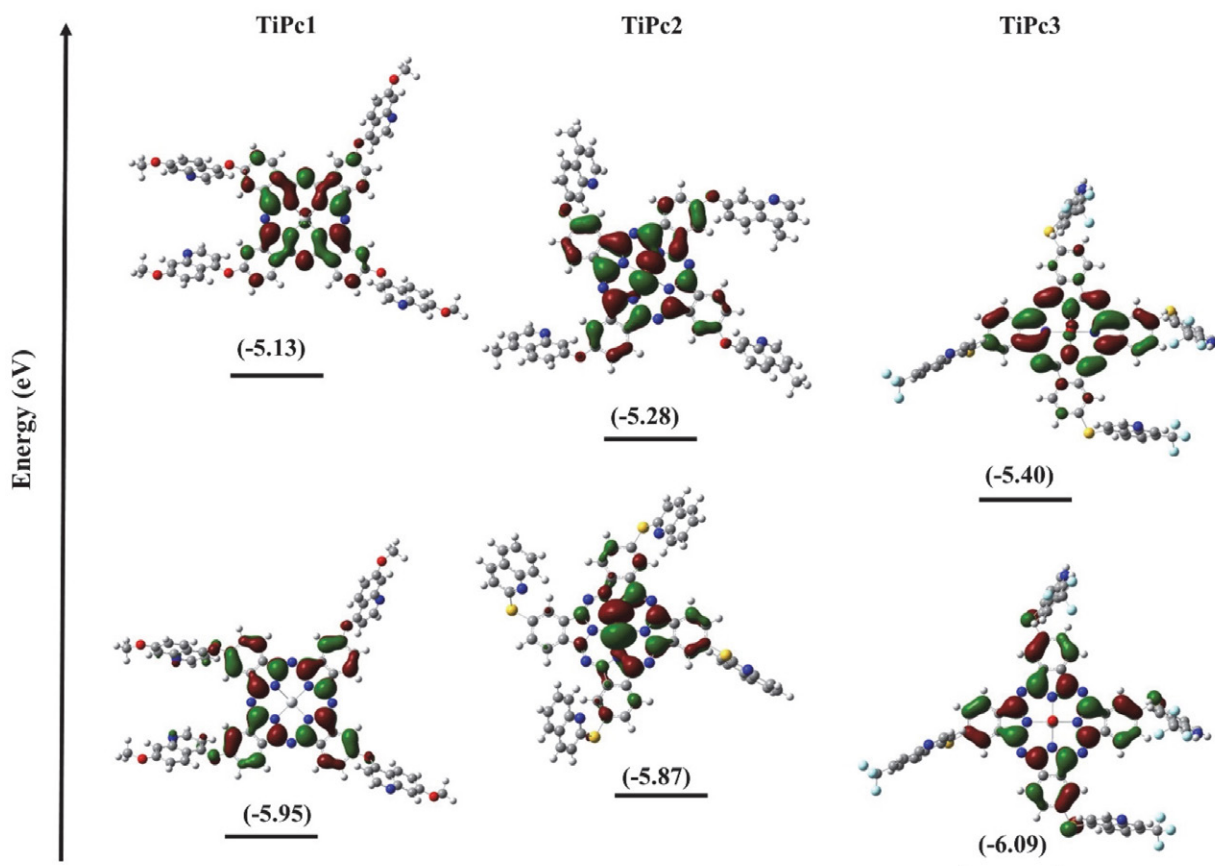
The frontier molecular orbitals (HOMO, LUMO) structures and their energies are given in Fig. 4, Fig. S6-7 and Table S2. It is understood from Fig. 4 that HOMO orbitals are all π type orbitals and LUMO orbitals are π^* type orbitals. HOMO orbitals are mainly distributed at the Pc ring for **TiPc1**. For **TiPc2**, the HOMO orbital is mainly located at the metallic part of the compound. As seen from the molecular orbital structure of the compound **TiPc3**, electron-withdrawing fluorine atoms of substituent leads to changing of electrons location in the HOMO orbital. Unlike **TiPc1** and **TiPc2** compounds, the HOMO orbital of **TiPc3** is not located in the metal atom or Pc ring but is distributed from the Pc ring to the sulfur linkage of the substituent. This may be the result of the highly electronegative character of its substituent. Thus it is important to note that substitutions with different groups have contributed to Frontier Molecular Orbital electronic structures. LUMO orbitals are distributed all over the Pc ring and metal atoms in all three compounds. Except for the HOMO orbital of **TiPc1** in DMSO, the HOMO and LUMO orbitals

Table 2. Calculated UV Results of Compounds.

	ΔE (eV)	λ (nm)	f	Transition	λ_{exp} (nm)
<i>DMSO</i>					
TiPc1	1.87	663.64	0.66	HOMO→LUMO (96.34%)	–
TiPc2	1.84	672.63	0.62	HOMO→LUMO (96.74%)	689
TiPc3	1.84	672.67	0.64	HOMO→LUMO (96.59%)	–
<i>DMF</i>					
TiPc1	1.87	664.16	0.66	HOMO→LUMO (96.39%)	690
TiPc2	1.84	673.14	0.62	HOMO→LUMO (97.78%)	700
TiPc3	1.84	673.13	0.64	HOMO→LUMO (96.62%)	683
<i>THF</i>					
TiPc1	1.85	669.90	0.61	HOMO→LUMO (96.17%)	697
TiPc2	1.85	671.19	0.61	HOMO→LUMO (96.70%)	703
TiPc3	1.85	670.17	0.63	HOMO→LUMO (96.52%)	702
<i>CHCl₃</i>					
TiPc1	1.87	663.88	0.66	HOMO→LUMO (96.17%)	694
TiPc2	1.84	672.33	0.63	HOMO→LUMO (96.80%)	708
TiPc3	1.85	671.52	0.65	HOMO→LUMO (96.62%)	707

of **TiPc1**, **TiPc2**, and **TiPc3** in DMF, THF, CHCl₃, and vacuum are distributed on the metallic part or Pc ring of the compounds. The HOMO of **TiPc1** is located on the substituent part for the DMSO.

The energy values of HOMO and LUMO of compounds are given in Table S2. The negative energy values of the HOMO and LUMO of the compounds indicate the chemical stability of the compounds in both aprotic and

**Figure 4.** Frontier orbitals energies of **TiPc1**, **TiPc2** and **TiPc3** in CHCl₃.

non-polar solvents. The lowest HOMO energy belongs to the **TiPc3** compound and its values are –6.21, –6.20, –6.06, –6.09, and –5.96 eV for DMSO, DMF, THF, chloroform, and vacuum, respectively. HOMO energy values of **TiPc1** and **TiPc2** are lower in aprotic solvents. Energies of LUMO orbitals are, –5.13 eV, –5.28 eV, and –5.40 eV for **TiPc1**, **TiPc2** and **TiPc3** for chloroform medium respectively. As seen in Fig. 4, the electron donor energy of **TiPc3** is smallest in chloroform (–6.09 eV). We can conclude that the solvent not only affects the structures of the boundary molecular orbitals, but also the energies.

For using a compound as a dye-sensitized solar cell some criteria like the red-shifted absorption spectrum and small ΔE values (near 1.4 eV) are needed.^{19,43} Light harvesting efficiency (*LHE*) is another important factor for examining a compound's optical usability as a dye-sensitized solar cell. High *LHE* values play a pivotal role in getting maximum photocurrent from a compound.^{44,45} The excited state lifetime (τ) is another factor for getting high

charge transfer efficiency. When the excited state lifetime of a material increases, its optical stability as well as its charge transfer ability increases. *LHE* and the excited lifetime can be calculated as follows:^{44,46}

$$LHE = 1 - 10^{-f} \quad (9)$$

$$\tau = \frac{1.499}{fE_{ex}^2} \quad (10)$$

In Eq. 9 and 10 f is the oscillator strength and E_{ex} is excitation energy in cm^{-1} unit. *LHE* and τ values of the compounds are shown in Table 3. According to Table 3, the *LHE* and τ values of all compounds are greater than 0.75 and 9.98 ns. So, **TiPc1**, **TiPc2** and **TiPc3** can absorb more photons from UV light.⁴⁴ The highest *LHE* values of the compounds are in CHCl_3 solvent and the *LHE* order is **TiPc2** < **TiPc1** = **TiPc3**. It can be concluded that **TiPc1**, **TiPc2** and **TiPc3** are suitable compounds for dye-sensitized solar cell applications. With comparing literature de-

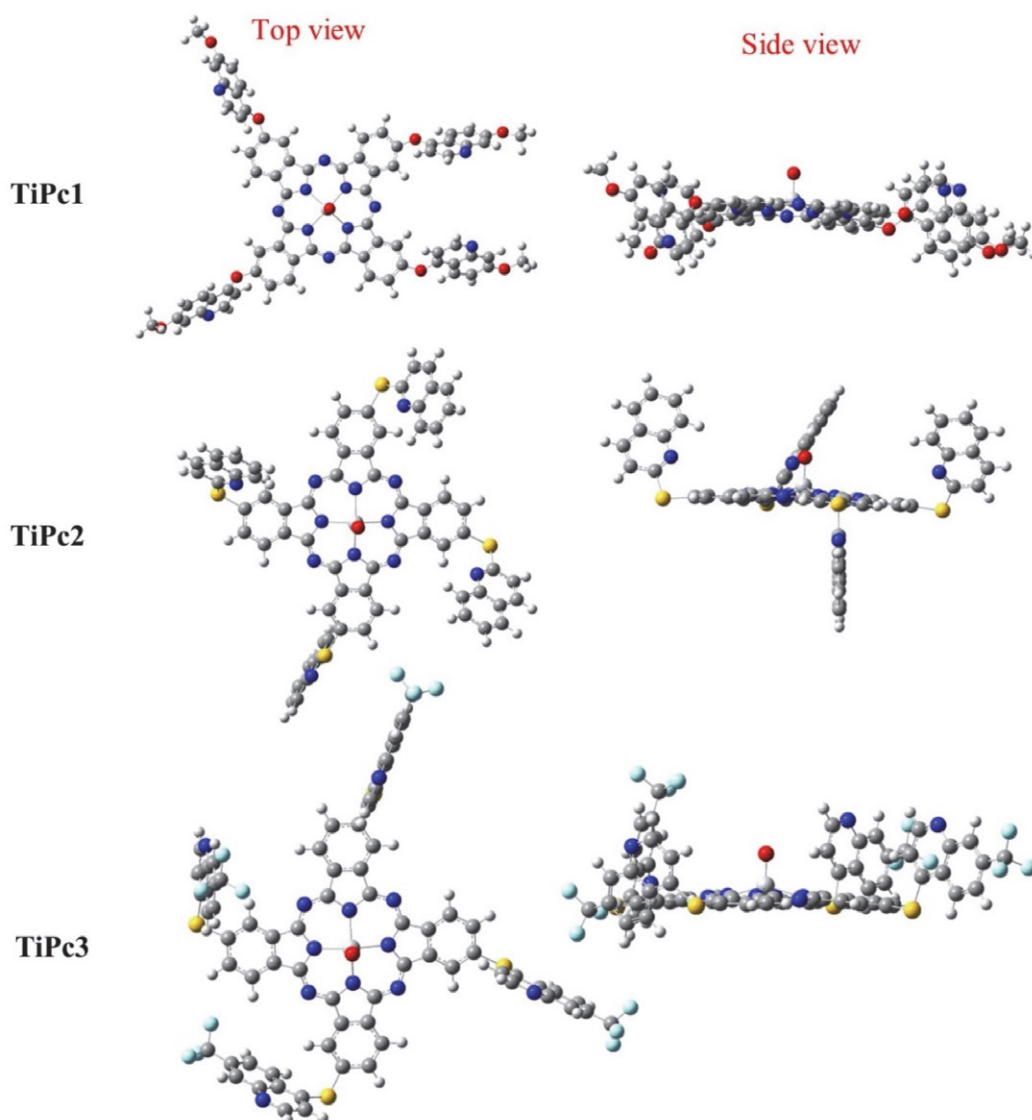


Figure 5. Optimized molecular geometries of **TiPc1**, **TiPc2** and **TiPc3**.

signing Pc with the oxo-titanium moiety may be also suitable method for obtaining higher excited state lifetimes.⁴⁴

Table 3. Calculated *LHE* and τ values of **TiPc1**, **TiPc2** and **TiPc3**.

	<i>LHE</i>			τ (ns)		
	TiPc1	TiPc2	TiPc3	TiPc1	TiPc2	TiPc3
DMSO	0.78	0.76	0.77	9.98	10.98	10.63
DMF	0.78	0.76	0.77	9.98	10.98	10.63
THF	0.75	0.75	0.77	11.04	11.04	10.63
CHCl ₃	0.78	0.77	0.78	9.98	10.80	10.36

3. 4. Calculated Electronic Properties

To examine the effects of the substituent groups on the molecular structure and reactivity in **TiPc1**, **TiPc2** and **TiPc3** compounds, calculations are also made for **TiPc0**, which does not contain substituents. The optimum geometric structures and geometric parameters of the compounds are given in Fig. 5 and Supplementary Material. As expected, the geometric parameters are very close to each other due to the planarity in the center of the complexes.

When the optimized compounds are viewed from the top position, it is seen that the peripherally substituted

parts of the synthesized compounds disrupt the planarity of the compounds (Figure 5). 4-((7-methoxyquinolin-4-yl)oxy), 4-(quinolin-2-ylthio) and 4-((7-(trifluoromethyl)quinolin-4-yl)thio) peripherally substituted parts of oxotitanium phthalocyanines orientates out of the plane when viewed from the side position. This orientation in the compound causes the dipole moment and solubility of the compound to increase. Thus, this result also verifies the experimental part result for the solubility ability of compounds in the THF, DMF and CHCl₃.

Geometric parameters of the compounds (Table S3) are also given. The bond lengths of Ti and pyrrole nitrogen are 2.08, 2.07, 2.08, and 2.08 Å for **TiPc0**, **TiPc1**, **TiPc2**, and **TiPc3**, respectively. Substituents containing oxygen bridge affects this bond length, but substituents with sulfur bridges do not affect this bond length. The bond length of Ti and meta nitrogen atoms is 3.47 Å for all compounds. The angle between the substituents and Pc ring is 122.02°, 102.71°, and 102.52° for **TiPc1**, **TiPc2**, and **TiPc3** respectively.

Electronic energies, dipole moments, energy differences of FMOs, and global reactivity indices are given in Table 4. As seen in Table 4, **TiPc3** is the compound with the smallest electronic energy and therefore the most stable in all solvents. The order of stability decreases to **TiPc3** < **TiPc2** < **TiPc1** < **TiPc0**. The electronegative fluorine

Table 4. Calculated energy (Energy (*E*), energy difference of the frontier orbital (ΔE)) and reactivity parameters (hardness (η), chemical potential (μ), electrophilic index (ω), and softness (*S*)) for complexes.

	<i>E</i> (Hartree)	<i>D</i> (Debye)	ΔE (eV)	η (eV)	μ (eV)	ω (eV)	<i>S</i> (eV)
<i>DMSO</i>							
TiPc0	−2592.01	4.85	2.05	1.03	−4.28	8.94	0.49
TiPc1	−4357.99	13.97	0.68	0.34	−5.73	48.15	1.47
TiPc2	−5191.73	14.10	0.78	0.39	−5.79	42.95	1.28
TiPc3	−6539.90	25.50	0.80	0.40	−5.87	43.14	1.25
<i>DMF</i>							
TiPc0	−2592.01	4.84	2.05	1.03	−4.28	8.93	0.49
TiPc1	−4357.99	13.91	0.68	0.34	−5.72	47.93	1.46
TiPc2	−5191.73	14.05	0.77	0.38	−5.78	43.46	1.30
TiPc3	−6539.90	25.42	0.79	0.39	−5.86	43.52	1.27
<i>THF</i>							
TiPc0	−2592.20	4.63	2.06	1.03	−4.25	8.78	0.49
TiPc1	−4357.97	12.54	0.69	0.35	−5.66	46.40	1.45
TiPc2	−5191.71	12.96	0.65	0.32	−5.62	48.67	1.54
TiPc3	−6539.89	23.92	0.70	0.35	−5.78	47.52	1.42
<i>CHCl₃</i>							
TiPc0	−2592.00	4.48	2.06	1.03	−4.23	8.69	0.48
TiPc1	−4357.96	11.61	0.67	0.34	−5.61	46.86	1.49
TiPc2	−5191.70	12.15	0.59	0.29	−5.58	52.82	1.70
TiPc3	−6539.87	22.91	0.68	0.34	−5.75	48.41	1.46
<i>Vacuum</i>							
TiPc0	−2591.99	3.43	2.09	1.04	−4.09	8.00	0.48
TiPc1	−4357.88	6.72	0.91	0.46	−5.22	29.88	1.10
TiPc2	−5191.63	7.32	0.62	0.31	−5.17	42.85	1.60
TiPc3	−6539.80	16.52	0.70	0.35	−5.72	47.03	1.44

atom in the **TiPc3** structure may lead to the stabilization of the compound. The energies of compounds are lower in solvents than in vacuum.

As seen in Table 4, the dipole moments of the compounds are lower in vacuum. Dipole moment values of compounds are related to their molecular structures, as mentioned before. Generally, the large dipole moment causes the molecule to self-assemble.⁴⁷ **TiPc3** contains more electronegative atoms than other compounds. Therefore, this may be the reason why **TiPc3**, which has the highest dipole moment among all phases, is also the most photochemically stable character. A high dipole moment is a desired feature in the drug distribution process.⁴⁸ Therefore, **TiPc3** may be a suitable drug candidate. These results show that substituents of molecular structures have an important effect on the electronic nature. Therefore, theoretical calculations are essential to obtain substituent effects on molecular properties.

The energy difference of the frontier orbital (ΔE) determines the reactivity of a compound. The small energy gap indicates that the molecule is more reagent.⁴⁹ As seen in Table 4, the reactivity of the compounds changes as the solvent changes. The molecular reactivity of the compounds is highest in non-polar chloroform. A high electron population in the conductive bond is a desired feature in the drug delivery system. Decreasing the energy difference between the boundary orbitals increases the electron population in the conductive bond.⁵⁰ As seen from the ΔE values in Table 4, **TiPc0** has the lowest reactivity among

all compounds. Compared to **TiPc0**, it appears that **TiPc1**, **TiPc2** and **TiPc3** are candidates for drug delivery. This shows that adding new substituents to the molecular structure of Pcs increases their reactive properties.

Hardness is an important global reactivity indice to understand the chemical stability of compounds. While the **TiPc1** compound is the most reactive compound in DMSO and DMF with the smallest hardness value of 0.34 eV, **TiPc0** is the most stable in vacuum with the highest hardness value of 0.46 eV. In chloroform, the chemical potential value (−5.75 eV) of **TiPc3** is the smallest while the chemical potential value (−4.23 eV) of **TiPc0** is the highest. The electrophilic index value of **TiPc0** is smaller than other compounds in all mediums. As the softness has an inverse relationship with hardness, it can be deduced from Table 4 that the softness values of **TiPc0** and **TiPc3** are the smallest ones in DMSO and DMF and vice versa with hardness results.

Thermodynamic parameters of the compounds are given in Table S4. Heat capacity, entropy, enthalpy, and Gibbs free energy calculations are conducted at 298.15 K and 1 atm. As seen from the table values, the substituent also affects the thermodynamic properties of the compounds. The heat capacity of **TiPc0** is 118.46 cal.mol^{−1}K^{−1} which is smaller than **TiPc1** (171.52 cal.mol^{−1}K^{−1}), **TiPc2** (141.33 cal.mol^{−1}K^{−1}) and **TiPc3** (194.38 cal.mol^{−1}K^{−1}) respectively. It is generally understood that the reactivity of Pcs can be regulated as a function of the electronic character of the ring, substituents, and solvent.

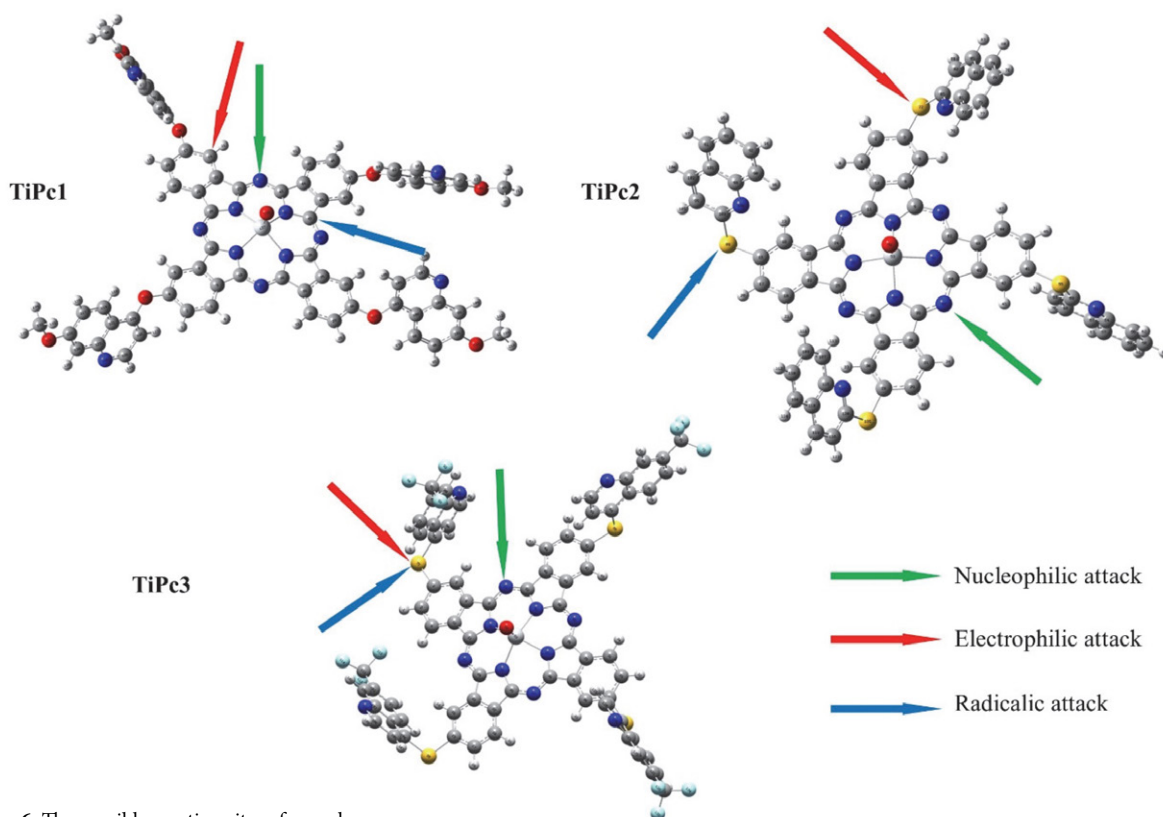


Figure 6. The possible reaction sites of complexes.

3. 5. Mulliken Charges And Local Reactivity Indices

The Mulliken charges are essential for understanding the properties of compounds.²¹ The Mulliken charges of **TiPc1**, **TiPc2**, and **TiPc3** are listed in the supplementary material (Table S5-7).

Titanium atoms of **TiPc1**, **TiPc2**, and **TiPc3** are the most positively charged atom (1.17) for all compounds. In the **TiPc1** structure, 19 C is the most negatively charged atom (−0.56). The phenyl carbon to which the substituent is connected to the ligand by an oxygen bridge is more positively charged than the other carbon atoms in the ring. Due to the electronegative character of the oxygen atom, the hydrogen atoms of methoxy groups are more positively charged than other hydrogen atoms. Meta nitrogen atoms are positively charged. The most negatively charged atom in **TiPc2** is the 25 N atom in the pyrrole ring with a value of −0.49. In this compound, the sulfur bridge atoms have positive charges. In the **TiPc3** compound, the sulfur bridge atoms are positively charged. The most negatively charged atom of **TiPc3** is the pyrrole nitrogen atom (38 N) and its Mulliken charge is −0.49. As a result of the electronegativity of the fluoride atoms in **TiPc3**, the positive charge on the carbon atoms in the trifluoromethyl groups decreases.

The local reactivity indices are important to determine suitable sites of compounds for nucleophilic, electro-

philic, and radical attacks. With the help of these indices, possible reaction mechanisms of compounds can be predicted.⁵¹ Getting information about the nucleophilic and electrophilic regions is also important for complex and protein interactions.²¹ Fig. 6 and Table S8-10 provide information on the results of the local reactivity indices.

By examining the values of local reactivity descriptors, it is clear that meta nitrogen atoms (27 N, 40 N, 14 N) of all compounds (**TiPc1**, **TiPc2**, **TiPc3**) are suitable sites for nucleophilic attack. The electrophilic attack regions of the compounds are 19 C, 72 S, and 75 S atoms of **TiPc1**, **TiPc2**, and **TiPc3** respectively. The carbon atom of the benzene ring, and bridge sulfur atoms of compounds attract to electrophilic chemicals. It is understood that changing the bridging atom of substituent groups affects the reactivity. The sulfur atom bridge is an important reaction site for **TiPc2** and **TiPc3** in comparison with the oxygen bridge in **TiPc1**. The radical attack sites of **TiPc1**, **TiPc2**, and **TiPc3** are 41 C, 89 S, and 75 S atoms of the compounds, respectively. In general, bridge atoms and meta-nitrogen atoms of compounds are suitable sites for different types of reactants.

3. 6. Molecular Electrostatic Potential

The Molecular Electrostatic Potential (MEP) surface is a pictorial demonstration of the distribution of

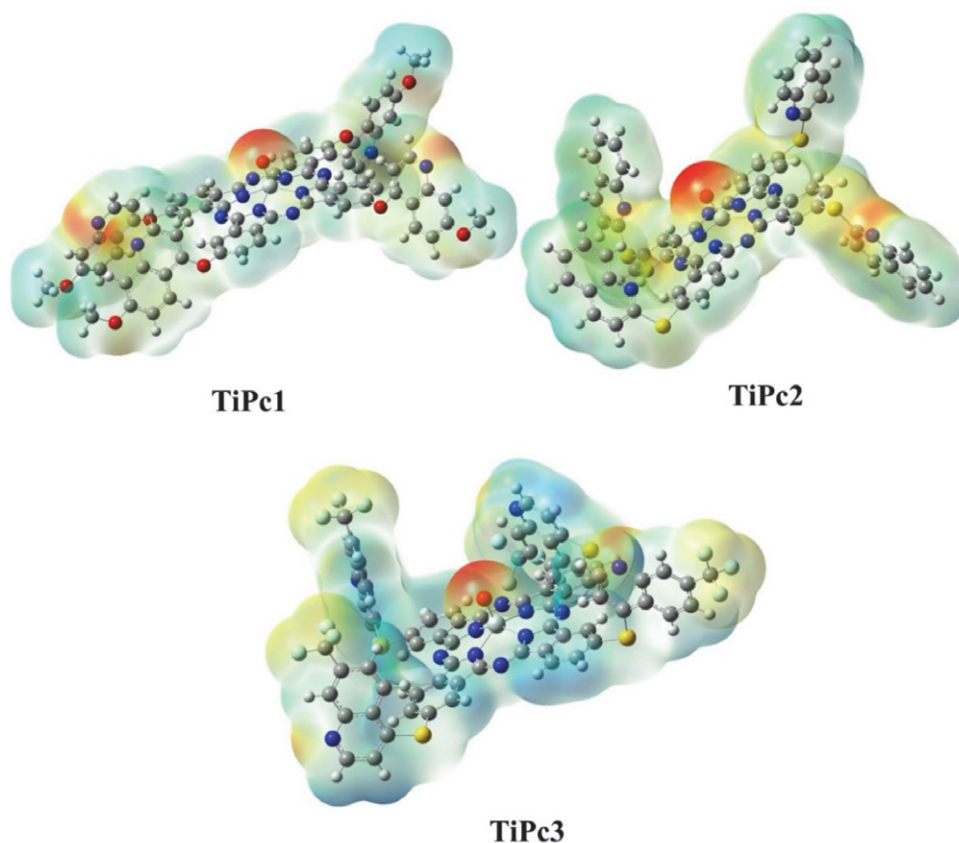


Figure 7. The MEP plots for **TiPc1**, **TiPc2** and **TiPc3**.

electrons on the molecular structure. These surfaces are mainly used for determining the reactive sites of compounds. On these surfaces, the blue color regions represent the electron-deficient areas, while the red color regions represent electron-abundant areas.⁴⁹ The MEP surfaces are simulated with the B3LYP method and given in Fig. 7.

As illustrated in Fig 7 the most negative parts of all compounds are over the oxygen atom of the oxotitanium part, while the most positive parts of compounds are titanium atoms and hydrogen atoms. As can be observed, there are also some negative areas on the substituent parts of compounds, such as fluoride and nitrogen atoms, indicating that substituent groups are affecting the electronic distribution of compounds. As seen on the MEP surfaces, **TiPc3** has more negative parts than other compounds. This is because **TiPc3** has fluoride atoms in its molecular structure.

4. Conclusions

In this study, new peripherally substituted oxo-titanium phthalocyanines (**TiPc1**, **TiPc2** and **TiPc3**) containing three different substituents were synthesized. Characterization of all compounds by spectroscopic methods (FT-IR, ¹H-NMR, UV/Vis, and mass) was examined and their electronic properties were calculated by quantum chemical methods. The results of experimental and quantum chemical calculations are consistent with each other. It has been found that the main electronic transition in molecules occurs between HOMO and LUMO orbitals. The electron distributions in these orbitals are affected by the electron-withdrawing properties of the substituent groups. Experimentally, the Q-band of unsubstituted Ti(IV)Pc to the red shifted after the addition of the substituent in all solvents, and this was confirmed by the calculation results. Quantum chemical calculation results show that the electronegativity of the substituents leads to the formation of more stable compounds. In addition, changing the solvent also affects the electronic structure, energies, and reactivity. The effect of substituents on solubility was investigated in DMSO, DMF, THF and CHCl₃. Experimental and computational results showed that adding substituents to Ti(IV)Pc increased the solubility of the compounds in THF, DMF, and CHCl₃. In non-polar chloroform, compounds become more reactive. Electrophilic, nucleophilic, and radical attack sites of Pcs were also determined with the calculated local reactivity indices. In the complexes, the meta nitrogen atoms and the sulfur bridges connected by the substituent to the ligand are reactive centers where reactions can take place. As a result, it can be said that the synthesized compounds are suitable for dye-sensitized solar cells, photodynamic therapy, and drug delivery applications.

Declaration of competing interest

Authors declare that they have no conflicts of interest.

Acknowledgements

This study is supported by Yildiz Technical University Research Coordination with Project Number: FBA-2020-4025.

Supplementary material

Supplementary material associated with this article can be found at

5. References

1. J. D. Spikes, *Photochem. Photobiol.* **1986**, 43, 691–699. DOI:10.1111/j.1751-1097.1986.tb05648.x
2. A. Q. Alosabi, A. A. Al-Muntaser, M. M. El-Nahass, A. H. Oraby, *Opt. Laser Technol.* **2022**, 155, 108372. DOI:10.1016/j.optlastec.2022.108372
3. F. Ayaz, D. Yetkin, A. Yüzer, K. Demircioğlu, M. Ince, *Photodiagnosis Photodyn. Ther.* **2022**, 39, 103035. DOI:10.1016/j.pdpdt.2022.103035
4. I. Paramio, T. Torres, G. de la Torre, *Org. Chem. Front.* **2023**, 11, 60–66. DOI:10.1039/D3QO01630G
5. R. Ağcaabat, C. Bilen Şentürk, Z. Odabaş, *Polyhedron* **2022**, 222, 115929. DOI:10.1016/j.poly.2022.115929
6. Ö. Güngör, Altınbaş G. Özpınar, M. Durmuş, V. Ahsen, *Dalton Trans.* **2016**, 45, 7634–7641. DOI:10.1039/C6DT00874G
7. S. Aydogdu, G. Yaşa-Atmaca, A. Erdoğan, A. Hatipoğlu, *Polyhedron*, **2024**, 256, 116989. DOI:10.1016/j.poly.2024.116989
8. I. Gusev, M. Ferreira, M. Krzywiecki, A. Przybyła, S. Pluczyk-Malek, D. Nastula, A. Duda, K. Nastula, K. Erfurt, P. Data, A. Blacha-Grzechnik, *Dyes and Pigm.* **2023**, 214, 111217. DOI:10.1016/j.dyepig.2023.111217
9. X. Zhao, Q. Wang, X. Jia, J. Xue, J. A. Chen, *Dyes and Pigm.* **2022**, 207, 110717. DOI:10.1016/j.dyepig.2022.110717
10. S. Bhattacharya, G. Reddy, S. Paul, S. S. Hossain, S. S. Kumar Raavi, L. Giribabu, A. Samanta, V. R. Soma, *Dyes and Pigm.* **2021**, 184, 108791. DOI:10.1016/j.dyepig.2020.108791
11. M. Halaskova, A. Rahali, V. Almeida-Marrero, M. Machacek, R. Kucera, B. Jamoussi, T. Torres, V. Novakova, A. De La Escosura, P. Zimcik, *ACS Med. Chem. Lett.* **2021**, 12, 502–507. DOI:10.1021/acsmchemlett.1c00045
12. J. Liu, D. W. Kang, Y. Fan, G. T. Nash, X. Jiang, R. R. Weichselbaum, W. Lin, *J. Am. Chem. Soc.* **2024**, 146, 849–857. DOI:10.1021/jacs.3c11092
13. F. A. Kılıçarslan, A. Erdoğan, Ö. Budak, A. Koca, *Inorg. Chim. Acta* **2024**, 561, 121870. DOI:10.1016/j.ica.2023.121870
14. S. Aydogdu, A. Hatipoğlu, A. Erdoğan, *J. Comput. Biophys. Chem.* **2022**, 21, 599–609. DOI:10.1142/S2737416522500235

15. M. Murali krishnan, S. Baskaran, M. N. Arumugham, *Inorg. Nano-Met. Chem.* **2021**, *51*, 1165–1176. DOI:10.1080/24701556.2020.1815775
16. M. Khazri, K. Sahra, A. Milet, B. Jamoussi, S. Messaoudi, *J. Struct. Chem.* **2020**, *61*, 844–851. DOI:10.1134/S0022476620060025
17. J. M. Mir, N. Jain, P. S. Jaget, R. C. Maurya, *Photodiagnosis Photodyn. Ther.* **2017**, *19*, 363–374. DOI:10.1016/j.pdpdt.2017.07.006
18. M. Lamač, D. Dunlop, K. Lang, P. Kubát, *J. Photochem. Photobiol. A Chem.* **2022**, *424*, 113619. DOI:10.1016/j.jphotochem.2021.113619
19. M. Khalid, M. U. Khan, S. Ahmed, Z. Shafiq, M. M. Alam, M. Imran, A. A. C. Braga, M. S. Akram, *Sci. Rep.* **2021**, *11*, 21540. DOI:10.1038/s41598-021-01070-3
20. A. Erdoğan, T. Nyokong, *J. Mol. Struct.* **2010**, *977* (1–3), 26–38. DOI:10.1016/j.molstruc.2010.04.048
21. A. Ram Kumar, S. Selvaraj, G. P. Sheeja Mol, M. Selvaraj, L. Ilavarasan, S. K. Pandey, P. Jayaprakash, S. Awasthi, O. Albormani, A. Ravi, *J. Mol. Liq.* **2024**, *393*, 123661. DOI:10.1016/j.molliq.2023.123661
22. E. S. Aazam, R. Thomas, *J. Mol. Liq.* **2024**, *395*, 123820. DOI:10.1016/j.molliq.2023.123820
23. A. A. Otlyotov, I. V. Ryzhov, I. A. Kuzmin, Y. A. Zhabanov, M. S. Mikhailov, P. A. Stuzhin, *Int. J. Mol. Sci.* **2020**, *21*, 2923. DOI:10.3390/ijms21082923
24. M. Wierzchowski, L. Sobotta, D. Łażewski, Kasprzycki, P., Fita, P., Goslinski, T. *J. Mol. Struct.* **2020**, *1203*, 127371. DOI:10.1016/j.molstruc.2019.127371
25. I. D. Karagöz, Y. Yilmaz, K. Sanusi, *J. Fluoresc.* **2020**, *30*, 1151–1160. DOI:10.1007/s10895-020-02584-1/Published.
26. M. J. Frisch, C. Adamo, A. J. Austin, et al. **2009**, Gaussian 09 Revision B.01. Gaussian Inc., Wallingford
27. R. Dennington, T. Keith, J. Millam, **2009**, GaussView, Version 5, Semichem Inc., Shawnee Mission, KS.
28. J. Foresman, E. Frish Exploring chemistry. **1996**, Gaussian Inc, Pittsburg.
29. R. G. Parr, Y. Weitao, *Density Functional Theory of Atoms and Molecules*, **1995**, Oxford University Press: New York.
30. R. K. Roy, N. Tajima, K. A Hirao, *J. Phys. Chem. A*, **2001**, *105*, 2117–2124. DOI:10.1021/jp0040087
31. R. K. Roy, S. Pal, K. Hirao, *J. Chem. Phys.* **1999**, *110*, 8236–8245. DOI:10.1063/1.478792
32. C. C. Leznoff, A. B. P. Lever, *Phthalocyanines: Properties and applications*, **1989**, VCH, New York
33. O. Bakaroglu, *Appl. Organomet. Chem.* **1996**, *10*, 605–622. DOI:10.1002/(SICI)1099-0739(199610)10:8<605::AID-AO-C527>3.0.CO;2-U
34. N. B. McKeown, *Phthalocyanine materials: Synthesis, structure and function*, **1998**, Cambridge University Press, Cambridge.
35. K. M. Kadish, K. M. Smith, R. Guilard, *The Porphyrin Handbook Phthalocyanines: Spectroscopic and Electrochemical Characterization*, **2003**, Academic Press, Boston
36. G. Socrates, *Infrared and Raman Characteristic Group Frequencies: Tables and Charts*, **2001**, John Wiley and Sons: Chichester.
37. N. Sundaraganesan, S. Ilakiamani, H. Saleem, P. M. Wojciechowski, D. Michalska, *Spectrochim. Acta A Mol. Biomol. Spectrosc.* **2005**, *61*, 2995–3001. DOI:10.1016/j.saa.2004.11.016
38. Ö. D. Kutlu, A. Erdoğan, P. Şen, S. Z. Yıldız, *J. Mol. Struct.* **2023**, *1284*, 135375. DOI:10.1016/j.molstruc.2023.135375
39. A. M. Sevim, H. Y. Yenilmez, M. Aydemir, A. Koca, Z. A. Bayir, *Electrochim. Acta* **2014**, *137*, 602–615. DOI:10.1016/j.electacta.2014.05.149
40. P. Tau, T. Nyokong, *Electrochim. Acta* **2007**, *52*, 3641–3650. DOI:10.1016/j.electacta.2006.10.023
41. P. Koza, T. Koczorowski, D. T. Mlynarczyk, T. Goslinski, Zinc (II) *Appl. Sci.* **2022**, *12*, 6825. DOI:10.3390/app12136825
42. T. Nyokong, *Coord. Chem. Rev.* **2007**, *251*, 1707–1722. DOI:10.1063/1.334486
43. P. A. Baruch, *J. Appl. Phys.* **1985**, *57*, 1347–1355. DOI:10.1063/1.334486
44. A. C. Yüzer, G. Kurtay, T. Ince, S. Yurtdaş, E. Harputlu, K. Ocakoglu, M. Güllü, C. Tozlu, M. Ince, *Mater. Sci. Semicond. Process* **2021**, *129*, 105777. DOI:10.1016/j.mssp.2021.105777
45. S. Samiee, P. Hossienpour, *Inorg. Chim. Acta* **2019**, *494*, 13–20. DOI:10.1016/j.ica.2019.05.006
46. O. Britel, A. Fitri, A. T. Benjelloun, M. Benzakour, M. Mcharfi, *Struct. Chem.* **2023**, *34*, 1827–1842. DOI:10.1007/s11224-023-02122-2
47. J. Zhang, S. Peng, S. Zheng, *Mater. Chem. Phys.* **2021**, *263*, 124420. DOI:10.1016/j.matchemphys.2021.124420
48. S. Aydogdu, A. Hatipoglu, *Acta Chim. Slov.* **2022**, *69*, 647–656. DOI:10.17344/acsi.2022.7522
49. I. Erden, A. Hatipoglu, C. Cebeci, S. Aydogdu, *J. Mol. Struct.* **2020**, *1201*, 127202. DOI:10.1016/j.molstruc.2019.127202
50. A. A. Piya, S. U. D. Shamim, M. N. Uddin, K. N. Munny, A. Alam, M. K. Hossain, F. Ahmed, *Comput. Theor. Chem.* **2021**, *1200*, 113241. DOI:10.1016/j.comptc.2021.113241
51. S. Aydogdu, A. Hatipoglu, *J. Indian Chem. Soc.* **2022**, *99*, 100752. DOI:10.1016/j.jics.2022.100752

Povzetek

V prispevku opisujemo sintezo, karakterizacijo in elektronske lastnosti novih 4-((7-metoksikinolin-4-il)oksi), 4-(kinolin-2-iltio) in 4-((7-(trifluorometil)kinolin-4-il)tio) periferno substituiranih okso-titanovih ftalocianinov. Strukture spojin smo določili z metodami UV-Vis, FTIR, ^1H NMR in MALDI-TOF masno spektrometrijo. Elektronske spektre teh molekulske in elektronske lastnosti spojin smo izračunali z metodama teorije gostotnega funkcionala (DFT) in **časovno** odvisno teorijo gostotnega funkcionala (TD-DFT). Preučevali smo vpliv topila na elektronske in geometrijske lastnosti spojin in njihovo reaktivnost. Izračunali smo globalne in lokalne indekse reaktivnosti in molekularni elektrostatski potencial na površinah spojin. Reaktivnost in elektronska struktura molekul se spreminja v odvisnosti od topila in substituent. Ugotovili smo, da so sintetizirane spojine uporabne na različnih področjih, npr. za solarne celice ali v fotodinamični terapiji.



Except when otherwise noted, articles in this journal are published under the terms and conditions of the Creative Commons Attribution 4.0 International License

Scientific paper

Exploring Teachers' Technological Pedagogical Content Knowledge as an Indicator for the Planning of In-service Teacher Training in Chemistry Education

Mojca Orel,^{1,*} Cirila Peklaj² and Vesna Ferk Savec³

¹ Gimnazija Moste, Zaloška 49, 1000 Ljubljana, Slovenia

² Faculty of Arts, Aškerčeva 2, 1000 Ljubljana, Slovenia

³ Faculty of Education, Kardeljeva ploščad 16, 1000 Ljubljana, Slovenia

* Corresponding author: E-mail: mojca.orel@guest.arnes.si

Received: 04-25-2024

Abstract

This study examined how teachers teaching chemistry at different levels of education perceive their levels of technological pedagogical content knowledge (TPACK) and examined the relationship of TPACK perceive levels with age, gender, teaching at different levels of education, time spent teaching chemistry, and frequency of information and communication technology (ICT) use. The study involved 261 teachers, 246 women and 15 men, from all over Slovenia, who have been teaching chemistry for an average of 18 years at different levels of education, with an average age of 45 years. The results showed that teachers teaching chemistry content perceive a high level of TPACK. There is a statistically significant correlation between age, time spent teaching chemistry, and frequency of ICT use with the perceived level of technological pedagogical content knowledge. Younger teachers, those with less professional experience and teachers who use ICT more frequently rated their TPACK higher. Based on the results of the survey, guidelines for planning the in-service teacher training that would support the development of TPACK of teachers teaching chemistry content were developed.

Keywords: Teacher demographic characteristics; information and communication technology; technological pedagogical content knowledge; chemistry teaching; in-service teacher training.

1. Introduction

In the information age, science teachers are constantly confronted with new opportunities and challenges resulting from the rapid pace of discovery in science and the remarkable development of information and communication technology (ICT), both of which simultaneously provide new opportunities and are a source of new ideas that can be effectively implemented in the processes of learning and teaching in science,¹ which also implies for chemistry education being one of the science education disciplines. With the development of ICT, it has become imperative for teachers to use modern technologies in the processes of learning and teaching, and it is necessary to transform pedagogical knowledge and redefine teachers' qualifications accordingly.² The role of ICT should not be understood as a potential replacement for great teachers but as a valuable tool that can be used transformatively in their hands.³ Therefore, contin-

uous in-service teacher training that would support the development of technological pedagogical content knowledge (TPACK) is crucial for successfully integrating teachers' technological pedagogical content knowledge in the planning and delivering science content instruction. Research results have shown that teacher training positively affects the development of TPACK.^{4–7} It is important that the delivery of in-service teacher training that would support their development of TPACK is directly linked to teachers' needs and the use of pedagogical approaches in the classroom and that training does not focus only on technological skills.^{8,9} Thus, it is important to note that it is not only technological knowledge that suffices to bridge this gap, but the integration of pedagogical, content and technological knowledge.^{10–12} In order to plan relevant in-service teacher training in chemistry education that would support their development of TPACK, it is, therefore, valuable to use teachers' perceived level of technological pedagogical con-

tent knowledge as one of the indicators of teachers' needs related to the efficient use of ICT in chemistry learning.

1. 1. TPACK

Technological pedagogical content knowledge (TPACK) is the integration of technological knowledge (TK), which includes knowledge of how to use different software and hardware; pedagogical knowledge (PK), which includes knowledge of learning processes, different strategies and methods of teaching and learning, and content knowledge (CK).^{13,14} Mishra and Koehler¹³ also included technological knowledge in Shulman's¹⁴ concept of pedagogical content knowledge (PCK). This was not an entirely new concept, but they were the first to clarify the links between all three components and their intersections in pairs.¹⁵ They emphasized that to integrate ICT and pedagogical knowledge into subject area teaching effectively, it is important to establish a dynamic relationship between all knowledge components.¹⁶

Because content knowledge (CK), pedagogical knowledge (PK), and technological knowledge (TK) are integrated, four new skills emerge: pedagogical content knowledge (PCK), technological content knowledge (TCK), technological pedagogical knowledge (TPK), and technological pedagogical content knowledge (TPACK).¹³ Thus, a total of seven skills are summarized in Table 1 and schematically depicted in Figure 1.

In 2007, the TPACK model was renamed to make it easier to pronounce the acronym; 'TPACK' stands for 'Technological Pedagogical And Content Knowledge'.¹⁷ In 2008, Koehler and Mishra added contexts to the TPACK model, with the intention that the TPACK model not exist in a vacuum but be placed in specific contexts, as represented by the outer dashed circle in the TPACK model in Figure 1.¹⁶ In 2019, the word 'context' in the basic TPACK model was replaced by 'contextual knowledge' (XK, derived from 'conTeXtual Knowledge'). Contextual Knowledge (XK) in the TPACK model is encompassed by a dotted circle and represents the teacher's knowledge of the

context, which includes everything from the teacher's awareness of the available technologies to the teacher's knowledge of the school, state or national politics.¹⁸

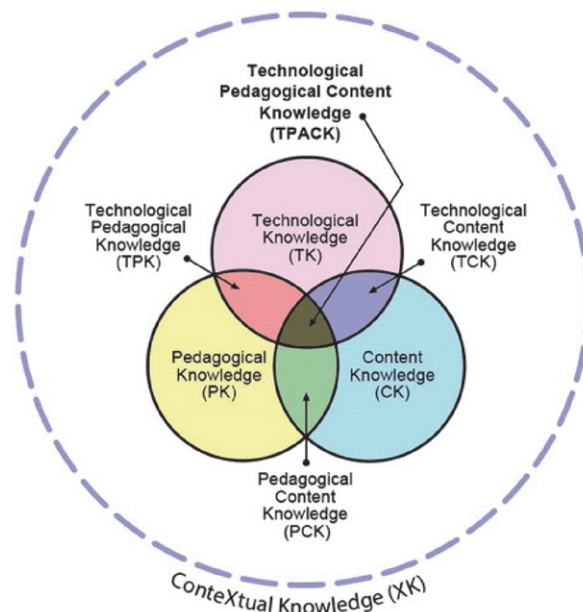


Figure 1: TPACK Model.¹⁸

There are three levels of TPACK perception: low, average and high. According to research, teachers perceive a high level of TPACK.^{2,4,19–22} In a study involving pre-service teachers found that for the factor (part of the items in the TPACK questionnaire) design, exertion and ethics, teachers perceived high level of TPACK, while for proficiency, they perceived an average level of TPACK.²¹ Çoklar and Özbek also reached the same results for primary and secondary school teachers,¹⁹ while Arslan found that pre-service teachers perceived high TPACK in all four factors.⁴ The same results were reached by Şentürk et al., who found that primary and secondary school teachers and educators perceived a high level of TPACK in all factors.²²

Table 1: Description of TPACK.¹³

Knowledge	Description
Content knowledge (CK)	Knowledge of subject matter.
Pedagogical knowledge (PK)	Knowledge of learning processes, different strategies and methods and techniques of teaching and learning.
Technological knowledge (TK)	Knowledge of how to use different software and hardware.
Pedagogical content knowledge (PCK)	Knowledge of strategies and methods for teaching and learning content with respect to subject matter content.
Technological content knowledge (TCK)	Knowledge of how to use appropriate technology to present content in a subject area.
Technological pedagogical knowledge (TPK)	Knowledge of which technology to choose when using a teaching and learning strategy or method.
Technological pedagogical content knowledge (TPACK)	It is the integration of technological knowledge, pedagogical knowledge and content knowledge.

1. 2. Teachers' Demographic Characteristics and Association with Perceived Levels of TPACK

Older teachers find it more difficult than younger teachers to integrate TPACK into the classroom.²³ Younger teachers are more likely to use ICT daily, making it easier to incorporate it into the classroom.²⁴ Younger teachers are more confident and experienced in adapting to and using new technologies. Their greater confidence and experience allow them to pick up new tools more quickly and adapt them to the specific needs of their students. Age may affect ICT integration and TPACK because older teachers tend to perceive greater barriers to ICT integration.²⁵ Existing research confirms that older teachers perceive lower TPACK levels than younger teachers.^{26,27}

Research on the association of teachers' gender with perceived levels of TPACK is inconsistent. Some research has shown no statistically significant gender differences in perceived TPACK.^{4,20,28–31} The gender difference in TPACK scores could be because male teachers tend to demonstrate more confidence and efficacy in ICT knowledge and skills.³² In addition, male teachers are more interested in technology than female teachers are.³³ In a study,³⁴ it was found that male teachers perceived higher levels of TPACK than female teachers do. This finding suggests that researchers and practitioners must consider gender when designing training programmes to develop teachers' knowledge of integrating technology into the classroom.

Liu et al. found that teachers with less teaching experience (1–5 years and 6–10 years) perceived significantly higher levels of TPACK than those with more teaching experience (11–20 years and over 20 years).³⁵ Teachers with less experience are also younger, having been introduced to ICT at a young age, and also use it more frequently in their daily lives, which allows them to integrate it more easily into the classroom.²⁴ Less-experienced science and mathematics teachers tended to perceive their level of TPACK significantly higher than more experienced teachers do.³⁰ These findings were consistent with those of other researchers.^{26,36}

Frequent ICT use is also related to teachers' perceptions of TPACK levels.⁴ The frequency of ICT use increases perceptions of TPACK levels.^{2,4,21,37}

However, unlike frequent ICT use, the level at which a teacher teaches is not related to the perceived level of TPACK.^{34,38}

2. Research Problem and Research Questions

TPACK has become very important as technology has become integral to teaching and learning chemistry. In reviewing research on TPACK, the number of studies in

this area increased from 2003 to 2013.³⁹ More than half of the research on TPACK has focused on TPACK in teachers in general, while relatively little research has examined TPACK in teachers of specific subject areas. However, most of the research was conducted in science and mathematics education. Most research has been conducted with preservice teachers, followed by secondary, primary and university teachers.

The number of publications on TPACK in chemistry education increased slightly between 2018 and 2020, while it decreased in the 2020–2023 period. They selected 22 publications from the Scopus database that were published between 2011 and 2022. No articles were published on the subject in 2012, 2013, 2016 and 2018, while the number of citations to articles increased during the 2018–2022 period and fluctuated during the 2011–2018 period. In addition, most of the articles were published by Indonesian researchers.⁴⁰

Despite a variety of research,^{4,5,7,39,41,42} the use of TPACK in teaching chemistry remains relatively unexplored, especially in terms of opportunities for more effective planning of training for teachers on the potential of ICT to support the learning and teaching of chemistry content, respectively. This area, therefore, represents a good opportunity for further research in the future. As technology has become an integral part of teaching and learning chemistry, ICT in chemistry has become important, and therefore, teacher training in this area is essential. Before developing worthwhile training, examining the relationship between teacher demographics and TPACK is essential in order to apply these findings to the design of training and to encourage, for example, age groups that are weaker in the integration of TPACK in the classroom to undertake in-service teacher training that would support their development of TPACK.

This study aims to investigate how teachers teaching chemistry content at different levels of education perceive their level of TPACK and to examine the factors that influence it.

The following two research questions were asked in the context of the study:

1. Which of the three levels of TPACK are perceived by teachers teaching chemistry?
2. Is there a statistically significant relationship between a teacher's perceived level of TPACK and the teacher's age, gender, the level of education they teach, the time spent teaching chemistry content and the frequency of ICT use?

3. Method

A quantitative research approach and a descriptive research method were used to examine the overall TPACK status of chemistry teachers and the association of teacher-perceived TPACK levels with age, gender, level

of education, time teaching chemistry, and frequency of ICT use.

3. 1. Sample

The survey used a representative sample: 261 teachers participated, 246 (94.25%) women and 15 (5.75%) men. Their ages ranged from 24 to 66 years, with mean age $M = 45.30$; $SD = 9.72$. Ten percent of primary and secondary schools in Slovenia were selected, equally represented from all 12 statistical regions, from a list published on the website of the Ministry of Education. The participants were teachers teaching chemistry at different levels of education. Sample included 18 (6.90%) secondary school chemistry teachers, 68 (26.05%) primary school chemistry teachers, 44 (16.86%) science teachers and 131 (50.19%) classroom teachers. They have been teaching chemistry for between 1 and 45 years, with an average of $M = 18.10$ and $SD = 10.80$.

3. 2. Instruments

We used two measuring instruments to collect the data:

- 1) The ICTCHEM questionnaire on the use of ICT for teaching chemistry.
- 2) The Technology Pedagogical Content Knowledge Questionnaire (TPACK) to measure the level of teachers' perception of TPACK.⁴³

The ICTCHEM questionnaire on the use of ICT for teaching chemistry was developed for the survey. Sensitivity was ensured by a multilevel or multiple-choice scale, and the objectivity of the performance was ensured by standardized instructions.

The questionnaire consists of questions to determine the following variables (gender, age, level of education, years of teaching chemistry). In addition, it contains a question on the frequency of use of ICT in teaching chemistry. For this question, a 5-point scale was used: '1 – never', '2 – rarely (up to 25% of teaching hours)', '3 – occasionally (25% to 50% of teaching hours)', '4 – often (50% to 75% of teaching hours)', and '5 – very often (75% to 100% of teaching hours)'.

To measure teachers' perceptions of TPACK levels, we used the TPACK questionnaire.⁴³ The questionnaire contains 33 items that include four factors: design (10 items), exertion (12 items), ethics (6 items), and proficiency (5 items).

The design factor covers items 1–10, which include an analysis of the current situation prior to the teaching process, the selection of methods, techniques and technologies, and the preparation of activities, materials, and instruments to be used in the teaching process (e.g., I can plan the teaching and learning process according to available technological resources.).

The exertion factor includes items 11–22 on implementing ICT-enhanced teaching and assessment plans (e.g., I can use technology to evaluate students' achievement in related content areas).

The ethics factor includes items 23–28 on ethical behavior in the use of ICT (e.g., I can behave ethically regarding the appropriate use of technology in educational environments.).

The proficiency factor includes items 29–33 related to the teacher's ability to integrate ICT into the teaching and learning process by demonstrating effective use of ICT. This factor refers to maintaining the teacher's capacity to integrate technological knowledge with content and pedagogical knowledge to become an expert in the teaching profession, to put forward proposals for solving problems related to the subject area, the teaching process and technology, and to choose the most appropriate one among these proposed solutions (e.g., I can use technology to find solutions to problems (structuring, updating and relating the content to real life, etc.)).

For each item, the teachers chose the most appropriate answer according to a 5-point Likert scale: '1 – strongly disagree', '2 – disagree', '3 – neither agree nor disagree', '4 – agree', '5 – strongly agree'.

There are three levels of TPACK perception: a low level of TPACK perception has an arithmetic mean between 1.00 and 2.33; an intermediate level of TPACK perception has an arithmetic mean between 2.34 and 3.67; and an advanced level of TPACK perception has an arithmetic mean between 3.68 and 5.00.²¹ In the study by Kabakçı Yurdakul et al.,⁴³ the Cronbach alpha reliability coefficient is 0.95 for the overall questionnaire, 0.92 for the design, 0.91 for the exertion, 0.86 for the ethics and 0.85 for the proficiency factor. In our study, the Cronbach alpha reliability coefficient for the whole questionnaire is 0.96; for the design factor, the Cronbach alpha reliability coefficient is 0.90; for the exertion factor, 0.92; for the ethics factor, 0.83; and for the proficiency factor, 0.85. Cronbach alpha reliability index values above 0.70 are acceptable, and values above 0.80 are defined as reliable.⁴⁴ In our study, we obtained similar Cronbach alpha reliability index values as in the original study. The calculated values indicate that the questionnaire is reliable.

The KMO test value in Kabakçı Yurdakul et al.⁴³ is 0.96, while in our study, it is 0.94, indicating that the data are suitable for factor analysis. The KMO test value, which can be between 0 and 1, is interpreted as normal if it is between 0.50 and 0.70, as good if it is between 0.70 and 0.80, as very good if it is between 0.80 and 0.90, and as excellent if it is above 0.90.⁴⁵ Since the KMO test value is very high (close to 1), it is interpreted as excellent, which means that the data are very suitable for pooling into factors. In our study, as in the study by Kabakçı Yurdakul et al.,⁴³ the four-factor structure of the TPACK questionnaire was validated by confirmatory factor analysis (CFA). We used the method of principal axes and Varimax rotation.

3. 3. Data Collection

The survey was conducted from 21 August to 16 October 2021. Questionnaires were sent to a selected sample

of primary and secondary school teachers. Participants completed the measuring instruments in digital format. Anonymity was ensured by encrypting the measuring instruments.

For the first research question, the data were analysed using descriptive statistics and the results are presented in terms of relative frequencies ($f\%$).

For the second research question, a chi-square test was used to determine whether age, gender, teaching at different levels of education, time spent teaching chemistry, and frequency of ICT use were statistically significantly related to the teacher's perceived level of TPACK, also for the individual TPACK factor (design, exertion, ethics, proficiency). To measure the effect size of the chi-square test, we used Cramér's V . To determine whether the correlation was highly proportional or inversely proportional, we used Kendall's τ coefficients. Associations between results are given at the 5% risk level.⁴⁴

The age of teachers was divided into five parts according to the life stages published in the study:⁴⁶ late adolescence (17–25 years), early adulthood (26–35 years), late adulthood (36–45 years), early elderly (46–55 years) and late elderly (56–66 years).

The years of chemistry content teaching were divided into five parts according to the periods published in the study:¹⁹ 1–5 years, 6–10 years, 11–15 years, 16–20 years, and 21 years and older.

The teaching of chemistry content was divided into four levels according to the level of education, depending on the grade or year taught by the teacher, to cover the vertical from the beginning of primary school to the end of secondary school: (Primary School – Classroom (Grades 1–5), Primary School – Science (Grades 6–7), Primary School – Chemistry (Grades 8–9), and Secondary School – Chemistry (Grades 1–4)).

4. Results and Discussion

4.1. Perceived Level of TPACK of Teachers Teaching Chemistry Content

Teachers teaching chemistry content perceive a high level of TPACK according to the value of the arithmetic mean ($M = 3.68$; $SD = 0.60$), which coincides with the results of other research.^{2,4,19–22} The majority of teachers teaching chemistry content perceive a high level of TPACK, while the least number of teachers teaching chemistry content perceive a low level of TPACK (Figure 2).

For the design factor, teachers teaching chemistry content perceive a high level of TPACK according to the value of the arithmetic mean ($M = 4.35$; $SD = 0.63$) which is consistent with other research.^{4,19,21,22} Most of the teachers teaching chemistry content perceive a high level of TPACK, while the least number of teachers who teach chemistry content perceive a low level of TPACK (Figure 3).

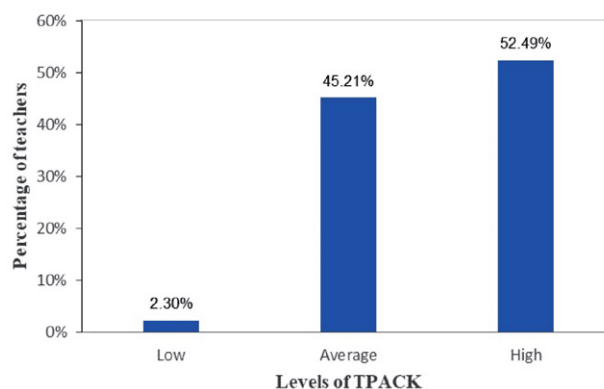


Figure 2: Percentage of teachers teaching chemistry according to each TPACK perception level for the whole TPACK questionnaire ($N = 261$).

Within the design factor, the item 'I can use technology to appropriately design materials to the needs for an effective teaching and learning process (e.g., PowerPoint presentations)' has the highest arithmetic mean ($M = 4.36$; $SD = 0.75$), followed by the item 'I can plan the teaching and learning process according to available technological resources' with the second highest arithmetic mean ($M = 4.18$; $SD = 0.64$).

Within the design factor, the item 'I can develop appropriate assessment tools by using technology' has the lowest arithmetic mean ($M = 3.51$; $SD = 0.95$), followed by the item 'I can optimise the duration of the lesson by using technologies (educational software, virtual labs, etc.)' with the second lowest arithmetic mean ($M = 3.58$; $SD = 0.89$), with the third lowest arithmetic mean ($M = 3.67$; $SD = 0.83$) for the item 'I can combine appropriate methods, techniques and technologies by evaluating their attributes in order to present the content effectively.'

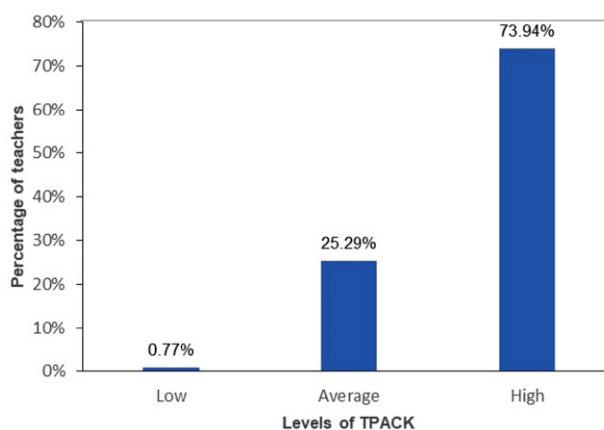


Figure 3: Percentage of teachers teaching chemistry according to each TPACK perception level for the design factor ($N = 261$).

For the exertion factor, teachers teaching chemistry content perceive a high level of TPACK according to the value of the arithmetic mean ($M = 3.72$; $SD = 0.62$), which

is consistent with other researchers.^{4,19,21,22} Most of the teachers teaching chemistry content perceive a high level of TPACK, while the least number of teachers teaching chemistry content perceive a low level of TPACK (Figure 4).

Within the exertion factor, the item 'I can implement effective classroom management in the teaching and learning process in which technology is used' has the highest arithmetic mean ($M = 4.11$; $SD = 0.73$), followed by the statement 'I can use technology to keep my content knowledge updated' with the second highest arithmetic mean ($M = 4.00$; $SD = 0.76$).

Within the exertion factor, the item with the lowest arithmetic mean ($M = 2.90$; $SD = 1.20$) is 'I can use innovative technologies (Facebook, blogs, Twitter, podcasting, etc.) to support the teaching and learning process', followed by the second lowest ($M = 3.49$; $SD = 1.00$) item 'I can guide students in the process of designing technology-based products (presentations, games, films, etc.)', followed by the third lowest ($M = 3.53$; $SD = 0.90$) item 'I can use technology for evaluating students' achievement in related content areas'.

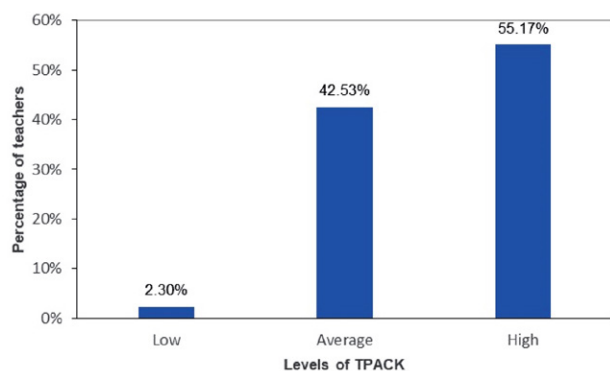


Figure 4: Percentage of teachers teaching chemistry according to each TPACK perception level for the exertion factor ($N = 261$).

For the ethics factor, teachers teaching chemistry content perceive an average level of TPACK according to the value of the arithmetic mean ($M = 3.66$; $SD = 0.70$), which does not coincide with other research in which teachers perceived a high level of TPACK.^{4,19,21,22} Most teachers teaching chemistry content perceive a high level of TPACK, while the least of the teachers teaching chemistry content perceive a low level of TPACK (Figure 5).

Within the ethics factor, the item 'I can behave ethically regarding the appropriate use of technology in educational environments' has the highest arithmetic mean ($M = 4.00$; $SD = 0.80$), followed by the item 'I can behave ethically in acquiring and using special/private information which will be used in teaching a subject area – via technology (audio records, video records, documents etc.)' with the second-highest arithmetic mean ($M = 3.91$; $SD = 0.88$).

Within the ethics factor, the item 'I can provide each student equal access to technology' has the lowest arith-

metic mean ($M = 3.13$; $SD = 1.16$), followed by the second lowest arithmetic mean ($M = 3.60$; $SD = 1.06$) for 'I can follow the teaching profession's codes of ethics in online educational environments (WebCT, Moodle, etc.)' followed by the third lowest arithmetic mean ($M = 3.62$; $SD = 0.92$) item 'I can use technology in every phase of the teaching and learning process by considering the copyright issues (e.g., license)'.

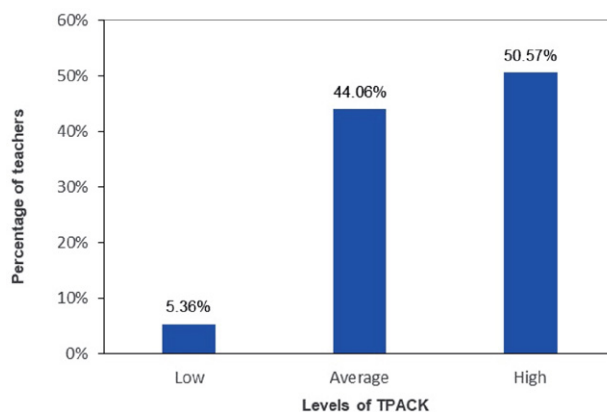


Figure 5: Percentage of teachers teaching chemistry according to each TPACK perception level for the ethics factor ($N = 261$).

For the proficiency factor, teachers teaching chemistry content perceive an intermediate level of TPACK according to the value of the arithmetic mean ($M = 2.98$, $SD = 0.80$), which is consistent with the research of Çoklar and Özbek¹⁹ and Şentürk et al.,²² but not consistent with the research of Arslan⁴ and Kabakçı Yurdakul,²¹ in which teachers perceived an advanced level of TPACK. Most teachers teaching chemistry content perceive an average level of TPACK, while the least number of teachers teaching chemistry content perceive a low level of TPACK (Figure 6).

Within the proficiency factor, the item 'I can use technology to find solutions to problems (structuring, updating and relating the content to real life, etc.)' has the highest arithmetic mean ($M = 3.55$; $SD = 0.90$), followed by the item 'I can cooperate with other disciplines regarding the use of technology to solve problems encountered in the process of presenting content' with the second-highest arithmetic mean ($M = 3.44$; $SD = 0.99$).

Within the proficiency factor, the item 'I can become a leader in spreading the use of technological innovations in my future teaching community' has the lowest arithmetic mean ($M = 2.46$; $SD = 1.13$), followed by the second lowest arithmetic mean ($M = 2.70$; $SD = 1.04$) for 'I can troubleshoot problems that could be encountered with online educational environments (WebCT, Moodle, etc.)' and with the third lowest arithmetic mean ($M = 2.75$; $SD = 0.98$) the statement 'I can troubleshoot any kind of problem that may occur while using technology in any phase of the teaching-learning process'.

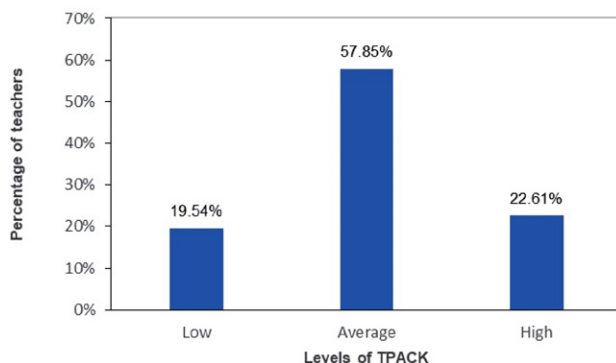


Figure 6: Percentage of teachers teaching chemistry according to each TPACK perception level for the proficiency factor ($N = 261$).

The highest arithmetic mean ($M = 4.36$, $SD = 0.75$) of all the items in the questionnaire is 'I can use technology to appropriately design materials to the needs for an effective teaching and learning process (e.g. PowerPoint presentations)', which is from the design factor, while Arslan had the highest value of arithmetic mean for the statement from the ethics factor in his study 'I can behave ethically regarding the appropriate use of technology in educational environments', which otherwise had the highest arithmetic mean within the ethics factor in our study.⁴

The lowest arithmetic mean ($M = 2.46$, $SD = 1.13$) is for the statement 'I can become a leader in spreading the use of technological innovations in my future teaching community', which is from the proficiency factor; had the lowest arithmetic mean value for the proficiency factor item 'I can troubleshoot problems that could be encountered with online educational environments (WebCT, Moodle, etc.)',⁴ which has the second lowest arithmetic mean of all the items in our study.

According to the value of the arithmetic mean, teachers teaching chemistry content perceive a high level of TPACK for the design and exertion factor, while they perceive an average level of TPACK for the ethics and proficiency factor (Figure 7).

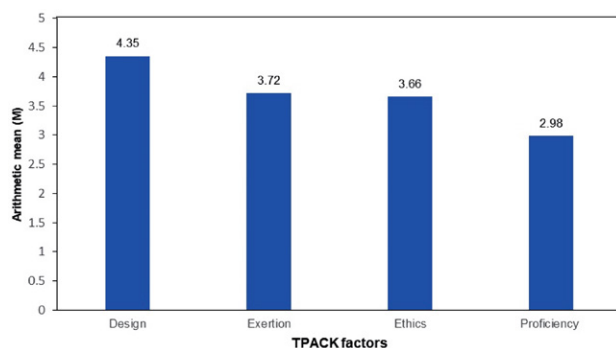


Figure 7: Arithmetic mean value for each factor of the TPVZ questionnaire.

Unlike the research in which teachers perceived a high level of TPACK,^{4,19,21,22} in our study, teachers

teaching chemistry content perceived an average level of TPACK in the ethics factor. Similarly, in the proficiency factor, teachers teaching chemistry content perceived an average level, which coincides with the findings of Kabakçı Yurdakul²¹ and Çoklar and Özbek,¹⁹ but not with those of Arslan⁴ and Kabakçı Yurdakul.²¹ For this reason, in the organization of TPACK training, we would devote more hours to proficiency in ethical behavior in the use of ICT, in which we would present the recommendations of the code of ethics for teachers in online educational environments. Therefore, more in-service teacher training hours should be devoted to the topics covered in the ethics and proficiency factor, as chemistry teachers perceived both factors as having an average level of TPVZ. We would also devote more TPACK training hours to the effective use of ICT in the classroom and, by presenting concrete examples of good practice, train teachers to link technological knowledge with content and pedagogical knowledge so that they become experts in the teaching profession, are able to put forward problem-solving proposals, and can become leaders in spreading the use of technological innovations in their teaching community.

4. 2. Relation of Demographic Variables to the Perceived Level of TPACK Relation of Age of Teachers to Perceived TPACK Level

The correlation between the age of the teachers teaching chemistry and the perceived level of TPACK is statistically significant ($\chi^2(8, N = 261) = 26.29$, $p = 0.001$, $V = 0.21$). Teachers' age is strongly correlated with teachers' perceived TPACK level. The direction of the association is inversely proportional because Kendall's τ coefficient is negative ($\tau = -0.21$), implying that in our study, as in the findings of other researchers,^{23,24,26,27} older teachers perceive a lower level of TPACK.

Teachers who perceive a low level of TPACK have a mean age of 54 years ($M = 53.80$; $SD = 4.71$), those who perceive an average level have a mean age of 47 years ($M = 47.20$; $SD = 9.35$), and those who perceive an advanced level have a mean age of 43 years ($M = 43.30$; $SD = 9.71$).

For the design factor ($\chi^2(8, N = 261) = 7.10$, $p = 0.53$), exertion ($\chi^2(8, N = 261) = 14.80$, $p = 0.063$) and ethics ($\chi^2(8, N = 261) = 13.18$, $p = 0.45$), the correlation between the age of the teachers teaching chemistry content and the perceived level of TPACK is not statistically significant.

In the proficiency factor ($\chi^2(8, N = 261) = 18.30$, $p = 0.00100$, $V = 0.23$), the correlation between the age of teachers teaching chemistry content and the perceived level of TPACK is statistically significant. Age is strongly correlated with the perceived level of TPACK. The direction of the association is inversely proportional because Kendall's τ coefficient is negative ($\tau = -0.23$).

We suggest more training for older teachers on integrating TPACK in the classroom, encouraging them to use ICT more often, overcoming barriers (e.g., fear of change, use of novelty) and developing their competencies to troubleshoot problems with online environments to become more flexible in implementing change.

The correlation of teachers' gender with perceived TPACK levels

The gender of the teacher teaching chemistry content is not related to the teacher's perceived level of TPACK ($\chi^2(2, N = 261) = 0.63, p = 0.73$), which is consistent with the results of other research.^{4,20,28–31}

For the design ($\chi^2(2, N = 261) = 0.14, p = 0.69$), exertion ($\chi^2(2, N = 261) = 1.01, p = 0.60$), ethics ($\chi^2(2, N = 261) = 0.90, p = 0.64$) and proficiency factor ($\chi^2(2, N = 261) = 3.54, p = 0.17$), the correlation of teacher gender with teacher perceived levels of TPACK is also not statistically significant.

Therefore, there is no need to differentiate between male and female teachers when designing in-service teacher training programmes that would support their development of TPACK because they have the same perceived level of TPACK.

The correlation of teaching at different levels of education with the perceived level of TPACK

Teaching at different levels of education is not related to teachers' perceived levels of TPACK ($\chi^2(6, N = 261) = 2.68, p = 0.85$), which is consistent with the other research.^{34,38} Also for the design ($\chi^2(6, N = 261) = 3.59, p = 0.73$), exertion ($\chi^2(6, N = 261) = 3.04, p = 0.80$), ethics ($\chi^2(6, N = 261) = 3.58, p = 0.73$), and proficiency factor ($\chi^2(6, N = 261) = 12.10, p = 0.060$), teaching at different educational levels is not related to teachers' perceived level of TPACK. Thus, teachers at varying levels of education (e.g., as a secondary school chemistry teacher, or as a primary school chemistry teacher, or as a science or classroom teacher) do not differ in their perceived level of TPACK.

The correlation of years of experience in teaching chemistry with perceived levels of TPACK

The experience in teaching chemistry is statistically significantly related to the teacher's perceived TPACK level ($\chi^2(8, N = 261) = 17.91, p = 0.02, V = 0.17$). It is also moderately strongly related to the teacher's perceived TPACK level.

In the proficiency factor ($\chi^2(8, N = 261) = 29.30, p = 0.001, V = 0.23$), years of experience in teaching chemistry is statistically significantly related to the teacher's perceived level of TPACK. The correlation is strong. For the design factor ($\chi^2(8, N = 261) = 9.05, p = 0.34$), exertion ($\chi^2(8, N = 261) = 9.84, p = 0.28$) and ethics ($\chi^2(10, N = 261)$

$= 14.02, p = 0.081$), the correlation of time spent teaching chemistry content with the teacher's perceived level of TPACK is not statistically significant.

Teachers perceiving a low TPACK level have been teaching chemistry for an average of 25 years ($M = 25.20; SD = 8.98$), those perceiving an average level of TPACK teach for an average of 20 years ($M = 20.40; SD = 11.10$), and those who perceive a high level of TPACK teach chemistry for an average of 16 years ($M = 15.80; SD = 10.10$).

The more years a teacher has been teaching chemistry, the lower their TPACK perception. In their research,^{26,30,35,36} the same findings were reached, that less experienced teachers tend to perceive their TPACK level significantly higher than more experienced teachers. This finding can be supported by the fact that less experienced teachers are also younger teachers who have been introduced to ICT in childhood, and their ICT training was also different and also use it more frequently in their daily lives, which allows them to integrate it more easily into their classrooms.²⁴ Teachers who have been teaching chemistry for a longer period should be encouraged to attend in-service teacher training that would support their development of TPACK in teaching and suggested integrating more ICT in their lessons, which could help them improve their perception of TPACK and better adapt to modern educational trends.

The correlation of frequency of ICT use with perceived TPACK levels

The frequency of ICT use is statistically significantly related to the teacher's perceived level of TPACK ($\chi^2(8, N = 261) = 44.55, p = 0.00100, V = 0.32$). The frequency of ICT use is strongly related to the teacher's perceived level of TPACK. Kendall's τ coefficient is positive ($\tau = 0.28$), meaning teachers who use ICT more frequently perceive a higher level of TPACK.

In the design ($\chi^2(8, N = 261) = 39.41, p = 0.00100, V = 0.42$), exertion ($\chi^2(8, N = 261) = 23.54, p = 0.00300, V = 0.26$), ethics ($\chi^2(8, N = 261) = 30.77, p = 0.00100, V = 0.32$) and proficiency factors ($\chi^2(8, N = 261) = 34.01, p = 0.00100, V = 0.26$), a statistically significant association of the frequency of ICT use with the teacher's perceived level of TPACK exists. For all factors, the frequency of ICT use is strongly correlated with the perceived level of TPACK.

Teachers who use ICT more frequently perceive higher levels of TPACK, which is consistent with the results of other research.^{2,4,21,37} Teachers who use ICT frequently also have more opportunities to collaborate with other teachers and exchange teaching ideas. This can help them to develop their TPACK as they can learn new ideas and examples of good use for teaching, which allows them to create more effective and engaging lessons for their students. By gaining new knowledge and experience and by continuously improving their ICT use, teachers' perception of the level of TPACK can increase over time.

5. Conclusions and Implications for Planning of In-service Teacher Training in Chemistry Education

The aims of our study were to investigate how teachers teaching chemistry at different levels of education perceive their level of TPACK and to examine the factors that influence it.

It was found that teachers teaching chemistry content perceive a high level of TPACK. There is a statistically significant relationship between age, time teaching chemistry content and frequency of ICT use with teachers' perceived TPACK, while there is no statistically significant relation between teacher gender and teaching at different levels of education with teachers' perceived level of TPACK. Therefore, when designing training to stimulate the development of teachers' TPACK in chemistry education, it is not necessary to design specific adjustments to the training according to teachers' gender. Given the different levels of education, adjustments in promoting the development of teachers' TPACK are not really necessary in terms of technological and pedagogical knowledge. It is important to adapt in-service teacher training in a way that empowers teachers of a particular level of chemistry education in the use of ICT in a way that is most supportive of the acquisition of chemistry knowledge of the level of education at which teachers are teaching.

The survey results suggest that it makes sense to encourage more intensive in-service teacher training that would support the development of TPACK for older teachers or those teachers who have been teaching chemistry for a longer period because they perceive a lower level of TPACK than younger teachers or those teachers who have been teaching chemistry for a shorter period. At the same time, it is important to continuously involve teachers in training sessions that promote the use of ICT and empower teachers with innovations, as research shows that teachers who use ICT more often perceive a higher level of TPACK. It would be better for these teachers to be involved in longer training sessions in which they actively experiment with the use of TPACK, get ongoing feedback and try things out again in practice.

The results of the research on teachers' perception of TPACK levels within the factor (design, exertion, ethics and proficiency) suggest that in-service teacher training in TPACK planning needs to include content and process skills that enable the development of appropriate assessment tools (e.g., quizzes, online surveys, online tests, etc.) through ICT and to present ways to use ICT to optimize the duration of a lesson (e.g. use of videos, animations, interactive multimedia, etc.) and to show, through concrete examples, how to combine appropriate teaching methods with the use of ICT to enable teachers to present the content effectively (e.g., use of multimedia, interactive assign-

ments, interactive textbooks, etc.).

As part of the support of the development of teachers' TPACK, in-service teacher training that would support their development of TPACK should include content and process skills that enable the use of innovative ICT (e.g., Facebook, blogs, Twitter, podcasts, etc.) to support the teaching and learning process, and teachers should be provided with guidelines to help them guide students in making products using ICT (e.g. presentations, games, films, etc.). In addition, in-service teacher training that would support their development of TPACK should present teachers with effective and field-tested ways of using ICT to assess pupils' achievement in related content areas and demonstrate appropriate teaching approaches and methods that consider individual differences between pupils when using ICT.

As the majority of teachers in the survey perceived an average level of TPACK in the ethics factor, to improve the situation in in-service teacher training that would support their development of TPACK, we would add to the content design guidelines for teachers on how to guide students to valid and reliable electronic resources, present rules of ethical behavior when using ICT in the educational environment and when obtaining specific/personal information to be used in teaching the subject area using ICT (audio recordings, video recordings, documents, etc.). We would detail the recommendations of the code of ethics for teachers in online educational environments (WebCT, Moodle, etc.) and demonstrate through concrete examples how to use ICT in all phases of the teaching and learning process, considering the relevant copyright (e.g., permissions for use).

Most teachers perceived an average level of TPACK in the proficiency factor of the research, and in-service teacher training that would support their development of TPACK would therefore include content and process skills that enable teachers to be able to troubleshoot problems that might arise when using online learning environments or that might arise during the use of ICT at any stage of the teaching or learning process. Also, more hours of training, with the demonstration of concrete and proven examples of good practice and testing what has been learnt in practice, would enable teachers to link technological knowledge with content and pedagogical knowledge so that they become experts in the teaching profession, able to use ICT to put forward proposals to find solutions to problems (structuring, updating and linking learning content to everyday life, etc.), to be able to collaborate with other disciplines in the use of ICT to solve the problems encountered in using online environments, and to be trained to become leaders in spreading the use of technological innovations in their teaching community.

The research also has the limitation that it was based on self-reported data derived from teachers' perceptions. To overcome this limitation, further research could test the TPACK of teachers teaching chemistry content in real sit-

uations where they could demonstrate their knowledge of specific subject areas. Therefore, to refine the design of the training further, further research would include a TPACK test consisting of practical tasks in the field of chemistry to test the TPACK of teachers teaching chemistry in real-life situations. One possibility is to have external assessors or students assess their TPACK as it is demonstrated in classroom work.

In conclusion, we suggest that changes in teaching approaches are inevitable, and therefore, we recommend that teachers teaching chemistry content should be prepared to adapt their teaching style to new challenges and to attend training courses, as improving technological pedagogical content knowledge is a process that requires time, openness to learning and adaptation. However, we recommend that the organizers of in-service teacher training courses that would support their development of TPACK in chemistry content areas check the teacher's perception of the level of TPACK with the TPACK questionnaire and the technological pedagogical content knowledge with the TPACK test prior to the training and plan the training in detail based on the results of the survey, which show the gaps in teachers' knowledge and indicates their needs.

6. References

- V. Ferk Savec, *LUMAT* **2017**, *51*, 12–22. DOI:10.31129/LUMAT.5.1.256
- C. Kadioğlu-Akbulut, A. Cetin-Dindar, Acar-Şeşen, B., S. Küçük, *Educ. Inf. Technol.* **2023**, *28*, 11657–11670. DOI:10.1007/s10639-023-11657-0
- A. Roy, *Int. J. Innov. Educ. Res.* **2019**, *7*, 414–422. DOI:10.31686/ijier.vol7.iss4.1433
- Y. Arslan, *J. Teach. Phys. Educ.* **2015**, *34*, 225–241. DOI:10.1123/jtpe.2013-0054
- R. Blonder, M. Jonatan Bar-Dov, Z., N. Benny, S. Rapand, S. Sakhnini, *Chem. Educ. Res. Pract.*, **2013**, *14*, 269–285. DOI:10.1039/C3RP00001J
- J. B. Harris, M. J. Hofer, *J. Res. Technol. Educ.* **2011**, *43*, 211–229. DOI:10.1080/15391523.2011.10782570
- L. Rogers, J. Twidle, *Res. Sci. Technol. Educ.* **2013**, *31*, 227–251. DOI:10.1080/02635143.2013.833900
- T. J. Kopcha, *Comput. Educ.* **2012**, *59*, 1109–1121. DOI:10.1016/j.compedu.2012.05.014
- F. M. Rokenes, R. J. Krumsvik, *Comput. Educ.* **2016**, *97*, 1–20. DOI:10.1016/j.compedu.2016.02.014
- A. Aslan, C. Zhu, *Int. J. Res. Educ. Sci.* **2016**, *2*, 359–370. DOI:10.21890/ijres.81048
- I. N. Umar, A. S. A. Hassan, *Procedia Soc. Behav. Sci.* **2015**, *197*, 2015–2021. DOI:10.1016/j.sbspro.2015.07.586
- M. E. Williams, *JIP*, **2017**, *19*, 1–20, <http://files.eric.ed.gov/fulltext/EJ1158372.pdf>, (assessed: March 1, 2024)
- P. Mishra, M. J. Koehler, *Teach. Coll. Rec.* **2006**, *108*, 1017–1054. DOI:10.1111/j.1467-9620.2006.00684.x
- L. S. Shulman, *Educ. Res.* **1986**, *15*, 4–14. DOI:10.3102/0013189X015002004
- S. Cox, *A Conceptual Analysis of Technological Pedagogical Content Knowledge* [Doctoral dissertation, Brigham Young University, Department of Instructional Psychology & Technology]. ScholarsArchive. **2008**. <https://scholarsarchive.byu.edu/cgi/viewcontent.cgi?article=2481&context=etd>, (assessed: March 1, 2024)
- M. J. Koehler, P. Mishra, *Contemp. Issues Technol. Teach. Educ.* **2009**, *9*, 60–70, <https://citejournal.org/volume-9/issue-1-09/general/what-is-technological-pedagogical-content-knowledge>, (assessed: March 1, 2024)
- A. D. Thompson, P. Mishra, *J. Comput. Teach. Educ.*, **2007**, *24*, 38–64. DOI:10.1080/10402454.2007.10784583
- P. Mishra, *J. Digit. Learn. Teach. Educ.* **2019**, *35*, 76–78. DOI:10.1080/21532974.2019.1588611
- A. N. Çoklar, A. Özbek, *J. Hum. Sci.* **2017**, *14*, 427–440. DOI:10.14687/jhs.v14i1.4413
- S. Farhadi, G. Öztürk, *Rev. Educ.*, **2023**, *47*. DOI:10.15517/revedu.v47i1.51920
- I. Kabakçı Yurdakul, *Hacet. Univ. J. Educ.* **2011**, *40*, 397–408, <https://hdl.handle.net/11421/10481>, (assessed: March 1, 2024)
- Ş. Şentürk, Uçar, H. T. İ. Gümüş, İ. Diksoy, *Educ. Q. Rev.* **2021**, *4*, 556–570. DOI:10.31014/aior.1993.04.02.266
- R. Scherer, F. Siddiq, T. Teo, *Comput. Educ.* **2015**, *88*, 202–214. DOI:10.1016/j.compedu.2015.05.005
- K., Cennamo, J. Ross, P. A. Ertmer, *Technology Integration for Meaningful Classroom Use: A Standards-Based Approach* (3rd ed.). Cengage Learning, **2018**.
- F. A. Inan, D. L. Lowther, *Educ. Technol. Res. Dev.* **2010**, *58*, 137–154. DOI:10.1007/s11423-009-9132-y
- J. H. L. Koh, C. S. Chai, C. C. Tsai, *J. Educ. Technol. Soc.* **2014**, *17*, 185–196. <http://www.jstor.org/stable/jeductechsoci.17.1.185>, (assessed: March 1, 2024)
- J.-C. Liang, C. S. Chai, J. H. L. Koh, C.-J. Yang, C.-C. Tsai, *Australas. J. Educ. Technol.* **2013**, *29*, 581–594. DOI:10.14742/ajet.299
- J. Castéra, C. C., Marre, M. C. K. Yok, K. Sherab, M. A. Impedovo, T. Sarapuu, A. D. Pedregosa, S. K. Malik, H. Armand, *Educ. Inf. Technol.* **2020**, *25*, 3003–3019. DOI:10.1007/s10639-020-10106-6
- T. Gnams, *Comput. Hum. Behav.* **2021**, *114*, 1–10. DOI:10.1016/j.chb.2020.106533
- S.-J. Jang, M.-F. Tsai, *Comput. Educ.* **2012**, *59*, 327–338.
- M. Li, *Eur. J. Math., Sci. Technol. Educ.* **2023**, *19*, em2301. DOI:10.29333/ejmste/13346
- L. Saikkonen, M.-T. Kaarakainen, *Comput. Educ.* **2021**, *168*, 104206. DOI:10.1016/j.compedu.2021.104206
- M. Marth, F. X. Bogner, *Int. J. Technol. Des. Educ.* **2019**, *29*(2), 217–229. DOI:10.1007/s10798-018-9447-2
- M. Mailizar, M. Hidayat, W. Artika, *J. Phys.: Conf. Ser.* **2021**, *1882*, 1–9. DOI:10.1088/1742-6596/1882/1/012041
- Q. Liu, S. Zhang, Q. Wang, *J. Educ. Comput. Res.* **2015**, *53*, 55–74. DOI:10.1177/0735633115585929
- F. N. Kumala, A. Ghufon, P. Pujiastuti, *Int. J. Instr.* **2022**, *15*, 77–100. DOI:10.29333/iji.2022.1545a

37. F. Paraskeva, H. Bouta, A. Papagianna, *Comput. Educ.* **2008**, *50*, 1084–1091. DOI:10.1016/j.compedu.2006.10.006
38. Ö. Simsek, F. Sarsar, *World J. Educ.* **2019**, *9*, 196–208. DOI:10.5430/wje.v9n1p196
39. Y.-T. Wu, *Br. J. Educ. Technol.* **2013**, *44*, E73–E76. DOI:10.1111/j.1467-8535.2012.01349.x
40. M. Marlina, A. Rahim, R. R. Peby Ria, H. S. Hadi, *Moroc. J. Chem.* **2023**, *14*, 742–755. DOI:10.48317/IMIST.PRSM/morjchem-v11i3.39572
41. J. Gil-Flores, J. Rodríguez-Santero, J.-J. Torres-Gordillo, *Comput. Hum. Behav.* **2017**, *68*, 441–449. DOI:10.1016/j.chb.2016.11.057
42. J. M. Rosenberg, M. J. Koehler, *J. Res. Technol. Educ.*, **2015**, *47*, 186–210. DOI:10.1080/15391523.2015.1052663
43. I. Kabakçı Yurdakul, H. F. Odabasi, K. Kilicer, A. N. Coklar, G. Birinci, A. A. Kurt, *Comput. Educ.* **2012**, *58*, 964–977. DOI:10.1016/j.compedu.2011.10.012
44. J. Pallant, *SPSS survival manual: a step by step guide to data analysis using SPSS*, 4th ed. Maidenhead: Open University Press/McGraw-Hill, **2010**.
45. A. Field, *Discovering statistics using SPSS*, 2nd ed. Sage Publications Ltd, **2005**.
46. P. P. Anzari, I. H. Al Shiddiq, S. S. Pratiwi, M. N. Fatanti, D. F. V. Silvallana, *Int. J. Emerg. Technol. Learn.* **2021**, *16*, 146–159. DOI:10.3991/ijet.v16i07.21229

Povzetek

V raziskavi smo preverjali, kako učitelji, ki poučujejo kemijske vsebine na različnih ravneh izobraževanja, zaznajo lastno raven tehnološko vsebinsko pedagoškega znanja ter preučili povezavo zaznane učiteljeve ravni tehnološko pedagoško vsebinskega znanja s starostjo, s spolom, s poučevanjem na različnih ravneh izobraževanja, s časom poučevanja kemijskih vsebin in s pogostostjo uporabe informacijsko-komunikacijske tehnologije. V raziskavi je sodelovalo 261 učiteljev od tega 246 žensk in 15 moških iz vse Slovenije, ki poučujejo kemijske vsebine v povprečju 18 let na različnih ravneh izobraževanja s povprečno starostjo 45 let. Rezultati so pokazali, da zaznajo učitelji, ki poučujejo kemijske vsebine, višoko raven tehnološko pedagoško vsebinskega znanja. Med starostjo, časom poučevanja kemijskih vsebin in pogostostjo uporabe informacijsko-komunikacijske tehnologije je statistično pomembna povezanost z zaznano ravno tehnološko pedagoško vsebinskega znanja. Na osnovi rezultatov raziskave so bile pripravljene smernice za načrtovanje strokovnega izobraževanja učiteljev, ki poučujejo kemijske vsebine.



Except when otherwise noted, articles in this journal are published under the terms and conditions of the Creative Commons Attribution 4.0 International License

Synthesis, Crystal Structures and Antibacterial Activity of Nickel(II), Cadmium(II) and Zinc(II) Complexes with Hydrazone Ligands

Wei-Guang Zhang

College of Chemistry and Chemical Engineering, Qiqihar University, Qiqihar 161006, P. R. China

* Corresponding author: E-mail: zhangweiguang1230@163.com

Received: 04-11-2024

Abstract

Three mononuclear nickel(II), cadmium(II) and zinc(II) complexes, $[\text{NiL}_2] \cdot 2\text{CH}_3\text{OH} \cdot \text{H}_2\text{O}$ (**1**), $[\text{CdL}_2(\text{HL})] \cdot \text{CH}_3\text{OH}$ (**2**) and $[\text{ZnL}_2]$ (**3**), have been synthesized from 3-hydroxy-4-methoxy-*N'*-[(*Z*)-(pyridin-2-yl)methylidene]benzohydrazide (HL) by microwave irradiation method. All complexes were characterized by CHN elemental analyses and infrared spectra. Structures of the complexes were further studied by single crystal X-ray determination, which reveals that the Ni and Zn atoms in complexes **1** and **3** are in octahedral coordination, and the Cd atom in complex **2** is in square pyramidal coordination. The biological activity of the complexes on the bacterial strains *Bacillus subtilis*, *Staphylococcus aureus*, *Pseudomonas aeruginosa* and *Escherichia coli* was evaluated. As a result, the zinc complex has interesting antibacterial activities.

Keywords: Hydrazone; nickel complex; cadmium complex; zinc complex; antibacterial activity

1. Introduction

Microwave-assisted synthesis of various organic and coordination compounds has received much attention in recent years because it can accelerate their reactions.¹ In addition, this method has obvious advantages in providing a cheap, clean and easy handling heating way in the synthesis of various types of compounds with higher yields and less reaction time by comparing with those heating at reflux in organic solvents or solvothermal method.² Till date, microwave irradiation is considered to be one of the robust and efficient techniques for the synthesis of Schiff base metal complexes. The greatest advantage of this technique is the extraordinary acceleration in reaction rate when compared to conventional method.³ Hydrazones can be prepared by reaction of aldehydes and aroylhydrazines. They and their metal complexes have various biological activities such as antibacterial,⁴ anticancer,⁵ antitubercular,⁶ as well as enzyme inhibition.⁷ When bioorganic molecules or drugs are bound to metal ions, there is drastic enhance in their biomimetic properties, therapeutic effects and pharmacological properties.⁸ Orojloo and coworkers reported some cobalt(II), nickel(II), copper(II) and zinc(II) complexes derived from the Schiff base ligands 4-((2,4-dichlorophenyl)diazanyl)-2-(3-hydroxypropylimino)methyl)phenol and 2-((3-hydroxypropylimino)methyl)-4-(thiazol-2-yl)diazanylphenol. As a result, the complexes have higher activities as compared with the free Schiff bases.⁹ Nickel, cadmium and zinc complexes are reported to be biological active like antimicrobial, anticancer, antioxidant, and DNA binding properties.¹⁰ As a continuation of our work on metal complexes with biological activities,¹¹ in this study, the synthesis, characterization and antibacterial properties of three new complexes $[\text{NiL}_2] \cdot 2\text{CH}_3\text{OH} \cdot \text{H}_2\text{O}$ (**1**), $[\text{CdL}_2(\text{HL})] \cdot \text{CH}_3\text{OH}$ (**2**) and $[\text{ZnL}_2]$ (**3**), derived from 3-hydroxy-4-methoxy-*N'*-[(*Z*)-(pyridin-2-yl)methylidene]benzohydrazide (HL), are presented.

2. Experimental

2.1. Materials and Physical Methods

Pyridine-2-carboxaldehyde, 3-hydroxyl-4-methoxybenzohydrazide, nickel acetate, cadmium iodide, and zinc acetate were obtained from TCI. The solvents were of AR grade and used as received. The microwave synthesis was carried out with a WX-4000 microwave digestion system. CHN elemental analyses were performed on a Perkin-Elmer 2400 Elemental Analyzer. Infrared spectra were recorded on a Bio-Rad FTS 135 spectrophotometer with KBr pellets.

X-ray single crystal structure diffraction was determined with a Bruker Smart 1000 CCD diffractometer.

2. 2. Synthesis of HL

Pyridine-2-carboxaldehyde (0.11 g, 1.0 mmol) and 3-hydroxyl-4-methoxybenzohydrazide (0.18 g, 1.0 mmol) were mixed in methanol, and stirred at reflux for 30 min. The reaction mixture was evaporated to give colorless solid, which was recrystallized from methanol to give crystalline product. Yield: 0.24 g (89%). Anal. Calcd. for $C_{14}H_{13}N_3O_3$ (%): C, 61.99; H, 4.83; N, 15.49. Found (%): C, 62.23; H, 4.90; N, 15.37. IR data (KBr, cm^{-1}): 3308, 3272, 1684, 1621, 1569, 1507, 1461, 1425, 1331, 1305, 1273, 1232, 1145, 1113, 1029, 885, 843, 817, 760, 713, 646, 578. 1H NMR (500 MHz, d_6 -DMSO): δ 9.49 (s, 1H, OH), 9.12 (s, 1H, NH), 8.63 (d, 1H, PyH), 7.87 (d, 1H, PyH), 7.81 (t, 1H, PyH), 7.60 (t, 1H, PyH), 7.45 (s, 1H, CH=N), 7.29 (m, 2H, ArH), 6.95 (d, 1H, ArH), 3.85 (s, 3H, CH_3). ^{13}C NMR (126 MHz, d_6 -DMSO): δ 165.8, 153.2, 150.0, 148.7, 145.9, 144.3, 136.2, 128.1, 126.7, 125.6, 121.3, 120.1, 115.3, 55.6.

2. 3. Synthesis of the Complexes

The three complexes were prepared with the same method as described. Pyridine-2-carboxaldehyde (0.11 g, 1.0 mmol), 3-hydroxyl-4-methoxybenzohydrazide (0.18 g, 1.0 mmol), methanol (30 mL) and metal salts (1.0 mmol as follows) were placed in a Teflon-lined autoclave (30

mL). The reaction mixture was maintained at 350 K and 200 W for 10 min at the cavity of the microwave reactor. Then the reaction mixture was cooled to room temperature for about 60 min. The mixtures were filtered and with the filtrate to slow evaporate in air for a week. Well shaped single crystals were formed and collected by filtration and washed with cold methanol.

2. 3. 1. $[NiL_2] \cdot 2CH_3OH \cdot H_2O$ (1)

Nickel acetate tetrahydrate (0.25 g, 1.0 mmol). Yield: 0.22 g (65%). Anal. Calcd. for $C_{30}H_{34}N_6NiO_9$ (%): C, 52.89; H, 5.03; N, 12.34. Found (%): C, 52.73; H, 5.10; N, 12.17. IR data (KBr, cm^{-1}): 1605, 1561, 1517, 1489, 1460, 1423, 1365, 1351, 1328, 1268, 1243, 1217, 1180, 1134, 1118, 1072, 1015, 971, 878, 855, 820, 765, 680, 643, 599, 555, 518, 493.

2. 3. 2. $[CdI_2(HL)] \cdot CH_3OH$ (2)

Cadmium iodide (0.37 g, 1.0 mmol). Yield: 0.41 g (61%). Anal. Calcd. for $C_{15}H_{17}CdI_2N_3O_4$ (%): C, 26.91; H, 2.56; N, 6.28. Found (%): C, 27.05; H, 2.47; N, 6.22. IR data (KBr, cm^{-1}): 1628, 1614, 1580, 1550, 1508, 1473, 1441, 1358, 1293, 1229, 1212, 1146, 1125, 1083, 1010, 968, 878, 827, 783, 767, 747, 638, 576, 532, 507, 472.

2. 3. 3. $[ZnL_2]$ (3)

Zinc acetate dihydrate (0.22 g, 1.0 mmol). Yield: 0.23 g (74%). Anal. Calcd. for $C_{28}H_{24}N_6O_6Zn$ (%): C, 55.50; H,

Table 1. Crystallographic data for the complexes

Complex	1	2	3
Formula	$C_{30}H_{34}N_6NiO_9$	$C_{15}H_{17}CdI_2N_3O_4$	$C_{28}H_{24}N_6O_6Zn$
Formula weight	681.34	669.52	605.90
Crystal system	Orthorhombic	Monoclinic	Triclinic
Space group	<i>Pbca</i>	<i>P2₁/c</i>	<i>P-1</i>
<i>a</i> (Å)	15.1673(10)	8.3494(13)	8.4352(10)
<i>b</i> (Å)	19.8159(10)	14.3589(15)	11.4227(11)
<i>c</i> (Å)	20.9173(13)	17.4204(13)	14.7073(15)
α (°)	90	90	88.9880(10)
β (°)	90	95.9160(10)	77.2480(10)
γ (°)	90	90	74.8700(10)
<i>V</i> (Å ³)	6286.8(7)	2077.4(4)	1333.0(2)
λ (Å)	0.71073	0.71073	0.71073
ρ_{calcd} (g cm ⁻³)	1.440	2.141	1.510
<i>Z</i>	8	4	2
μ (mm ⁻¹)	0.680	4.046	0.977
θ ranges (°)	1.95–25.50	1.84–25.50	2.28–25.50
Reflections collected	32240	11012	13780
Independent reflections	5852	3868	4953
Observed reflections ($I \geq 2\sigma(I)$)	3587	2927	2871
Restraints	25	2	2
Parameters	437	234	380
Goodness-of-fit on F^2	1.027	1.039	1.018
Final <i>R</i> indices [$I \geq 2\sigma(I)$]	0.0500, 0.1057	0.0321, 0.0607	0.0586, 0.1283
<i>R</i> indices (all data)	0.1028, 0.1293	0.0491, 0.0673	0.1180, 0.1513

3.99; N, 13.87. Found (%): C, 55.28; H, 4.07; N, 13.96. IR data (KBr, cm^{-1}): 1605, 1563, 1515, 1489, 1462, 1420, 1356, 1270, 1241, 1215, 1178, 1137, 1118, 1072, 1028, 1014, 973, 929, 878, 853, 818, 763, 680, 641, 601, 556, 516, 488, 438.

2. 4. X-Ray Structure Determination

X-ray single crystal diffraction was performed on a diffractometer equipped with a graphite monochromated Mo-K α radiation ($\lambda = 0.71073 \text{ \AA}$) at 298(2) K. The collected data were integrated and reduced with SAINT.¹² Structures of the five complexes were solved by direct methods and refined by full-matrix least-squares based on F^2 with SHELXL.¹³ The empirical absorption correction was applied with SADABS.¹⁴ All non-H atoms were anisotropically refined. The H atoms attached to O and N atoms in the complexes were located from difference Fourier maps and refined isotropically, with O–H, N–H and H...H distances restrained to 0.85(1), 0.90(1) and 1.37(2) \AA , respectively. Selected crystal data for the complexes are summarized in Table 1.

Table 2. Selected bond distances (\AA) and bond angles ($^\circ$) for the complexes

1			
Ni1–O1	2.119(3)	Ni1–O2	2.067(3)
Ni1–N2	1.974(3)	Ni1–N3	2.109(3)
Ni1–N5	1.971(3)	Ni1–N6	2.117(3)
N5–Ni1–N2	177.72(13)	N5–Ni1–O2	76.66(11)
N2–Ni1–O2	101.20(12)	N5–Ni1–N3	102.44(13)
N2–Ni1–N3	78.30(13)	O2–Ni1–N3	91.06(12)
N5–Ni1–N6	78.28(13)	N2–Ni1–N6	103.84(13)
O2–Ni1–N6	154.94(12)	N3–Ni1–N6	94.95(13)
N5–Ni1–O1	103.53(12)	N2–Ni1–O1	75.69(12)
O2–Ni1–O1	93.67(10)	N3–Ni1–O1	154.00(12)
N6–Ni1–O1	91.51(11)		
2			
Cd1–I1	2.7147(5)	Cd1–I2	2.7441(6)
Cd1–O1	2.445(3)	Cd1–N2	2.335(4)
Cd1–N3	2.383(4)		
N2–Cd1–N3	69.28(13)	N2–Cd1–O1	65.69(12)
N3–Cd1–O1	134.54(12)	N2–Cd1–I1	125.52(9)
N3–Cd1–I1	104.39(9)	O1–Cd1–I1	96.59(8)
N2–Cd1–I2	115.26(9)	N3–Cd1–I2	103.18(9)
O1–Cd1–I2	101.12(9)	I1–Cd1–I2	118.695(18)
3			
Zn1–O1	2.207(3)	Zn1–O2	2.141(3)
Zn1–N2	2.067(4)	Zn1–N3	2.219(4)
Zn1–N5	2.052(4)	Zn1–N6	2.291(4)
N5–Zn1–N2	177.60(16)	N5–Zn1–O2	74.66(14)
N2–Zn1–O2	106.23(14)	N5–Zn1–O1	105.27(13)
N2–Zn1–O1	72.42(14)	O2–Zn1–O1	100.22(13)
N5–Zn1–N3	106.92(15)	N2–Zn1–N3	75.27(16)
O2–Zn1–N3	96.50(14)	O1–Zn1–N3	146.64(14)
N5–Zn1–N6	74.60(15)	N2–Zn1–N6	104.71(15)
O2–Zn1–N6	148.77(14)	O1–Zn1–N6	92.99(13)
N3–Zn1–N6	87.25(15)		

rized in Table 1. Coordinate bond lengths and bond angles are provided in Table 2.

2. 5. Antibacterial Assay

The hydrazone HL and the three complexes were assayed *in vitro* antibacterial activities against two Gram-positive bacteria strains *Staphylococcus aureus* and *Bacillus subtilis*, and two Gram-negative bacteria strains *Escherichia coli* and *Pseudomonas aeruginosa* by agar well diffusion method with the literature method.¹⁵ The negative and positive references are DMSO and Ciprofloxacin, respectively.

2. 6. Determination of Minimum Inhibitory Concentration (MIC)

MIC values of the compounds was tested through a modified agar well diffusion method.¹⁶ A two-fold serial dilution of each compound was prepared by first reconstituting in DMSO followed by dilution in sterile distilled water to achieve a decreasing concentration range 256 μM . Each dilution (100 μL) was introduced into wells in the agar plates seeded with 100 μL of standardized inoculums (10^6 cfu mL^{-1}) of the microbial strain. All test plates were incubated aerobically at 37 $^\circ\text{C}$ for 24 h and observed for the inhibition zones.

3. Results and Discussion

3. 1. Chemistry

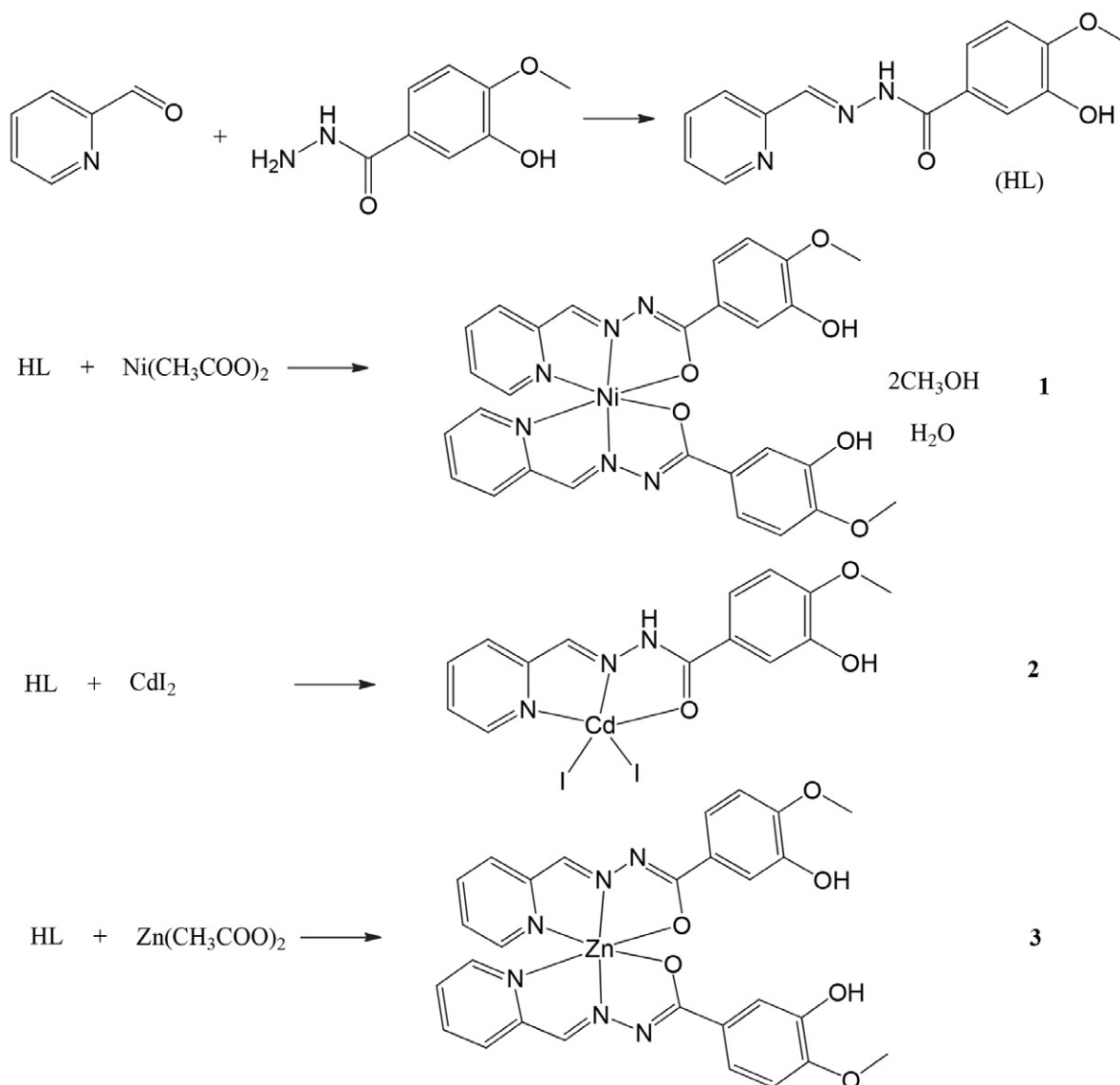
Reaction of in situ formed HL with nickel acetate (for **1**), cadmium iodide (for **2**) and zinc acetate (for **3**), respectively, afforded the complexes (Scheme 1).

3. 2. IR Spectra

In the IR spectra of complexes **1** and **3**, the characteristic imine stretching is observed at 1605 cm^{-1} as strong signals.¹⁷ In complex **2**, the imine stretching is observed at 1614 cm^{-1} . This is in agreement with the different lengths of C=N bonds in these complexes. There is an obvious strong absorption at 1628 cm^{-1} in the spectrum of complex **2**, while absence in the other two complexes, which is assigned to C=O vibration.¹⁸ Coordination of the ligands is further confirmed by the appearance of weak bands in the low wave numbers 400–600 cm^{-1} , corresponding to $\nu(\text{M–N})$, $\nu(\text{M–O})$ and $\nu(\text{M–I})$.¹⁹

3. 3. Structure Description of Complex 1

The molecular structure of complex **1** is shown in Fig. 1. The compound contains a mononuclear $[\text{NiL}_2]$ complex molecule, and one water and two methanol molecules of crystallization. The Ni atom is coordinated by two pyri-



Scheme 1. The synthetic procedure for HL and the complexes.

dine nitrogens (N3, N6), two imino nitrogens (N2, N5), and two enolate oxygens (O1, O2) from two hydrazone ligands, forming octahedral geometry. The octahedral coordination is distorted from the ideal model, which can be evidenced by the bond angles, ranging from 75.69(12) to 103.84(13)° for the *cis* angles, and from 154.00(12) to 177.72(13)° for the *trans* angles. The distortion arises from the strain created by the four five-membered chelate rings. The lengths of Ni–O bonds (2.067(3)–2.119(3) Å) and Zn–N bonds (1.971(3)–2.117(3) Å) are comparable to those observed in Schiff base nickel complexes with octahedral coordination.²⁰ The C1–C6 benzene ring and the C9–C13–N3 pyridine ring form a dihedral angle of 19.6(5)°. The C15–C20 benzene ring and the C23–C27–N6 pyridine ring form a dihedral angle of 2.3(5)°. In the crystal structure, the complex molecules and the solvent molecules are linked through intermolecular hydrogen bonds

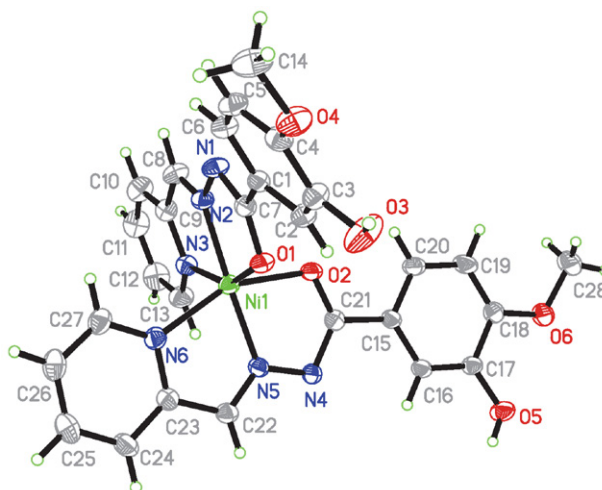


Fig. 1. Molecular structure of complex 1. Displacement ellipsoids are drawn at the 30% probability level. The solvent molecules are omitted for clarity.

of O–H...N, O–H...O and C–H...O, to form a three-dimensional network (Fig. 2).

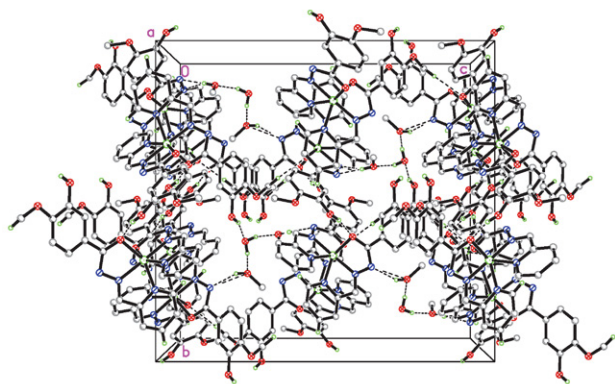


Fig. 2. Molecular packing diagram of complex 1, viewed along the *a* axis. Hydrogen bonds are shown as dashed lines. H atoms not involved in hydrogen bonding are omitted for clarity.

3. 4. Structure Description of Complex 2

The molecular structure of complex 2 is shown in Fig. 3. The compound contains a mononuclear $[\text{CdI}_2(\text{HL})]$ complex molecule and a methanol molecule of crystallization. The Cd atom is coordinated by one pyridine nitrogen (N3), one imino nitrogen (N2), and one carbonyl oxygen (O1) of a hydrazone ligand, and two I ligands (I1, I2), forming square pyramidal geometry. The basal plane is defined by N2, N3, O1 and I1 atoms, and the apical position is occupied by I2 atom. The square pyramidal coordination is distorted from the ideal model, which can be evidenced by the bond angles. The angles in the basal plane are range from $65.69(12)$ to $104.39(9)^\circ$ for *cis* angles and from $125.52(9)$ to $134.54(12)^\circ$ for *trans* angles. The angles among the apical and basal donor atoms are $101.12(9)$ – $118.695(18)^\circ$. The distortion arises from the strain created by the two five-membered chelate rings. The square pyramidal geometry is evidenced by the index value τ of 0.15.²¹ The lengths of Cd–O bond ($2.445(3)$ Å) and Cd–N bonds ($2.335(4)$ – $2.383(4)$ Å) are comparable to those observed in Schiff base cadmium complexes.²² The

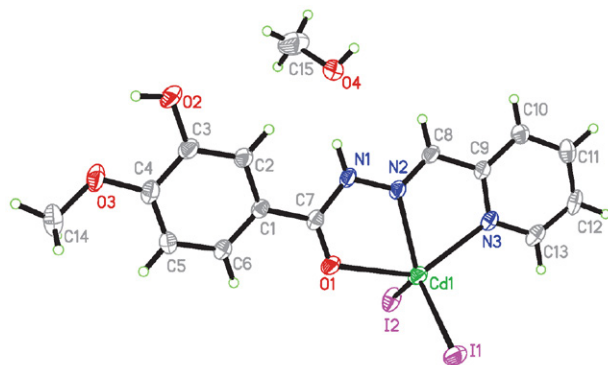


Fig. 3. Molecular structure of complex 2. Displacement ellipsoids are drawn at the 30% probability level.

C1–C6 benzene ring and the C9–C13–N3 pyridine ring form a dihedral angle of $11.1(3)^\circ$. In the crystal structure, the complex molecules and the solvent molecules are linked through intermolecular hydrogen bonds of N–H...O, O–H...O and O–H...I, to form a three-dimensional network (Fig. 4).

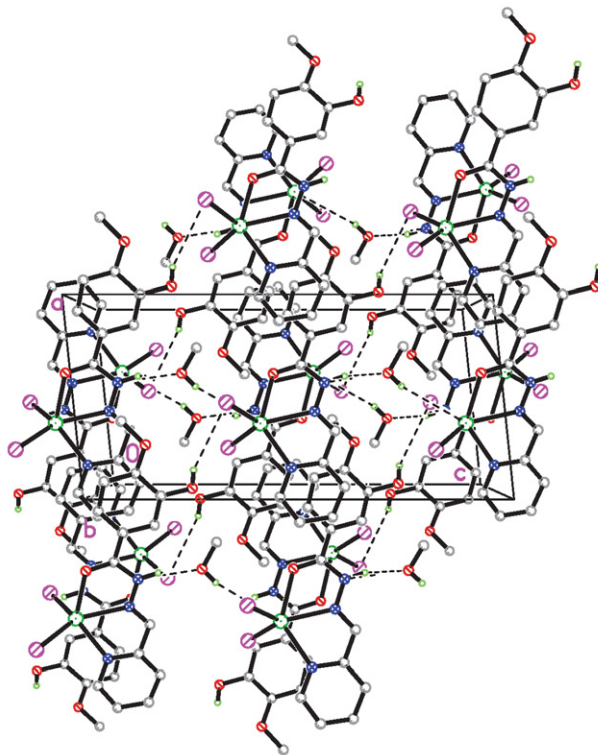


Fig. 4. Molecular packing diagram of complex 2, viewed along the *b* axis. Hydrogen bonds are shown as dashed lines. H atoms not involved in hydrogen bonding are omitted for clarity.

3. 5. Structure Description of Complex 3

The molecular structure of complex 3 is shown in Fig. 5. The Zn atom is coordinated by two pyridine nitrogens (N3, N6), two imino nitrogens (N2, N5), and two enolate oxygens (O1, O2) from two hydrazone ligands, forming octahedral geometry. The octahedral coordination is distorted from the ideal model, which can be evidenced by the bond angles, ranging from $74.60(15)$ to $106.92(15)^\circ$ for the *cis* angles, and from $146.64(14)$ to $177.60(16)^\circ$ for the *trans* angles. The distortion arises from the strain created by the four five-membered chelate rings. The lengths of Zn–O bonds ($2.141(3)$ – $2.207(3)$ Å) and Zn–N bonds ($2.052(4)$ – $2.291(4)$ Å) are comparable to those observed in Schiff base zinc complexes with octahedral coordination.²³ The C1–C6 benzene ring and the C9–C13–N3 pyridine ring form a dihedral angle of $40.3(6)^\circ$. The C15–C20 benzene ring and the C23–C27–N6 pyridine ring form a dihedral angle of $18.3(6)^\circ$. In the crystal structure, the complex molecules are linked through intermolecular hydrogen

bonds of O–H...N, O–H...O, C–H...N and C–H...O, to form a three-dimensional network (Fig. 6).

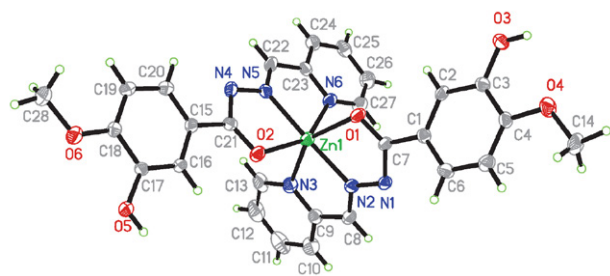


Fig. 5. Molecular structure of complex 3. Displacement ellipsoids are drawn at the 30% probability level. Hydrogen bonds are shown as dashed lines.

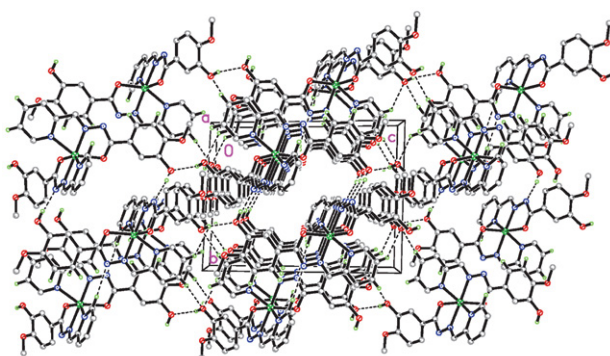


Fig. 6. Molecular packing diagram of complex 3, viewed along the *a* axis. Hydrogen bonds are shown as dashed lines. H atoms not involved in hydrogen bonding are omitted for clarity.

3. 6. Antibacterial Activities

The results of the antibacterial activities are given in Tables 4 and 5. All the complexes showed enhanced antibacterial activities as compared with the free Schiff base HL. Ciprofloxacin produced significantly sized inhibition zones against the bacteria, while DMSO produced no inhibitory effect against any of the tested organisms. HL gave inhibition zones in the range of 1.9–6.5 mm against the bacteria. The MIC results showed that complex 1 has weak activity against *Staphylococcus aureus* and *Pseudomonas aeruginosa*, and medium activity against *Bacillus subtilis* and *Escherichia coli*. Complex 2 has medium activity against *Staphylococcus aureus*, *Bacillus subtilis* and *Pseudomonas aeruginosa*, and strong activity against *Escherichia coli*. Complex 3 has good activity against *Staphylococcus aureus* and *Pseudomonas aeruginosa*, and strong activity against *Bacillus subtilis* and *Escherichia coli*. The results of this study agree well with those reported previously that metal complexes have higher activities than their precursors.²⁴ The overtone's concept²⁵ and Tweedy's chelation theory²⁶ can explain the enhanced antibacterial activity of the metal complexes. In addition, the or-

Table 3. Hydrogen bond distances (Å) and bond angles (°) for the complexes

<i>D</i> –H... <i>A</i>	<i>d</i> (<i>D</i> –H)	<i>d</i> (H... <i>A</i>)	<i>d</i> (<i>D</i> ... <i>A</i>)	Angle (<i>D</i> –H... <i>A</i>)
1				
O7–H7...N5 ^{#1}	0.85(1)	2.57(4)	3.316(5)	147(6)
O7–H7...N4 ^{#1}	0.85(1)	1.90(1)	2.749(5)	178(7)
O3–H3...O9	0.85(1)	1.83(3)	2.636(5)	159(6)
O9–H9A...O7 ^{#2}	0.85(1)	1.90(2)	2.724(5)	163(6)
O5–H5...O1 ^{#3}	0.85(1)	1.85(2)	2.671(4)	164(6)
O9–H9B...O8	0.87(1)	1.79(2)	2.621(8)	158(6)
C11–H11...O5 ^{#4}	0.93	2.54(2)	3.074(7)	117(6)
C14–H14A...O2 ^{#5}	0.96	2.39(2)	3.306(7)	160(6)
2				
N1–H1...O4	0.90(1)	1.87(3)	2.743(6)	162(8)
O4–H4...I2 ^{#6}	0.82	3.29	3.869(7)	130(8)
O2–H2...I2 ^{#7}	0.85(1)	3.09(4)	3.820(4)	146(6)
O2–H2...O3	0.85(1)	2.22(6)	2.649(6)	111(5)
3				
O3–H3...O5 ^{#8}	0.85(1)	2.06(5)	2.828(5)	149(9)
O5–H5...N1 ^{#9}	0.85(1)	1.84(2)	2.660(5)	161(5)
C13–H13...N4 ^{#10}	0.93	2.55(2)	3.452(5)	165(5)
C19–H19...O1 ^{#11}	0.93	2.60(2)	3.506(5)	165(5)
C25–H25...O3 ^{#12}	0.9	2.49(2)	3.419(5)	173(5)
C26–H26...O3 ^{#13}	0.93	2.48(2)	3.204(5)	135(5)

Symmetry codes: #1: $-1/2 + x, 1/2 - y, 1 - z$; #2: $1/2 + x, y, 1/2 - z$; #3: $1 - x, 1 - y, 1 - z$; #4: $3/2 - x, -1/2 + y, z$; #5: $-1/2 + x, y, 1/2 - z$; #6: $x, 1/2 - y, -1/2 + z$; #7: $-1 + x, 1/2 - y, -1/2 + z$; #8: $x, y, -1 + z$; #9: $1 - x, 1 - y, 1 - z$; #10: $2 - x, -y, 1 - z$; #11: $1 - x, -y, 1 - z$; #12: $2 - x, -y, -z$; #13: $1 + x, y, z$.

der of antibacterial activities is **3** (Zn) > **2** (Cd) > **1** (Ni), which may be caused by the different cellular uptake of the metal ions.

4. Conclusion

Three nickel(II), cadmium(II) and zinc(II) complexes derived from 3-hydroxy-4-methoxy-*N'*-[(*Z*)-(pyridin-2-yl)methylidene]benzohydrazide have been synthesized with microwave assisted heating method. Structures of the complexes have been confirmed by X-ray single crystal determination, which reveals that the Ni and Zn atoms in the nickel and zinc complexes are in octahedral coordination, and the Cd atom in the cadmium complex is in square pyramidal coordination. The biological activity assay indicates that the three complexes have enhanced antibacterial activities on the bacterial strains *Bacillus subtilis*, *Staphylococcus aureus*, *Pseudomonas aeruginosa* and *Escherichia coli* as compared to the free hydrazone ligand. The order of antibacterial activities is **3** (Zn) > **2** (Cd) > **1** (Ni). The zinc complex has the most antibacterial activity against *Escherichia coli* with MIC value of 4 μM, which deserves further study to explore new drugs.

Table 4. Diameter of growth of inhibition zone (mm)

Compounds	<i>Staphylococcus aureus</i>	<i>Bacillus subtilis</i>	<i>Escherichia coli</i>	<i>Pseudomonas aeruginosa</i>
HL	3.7	6.5	4.1	1.9
1	5.2	8.3	8.8	3.7
2	8.6	13.7	19.2	5.5
3	13.1	18.6	20.2	13.5
Ciprofloxacin	25.0	21.5	25.0	23.0
DMSO	0.27	0.23	0.12	0.15

Table 5. MIC values (μM)

Compounds	<i>Staphylococcus aureus</i>	<i>Bacillus subtilis</i>	<i>Escherichia coli</i>	<i>Pseudomonas aeruginosa</i>
HL	64	64	128	128
1	32	32	64	64
2	16	16	8	16
3	8	8	4	8
Ciprofloxacin	16	8	16	16
DMSO	>128	>128	>128	>128

Supplementary Materials

The X-ray crystallographic data in the CIF format for the structures of the complexes reported in this paper have been deposited with the Cambridge Crystallographic Data Center (CCDC: 2347408 (**1**), 2347409 (**2**) and 2347410 (**3**)) and the supplementary crystallographic data can be obtained free of charge on request at www.ccdc.cam.ac.uk/contents/retrieving.html [or from The Director, Cambridge Crystallographic Data Center, CCDC, 12 Union Road, Cambridge CB2 1EZ, UK; fax: +44(0)1223-336033; email: deposit@ccdc.cam.ac.uk], quoting the CCDC numbers 2249782–2249786.

Acknowledgments

This project was supported by the Qiqihar University.

5. References

- (a) F. Nouali, J. L. C. Sousa, H. M. T. Albuquerque, R. F. Mendes, F. A. A. Paz, L. Saher, Z. Kibou, N. Choukchou-Braham, O. Talhi, A. M. S. Silva, *J. Mol. Struct.* **2023**, 1275, 134608; DOI:10.1016/j.molstruc.2022.134608
(b) I. Gurgul, O. Mazuryk, D. Rutkowska-Zbik, M. Lomzik, A. Krasowska, P. Pietrzyk, G. Stochel, M. Brindell, *Polyhedron* **2022**, 225, 116049; DOI:10.1016/j.poly.2022.116049
(c) E. Gabano, M. Ravera, *Molecules* **2022**, 27, 4249; DOI:10.3390/molecules27134249
(d) A. J. Winstead, K. Alabrash, B. V. Powell, S. J. Parnell, T. V. Hinton, T. Odebode, J. N. Peng, J. A. Krause, P. Y. Zavalij, S. K. Mandal, *J. Organomet. Chem.* **2021**, 936, 121718; DOI:10.1016/j.jorganchem.2021.121718
(e) R. A. Krishna, R. Dheepika, M. Muralisankar, S. Nagarajan, *J. Coord. Chem.* **2021**, 74, 838–849. DOI:10.1080/00958972.2021.1885650
- (a) S.-H. Zhang, Y.-L. Zhou, X.-J. Sun, L.-Q. Wei, M.-H. Zeng, H. Liang, *J. Solid State Chem.* **2009**, 182, 2991–2996; DOI:10.1016/j.jssc.2009.08.009
(b) S.-H. Zhang, C. Feng, *J. Mol. Struct.* **2010**, 977, 62–66. DOI:10.1016/j.molstruc.2010.05.010
- (a) S. Bargujar, S. Ratnani, R. Jain, *Inorg. Chem. Commun.* **2024**, 112250; DOI:10.1016/j.inoche.2024.112250
(b) D. Karati, K. R. Mahadik, D. Kumar, *Curr. Microwave Chem.* **2022**, 9, 99–104; DOI:10.2174/2213335609666220820153559
(c) S. Beniwal, A. Jain, N. Sharma, N. Fahmi, *J. Coord. Chem.* **2024**, 77, 601–618. DOI:10.1080/00958972.2024.2330995
- T. I. Kashar, S. S. Hassan, H. A. El-Boraey, *Inorg. Chim. Acta* **2024**, 563, 121903. DOI:10.1016/j.ica.2023.121903
- (a) Y.-T. Wang, X. Huang, X.-C. Cai, X.-X. Kang, H.-L. Zhu, *J. Mol. Struct.* **2024**, 1301, 137343; DOI:10.1016/j.molstruc.2023.137343
(b) H. Kekecmammed, M. Tapera, E. Aydogdu, E. Saripinar, E. A. Karatas, E. M. Uc, M. Akyuz, B. Tuzun, I. Gulcin, R. E. Bora, I. O. Ilhan, *Chem. Biodivers.* **2023**, 20; DOI:10.1002/cbdv.202200886
(c) K. Akdag, F. Tok, S. Karakus, O. Erdogan, O. Cevik, B. Kocyigit-Kaymakcioglu, *Acta Chim. Slov.* **2022**, 69, 863–875. DOI:10.17344/acsi.2022.7614
- M. S. Lone, M. M. Mubarak, S. A. Nabi, F. R. Wani, S. Amin, S. Nabi, H. A. Kantroo, M. Samim, S. Shafi, S. Ahmad, Z. Ahmad, S. O. Rizvi, K. Javed, *Med. Chem. Res.* **2023**, 32, 808–826. DOI:10.1007/s00044-023-03039-5
- (a) T. A. Farghaly, A. M. Al-Soliemy, R. Sabour, M. R. Shaaban, E. M. H. Abbas, *Bioorg. Chem.* **2022**, 121, 105684;

- DOI:10.1016/j.bioorg.2022.105684
- (b) S. Jagetiya, P. S. Auti, A. T. Paul, *Chem. Biodivers.* **2023**, *20*, DOI:10.1002/cbdv.202301154
- (c) M. Mollazadeh, H. Azizian, A. Fakhrioliaei, A. Iraj, L. Avizheh, Y. Valizadeh, K. Zomorodian, F. Elahi, A. Moazzam, H. Kazemzadeh, M. Amanlou, F. Garmciri, E. Hamidian, M. Biglar, B. Larijani, M. Mahdavi, *Med. Chem. Res.* **2023**, *32*, 930–943; DOI:10.1007/s00044-023-03050-w
- (d) A. E. Evren, D. Nuha, S. Dawbaa, B. N. Saglik, L. Yurttas, *Eur. J. Med. Chem.* **2022**, *229*, 114097; DOI:10.1016/j.ejmech.2021.114097
- (e) U. Salgin-Goksen, G. Telli, A. Eriksi, E. Dedecengiz, B. C. Tel, F. B. Kaynak, K. Yelekci, G. Ucar, N. Gokhan-Kelekci, *J. Med. Chem.* **2021**, *64*, 1989–2009. DOI:10.1021/acs.jmedchem.0c01504
8. (a) H. Kargar, *Trans. Met. Chem.* **2014**, *39*, 811–817; DOI:10.1007/s11243-014-9863-4
- (b) A. Sahraei, H. Kargar, M. Hakimi, M. N. Tahir, *J. Mol. Struct.* **2017**, *1149*, 576–584; DOI:10.1016/j.molstruc.2017.08.022
- (c) A. Sahraei, H. Kargar, M. Hakimi, M. N. Tahir, *Trans. Met. Chem.* **2017**, *42*, 483–489; DOI:10.1007/s11243-017-0152-x
- (d) A. Jamshidvand, M. Sahihi, V. Mirkhani, M. Moghadam, I. Mohammadpoor-Baltork, S. Tangestaninejad, H. A. Rudbari, H. Kargar, R. Keshavarzi, S. Gharaghani, *J. Mol. Liquids* **2018**, *253*, 61–71; DOI:10.1016/j.molliq.2018.01.029
- (e) H. Kargar, R. Behjatmanesh-Ardakani, V. Torabi, M. Kashani, Z. Chavoshpour-Natanzi, Z. Kazemi, V. Mirkhani, A. Sahraei, M. N. Tahir, M. Ashfaq, K. S. Munawar, *Polyhedron* **2021**, *195*, 114988; DOI:10.1016/j.poly.2020.114988
- (f) H. Kargar, F. Aghaei-Meybodi, R. Behjatmanesh-Ardakani, M. R. Elahifard, V. Torabi, M. Fallah-Mehrdardi, M. N. Tahir, M. Ashfaq, K. S. Munawar, *J. Mol. Struct.* **2021**, *1230*, 129908; DOI:10.1016/j.molstruc.2021.129908
- (g) H. Kargar, A. A. Ardakani, M. N. Tahir, M. Ashfaq, K. S. Munawar, *J. Mol. Struct.* **2021**, *1233*, 130112. DOI:10.1016/j.molstruc.2021.130112
9. M. Orojloo, P. Zolgharnein, M. Solimannejad, S. Amani, *Inorg. Chim. Acta* **2017**, *467*, 227–237. DOI:10.1016/j.ica.2017.08.016
10. (a) B. Ay, O. Sahin, B. S. Demir, Y. Saygideger, J. M. Lopez-de-Luzuriaga, G. Mahmoudi, D. A. Safin, *New J. Chem.* **2020**, *44*, 9064–9072; DOI:10.1039/D0NJ00921K
- (b) K. S. Neethu, S. Sivaselvam, M. Theetharappan, J. Ranjitha, N. S. P. Bhuvanesh, N. Ponpandian, M. A. Neelakantan, M. V. Kaveri, *Inorg. Chim. Acta* **2021**, *524*, 120419; DOI:10.1016/j.ica.2021.120419
- (c) G. A. El-Inany, H. S. Seleem, H. F. El-Shafiy, B. A. El-She-tary, A. I. Nabeel, A. Madyan, M. Shebl, *Appl. Organomet. Chem.* **2024**, *38*; DOI:10.1002/aoc.7367
- (d) A. A. Khandar, Z. M. Azar, M. Eskandani, C. B. Hubschle, S. van Smaalen, B. Shaabani, Y. Omid, *Polyhedron* **2019**, *171*, 237–248; DOI:10.1016/j.poly.2019.06.026
- (e) P. H. O. Santiago, M. B. Santiago, C. H. G. Martins, C. C. Gatto, *Inorg. Chim. Acta* **2020**, *508*, 119632; DOI:10.1016/j.ica.2020.119632
- (f) S. Dasgupta, S. Karim, S. Banerjee, M. Saha, K. D. Saha, D. Das, *Dalton Trans.* **2020**, *49*, 1232–1249; DOI:10.1039/C9DT04636D
- (g) Y.-L. Sang, X.-S. Lin, W.-D. Sun, *Acta Chim. Slov.* **2020**, *67*, 581–585. DOI:10.17344/acsi.2019.5595
11. (a) W.-G. Zhang, *Acta Chim. Slov.* **2023**, *70*, 421–429; DOI:10.17344/acsi.2023.8144
- (b) W.-G. Zhang, J.-H. Liang, *Acta Chim. Slov.* **2021**, *68*, 921–929. DOI:10.17344/acsi.2021.6902
12. Siemens, SAINT: Area Detector Control and Integration Software, Siemens Analytical X-ray Instruments Inc., Madison, WI, USA, **1996**.
13. G. M. Sheldrick, SHELXL97 and SHELXTL Software Reference Manual, Version 5.1, Bruker AXS Inc., Madison, WI, USA, **1997**.
14. G. M. Sheldrick, SADABS, University of Göttingen, Germany, **1996**.
15. K. Singh, Y. Kumar, P. Puri, C. Sharma, K. R. Aneja, *Med. Chem. Res.* **2012**, *21*, 1708–1716. DOI:10.1007/s00044-011-9683-4
16. M. I. Okeke, C. U. Iroegbu, E. N. Eze, A. S. Okoli, C. O. Esimone, *J. Ethnopharmacol.* **2001**, *78*, 119–127. DOI:10.1016/S0378-8741(01)00307-5
17. G. Kastias, C. A. Kastias, A. Tabak, *Spectrochim. Acta A* **2019**, *222*, 117198.
18. M.-L. Liu, J.-M. Dou, J.-Z. Cui, D.-C. Li, D.-Q. Wang, *J. Mol. Struct.* **2012**, *1011*, 140–144. DOI:10.1016/j.molstruc.2011.12.024
19. A. A. El-Sherif, A. Fetoh, Y. K. Abdulhamed, G. M. Abu El-Reash, *Inorg. Chim. Acta* **2018**, *480*, 1–15. DOI:10.1016/j.ica.2018.04.038
20. (a) R. N. Patel, A. Singh, V. P. Sondhiya, Y. Singh, K. K. Shukla, D. K. Patel, R. Pandey, *J. Coord. Chem.* **2012**, *65*, 795–812; DOI:10.1080/00958972.2012.662592
- (b) P. Sathyadevi, P. Krishnamoorthy, M. Alagesan, K. Thanigaimani, P. T. Muthiah, N. Dharmaraj, *Polyhedron* **2012**, *31*, 294–306; DOI:10.1016/j.poly.2011.09.021
- (c) C. M. Armstrong, P. V. Bernhardt, P. Chin, D. R. Richardson, *Eur. J. Inorg. Chem.* **2003**, 1145–1156. DOI:10.1002/ejic.200390146
21. A. W. Addison, T. N. Rao, J. Reedijk, J. van Rijn, G. C. Verschoor, *J. Chem. Soc., Dalton Trans.* **1984**, *7*, 1349–1356. DOI:10.1039/DT9840001349
22. (a) L.-X. Xie, D.-Y. Wu, C.-Y. Duan, B.-G. Zhang, Q.-J. Meng, *Chin. J. Inorg. Chem.* **2007**, *23*, 191–199;
- (b) K. Das, T. N. Mandal, S. Roy, S. Gupta, A. K. Gupta, A. K. Barik, P. Mitra, A. L. Rheingold, S. K. Kar, *Polyhedron* **2010**, *29*, 2892–2899. DOI:10.1016/j.poly.2010.07.015
23. (a) P. Barbazan, R. Carballo, E. M. Vazquez-Lopez, *CrystEngComm* **2007**, *9*, 668–675; DOI:10.1039/b703442c
- (b) B. Samanta, J. Chakraborty, S. Shit, S. R. Batten, P. Jensen, J. D. Masuda, S. Mitra, *Inorg. Chim. Acta* **2007**, *360*, 2471–2484. DOI:10.1016/j.ica.2006.12.019
24. K. Singh, Y. Kumar, P. Puri, M. Kumar, C. Sharma, *Eur. J. Med. Chem.* **2012**, *52*, 313–321. DOI:10.1016/j.ejmech.2012.02.053

25. N. Raman, A. Kulandaisamy, K. Jayasubramanian, *Polish J. Chem.* **2002**, 76, 1085–1094.
26. B. G. Tweedy, *Phytopathology* **1964**, 55, 910–915.

Povzetek

Z uporabo mikrovalovne metode smo sintetizirali tri komplekse z ligandom 3-hidroksi-4-metoksi-*N'*-[(*Z*)-(piridin-2-il)metiliden]benzohidrazid (HL): $[\text{NiL}_2] \cdot 2\text{CH}_3\text{OH} \cdot \text{H}_2\text{O}$ (**1**), $[\text{CdI}_2(\text{HL})] \cdot \text{CH}_3\text{OH}$ (**2**) in $[\text{ZnL}_2]$ (**3**). Vse spojine smo karakterizirali s CHN elementno analizo in infrardečo spektroskopijo. Strukture kompleksov smo določili z monokristalno rentgensko difrakcijo, ki je pokazala, da sta atoma Ni in Zn v spojinah **1** in **3** oktaedrično koordinirana, medtem ko je atom Cd v spojini **2** kvadratno piramidalno koordiniran. Biološko aktivnost kompleksov smo preverili na bakterijskih sevih *Bacillus subtilis*, *Staphylococcus aureus*, *Pseudomonas aeruginosa* in *Escherichia coli*. Izkazalo se je, da ima predvsem cinkov kompleks zanimivo antibakterijsko učinkovitost.



Except when otherwise noted, articles in this journal are published under the terms and conditions of the Creative Commons Attribution 4.0 International License

Scientific paper

Preparation of Porous Imidazole-based Poly(ionic liquid) Adsorbents and Their Toluene Adsorption Performance

Fangwen Luo,¹ Xujiao Tian,¹ Xian Dong,¹ Longchao Liang¹ and Zhuo Chen^{1,*}

School of Chemistry and Material Science, Key Lab for Functional Material Chemistry, Guizhou Normal University, Guiyang 550025, PR China

* Corresponding author: E-mail: chen-zhuo19@163.com

Received: 01-16-2024

Abstract

Efficient, economical, and durable adsorbents are required to remove volatile organic compounds (VOCs) from air. Cross-linked polyvinyl ionic liquids (PVIC) with porous structures were synthesized by quaternizing 1-vinylimidazole (1VI) with 1-bromobutane to obtain 3-butyl-1-vinylimidazolium bromide (VIC), which was then co-polymerized with divinylbenzene (DVB) radicals. ¹H NMR, ¹³C NMR, scanning electron microscopy, X-ray photoelectron spectroscopy, Fourier-transform infrared spectroscopy, and N₂ adsorption-desorption isotherms were applied in characterizing the composites. Through modification of the polymer structure by adjustment of DVB concentration (the ratio of DVB concentration to VIC concentration was x: 1 (x = 0.4, 0.6, 0.8, 1.0) and the product was named PVIC-x (x = 2, 3, 4, 5)), the optimal PVIC-4 pore structure was obtained, with a specific surface area and total pore volume of 192.5 m² g⁻¹ and 0.192 cm³ g⁻¹, respectively. A toluene adsorption test verified the adsorption capacity. The adsorption behavior for VOCs, based on toluene, was investigated using adsorption breakthrough curves, adsorption kinetics, and isotherms. The adsorption process is well describing by the Bangham kinetic and Langmuir isotherm models. The dynamic adsorption of toluene was in the order of PVIC-4 > PVIC-5 > PVIC-3 > PVIC-2. The optimal toluene adsorption capacity of PVIC-4 was 264.4 mg g⁻¹ with an equilibrium time of 56 minutes, which was attributed to its excellent pore structure. PVIC-4 also performed well in terms of recycling rate, maintaining 91.19% adsorption efficiency after 5 cycles of recycling. PVIC-4 has the potential to remove volatile organic compounds from the air.

Keywords: Poly (ionic liquid)s; Imidazole; VOCs adsorption; Air purification

1. Introduction

Volatile organic compounds (VOCs) are toxic air-borne pollutants that deplete the ozone layer, contribute to global warming, and have major impacts on human health and the natural environment.^{1,2} Toluene is a VOC widely used as an organic solvent and a raw material in the synthesis of pharmaceuticals, explosives, and pesticides. It is also an essential component of many industrial and household products. Long-term exposure to toluene can cause severe damage to human respiratory, nervous, and hematopoietic systems.^{3–5}

Previous studies have identified various methods for toluene removal from the atmosphere including adsorption,^{6,7} thermal/catalytic oxidation,^{8,9} photocatalytic degradation,¹⁰ plasma-catalyzed processes,¹¹ and biodegradation,¹² with adsorption being recognized as the optimal method due to its low cost, high efficiency, and simplicity. Adsorbent structure is the critical factor affecting adsorp-

tion capacity, directly influencing removal efficiency and operating cost. Various materials such as zeolites,¹³ metal-organic materials,¹⁴ bio-carbon materials,¹⁵ carbon nanotubes,¹⁶ and graphene,¹⁷ have been applied as adsorbents, but their high cost, poor selectivity, low adsorption efficiency, and limited stability require improvement. The development of rapid and efficient adsorbents of high capacity is thus of practical importance in removing VOCs from the atmosphere.

Polyionic liquids (PILs) are polymeric materials synthesized by copolymerization of ionic liquids (ILs) with another monomer. They combine the unique features of ILs and polymer structures with excellent performance in areas such as VOC adsorption, electrochemistry, and catalysis.^{18,19} PILs have unique composite frameworks that maintain the superior properties of ILs combined with the stability, processability, durability, and controllability of polymeric materials, thereby overcoming many of the limitations of monomeric ILs.

Ionic liquids have received attention recently due to their excellent structural modifiability. Of 200 tested ILs, imidazolium-based ILs are ideal for toluene absorption,²⁰ and they have been used effectively for this purpose.^{21,22} Use of poly-imidazolium ionic liquids (PVIMs) has been reported for the adsorption of dyes in water,²³ CO₂ in air,²⁴ and hemoglobin,²⁵ with a wide range of applications; however, efficient PVIM adsorption of toluene has yet to be reported. Frontier molecular orbital analysis indicates that the uptake of toluene by ILs is a physical process,²⁶ and their adsorption performance after polymerization depends mainly on pore volume, diameter, and shape, and specific surface area. Thus, the reproducible synthesis of porous poly imidazolium ILs (PVILs) as toluene adsorbents under mild conditions is challenging.

Here, PVIC-*x* of different structures were synthesized by quaternization and co-polymerization reactions involving 1-vinylimidazole (1VI), *n*-bromobutane, and divinylbenzene (DVB) with different DVB concentrations. The effect of crosslinker concentration on product pore structure was investigated, together with the reusability, adsorption breakthrough curves, kinetics, and isotherms characterizing the toluene adsorption behavior of PVIC-*x*. Their toluene adsorption mechanism was investigated through correlation of pore structure and adsorption capacity. The temperature of the adsorption process was 25 °C to simulate an indoor environment, which is expected to play a role in removing toluene indoors.

2. Experimental

2.1. Materials

Chemicals used in this study were sourced in China as follows: 1-vinylimidazole, *n*-butyl bromide, divinylbenzene, and azodiisobutyronitrile from Aladdin Biochemical Technology, Shanghai; methanol, dichloromethane, anhydrous ethanol, and ethyl acetate from Fuyu Fine Chemical, Tianjin; toluene from Sinopharm Chemical Reagent, Shanghai; and anhydrous ether from Chuandong Chemical, Chongqing. All the chemicals were analytically pure and used without further purification. Water used in the experiments was deionized.

2.2. Synthesis of Imidazolium-based ILs

The IL precursor 3-*n*-butyl-1-vinylimidazolium bromide (VIC) was synthesized using published methods,²⁷

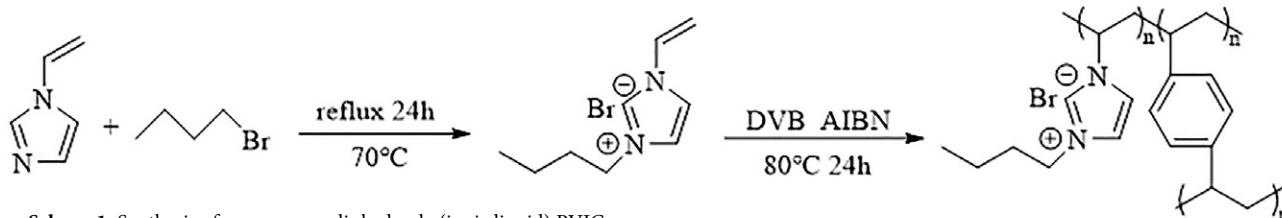
as described in Scheme 1. Typically, 1-vinylimidazole (20 mmol) and *n*-butyl bromide (20 mmol) were mixed in a 100 mL flask with vigorous stirring under a nitrogen atmosphere. The mixture was refluxed at 70 °C for 24 h. After the reaction, the liquid phase was decanted off and the solid residue washed three times with ethyl acetate and ether, and dried at 50 °C for 12 h under vacuum. Found: ¹H NMR (400 MHz, DMSO) δ 9.76 (s, 1H), 8.29 (s, 1H), 8.01 (s, 1H), 7.35 (d, 1H), 6.01 (d, 1H), 5.41 (d, 1H), 4.23 (t, 2H), 1.80 (m, 2H), 1.27 (d, 2H), 0.88 (t, 3H). ¹³C NMR (101 MHz, DMSO) δ 135.77, 129.32, 123.73, 119.65, 109.11, 49.39, 31.53, 19.26, 13.77.)

2.3. Synthesis of Porous Copolymer

The porous poly(ionic liquid) was prepared through the radical co-polymerization of VIC and DVB and DVB,²⁸ as shown in Scheme 1. First, 10 mmol VIC was mixed with DVB at VIC/DVB mass ratios of 5:2, 5:3, 5:4, and 5:5 in round-bottomed flasks; 5 mmol of initiator Azodiisobutyronitrile (AIBN) was then added sequentially with 5 mL anhydrous ethanol, 25 mL ethyl acetate, and 5 mL water. The mixture was refluxed under nitrogen at 80 °C for 24 h on an oil bath. After reaction, the white solid residue was filtered off and washed three times with anhydrous ethanol and ultrapure water before drying under vacuum at 50 °C for 12 h to obtain poly(3-*n*-butyl-1-vinylimidazolium bromide) or 'PVIC-*x*', where *x* denotes the concentration of DVB in the VIC/DVB mass ratio.

2.4. Sample Characterization

¹H NMR and ¹³C-NMR spectra were obtained with an NMR spectrometer (Avance Neo 400M; Bruker, United States of America) in Deuterium with dimethyl sulfoxide using Tetramethylsilane as an internal reference. Fourier-transform infrared (FTIR) spectra were recorded with a Nicolet iS50 (Nicolet iS50; Thermo, United States of America) spectrometer in the 4000–400 cm⁻¹ region. X-ray photoelectron spectroscopy (XPS, Thermo, USA) is used to study the surface composition of materials. High-resolution field-emission scanning electron microscopy (FESEM; Supra55 Sapphire, Zeiss, German; 10Kv) was used to study the geometric morphology of materials. A fully automated specific surface area and porosity analyzer (ASAP 2460, Micrometrics, United States of America) was used in nitrogen adsorption–desorption performance tests. The sample was outgassed in the degassing port of the appa-



Scheme 1. Synthesis of porous cross-linked poly (ionic liquid) PVIC-*x*

ratus at 503 K for 3 h before testing. The Brunauer Emmett Teller (BET) specific surface area, pore volume, and average pore size (Barrett Joyner-Halenda method) were calculated by device software.

2. 5. Dynamic Adsorption Measurements

Dynamic adsorption test of toluene using a GC2060 gas chromatograph from Shanghai Ruimin Instrument Co. The specific parameters of the gas chromatograph are as follows: column temperature 130 °C, inlet temperature 200 °C, hydrogen flame detector temperature 135 °C, carrier gas N₂. Before adsorption measurements, the material was heated at 373 K for 3 h to remove any water molecules already adsorbed. Toluene steam was produced by blowing a stream of nitrogen gas into liquid toluene using N₂ carrier gas at a flow rate of 200 mL min⁻¹. Adsorption took place within a quartz tube of 6 mm internal diameter and 650 mm length. Quartz wool was used to prevent material being blown out. The toluene concentration was stable at 400 ppm. The adsorption temperature was 298 K, and 50 mg of adsorbent was used in each test. An online gas chromatograph with a flame-ionization detector was used to monitor toluene concentrations at reactor inlet and outlet. The toluene breakthrough time was defined as the time required for the outlet concentration to reach 5% of the inlet concentration. The adsorption capacity of the adsorbent was calculated by integrating the area under the obtained penetration curve, as follows (Eq. (1)):²⁹

$$q_t = \frac{1}{m} \int_0^t v(C_0 - C_t) dt \quad (1)$$

Where q_t (mg g⁻¹) is the amount of toluene adsorbed per unit mass of adsorbent at a given time t ; m (g) is the quantity of adsorbent; v (mL min⁻¹) is the gas flow rate; and C_0 and C_t (mg mL⁻¹) are the initial inlet and outlet toluene concentrations at time t , respectively. After the adsorbent was saturated, the toluene gas flow was closed, and toluene desorbed at 100 °C at a nitrogen flow rate of 50 mL min⁻¹ until the concentration of toluene gas stream at the outlet was 0

2. 6. Adsorption Theory and Models

Pseudo-first order (Eq. (2)),³⁰ pseudo-second order (Eq. (3)),³¹ and Bangham (Eq. (4))³² kinetics were used to describe the adsorption of toluene. The Weber-Morris pore diffusion model (Eq. (5))³³ was used to further analyze the diffusion mechanism of toluene within the material.

$$q_t = q_e [1 - e^{-k_1 t}] \quad (2)$$

$$q_t = \frac{k_2 q_e^2 t}{1 + k_2 q_e t} \quad (3)$$

$$q_t = q_e - \frac{q_e}{e^{kt^z}} \quad (4)$$

$$q_t = k_i t^{1/2} + C_i \quad (5)$$

where q_e (mg g⁻¹) is the amount of toluene adsorbed at adsorption equilibrium; t (min) is the adsorption time; k_1 (min⁻¹), k_2 (g mg⁻¹ min⁻¹), and k (min⁻¹) are rate constants for the proposed first-order, second-order, and Bangham kinetic equations, respectively; k_i (mg (g·min^{1/2})) and C_i (mg g⁻¹) are the intra-particle diffusion coefficient and intercept, respectively; and z is a constant

The adsorption process of toluene by each material was elucidated by the fitting of isotherms using the Langmuir (Eq. (6)), (Eq. (7))³⁴ and Freundlich (Eq. (8))³⁵ models

$$q_e = \frac{q_m K_L C}{1 + K_L C} \quad (6)$$

$$R_L = \frac{1}{1 + K_L C} \quad (7)$$

$$q_e = K_F C^{1/n} \quad (8)$$

where q_e and q_m (mg g⁻¹) are the equilibrium and maximum adsorption volumes, respectively; C (mg m⁻³) is the equilibrium concentration; K_L (L mg⁻¹) and K_F ((mg g⁻¹)/(mg L⁻¹)^{1/n}) are constants of the Langmuir and Freundlich models, R_L stands for Langmuir dimensionless separation factor, respectively; and n is Freundlich heterogeneity factor.

3. Results and Discussion

3. 1. Characteristics of PVIC-x

Copolymer material polymerized from DVB and VIC, the copolymer materials were further characterized by FTIR spectroscopy. The spectra of synthesized PVIC-x are shown in Fig. 1 for characteristic vibrations in the pol-

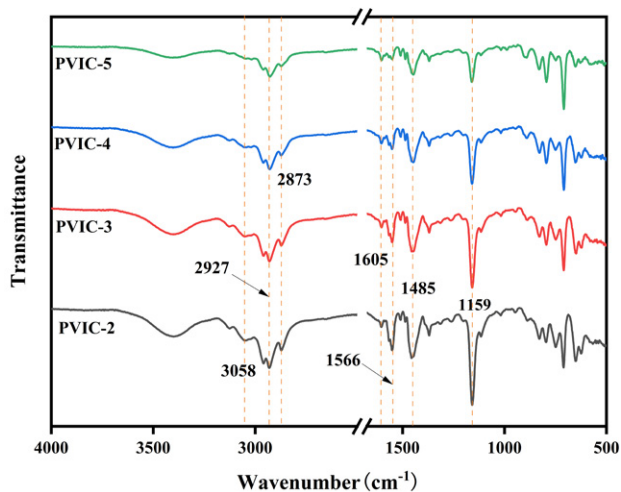


Figure 1. FT-IR of PVIC-x

ymers regarding DVB correlation: bands at 3058 and 3016 cm^{-1} represent aromatic C–H stretching vibrations, and the band at 2927 cm^{-1} represents aliphatic C–H stretching vibrations. Bands at 1485 and 1446 cm^{-1} represent aromatic C–H in-plane and bending vibrations, respectively.^{36,37} For the imidazole-IL portion of the polymer, the aliphatic C–H turning vibration band is at 2873 cm^{-1} , and the imidazole ring backbone band at 1566 cm^{-1} . The imidazole ring in-plane C–H bond bending vibration is at 1159 cm^{-1} .³⁸ As the synthesized polymers differed only in the ratio of reactants, there was little variation in IR spectra of the corresponding copolymers. These results indicate that both imidazole-IL and DVB precursors were retained in the copolymers, and the polymers were successfully synthesized.

The chemical states of the elements in PVIC-*x* were investigated using X-ray photoelectron spectroscopy (XPS). Taking PVIC-4 as an example, the investigated XPS spectra (Fig. 2a) clearly show the presence of C 1s, N 1s, and Br 3d. The high-resolution spectra of these

elements are shown in Fig. 2b–d. For example, the C 1s spectrum has three peaks at 284.8, 285.9, and 286.8 eV attributed to carbon atoms in the carbon chain, C–N, and benzene ring, respectively.³⁹ In the N 1s spectrum, peaks at 400.4 eV and 398.3 eV can be assigned to N–C and N=C in imidazole indicating successful incorporation of imidazole moiety.⁴⁰ In the Br 3d spectrum, the peaks at 70.0 eV and 68.9 eV are from the Br 3d_{5/2} spin orbital and Br 3d_{3/2}, respectively.

The surface morphologies of the fabricated polymeric adsorbents (PVIC-2, PVIC-3, PVIC-4, and PVIC-5) were studied by FESEM (Fig. 3). For a ratio of cross-linker DVB of 2/5 (PVIC-2), the prepared polymer had a ‘lumpy’ structure with a rough surface, cracks, and irregular particles on the surface (Fig. 3a). As the DVB ratio increased, unstable particles on the surface became smaller, and pore structures became evident with a trend towards a spherical shape (Fig. 3b), increasing to a large number of spherical and globular like combinations of the

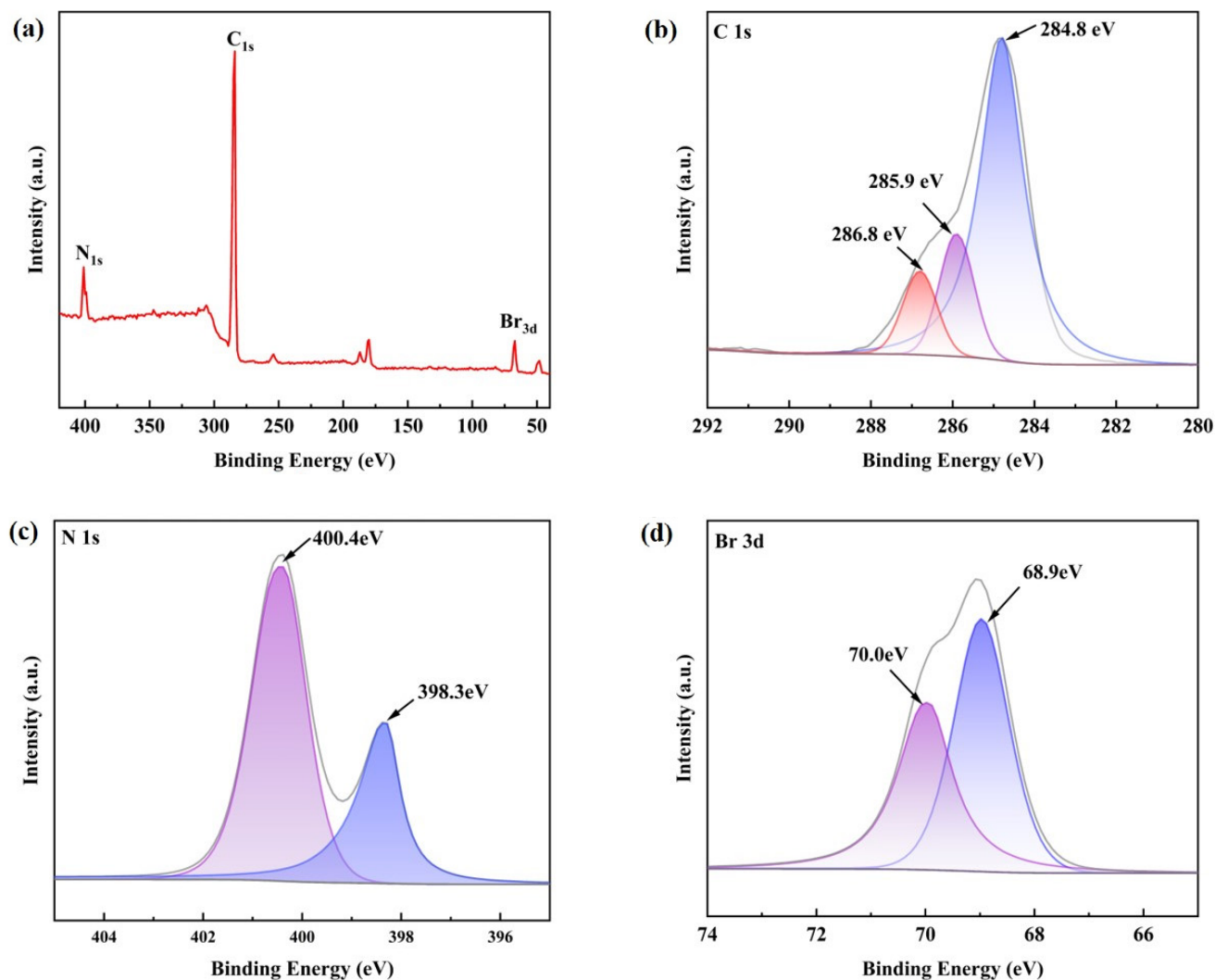


Figure 2. XPS spectra of PVIC-4: (a) survey spectra, (b) C 1 s, (c) N 1 s, (d) Br 3 d

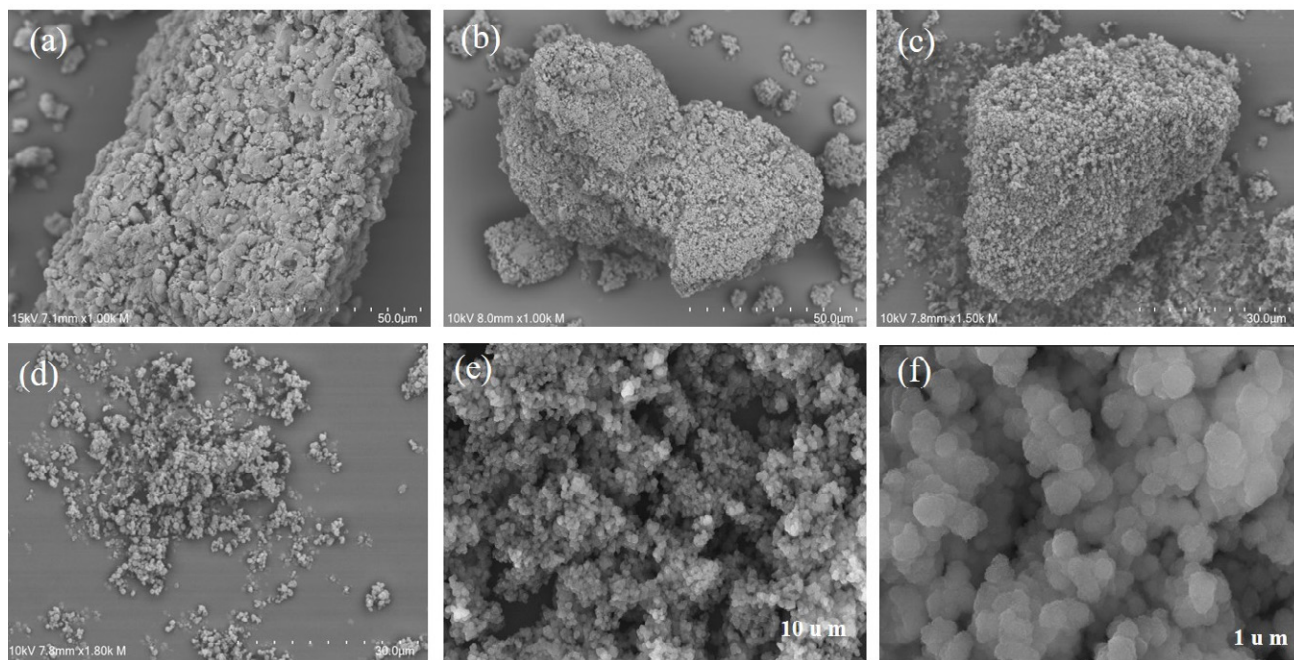


Figure 3. SEM images: (a) PVIC-2; (b) PVIC-3; (c) PVIC-4; (d) PVIC-5; (e) PVIC-4; (f) PVIC-4

clusters (Fig. 3c). Finally, the globular cluster structure collapsed to form a dispersed disordered state (Fig. 3d). The disordered pore structure is a typical feature of adsorbent materials, providing both transport channels and adsorption sites for adsorbate molecules.⁴¹ PVIC-4 had a porous structure (Fig. 3e–f), with macropores providing the main diffusion channels for adsorbate molecules to enter the interior of the adsorbent, with adsorption increasing with the proportion of cross-linker DVB. However, when the DVB ratio reached the same proportion as that of VIC, the cluster structure collapsed, resulting in a dense and disordered surface (PVIC-5) with a reduced pore structure.

The structure characteristics of PVIC-2, PVIC-3, PVIC-4, and PVIC-5 adsorbents were characterized by BET technology. The results are shown in Figure 4, and the pore structure parameters are shown in Table 1.

Based on the International Union of Pure and Applied Chemistry adsorption isotherm classification, the prepared PVIC-2, PVIC-3, PVIC-4, and PVIC-5 adsorbents had type IV isotherms with H_4 -type hysteresis loops (Fig. 4a). The hysteresis loops closed at a relative pressure of $P/P_0 = 0.4$, due to capillary condensation of N_2 molecules in the mesoporous structure, thereby indicating the presence of smaller mesopores. At low relative pressure ($P/P_0 < 0.01$), the material exhibited some adsorption of N_2 ,

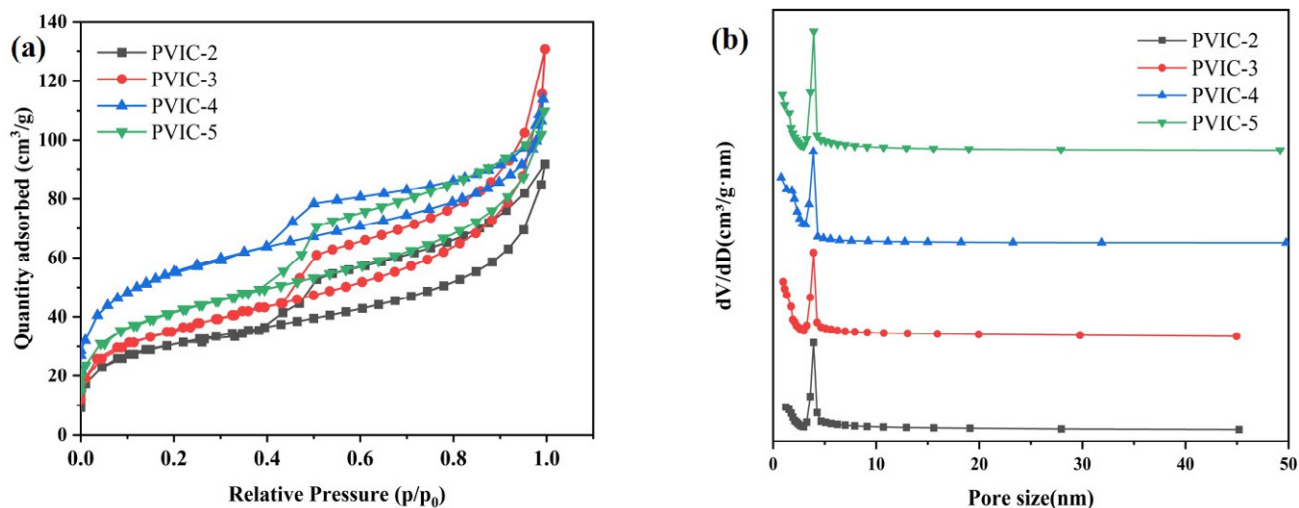


Figure 4. (a) N_2 adsorption-desorption isotherms (b) N_2 adsorption-desorption isotherm: log scale and the pore size distribution curves

Table 1. Physical parameters of PVIC-x

Adsorbents	Surface (m ² /g)				Pore volume (cm ³ /g)			D _p (nm)
	S _{BET}	S _{mic}	S _{mes}	S _{mic} /S _{BET}	V _{tot}	V _{mic}	V _{mic} /V _{tot}	
PVIC-2	109.8	17.9	91.9	16.3%	0.142	0.0131	9.20%	5.83
PVIC-3	128.3	27.1	101.2	21.1%	0.151	0.0198	13.10%	7.11
PVIC-4	192.5	41.8	150.7	21.7%	0.192	0.0323	16.80%	4.36
PVIC-5	152.4	35.9	116.5	23.5%	0.169	0.0241	14.30%	5.28

S_{BET}: total specific surface area; S_{mic}: microporous surface area; S_{mes}: mesoporous surface area; V_{tot}: total pore volume; V_{mic}: microporous pore; D_p: average pore size

likely due to the strong interaction between the microporous structure and N₂ molecules increasing the adsorption capacity of N₂, and indicating the presence of micropores.⁴²

The pore-size distribution curves (Fig. 4b) indicate bimodal distributions for PVIC-3, PVIC-4, and PVIC-5, with peaks at 1 and 4 nm. This further indicates that the adsorbents had typical micro mesoporous structures.⁴³ All

adsorbents were porous, predominantly with mesopores and some micropores (Table 1). The specific surface area and total pore volume of the adsorbents tended to increase then decrease with increasing cross-linker concentration. This was likely due to an increase in the number of DVB molecules and changes of reaction sites within VIC during cross-linking, which promoted the formation of the pore structure. PVIC thus has an effective pore structure

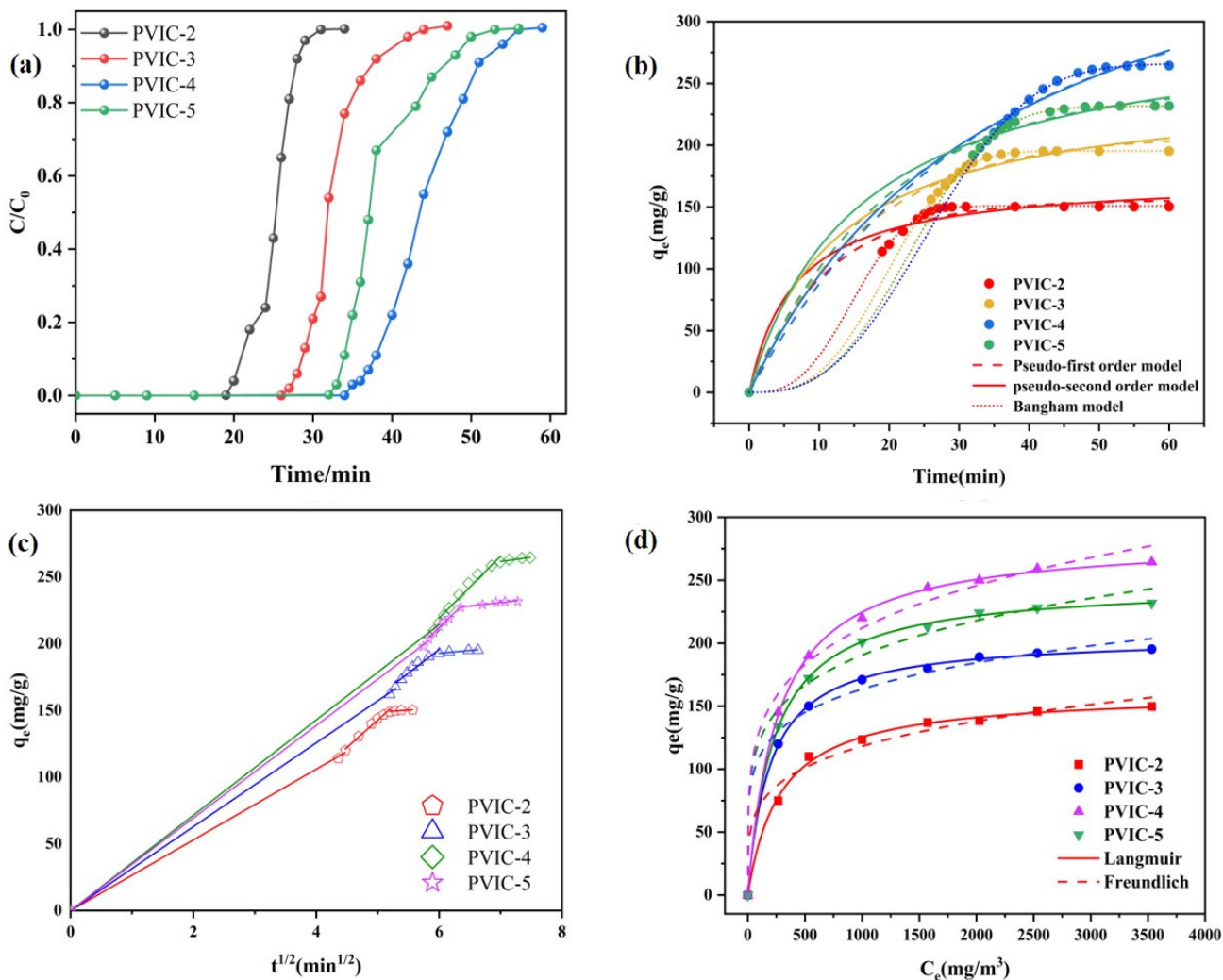


Figure 5. (a) Adsorption breakthrough curves of toluene on PVIC-x. (b) pseudo-first order, pseudo-second order models and Bangham model, (c) intra-particle diffusion model, (d) Langmuir and Freundlich models

at PVIC-4, with a specific surface area of $192.5 \text{ m}^2 \text{ g}^{-1}$, total pore volume of $0.192 \text{ cm}^3 \text{ g}^{-1}$, and microporous ratio of 16.8%. As the DVB concentration continued to increase towards PVIC-5, the specific surface area of the adsorbent decreased to $152.4 \text{ m}^2 \text{ g}^{-1}$ and the pore volume to $0.169 \text{ cm}^3 \text{ g}^{-1}$. This may be due to excess DVB molecules filling the pore volume. Finally, the adsorbent could not maintain the clustering, and it collapsed.

3. 2. Dynamic Adsorption Performance of Toluene

The prepared PVIC-2, PVIC-3, PVIC-4, and PVIC-5 PIL adsorbents were used for the adsorptive removal of toluene, with results shown in Fig. 4a. The toluene breakthrough time, adsorption equilibrium time, and equilibrium adsorption capacity of the PILs are provided in Table S1

The adsorption process of all adsorbents could be divided into three stages (Fig. 5a) as follows. (1) During the initial stage of pre-adsorption, the adsorption curve is nearly level at zero, and the adsorbent adsorbs all the surface toluene molecules with a zero-export concentration. (2) During the middle stage, the adsorbent is penetrated by toluene molecules. As adsorption proceeds, the export concentration gradually increases, as indicated by the rising adsorption curve (Fig. 5a). (3) During the late stage, an increasing number of toluene molecules penetrate the adsorbent, with increasing export concentration. When the toluene concentrations in the inlet and outlet are approximately equal, the adsorption has reached dynamic equilibrium.⁴⁴ Toluene adsorption followed the order PVIC-4 > PVIC-5 > PVIC-3 > PVIC-2 (Table S1). Changes in DVB concentration affected the adsorbent pore structure, and adsorption by PVIC-4 was highest due to its optimal BET and total pore volume, consistent with its structural properties.

The toluene adsorption mechanism of the prepared PVIC-x was investigated by nonlinear fitting of the adsorption curves using the proposed first-order, second-order, and Bangham kinetic models (Fig. 5b). The relevant parameters for the three model fittings are given in Table S2

For the three dynamic models, there was little difference between the theoretical adsorption obtained by fitting of the Bangham equation and experimentally observed adsorption (Fig. 5b; Table S2). determination coefficients (R^2) were all >0.999, indicating that the Bangham kinetic model is most suitable for describing the adsorption of toluene by PVIC-x, this is consistent with the presence of both mesopores and micropores in its structure. The Bangham model is generally used to describe orifice diffusion processes. Adsorption by all PVIC adsorbents involves mainly surface and pore diffusion. Surface diffusion occurs mainly in the adsorption stage, when toluene molecules occupy adsorption sites on the adsorbent surface, with high adsorption efficiency.⁴⁵ As the adsorption

process continues, the increasing number of toluene molecules on the surface reduces the number of adsorption sites available, causing some toluene molecules to diffuse into the interior of the pore structure to occupy internal adsorption sites. The pore structure of PVIC-x thus has a major influence on the adsorption process. The proposed first-order kinetic model describes the physical adsorption process, while the quasi-second-order model is more suitable for describing the chemical adsorption process. The fitting of the former was significantly better than that of the latter, indicating that physical interaction is the main control of the adsorption rate of toluene.⁴⁶

The fitting curves and parameters of the intra-particle diffusion model are provided in Fig. 5c and Table S3, which indicate that the physical adsorption of toluene by PVIC-x can be also divided into three stages⁴⁷ as follows. (1) During the external diffusion stage, the main influencing factor is the specific surface area; the larger the area, the higher the diffusion coefficient k_1 . (2) During the internal diffusion stage, C_2 is non-zero and, in addition to diffusion resistance inside the particles, the adsorption process may be subject to other influencing factors.⁴⁸ (3) During the adsorption equilibrium stage, a comparison of the diffusion coefficients (k) of the three stages indicated that $k_2 > k_1 > k_3$. The adsorption rate was thus highest in stage (2), with internal diffusion playing an essential role.

The experimental data were also fitted according to the Langmuir and Freundlich models (Fig. 5d; Tables S4), with the correlation coefficient of the former being nearer 1 than that of the latter, implying that toluene adsorption involves monolayer adsorption. The difficulty of adsorption was assessed by calculating the dimensionless separation factor, R_L (If $R_L = 0$ means that the process is irreversible, $0 < R_L < 1$ means that the adsorption is favorable, $R_L = 1$ means that the adsorption is linear, and $R_L > 1$ means that the adsorption process is unfavorable), with all R_L values being between 0 and 1, implying that toluene has a strong affinity for each material.⁴⁹ The n values (heterogeneity factors) in the Freundlich model were used to identify adsorption processes; $1/n$ was < 1, implying that toluene adsorption involved a physical process.⁵⁰

3. 3. Relationship Between Pore Structure and Adsorption Capacity

To understand the effect of pore structure on the material's performance in the adsorption of toluene, a linear correlation analysis was performed between the adsorption capacity and the specification of the material's micropores and mesoporous.

The effect of pore structure on toluene adsorption performance was investigated by correlation analysis between adsorption capacity and characteristics of material micro- and mesopores. Adsorption capacity was strongly correlated with surface area and micropore volume ($R^2 = 0.9966$ and 0.9636 , respectively; Fig. 6a, c) compared with

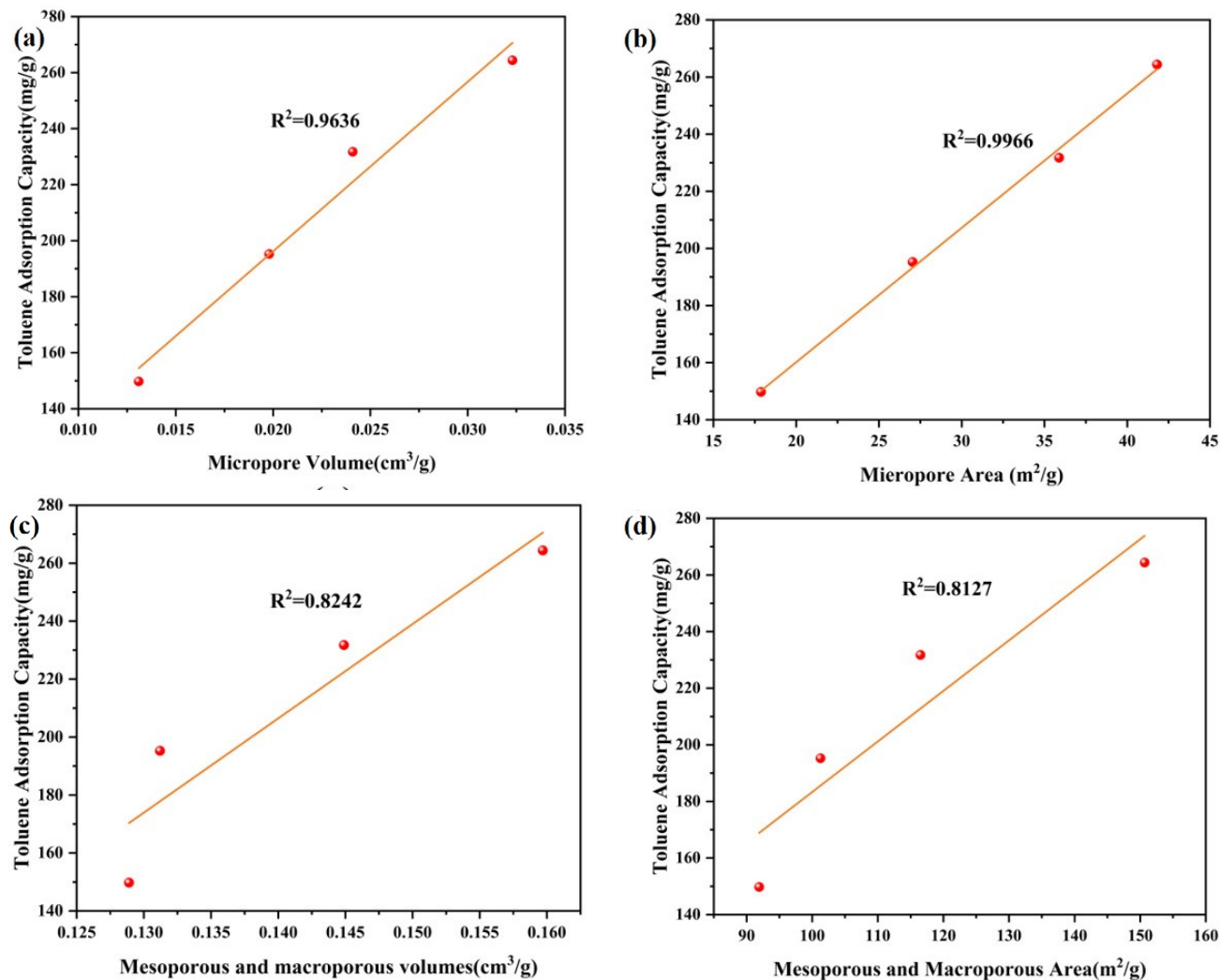


Figure 6. The relationship between toluene adsorption capacity and (a) microporous volume, (b) micropore area, (c) mesopores and macropore volume, and (d) mesopore and macropore area.

surface area or mesopore volume ($R^2 = 0.8127$ and 0.8242 , respectively; Fig. 6b, d). The adsorption capacity of PVIC for toluene is thus affected mainly by the microporous structure of the material itself. The weaker contribution of meso- and macro-pores to toluene adsorption is likely due to their acting mainly as transport channels during adsorption, rather than acting as adsorption sites.⁵¹ It follows that the microporous structure is the main site of toluene adsorption by PVIC-x.

Table 2 systematically lists the comparison between the materials synthesized in this study and the commonly used toluene trapping adsorbents in the literature. The results show that the adsorption of toluene by the PVIC-4 material is improved compared to zeolite and organic polymers, but it has some shortcomings compared to IL/MOF composites and there is room for further optimization, which can be achieved by modulating the anionic and cationic structure of the ionic liquids.⁵⁶

Table 2. Comparison of toluene capture performances with other adsorbents from literature.

Material	Toluene sorption capacity	Ref
Triphenylamine-based conjugated organic polymers	78mg/g	Lan et al ⁵² ,2021
S-S spherical zeolite	93mg/g	Chen et al ⁵³ ,2022
[BMIM][CH ₃ COO]/UiO-66 (1% wt.)	197mg/g	Ramos et al ⁵⁴ ,2022
[BMIM][CH ₃ COO]/MIL101 (10% wt.)	680mg/g	Ramos et al ⁵⁵ ,2023
PVIC-4	264mg/g	This work

In terms of adsorption mechanism, the adsorption of toluene by PVIC-x is mainly physical adsorption. The process can be divided into three stages, the first is the outer surface diffusion stage, where toluene is transferred to the outer surface of the adsorbent. Secondly, there is an internal diffusion stage, in which toluene diffuses through the pores into the inner surface, and the pore structure and volume are the dominant factors. Finally, there is the adsorption equilibrium stage, in which the adsorption sites are fully occupied and the adsorption slowly reaches equilibrium. In addition to physical adsorption, there is also some chemical adsorption, which is mainly attributed to π - π stacking interactions between toluene molecules and aromatic molecules of PIL, hydrogen bonding, and electrostatic interactions.

3. 4. Reusable Properties of Adsorbents

Adsorbent reusability is vital for practical commercial applications. As PVIC-4 had the optimal adsorption performance, it was selected for reproducibility performance study.

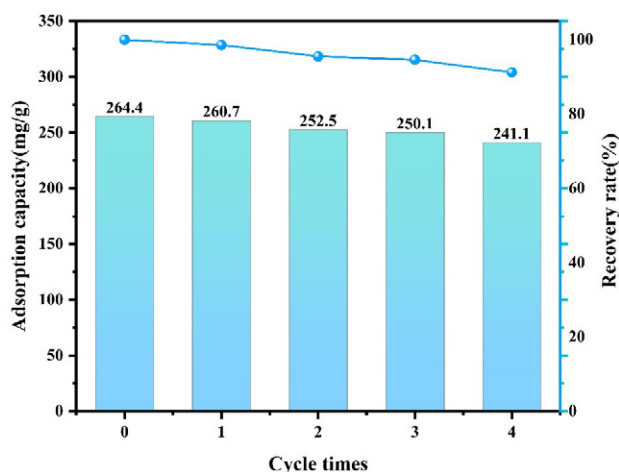


Figure 7. The reusability performance of PVIC-4.

The cyclic adsorption experiments of the adsorbent were carried out in the dynamic adsorption experimental setup. The desorption temperature of the adsorbent was increased from 25 °C to 130 °C at a rate of 10 °C/min, and the desorption gas flow was a 20 ml/min nitrogen flow, and the temperature was maintained at 130 °C until no toluene was detected at the gas chromatography detection outlet.

In five adsorption–desorption cycling experiments with new PVIC-4 material, the adsorption efficiency was 98.60%, 95.50%, 94.59%, and 91.19% (from the second cycle) (Fig. 7). The decrease in adsorption capacity may be due to pore blockage and coalescence, which would hinder the desorption of adsorbed toluene.⁵⁷

However, PVIC-4 still maintained >90% adsorption after several cycles, demonstrating satisfactory reusability.

4. Conclusions

PVIC adsorbents with different pore structures were synthesized using imidazolium-based ILs as raw materials and DVB as a cross-linking agent. FTIR spectroscopy confirmed that monomer copolymerization with DVB was successful. With specific microporous structures, BET-specific surface areas of PVIC-x tended to increase and then decrease with an increasing proportion of cross-linking agents. Breakthrough curves indicate that surface area and pore volume improve toluene adsorption capacity. Bangham kinetics and Langmuir isotherms adequately described the toluene adsorption behavior of PVIC-4 material, with its adsorption mechanism involving mainly physical interaction where toluene is adsorbed on the surface before diffusion within pore space. Together with a model of intra-particle distribution, this suggests that the intraparticle diffusion stage is the primary rate-limiting step for toluene adsorption by PVIC-x. The adsorption capacity of PVIC-4 remained above 90% after five use cycles, with robust toluene adsorption and regeneration performance. Analysis of the relationship between pore structure and adsorption capacity indicated that the microporous structure had a major influence on PVIC toluene adsorption capacity. Our findings indicate that PVIC-x are a promising adsorption material, indicating the need for future studies of VOC adsorption by PILs.

Supporting Information

Supporting information sheets S1, S2, S3 and S4 are available from the Annex.

5. References

1. X. Li, L. Zhang, Z. Yang, P. Wang, Y. Yan and J. Ran, *Sep. Purif. Technol.*, **2020**, 235. DOI:10.1016/j.seppur.2019.116213
2. C. Liu, W. Cai and L. Liu, *Appl. Clay Sci.*, **2018**, 162, 113–120. DOI:10.1016/j.clay.2018.06.005
3. M. Tang, X. Huang, Y. Peng and S. Lu, *Fuel*, **2020**, 270. DOI:10.1016/j.fuel.2020.117478
4. L. Lan, Y. Huang, Y. Dan and L. Jiang, *React. Funct. Polym.*, **2021**, 159. DOI:10.1016/j.reactfunctpolym.2020.104804
5. A. A. Rico-Barragán, J. R. Álvarez, S. Pioquinto-García, J. Rodríguez-Hernández, P. Rivas-García and N. E. Dávila-Guzmán, *Sustain. Prod. Consump.*, **2023**, 40, 159–168. DOI:10.1016/j.spc.2023.06.011
6. J. Yang, M. Gao, S. Wang, M. Zhang, L. Chen, J. Su, Y. Huang, Y. Zhang, X. Wang and B. Shen, *ACS Appl. Mater. Interfaces*, **2022**, 14, 40052–40061. DOI:10.1021/acsami.2c11700

7. X. Pan, N. Zhang, L. Yang, C. He, X. Ma, X. Liu, L. Liu, T. Hou and Y. Jiao, *ACS Omega*, **2023**, 8, 39329–39344. DOI:10.1021/acsomega.3c04866
8. J. Shao, F. Lin, Z. Wang, P. Liu, H. Tang, Y. He and K. Cen, *Appl. Catal., B*, **2020**, 266. DOI:10.1016/j.apcatb.2020.118662
9. S. Mo, Q. Zhang, J. Li, Y. Sun, Q. Ren, S. Zou, Q. Zhang, J. Lu, M. Fu, D. Mo, J. Wu, H. Huang and D. Ye, *Appl. Catal., B*, **2020**, 264. DOI:10.1016/j.apcatb.2019.118464
10. J. Zhang, Y. Hu, J. Qin, Z. Yang and M. Fu, *Chem. Eng. J.*, **2020**, 385. DOI:10.1016/j.cej.2019.123814
11. B. Zhu, L.-Y. Zhang, M. Li, Y. Yan, X.-M. Zhang and Y.-M. Zhu, *Chem. Eng. J.*, **2020**, 381. DOI:10.1016/j.cej.2019.122599
12. R. Ghasemi, F. Golbabaei, S. Rezaei, M. R. Pourmand, R. Nabizadeh, M. J. Jafari and E. Masoorian, *AMB Express*, **2020**, 10, 8. DOI:10.1186/s13568-019-0941-z
13. M. Kraus, U. Trommler, F. Holzer, F.-D. Kopinke and U. Roland, *Chem. Eng. J.*, **2018**, 351, 356–363. DOI:10.1016/j.cej.2018.06.128
14. K. Vellingiri, P. Kumar, A. Deep and K.-H. Kim, *Chem. Eng. J.*, **2017**, 307, 1116–1126. DOI:10.1016/j.cej.2016.09.012
15. E. David, *Materials (Basel)*, **2022**, 16 (1). DOI:10.3390/ma16010389
16. A. E. Memetova, I. V. Burakova, A. E. Burakov, N. R. Memetov and A. G. Tkachev, *Adsorpt.-J. Int. Adsorpt. Soc.*, **2023**, 29, 335–349. DOI:10.1007/s10450-023-00405-y
17. L. Wang and L. Hong, *J. Spat. Sci.*, **2019**, 66, 75–87. DOI:10.1080/14498596.2019.1601137
18. M. H. Jing, X. M. Song, D. W. Fang, L. Zhang and Q. Zhang, *Talanta*, **2019**, 197, 277–283. DOI:10.1016/j.talanta.2018.12.101
19. D.-J. Tao, F. Liu, L. Wang and L. Jiang, *Appl. Catal., A: General*, **2018**, 564, 56–63. DOI:10.1016/j.apcata.2018.07.018
20. J. Bedia, E. Ruiz, J. de Riva, V. R. Ferro, J. Palomar and J. J. Rodriguez, *AIChE J.*, **2012**, 59, 1648–1656. DOI:10.1002/aic.13926
21. X. Yan, S. Anguille, M. Bendahan and P. Moulin, *Chem. Eng. J.*, **2021**, 404. DOI:10.1016/j.cej.2020.127109
22. X. Ma, W. Wang, C. Sun and J. Sun, *Environ Pollut*, **2021**, 285, 117675. DOI:10.1016/j.envpol.2021.117675
23. J. Lin, T. Su, J. Chen, T. Xue, S. Yang, P. Guo, H. Lin, H. Wang, Y. Hong, Y. Su, L. Peng and J. Li, *Chemosphere*, **2021**, 272, 129640. DOI:10.1016/j.chemosphere.2021.129640
24. L. Sun, M. Gao and S. Tang, *Chem. Eng. J.*, **2021**, 412. DOI:10.1016/j.cej.2021.128764
25. X.-F. Wang, Y. Zhang, Y. Shu, X.-W. Chen and J.-H. Wang, *RSC Adv*, **2015**, 5, 31496–31501. DOI:10.1039/C5RA00036J
26. L. Tan, J. Zhu, M. Zhou, X. He and S. Zhang, *J. Mol. Liq.*, **2020**, 298. DOI:10.1016/j.molliq.2019.112054
27. M. Xin, J. Qiang, L. Zi, and K. Yuan, *J. Am. Chem. Soc.* **2005**, 127 (27), 9694–9695. DOI:10.1021/ja051803v
28. P. Zhao, Y. Leng and J. Wang, *Chem. Eng. J.* **2012**, 204–206, 72–78. DOI:10.1016/j.cej.2012.07.097
29. B. Lei, H. Xie, S. Chen, B. Liu and G. Zhou, *Environ Sci Pollut Res Int*, **2020**, 27, 27072–27092. DOI:10.1007/s11356-020-09115-2
30. M. Li, Y. Li, W. Li, F. Liu, X. Qi, M. Xue, Y. Wang and C. Zhao, *Environ Sci Pollut Res Int*, **2020**, 27, 6052–6065. DOI:10.1007/s11356-019-07293-2
31. X. Yang, H. Yi, X. Tang, S. Zhao, Z. Yang, Y. Ma, T. Feng and X. Cui, *J Environ Sci (China)*, **2018**, 67, 104–114. DOI:10.1016/j.jes.2017.06.032
32. B. Lei, B. Liu, H. Zhang, L. Yan, H. Xie and G. Zhou, *J Environ Sci (China)*, **2020**, 88, 122–132. DOI:10.1016/j.jes.2019.07.001
33. T. B. Nuria Fiol, *J. Chem. Eng. Process Technol*, **2013**, 04 (06). DOI:10.4172/2157-7048.1000165
34. G. Zhang, Y. Liu, S. Zheng and Z. Hashisho, *J Hazard Mater*, **2019**, 364, 317–324. DOI:10.1016/j.jhazmat.2018.10.031
35. M. Mozaffari Majd, V. Kordzadeh-Kermani, V. Ghalandari, A. Askari and M. Sillanpaa, *Sci Total Environ*, **2022**, 812, 151334. DOI:10.1016/j.scitotenv.2021.151334
36. X. Huang, Y. Wang, Y. Liu and D. Yuan, *J Sep Sci*, **2013**, 36, 3210–3219. DOI:10.1002/jssc.201300355
37. A. Pourjavadi, S. H. Hosseini and Z. S. Emami, *Chem. Eng. J.*, **2013**, 232, 453–457. DOI:10.1016/j.cej.2013.07.090
38. X. Feng, C. Gao, Z. Guo, Y. Zhou and J. Wang, *RSC Adv*, **2014**, 4, 23389–23395. DOI:10.1039/C4RA03163F
39. X. Tian, F. Luo, X. Dong, L. Liang, Y. Duan, J. Zhuang and Z. Chen, *Colloids Surf., A*, **2024**, 682. DOI:10.1016/j.colsurfa.2023.132883
40. J. Olvera-Mancilla, C. Aguilar-Lugo, L. Fomina, F. M. Sanchez-Arevalo, M. O. González-Díaz, R. Sulub-Sulub, M. Aguilar-Vega and L. Alexandrova, *Ind. Eng. Chem. Res.*, **2022**, 61, 6587–6599. DOI:10.1021/acs.iecr.2c00020
41. Y. Wang, W. Chen, B. Zhao, H. Wang, L. Qin and J. Han, *RSC Adv*, **2020**, 10, 23749–23758. DOI:10.1039/D0RA02225J
42. W. Sun, J. Li, H. Li, B. Jin, Z. Li, T. Zhang and X. Zhu, *Chemosphere*, **2022**, 296, 133962. DOI:10.1016/j.chemosphere.2022.133962
43. G. Zhang, B. Lei, S. Chen, H. Xie and G. Zhou, *J. Environ. Chem. Eng*, **2021**, 9. DOI:10.1016/j.jece.2021.105387
44. Y. Chen, C. Fan, X. Li, J. Ren, G. Zhang, H. Xie, B. Liu and G. Zhou, *J. Chem. Technol. Biotechnol*, **2022**, 98, 117–128. DOI:10.1002/jctb.7220
45. L. Largitte, T. Brudey, T. Tant, P. C. Dumesnil and P. Lodewyckx, *Microporous Mesoporous Mat*, **2016**, 219, 265–275. DOI:10.1016/j.micromeso.2015.07.005
46. M. Ş. Ece, S. Kutluay, Ö. Şahin and S. Horoz, *Ind. Eng. Chem. Res*, **2020**, 59, 21106–21123. DOI:10.1021/acs.iecr.0c03883
47. X. Zhang, X. Miao, W. Xiang, J. Zhang, C. Cao, H. Wang, X. Hu and B. Gao, *J Hazard Mater*, **2021**, 403, 123540. DOI:10.1016/j.jhazmat.2020.123540
48. T. K. Das, Q. Scott and A. N. Bezbaruah, *Chemosphere*, **2021**, 281, 130837. DOI:10.1016/j.chemosphere.2021.130837
49. W. Zou, B. Gao, Y. S. Ok and L. Dong, *Chemosphere*, **2019**, 218, 845–859. DOI:10.1016/j.chemosphere.2018.11.175
50. O. Sahin, S. Kutluay, S. Horoz and M. S. Ece, *Environ Sci Pollut Res Int*, **2021**, 28, 5231–5253. DOI:10.1007/s11356-020-10885-y
51. Y. N. Prajapati, B. Bhaduri, H. C. Joshi, A. Srivastava and N. Verma, *Chemosphere*, **2016**, 155, 62–69. DOI:10.1016/j.chemosphere.2016.04.040

52. D. Chen, Q. Tang and W. Deng, *Microporous Mesoporous Mat.*, **2022**, 346:112275. DOI:10.1016/j.micromeso.2022.112275
53. L. Lan, Y. Huang and Dan Y., *React. Funct. Polym.*, **2021**, 159:104804. DOI:10.1016/j.reactfunctpolym.2020.104804
54. Ventura C. R., H. Wei and Yeung K. L., *Environ Res.*, **2022**, 215(Pt 3): 114341. DOI:10.1016/j.envres.2022.114341
55. Ventura C. R., H. Wei and Zhang X., *Environ Res.*, **2023**, 219: 115000. DOI:10.1016/j.envres.2022.115000
56. Ventura C. R., H. Wei and Yeung K. L., *Green Chem. Eng.*, **2020**, 1(2): 147–154. DOI:10.1016/j.gce.2020.10.008
57. Z. An, S. Kong, W. Zhang, M. Yuan, Z. An and D. Chen, *Materials (Basel)*, **2020**, 13. DOI:10.3390/ma13030716

Povzetek

Za odstranjevanje hlapnih organskih spojin (VOCs) iz zraka so potrebni učinkoviti, ekonomični in trajni adsorbenti. Zamrežene polivinilne ionske tekočine (PVIC) s porozno strukturo so bile sintetizirane s kvaternizacijo 1-vinilimidazola (1VI) z 1-bromobutanom, da smo dobili 3-butil-1-vinilimidazolijev bromid (VIC), ki je bil nato kopolimeriziran z radikali divinilbenzena (DVB). Za karakterizacijo kompozitov smo uporabili ^1H NMR, ^{13}C NMR, vrstično elektronsko mikroskopijo, rentgensko fotoelektronsko spektroskopijo, infrardečo spektroskopijo s Fourierjevo transformacijo in N_2 izoterme adsorpcije-desorpcije. S spremembo strukture polimera s prilagoditvijo koncentracije DVB (razmerje med koncentracijo DVB in koncentracijo VIC je bilo x : 1 ($x = 0,4, 0,6, 0,8, 1,0$) in product je bil poimenovan PVIC- x ($x = 2, 3, 4, 5$)), je bila pridobljena optimalna struktura por PVIC-4 s specifično površino in skupnim volumnom por $192,5 \text{ m}^2 \text{ g}^{-1}$ oziroma $0,192 \text{ cm}^3 \text{ g}^{-1}$. Preskus adsorpcije toluena je potrdil adsorpcijsko kapaciteto. Adsorpcijsko obnašanje za VOCs na osnovi toluena je bilo raziskano z adsorpcijskimi prebojnimi krivuljami, adsorpcijsko kinetiko in izotermami. Adsorpcijski proces dobro opisujeta Banghamov kinetični in Langmuirjev izotermni model. Dinamična adsorpcija toluena je bila v vrstnem redu PVIC-4 > PVIC-5 > PVIC-3 > PVIC-2. Optimalna adsorpcijska kapaciteta toluena PVIC-4 je bila $264,4 \text{ mg g}^{-1}$ z ravnotežnim časom 56 minut, kar je bilo pripisano njegovi odlični strukturi por. PVIC-4 se je dobro odrezal tudi glede stopnje recikliranja, saj je po 5 ciklih recikliranja ohranil 91,19-odstotno učinkovitost adsorpcije. PVIC-4 lahko odstrani hlapne organske spojine iz zraka.



Except when otherwise noted, articles in this journal are published under the terms and conditions of the Creative Commons Attribution 4.0 International License

Development of Eutectics of Pioglitazone with Citric Acid and its Effect on Crystallite Properties and Dissolution

Mouli Das,¹ Shibashis Panigrahy,¹ Rasmita Dash,^{1,2} Rudra Narayan Sahoo,¹ Rakesh Swain,¹ Souvik Nandi,¹ Sk Habibullah,¹ Tanisha Das¹ and Subrata Mallick^{1,*}

¹ Department of Pharmaceutics, School of Pharmaceutical Sciences, Siksha 'O' Anusandhan (Deemed to be University), Bhubaneswar 751003, Odisha, India.

² Centurion University of Technology and Management, Odisha, India.

* Corresponding author: E-mail: profsmallick@gmail.com
subratamallick@soa.ac.in

Received: 05-07-2024

Abstract

Eutectics of pioglitazone were developed using citric acid (CA) as the co-former, and the effect on crystallite properties and dissolution has correspondingly been studied. Pioglitazone-citric acid eutectics (PC1, PC2, PC3, and PC4) in different molar ratios (3:1, 3:2, 1:1, and 3:4 respectively) were prepared by simple solvent evaporation method. Difference in dislocation density and strain value of the eutectics were observed, and the maximum strain value of PC1 might be due to the highest deformation activity compared to PC2, PC3, and PC4. Carbonyl-thiazolidine or carboxyl-pyridine weak bond formation might be the reason of producing eutectics of PGZ-CA rather than cocrystal with a docking score of -2.2 kcal/mol. Likewise, lowest particle size was found with PC1 rather than that of pure PGZ and other eutectics. PC1 demonstrated highest dissolution of drug (68%) rather than other eutectics (54 to 61%) and PGZ (44%) after 360 min.

Keywords: Eutectics; pioglitazone; citric acid; *In vitro* dissolution; strain and dislocation density

1. Introduction

Currently, crystal engineering approach focuses on the formation of various systems like hydrate, solvate, polymorphs, solid solution, cocrystal, eutectic, etc. facilitating advancements in improving the pharmaceutical properties without compromising other physicochemical properties.^{1,2} Among all these rising systems, cocrystal and eutectic mixtures are playing a pivotal role in efficiently enhancing dissolution and consequently absorption particularly of drugs with limited solubility. Heteromolecular (adhesive) interaction between two compounds can overshadow a homomolecular (cohesive) interaction of distinct components creating co-crystals whereas, stronger homomolecular interaction compared to heteromolecular interaction leads to the formation of eutectic mixture.^{3,4} Non-covalent interactions such as van der Waals force, electrostatic interaction, halogen bonding, and hydrogen bonding between the drug molecule and the co-former suggest the structure of the cocrystal formation. Supramolecular synthons are the usual name used to describe these fundamental structural units found in supermolecules. Homosynthons (similar functional group) and heterosynthons (complementary but unlike functional group) are the two divided groups of supramolecular syn-

thons.⁵ Hydrogen bond formation between the acid group and the amide group or the amine or alcohol is required to create a supramolecular synthon.⁶ For instance, when a molecule possesses a carboxylic acid group, one can select a complementary partner molecule, often referred to as a cocrystal former or co-former, containing functionalities like acid, amide, or pyridyl groups, to form a cocrystal. Nevertheless, not every molecule possessing complementary functional groups is suitable for cocrystal formation. In addition to producing a cocrystal, the outcome of co-crystallization may result in a solid solution, a eutectic, or even a basic physical mixture of unreacted compounds. Eutectics have been suggested as transitional states leading to specific cocrystals, and it was observed that solution eutectic constants play a vital role in the formation and stabilization of cocrystals in solution.³ Eutectics are the formulations having low melting points as a result of combining two or more compounds in a certain molar ratio. It has been noted in many literatures that organic acids like benzoic acid,⁷ citric acid (CA), salicylic acid,⁸ and malic acid,⁹ among others, can produce eutectics. In a eutectic system, the different components are present in specific proportions that lead to a eutectic composition, and when this composition is heated or cooled, it undergoes a

phase transition at a single, well-defined temperature, forming a eutectic mixture. In a standard co-crystallization experiment, the development of multi-component adducts, such as salts, cocrystals, solid solutions, or eutectics, is contingent upon the characteristics of the components involved and the specific interactions that emerge between them.⁴ Generally, if a molecule contains a carboxylic acid group it can choose a co-former or a partner containing a complementary functional group like amide, acid, or pyridine to make a co-crystal. However, it is very rare to have a complementary functional group to prepare a cocrystal.

The molecule and the co-former are exploited to make a eutectic or a solid solution when cocrystal formation is hampered.³ In the case of eutectic formation, adhesive interaction is heteromolecular which is generally weaker because of the lack of lattice arrangement of any long-range order.¹⁰ A study demonstrated that the soluble carrier quickly dissolves, leaving the insoluble drug in an absolutely fine state of subdivision when the eutectic mixture is in contact with digestive fluids.¹¹ In a study solubility of itraconazole, griseofulvin, danazol, and benzoic acid in urea- and malonic acid-choline chloride deep eutectic solvent has been increased by many folds.¹²

Pioglitazone (PGZ), an ethylpyridin-thiazolidinedione-type oral drug, reduces insulin resistance in “type 2 diabetes mellitus”. It exhibits non-polar characteristics, rendering water incapable of efficiently disrupting the lattice structure of the molecules. Consequently, its solubility in aqueous medium is notably limited.¹³ Inadequate aqueous solubility and slow dissolution of PGZ contribute to sub-therapeutic plasma levels, potentially lacking in therapeutic success. Eutectics of pioglitazone were attempted to prepare using CA as the co-former in different molar ratios by simple solvent evaporation method as the cocrystal formation is hampered due to lack of complementary functional group. The combination of PGZ-CA could form eutectic rather than cocrystal via weak carbonyl-thiazolidinedione or carboxyl-pyridine bond development and may lack a long-range order arrangement. The eutectic products are supposed to exhibit enhanced drug dissolution.

2. Material and Methods

2.1. Materials

PGZ was received as a gift sample from Pattanaik Science Supply Syndicate, Bhubaneswar, Odisha, India. Citric acid was procured from Merck Specialties Pvt. Ltd., India. Ethanol was procured from Himedia Laboratories Pvt. Ltd., India. All other chemicals and reagents were of analytical grade and commercially available.

2.2. Preparation of PGZ Eutectic Formulation

Eutectic formulations of PGZ were prepared by solvent

evaporation method employing CA as a co-former in different molar ratios. Accurately weighed amounts of CA were mixed with precisely weighed amounts of PGZ before being dissolved in ethanol followed by drying the solution at 40–50 °C for 72 h. Eutectics were obtained as the solvent of the solution evaporated (Table 1). The chemical structure of PGZ with CA is presented in Fig. 2 in various possible ratios.

Table 1: Eutectic formulation of PGZ using CA as co-former from ethanolic solution by solvent evaporation technique

Eutectic code	Molar ratio	PGZ (mg)	CA (mg)	Solvent
PC1	3:1	1000	180	Ethanol
PC2	3:2	1000	360	Ethanol
PC3	1:1	1000	537	Ethanol
PC4	3:4	1000	716	Ethanol

2.2. Characterizations

2.3.1. Fourier Transform-infrared (FTIR) Spectroscopy

IR grade potassium bromide (KBr) was mixed with the samples separately in the ratio of 100:1 in order to obtain corresponding pellets with the help of applied 5 tons pressure for 2 min using a hydraulic press. The pellets were scanned between the range of 400–4000 cm⁻¹ frequency in FTIR spectrophotometer using *Spectra Manager* software version 2.0 (JASCO FT/IR-4100).

2.3.2. Differential scanning calorimetry (DSC)

Differential scanning calorimetry technique (DSC-1, Mettler Toledo) was used to obtain the thermograms of samples. 3 to 4 mg of test samples were placed in a hermetically sealed aluminum pan and another empty aluminum pan was used as a reference. Samples were subjected to a nitrogen flow with a flow rate of 20 ml/min and the scanning was carried out at a rate of 10 °C/min. The temperature of all the samples were maintained within the range of 30–300 °C.¹⁴

2.3.3. Powder X-ray Diffraction (PXRD)

PXRD was carried out for different samples to study their crystal structure, chemical composition followed by their physical characteristics. About 1 mg of dry powdered sample was placed on the glass slide and was subjected to powder X-ray diffractometer (Ultima, IV, Japan)¹⁵ Throughout the testing, an X-ray power of 40kV/40mA at a detection angle (2–75° 2θ) was employed for 120 sec.

2.3.3. Scanning Electron Microscopy (SEM)

The surface morphologies of different samples were recorded with a scanning electron microscope (Gemini

SEM 300). The dried samples were sputtered coated with gold-palladium and scanned at room temperature.

2. 4. *In vitro* Drug Dissolution Study

The *in vitro* dissolution study for pure drug (PGZ) and different PGZ-CA eutectic formulations were carried out following the guidelines of US pharmacopoeia XXIII rotating paddle method in a dissolution apparatus (Electrolab, India). A specific amount of the formulation was placed in 900 ml sodium lauryl sulphate (SLS) solution (0.5%) in the dissolution vessel and 50 rpm rotation speed was set up. The temperature was set at 37 ± 0.5 °C for the entire period of time. Aliquots of 10 ml sample was withdrawn at pre-determined time interval from dissolution media along with the replenishment of fresh medium of same volume to maintain the sink condition.¹⁶ Lambda max was set at 223 nm in UV-visible spectrophotometer (Shimadzu) for the analysis of samples in a triplicate manner.

2. 5. *In silico* Binding Interaction Study

Drug and excipient molecule interaction has been forecasted using AutoDock Vina 1.1.2 Software.¹⁷ With

the help of Marvin sketch the 3-D structures of PGZ, CA was generated. Since AutoDock Vina only recognizes PDBQT files, the MGL Tools software package was used to build PDBQT files for further enquiry.¹⁸ By resizing the grid box, all of the three-dimensional centers and axes were appropriately aligned. After the successful generation of PDBQT files, the docking was conducted using the command prompt.¹⁹ The PGZ was taken as a ligand against receptor CA. The finest binding was confirmed by the highest negative score.

2. 6. Statistical Analysis

All measured data are presented as mean \pm S.D. (standard deviation).

3. Results and Discussion

3. 1. PGZ Eutectic Product

In the current research, PGZ-CA eutectic formulations were prepared using the solvent evaporation method (Table 1). After the preparation, sharp needle-shaped crystals were observed (Figure 1). The possible structure

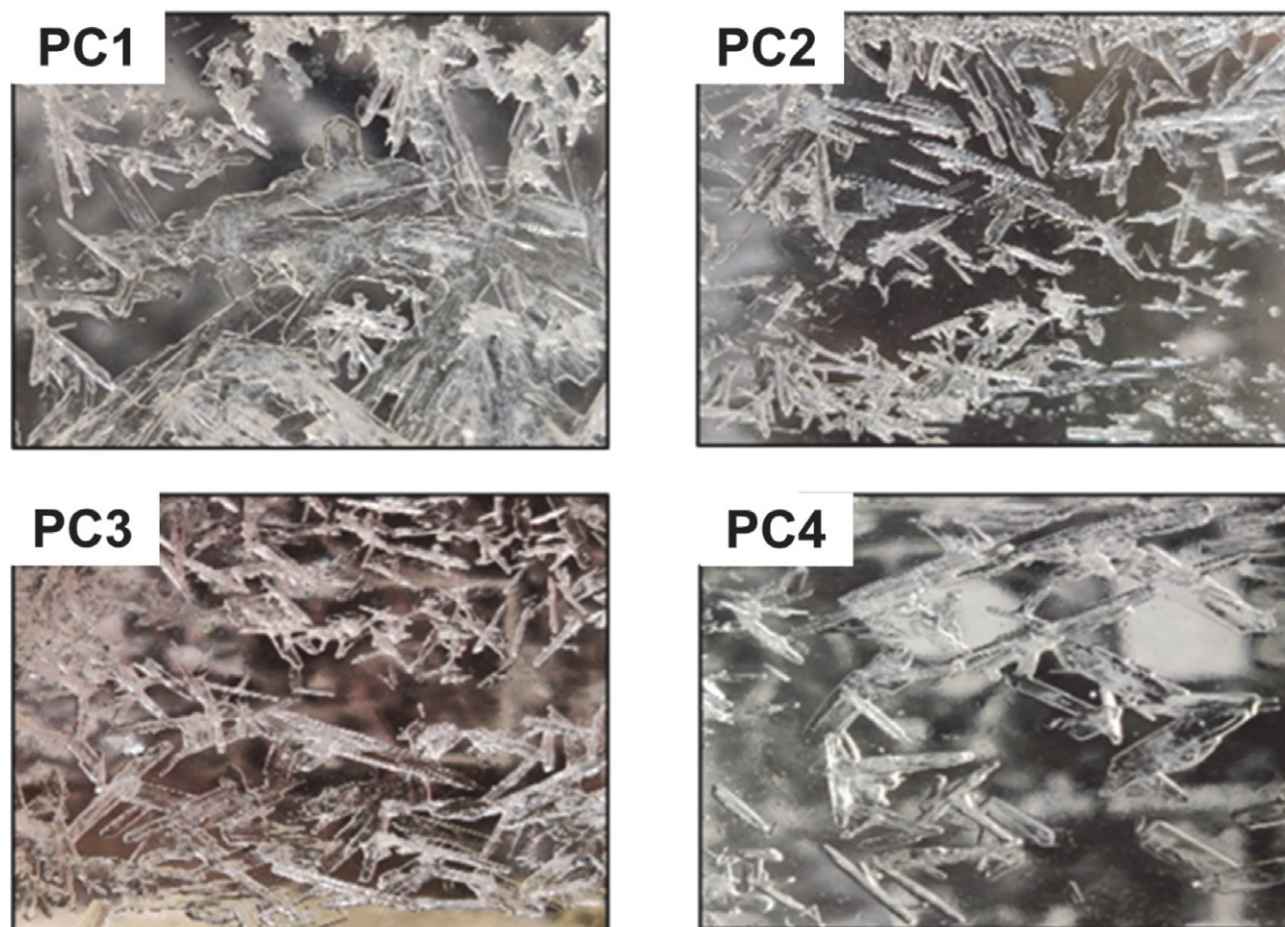


Figure 1. Photographs of prepared PGZ-CA eutectic product

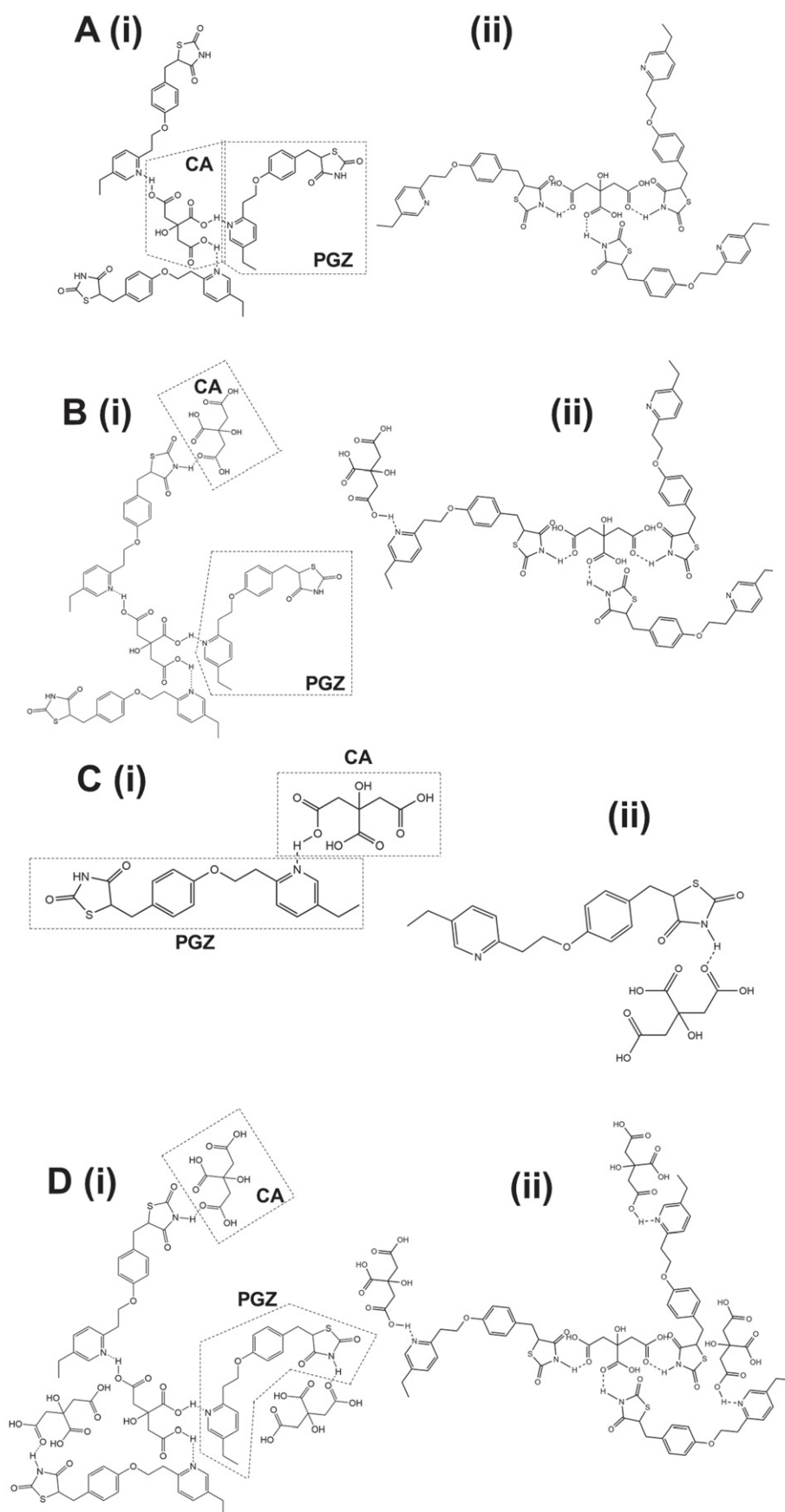


Figure 2 Proposed formation of eutectics of pioglitazone with CA: (A) PC1; (B) PC2; (C) PC3; (D) PC4

of co-crystal of PGZ with CA in different ratios are represented in Figure 2.

3. 2. Characterization

3. 2. 1. FTIR Spectroscopy

The FTIR spectra of pure PGZ and its eutectic formulations with CA are presented in Figure 3. The FTIR spectrum of pure PGZ showed the presence of a characteristic peak at 3416 cm^{-1} owing to N-H stretching of aromatic amine,²⁰ as well as two distinct peaks at 2927 and 2743 cm^{-1} representing aliphatic C-H stretching. The carbonyl (C=O) stretching vibration is assigned to the strong absorption peak at 1742 and 1684 cm^{-1} whereas, the peaks at 1618 and 1242 cm^{-1} are the indication of presence of aromatic ring and C-O group respectively.²¹

PGZ peak at 1509 and 1552 cm^{-1} due to N-H in-plane bending vibration (in general $1630\text{--}1500\text{ cm}^{-1}$) has little been broadened or shifted in prepared eutectic products.²² The changes might have occurred due to weak bond formation between N-H of thiazolidine and carbonyl group of citric acid (carbonyl-thiazolidinedione or carboxyl-pyridine bond development). FTIR results of the eutectics also revealed C=O stretching and C-S stretching within $1675\text{--}1685\text{ cm}^{-1}$ and $1330\text{--}1335\text{ cm}^{-1}$ respectively. In addition, these spectra of eutectic products presented a broadened peak in the range of $3412\text{--}3418\text{ cm}^{-1}$, which may be due to the formation of hydrogen bonding between CA and PGZ. The FTIR peak at 1742 and 1684 cm^{-1} in PGZ is either broadened or absent in prepared eutectics because of the interaction between PGZ and CA. As a result, the changes might be considered to be due to the formation of eutectics with the organic acid molecules.

3. 2. 2. DSC

The DSC thermograms of pure PGZ and its eutectic products with CA are presented in Figure 4. The characteristic single endotherm at $195.61\text{ }^{\circ}\text{C}$ confirmed the melting point of PGZ.^{23,24} The melting endotherm of prepared eutectic samples differed significantly from those of pure PGZ. All the eutectic formulations exhibited endotherm noticeably below the melting point of pure PGZ. Also the disappearance of the sharp endothermic peak of the PGZ in the formulations supported the formation of eutectics with co-former in different molar ratios. After analyzing all of the DSC data, it was found that the PGZ was formed its eutectics. Thus, DSC thermogram confirms that there is no sign of chemical incompatibility in developing non-covalent derivatives (eutectics).

3. 2. 4. PXRD

When the functional groups are compatible for effective formation of non-covalent bond, size and shape of the parent molecule favors a crystal packing, then a cocrystal will form but on the other hand, when the functional groups are compatible to form non-covalent bonding but they lack to form a crystal packing, then eutectic will produce. The PXRD pattern of pure PGZ and its eutectic formulations with CA are presented in Figure 5. Pure PGZ showed 2 θ values at 8.764 , 17.64 , 18.897 , 20.830 , and 21.223 indicating crystallinity.²³ The characteristic peaks of PGZ were either absent or shifted a little with smaller intensity or broadened in prepared PGZ-CA eutectic formulations. In addition, the intensity of the parent peak was found to be decreased may be due to the formation of eutectics. The data obtained from the PXRD analysis showed that the FWHM (full-width half maximum), particle size

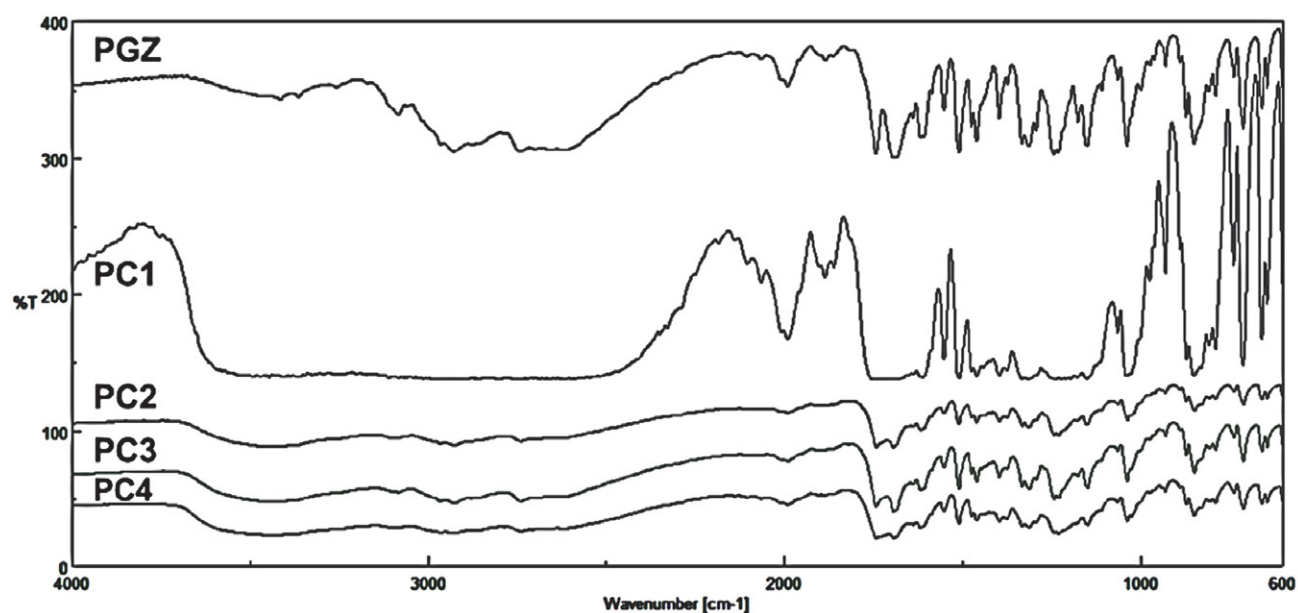


Figure 3. FTIR spectra of pure PGZ and PGZ-CA eutectic formulations

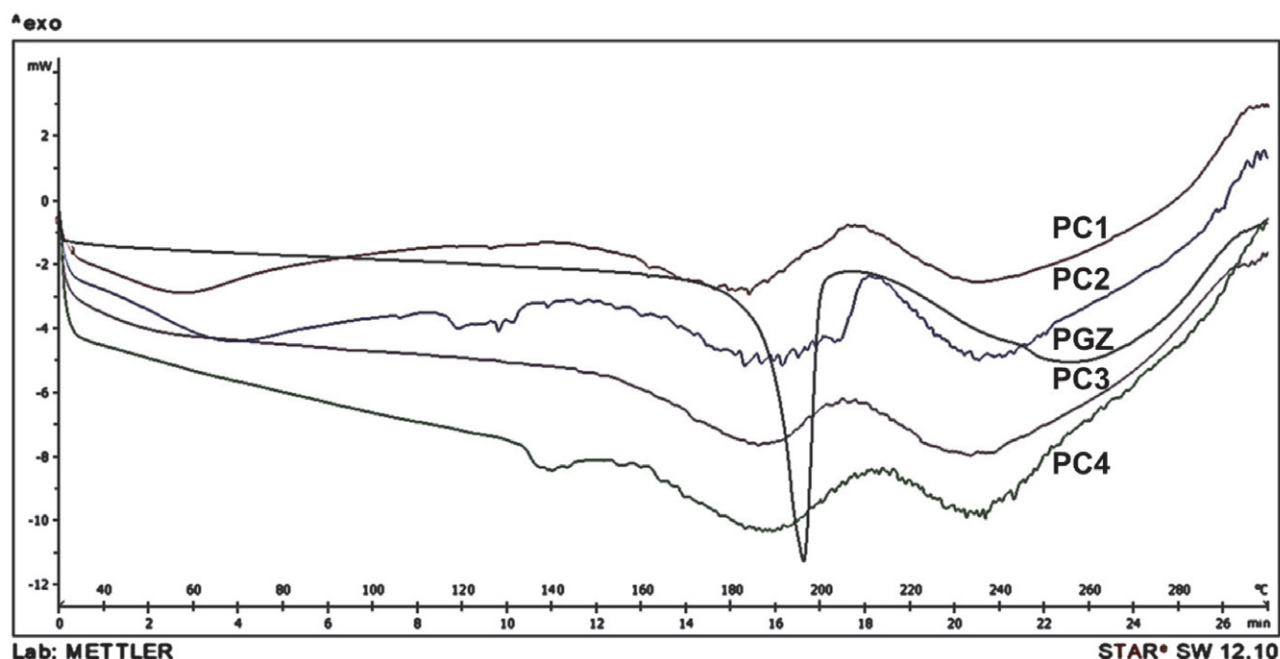


Figure 4. DSC thermograms of PGZ and PGZ-CA eutectic formulations

of the formed eutectics was found decreased than the pure drug (PGZ) (Table 3).

Table 2: List of XRD peaks observed in PGZ and prepared eutectic formulations

Sample code	2θ value observed
PGZ	8.76, 17.64, 18.90, 20.83, 21.22
PC1	8.94, 21.04, 23.29, 26.50, 32.02
PC2	10.80, 15.64, 21.14, 23.53
PC3	8.89, 15.87, 21.00, 23.26
PC4	9.08, 16.08, 20.56, 26.72, 28.77

Particle size is an important parameter to calculate because of proper understanding in microstructural parameters. To calculate crystallite particle size, Scherrer method is the most commonly used method depending on the XRD peaks broadening data. The most traditional method to calculate the crystallite size is the Scherrer method. For determination of crystallite size (D) of the prepared crystal, the Scherrer's equation is stated as:

$$D = \frac{k\lambda}{\beta \cos\theta} \quad (1)$$

Where, D is the crystalline size in nm; k is the shape factor which is taken as 0.9; λ is the wavelength of the X-rays i.e., 0.154056 nm for Cu K α 1 radiation; β is the broadening of the peaks and that is also known as peak width at half maxima (FWHM) measured in radians and finally θ is the Bragg's angle of diffraction.

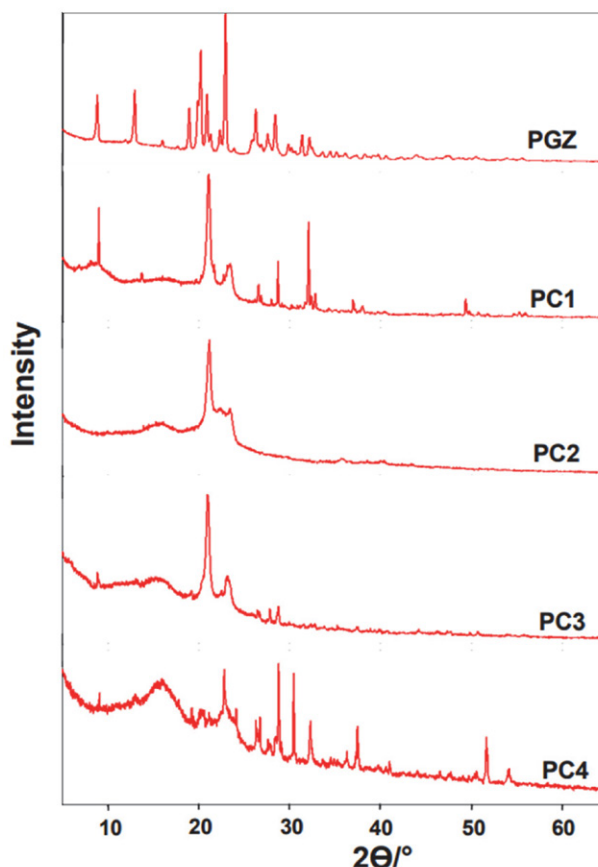


Figure 5. XRD pattern of PGZ and PGZ-CA eutectic formulation

Crystal distortion and deformity was occurred due to the induced strain and the strain was calculated by using the equation:¹⁵

$$\varepsilon = \frac{\beta}{4 \tan \theta} \quad (2)$$

Table 3. Crystallite properties of eutectics of pioglitazone with citric acid estimated from XRD

Eutectic code	FWHM	Particle size (nm)	Strain (10^{-3})	Dislocation Density (m^{-2})
PGZ	0.209±0.05	40.65±10.31	4.36±1.04	2.42±0.61
PC1	0.621±0.15	13.68±3.27	12.2±2.91	21.371±5.11
PC2	0.525±0.21	17.28±6.23	10.6±4.32	13.39±4.82
PC3	0.203±0.03	40.39±6.02	6.46±0.94	2.45±0.36
PC4	0.33±0.11	26.58±9.51	7.31±2.22	5.65±2.02

Particle size of PC1 was found lowest as compared to other eutectic formation as well as pure PGZ. The difference in dislocation density and strain value between PZA and PGZ-CA eutectics was observed because of weak bond formation between PGZ and CA. Eutectic PC1 showed highest strain value maybe due to higher deformation activity between molecules in a material. From this data we can assume PC1 formed a strong eutectic formation.

3. 2. 3. SEM

SEM photographs of pure PGZ (a) and PGZ-CA eutectic formulation (b) is presented in Figure 6. Characteristic crystal morphology is seen in the micrograph of pure PGZ while that geometry is slightly different in the eutectic product. Presence of lamellar structure or microstructure composed of alternating fine layers in the eutectic product attributed due to the partial deformation of PGZ crystal. The attainment of eutectic formation using CA as organic co-former was also supported by DSC and PXRD.

3. 3. *In vitro* Drug Dissolution

The presence of food disrupts absorption, leading to delays in peak plasma concentration, sometimes extending up to 5–6 hours. Several studies demonstrated various formulations of PGZ like SMEDDS,²⁶ nanosuspension,²⁷ multilayered tablet,²⁸ floating tablet,²⁹ transdermal patch,³⁰ etc. having limitations like entrapment efficacy of SNEDDS, physical stability of nanosuspension, lamination in multilayered tablets etc. Other approaches were also applied to enhance the solubility of PGZ like the preparation of inclusion complex,³¹ using poloxamer 188 and 407,³⁰ using natural polymer Pullulan³³ and all the studies exhibited an increase in solubility and dissolution profile as compared to pure PGZ. Other approaches were also applied to enhance the solubility of PGZ like the preparation of inclusion complex,³¹ using poloxamer 188 and 407,³² using natural polymer Pullulan³³ and all the studies exhibited an increase in solubility and dissolution profile as compared to pure PGZ.

In vitro drug dissolution is a crucial physicochemical parameter frequently used to assess the possible risk of the dissolution-rate controlled absorption of a chemical entity. Owing to its kinetic nature, *in vitro* drug dissolution assumes a better correlation with *in vivo* drug dissolution. Therefore, to quantitatively evaluate the impact of the solid-state modification on the drug dissolution behavior, *in vitro* drug dissolution was estimated in 0.5% SLS solution. *In vitro* PGZ release pattern of pure PGZ and its eutectic formulations with CA, at different molar ratios are presented in Figure 7. From the *in vitro* drug dissolution profile, it was observed that PC1 (containing 3:1 molar ratio) showed the highest release (67.55%) as compared to other PGZ-CA eutectic formulations. observed that among all prepared eutectic formulations of PGZ-CA. The potential reason for this increase in solubility could be linked to the poorly water-soluble active pharmaceutical ingredient (API) interacting non-covalently with a more water-soluble co-former.

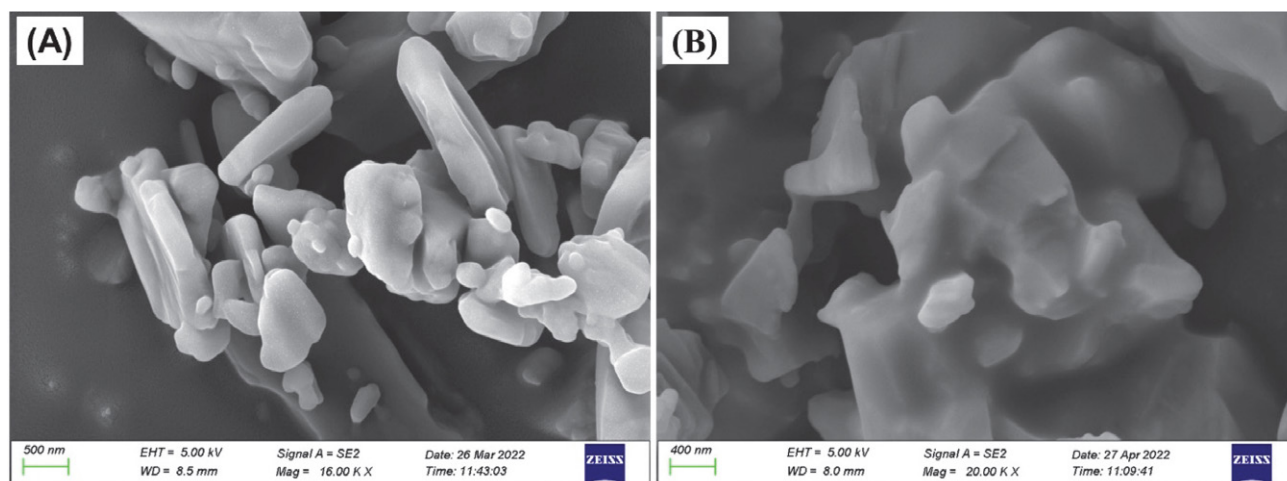


Figure 6. SEM photograph of (A) pure PGZ (magnification: 16k ×), (B) PGZ-CA eutectic formulation (PC1) (magnification: 20k ×)

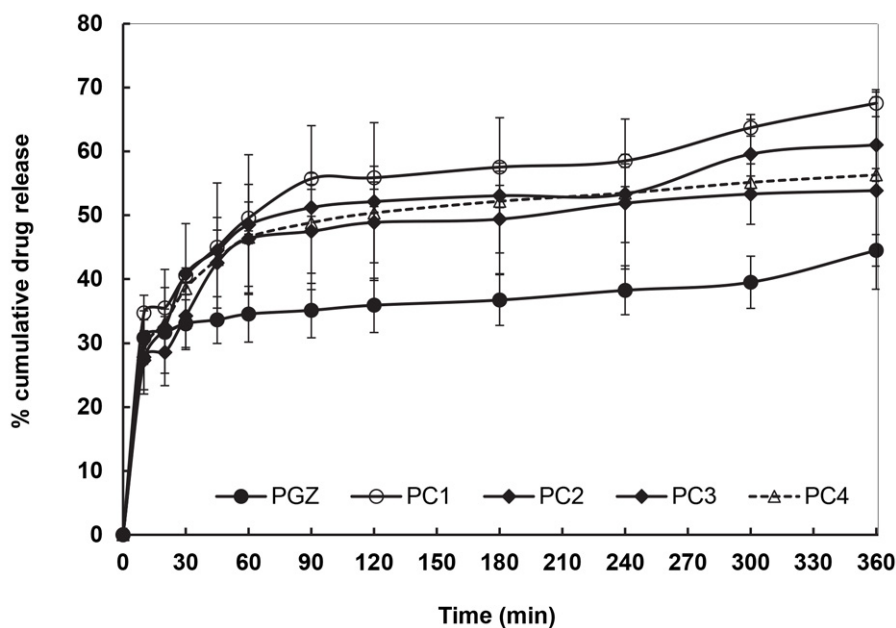


Figure 7. *In vitro* PGZ dissolution pattern of pure PGZ and PGZ-CA eutectic formulations

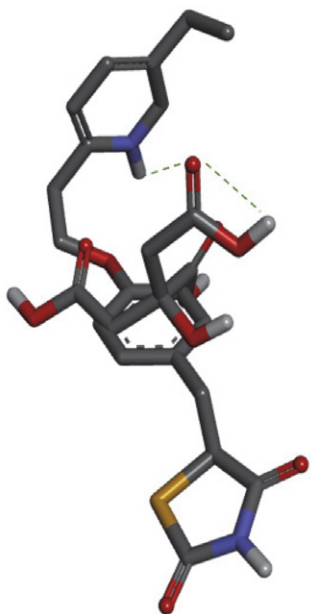


Figure 8: Pictorial elucidation of *In-silico* binding interactions of pioglitazone-CA

Linear defects on atomic scale are the reason behind dislocation which favorably enhanced the drug dissolution. Highest dislocation density was observed in PC1 which exhibited the maximum dissolution profile as compared to pure drug and other eutectic products.

3. 4. Drug-excipient Molecular Interaction

The objective of this *in silico* molecular docking study is to uncover specific information about the

drug-excipient molecule interaction affinity and types of interaction between them, if any.¹⁸ The PGZ was taken as a ligand against receptors like CA. The finest binding was confirmed by the highest negative score.¹⁹ The molecular interaction study revealed a stable binding interaction between PGZ and excipient molecules (organic acid molecule i.e., CA used to prepare eutectic formulations of PGZ). *In silico* binding interactions and potential binding sites are depicted using a pictorial format in Figure 8. The detailed binding interactions have been elucidated in Table 4. The negative energy verified that all of these eutectic formulations of PGZ had stable binding.

Table 4. *In silico* binding interaction and potential binding of PGZ-CA eutectic formation

Formulation code	Docking score (kcal/mol)	Bond type	Bond distance (Å)
PGZ-CA	-2.2	Conventional hydrogen bond	2.5

4. Conclusion

Eutectic products of pioglitazone were made ready using CA as the co-former in different molar ratios by solvent evaporation technique. The combination of PGZ-CA formed eutectic rather than cocrystal possibly by weak carbonyl-thiazolidine or carboxyl-pyridine bond development. The difference in dislocation density and strain value of PGZ vs PGZ-CA eutectics could be the cause of weak

bond formation between PGZ and CA and highest strain value of PC1 might be due to the peak deformation activity compared to PC2, PC3, and PC4. Particle size of PC1 was also found lowermost rather than that of pure PGZ and other eutectics. The findings of the *in vitro* dissolution test demonstrated that the PC1 (PGZ-CA as 3:1 molar ratio) exhibited maximum dissolution of drug (68%) compared to other prepared eutectic formulations (54 to 61%) and pure PGZ (44%) after 360 min. In addition, *in silico* molecular docking study demonstrated the binding score of -2.2 kcal/mol.

Acknowledgments

The authors are very much grateful to Prof. Manojranjan Nayak, Honorable President, Siksha 'O' Anusandhan (Deemed to be University) for providing laboratory facilities and lots of encouragement for carrying out the research work.

Conflict of interest:

The authors report that there is no potential conflict of interest to declare.

5. References

1. B. S. Satapathy, A. Patel, R. N. Sahoo, S. Mallick, *J. Serb. Chem. Soc.* **2020**, 85, 1–12. DOI:10.2298/JSC200705049S
2. W. J. Irwin, M. Iqbal, *Int. J. Pharm.* **1991**, 75, 211–218. DOI:10.1016/0378-5173(91)90195-T
3. S. Cherukuvada, A. Nangia, *Chem. Comm.* **2014**, 50, 906–923. DOI:10.1039/C3CC47521B
4. S. Cherukuvada, T. N. Guru Row, *Cryst. Growth Des.* **2014**, 14, 4187–4198. DOI:10.1021/cg500790q
5. M. Hemamalini, W. S. Loh, C. K. Quah, H. K. Fun, *Chem. Cent. J.* **2014**, 8, 1–9. DOI:10.1186/1752-153X-8-31
6. S. Karki, T. Friščić, W. Jones, *CrystEngComm* **2009**, 11, 470–481. DOI:10.1039/B812531G
7. R. Solaimalai, G. Shinde, A. Dharamsi, C. Kokare, *New J. Chem.* **2020**, 44, 17088–17098. DOI:10.1039/D0NJ03570J
8. S. Narwal, A. Kumar, M. Chaudhary, V. Budhwar, *Res. J. Pharm. Technol.* **2021**, 14, 1875–1879. DOI:10.52711/0974-360X.2021.00331
9. J. Tellers, M. Jamali, P. Willems, B. Tjeerdsma, N. Sbirrazzuoli, N. Guigo, *Green Chem.* **2021**, 23, 536–545. DOI:10.1039/D0GC03172K
10. N. B. Singh, S. S. Das, N. P. Singh, T. Agrawal, *J. Cryst. Growth.* **2008**, 310, 2878–2884. DOI:10.1016/j.jcrysgro.2008.01.054
11. L. M. Mayer, Z. Chen, R. H. Findlay, J. Fang, S. Sampson, R. F. Self, P. A. Jumars, C. Quet  l, O. F. Donard, *Environ. Sci. Technol.* **1996**, 30, 2641–2645. DOI:10.1021/es960110z
12. H. G. Morrison, C. C. Sun, S. Neervannan, *Int. J. Pharm.* **2009**, 378, 136–139. DOI:10.1016/j.ijpharm.2009.05.039
13. S. Soltanpour, A. Jouyban, *J. Solution Chem.* **2011**, 40, 2032–2045. DOI:10.1007/s10953-011-9767-2
14. L. Guan, H. Xu, D. Huang, *J. Polym. Res.* **2011**, 18, 681–689. DOI:10.1007/s10965-010-9464-7
15. M. A. Lemes, M. S. Godinho, D. Rabelo, F. T. Martins, A. Mesquita, F. N. Neto, Araujo O. A., A. E. De Oliveira, *Acta Chim. Slov.* **2014**, 61, 778–785.
16. A. Gauniya, S. Das, S. Mallick, S. P. Basu, *J. Pharm. Bioallied Sci.* **2010**, 2, 118–120. DOI:10.4103/0975-7406.67015
17. O. Trott, A. J. Olson, *J. Comput. Chem.* **2010**, 31, 455–461. DOI:10.1002/jcc.21334
18. R. Dash, R. N. Sahoo, S. Nandi, R. Swain, S. Mallick, *Indian J. Pharm. Edu. Res.* **2019**, 53, s580–s586. DOI:10.5530/ijper.53.4s.153
19. R. Dash, R. N. Sahoo, S. C. Si, S. Mallick, *Chemical Papers.* **2022**, 76, 2823–2832. DOI:10.1007/s11696-022-02065-8
20. D. Karimkhani, E. Rahimpour, A. Jouyban, M. Kouhkan, F. Azarbayjani, *Phys. Chem. Liq.* **2024**, 1–9. DOI:10.1080/00319104.2024.2344172
21. G. B. Vambhurkar, A. M. Jagtap, A. S. Gavade, D. S. Randive, M. A. Bhutkar, S. D. Bhinge, *J. Rep. Pharm. Sci.* **2021**, 10, 35–41. DOI:10.4103/jrtps.JRTPS_29_19
22. S. A. Sakib, M. F. Khan, M. Arman, F. B. Kader, M. O. Faruk, S. M. Tanzil, S. Brogi, *Biointerface Res. Appl. Chem.* **2021**, 11, 13806–13828. DOI:10.33263/BRIAC116.1380613828
23. R. D. Patel, M. K. Raval, *Results in Chemistry.* **2022**, 4, 100315. DOI:10.1016/j.rechem.2022.100315
24. M. Teaima, S. Hababeh, M. Khanfar, F. Alanazi, D. Alshora, M. El-Nabarawi, *Pharmaceutics.* **2022**, 14, 425. DOI:10.3390/pharmaceutics14020425
25. P. A. Gajare, C. H. Patil, N. A. Kalyane, Y. O. Pore, *Digest J. Nanomater. Biost.* **2009**, 4, 891–897.
26. V. Pandey, S. Kohli, *Future J. Pharm. Sci.* **2017**, 3, 53–59. DOI:10.1016/j.fjps.2017.02.003
27. R. Narayan, Z. Attari, M. S. Reddy, K. B. Koteswara, *Adv. Sci. Lett.* **2016**, 22, 987–994. DOI:10.1166/asl.2016.6979
28. Y. A. Chowdary, R. Raparla, M. Madhuri, *J. Pharm.* **2014**, 2014. DOI:10.1155/2014/848243
29. W. He, Y. Li, R. Zhang, Z. Wu, L. Yin, *Int. J. Pharm.* **2014**, 476, 223–231. DOI:10.1016/j.ijpharm.2014.09.056
30. A. B. Nair, S. Gupta, B. E. Al-Dhubiab, S. Jacob, P. Shinu, J. Shah, M. Aly Morsy, N. SreeHarsha, M. Attimarad, K. N. Venugopala, S. H. Akrawi, *Pharmaceutics.* **2019**, 11, 359. DOI:10.3390/pharmaceutics11070359
31. S. P. Kovvasu, K. P. Chowdary, *Int. J. App. Pharm.* **2018**, 10, 49–55. DOI:10.22159/ijap.2018v10i3.24558
32. V. A. Jagtap, A. N. Talele, A. R. Bendale, S. Narkhede, A. Jadhav, G. Vidyasagar, *Res. J. Pharm. Technol.* **2010**, 3, 1152–1157.
33. A. Kulkarni, T. Madane, N. Aloorkar, S. Mujumdar S. J. *Curr. Pharm. Res.* **2019**, 9, 3321–3324.

Povzetek

V tem delu smo razvili evtektike pioglitazone (PGZ) z uporabo citronske kisline (CA) kot sooblikovalca ter proučili vpliv CA na lastnosti kristalitev in raztapljanje. Evtektike pioglitazona in CA (PC1, PC2, PC3 in PC4) smo pripravili v različnih molskih razmerjih (3:1, 3:2, 1:1 in 3:4) z enostavno metodo izparevanja topila. Opazili smo razliko v gostoti dislokacij in vrednosti deformacije eutektikov. Najvišjo vrednost deformacije je imela PC1, kar bi lahko pripisali najvišji deformacijski aktivnosti v primerjavi s PC2, PC3 in PC4. Šibke vezi med karbonil-tiazolidinom ali karboksil-piridinom so verjetno povzročile nastanek evtektikov PGZ-CA namesto kokristala z vrednostjo sidranja $-2,2$ kcal/mol. Prav tako je PC1 imela najmanjšo velikost delcev v primerjavi s čistim PGZ in drugimi evtektiki. Po 360 minutah je PC1 dosegla najvišjo stopnjo raztapljanja zdravila (68 %) v primerjavi z drugimi evtektiki (54 do 61 %) in PGZ (44 %).



Except when otherwise noted, articles in this journal are published under the terms and conditions of the Creative Commons Attribution 4.0 International License

Phytochemical Analysis and Evaluation of the Antioxidant, Anti-Inflammatory, Hemolytic, and Antibacterial Effects of *Astragalus gombo* (L.) Leaves

Mohammed Laid Tlili,^{1,2*} Ibtissam Laib,^{1,3} Khadidja Salemi,¹ Imane Chetehouna,¹
Ines BenMoussa¹ and Elhafnaoui Lanez^{1,4}

¹ Department of Cellular and Molecular Biology, El Oued University, Algeria

² Biogeochemistry of Desert Environments laboratory, Ouargla University, Algeria

³ Higher School of Saharan Agriculture, El Oued, Algeria

⁴ VTRS Laboratory, Department of Chemistry, Faculty of Exact Sciences, El Oued University, Algeria*

* Corresponding author: E-mail: tili-laid@univ-eloued.dz

Tel.: +213 672613510

Received: 03-29-2024

Abstract

The purpose of this study was to determine the phytochemical content and biological activities of *Astragalus gombo* (endemic species). We conducted an HPLC analysis to identify the secondary metabolites. Antioxidant (DPPH and FRAP), anti-inflammatory, anti-hemolytic and antibacterial activities were evaluated. For the HPLC analysis, we obtained 65 peaks and identified six major bioactive compounds. The total concentration of polyphenols, flavonoids and condensed tannins varied, respectively, from 66.3 ± 0.9 mg GA eq/g, 34.31 ± 1.4 mg Q eq/g and 5.3 ± 2.7 mg Ca eq/g. In terms of antioxidant activity, the extract exhibited high inhibitory activity, equivalent to $IC_{50} = 62.81 \pm 0.01$ μ g/mL for DPPH and $IC_{50} = 19.37 \pm 0.04$ μ g/mL for FRAP. The anti-inflammatory activity was estimated to be high at 1615.8 ± 2.8 μ g/mL, the anti-hemolytic activity was weak and the antibacterial activity against the five strains under study was moderately strong. This study demonstrated that the aqueous extract of *A. gombo* from El Oued region has remarkable antioxidant, anti-inflammatory, and antibacterial activity.

Keywords: *Astragalus gombo*; phytochemical; biological activity; HPLC analysis.

1. Introduction

Medicinal plants are widely recognized for their therapeutic and nutritional benefits that help in the treatment of various illnesses and the development of new pharmaceuticals, according to a World Health Organization survey.^{1,2} Interest in the medicinal properties of plants, particularly their antioxidant, anti-inflammatory, and antibacterial effects, has notably increased. According to estimates by the World Health Organization, approximately 20,000 plant species are employed for medicinal purposes in 91 countries. The process of developing new pharmaceuticals involves several critical stages, including extraction, pharmacological screening, bioactive material isolation, characterization, toxicology, and clinical evalua-

tion.³ Polyphenol compounds, including flavonoids, tannins, and anthocyanins, have various biological activities and antioxidant properties, making them potential replacements for medical treatments.²

Algeria's diverse plant flora, with 3139 species across 150 botanical groups, includes 653 indigenous species. This has increased interest in medicinal plants with their antioxidant, anti-inflammatory and anti-bacterial capabilities significantly in recent years and among the therapeutic plants that we considered in our study is *Astragalus gombo*.⁴

Astragalus gombo is the most important genus of flowering plants and therefore of the family,^{5,6} comprising over 2,500 to 3,000 species.⁷ The species is widespread in Central Asia, South and North America, and North and

South Africa. The Algerian Sahara is also an indigenous to one of them, *Astragalus gombo*. It is a perennial plant, both common and endemic.⁸ *Astragalus gombo* thrives in well-drained, sandy loam soil with a pH range of 6.0 to 7.5. It is essential to avoid waterlogged conditions, as they can hinder root development and increase susceptibility to root diseases. This plant prefers moderate humidity levels, ideally between 40–60 %. Excessive humidity can promote fungal growth, whereas very low humidity might cause dehydration stress.⁶ In addition, optimal growth occurs at temperatures between 18 °C and 25 °C (64 °F to 77 °F). It can tolerate a slight frost, but prolonged exposure to temperatures below 10 °C or above 30 °C can negatively impact growth and yield. Further, *Astragalus gombo* requires full sunlight for at least 6–8 hours daily. Insufficient sunlight can lead to reduced photosynthetic activity and stunted growth.⁸ It is well used in the food industry, cosmetics and pharmacy. It is mainly used to treat diseases, among its active compounds are coumarins, alkaloids, tannins, phenolic acids, terpenes and flavonoids.⁹

Astragalus gombo is one of the astragalus plants found in Algerian flora. Several astragalus species are used in both traditional and modern medicine. Its leaves are used in traditional medicine to treat hemorrhoids, diabetes, leukemia and irregular menstruation, and the root is employed as an anti-stimulant.¹⁰

Considering the potential of this genus, it is important to reveal the phytochemical characteristics of *A. gombo*. The purpose of this work is to quantify the phenolic contents and identify the main phenolic compounds present in the crude extract of the leaf using HPLC analysis. The biological activity of the extract will be evaluated for antioxidant, anti-inflammatory, hemolytic, and antibacterial potentials for the first time in El Oued region (a north-east area in the Algerian Sahara).

2. Materials and Methods

2.1. Chemicals and Reagents

Sodium chloride (NaCl), Monobasic potassium phosphate (KH_2PO_4), Trichloroacetic acid (TCA), Butylated hydroxytoluene (BHT), Aluminum trichloride (AlCl_3) 2%, 2,2-diphenyl-1-picryl hydrazyl (DPPH), ascorbic acid, gallic acid, dimethyl sulfoxyl (DMSO), and ferric chloride (FeCl_3) were all obtained from Sigma-Aldrich (USA).

2.2. Preparation of Plant Material

In March 2023, during the *Astragalus gombo* flowering season, leaf portions of the plant were collected from the Southeast region of Algeria (specifically in the area of Hassi Khalifa, province of El-Oued). Professor Atef Chouikh (Faculty of Natural Science and Life, El Oued University) recognized the plant material. The aerial sec-

tion of the plant was washed with flowing water to remove dust and other extraneous objects. Then, it was powdered, dried, and kept for later use.

2.3. Preparation of Aqueous Extract

Approximately 10 grams of *Astragalus gombo* leaf powder were steeped in 100 mL of distilled water and left to stand at room temperature for 24 hours in darkness. Subsequently, filter paper was used to remove impurities. The material was extensively dried at 40 °C following extraction, according to Murugan and Parimelazhagan.¹¹ The extract was weighed and stored in a refrigerator at 4 °C for future study.

2.4. Phytochemical screening

Using the standard methods for phytochemical analysis (screening), the extract was examined for the presence of various compounds, including phenols, tannins (catechical and gallic tannins), alkaloids, steroids, saponins, flavonoids, and triterpenoids. A (+) indicates the existence of phytochemicals, whereas a (–) indicates their absence.¹²

2.5. Estimation of Total Phenolic Compounds

The total amount of phenolic was determined using the Folin-Ciocalteu method. To 1 mL of 10% Folin-Ciocalteu reagent, 0.2 mL of the aqueous extract of *A. gombo* was added. The addition of 800 L of saturated sodium carbonate (75 g/L) was made after 4 minutes. After 2 hours of incubation at room temperature, the absorbance was measured at 765 nm. To ensure that the results could be replicated, the tests were run three times.¹³ By using the linear calibration equation for gallic acid, the total phenolic content was computed as milligrams of gallic acid equivalent per gram of extract.

2.6. Estimation of Total Flavonoids

We used the aluminum chloride (AlCl_3) colorimetric method for determining the total flavonoid content of *A. gombo* extract,¹⁴ as follows: 1 mL of the AlCl_3 solution is mixed with 1 mL of the sample, and separately, with 1 mL of the standard. At 430 nm, the absorbance was measured, after 30 minutes against the prepared reagent blank. In order to determine the results, a linear calibration equation using quercetin as the standard was utilized. The results were represented as milligrams of quercetin per gram of extract.

2.7. Estimation of Condensed Tannin

The level of tannin in the extract was determined using spectrophotometry, according to Broadhurst and Jones¹⁵, catechin was used to make the calibration curve.

The sample was pipetted into an aluminum foil-wrapped tube along with 3.0 mL of newly prepared vanillin reagent (4% w/v vanillin in methanol), and the mixture was properly mixed before 1.5 mL of strong hydrochloric acid was added. After 15 minutes at 20 to 2 °C, the reaction's absorbance was assessed against water at 500 nm.

2. 8. HPLC Analysis

Phenolic compounds were qualitatively and quantitatively analyzed using a Shimadzu LC20 HPLC equipped with the universal injector (Hamilton 25l), an analytical column Shim-pack VP-ODSC18 (250 × 4.6 mm, 5 µm particle size), maintained at 25.0 °C and an injection volume of 20 µL. Chromatograms and UV spectra were collected using a Shimadzu UV-VIS detector SPD 20A. The mobile phase consisted of a gradient elution of a combination of acetonitrile and acetic acid (0.1%). The gradient program was initiated with 95% A and 5% B for the first 5 minutes, followed by a linear gradient to 50% A and 50% B from 5 to 25 minutes, further transitioning to 5% A and 95% B from 25 to 30 minutes, and concluded with re-equilibration at 95% A and 5% B from 30 to 35 minutes. The flow rate is maintained at 1.0 mL/min.

The sample preparation involves extracting phenolic compounds from the plant material using an aqueous solvent (ultra-pure distilled water). The resulting extract is then filtered through a 0.45 µm membrane filter to remove any particulate matter, and, if necessary, diluted with the mobile phase. The HPLC system is equipped with a UV-Vis detector set at 268 nm, a wavelength optimal for phenolic compounds based on their characteristic absorption.

Identification and quantification of chromatographic peaks were confirmed by comparison of the retention time (tR) of extract and standards.

2. 9. DPPH Free-Radical Scavenging Activity

1 mL of the DPPH• solution was mixed with 1 mL of each extract (or ascorbic acid as a control). To complete the reaction, the reaction mixture was stirred briefly and then kept at the room temperature for 30 minutes in the darkness, at 517 nm.¹⁶

2. 10.Reducing Power Assay (FRAP)

Oyaizu's methods were used to calculate the extract's reducing power. The sample was combined with phosphate buffer (2.5 mL, 0.2 M, pH 6.6) and 1% potassium ferricyanide water solution (2.5 mL, K₃[Fe(CN)₆]) at various concentrations (mg/mL) in distilled water. After aliquots of trichloroacetic acid (2.5 mL, 10% aqueous solution) were added, the mixture was incubated at 50 °C for 20 minutes before centrifuging for 10 minutes at 3000 rpm. The supernatant (2.5 mL) and filtered water were mixed with freshly prepared FeCl₃ (0.5 mL, 0.1%) solution (2.5 mL). The ab-

sorbance was measured at a wavelength of 700 nm. The use of ascorbic acid as a positive control was used.¹⁷

2. 11.Hemolytic Activity

The hemolysis experiment was conducted in accordance with the methodology outlined by Tlili and Benine, as detailed below.¹⁸ 5 mL of blood was centrifuged at 1000 rpm for 10 minutes at 40 °C in tubes containing 5.4 mg of EDTA to stop coagulation. The hemolytic assay was carried out on washed erythrocytes that were kept at 40 °C for 6 hours. 100 µL of test samples (containing an *A. gombo*) and 50 µL of erythrocyte suspension in 10 dilutions were employed. The positive and negative controls, 100 µL each of 1XPBS and 100 µL each of 1% SDS, were utilized. After that, the samples were incubated for 60 minutes in a water bath at 37 °C. 850 µL of XPB were added to the reaction mixture to bring the volume up to 1 mL. After centrifuging it for 3 minutes at 300 rpm, the hemolysis rate of the different extracts is calculated as a percentage (%) relative to the total hemolysis with a spectrophotometer at 540 nm, according to the following formula:

$$\text{Hemolysis Inhibition (\%)} = 100 - \left(\frac{DO_{\text{Sample}}}{DO_{\text{control}}} \times 100 \right) \quad (1)$$

2. 12. Anti-inflammatory Activity

The egg albumin denaturation inhibition method was used to investigate the anti-inflammatory potential of crude aqueous extract from *A. gombo*. The reaction mixture (5 mL) comprised 200 µL of fresh hen's egg albumin, 2.8 mL of phosphate buffer (pH 6.4), and 2 mL of various concentrations of the standard drug, Aspegic. 2 mL of distilled water was used instead of extract or Aspegic to prepare the control. Following a 15-minute incubation period at 37 °C in a water bath, the reaction mixtures underwent a 5-minute heating period at 70 °C. The reaction mixtures' absorbance was measured at 660 nm using a UV-visible spectrophotometer after cooling, with the buffer serving as the blank. Percentage of inhibition was calculated by using following equation¹⁹:

$$\text{Inhibition percentage} = \frac{DO_{\text{Control}} - DO_{\text{sample}}}{DO_{\text{control}}} \times 100 \quad (2)$$

2. 13.Antibacterial Activity

The agar well-diffusion method was used to evaluate the effectiveness of manufactured *A. gombo* against five hazardous bacteria. This included three Gram-negative bacteria (EC: *Escherichia coli* ATCC 8737; PA: *Pseudomonas aeruginosa* ATCC 9027; ST: *Salmonella typhimurium* ATCC 14028) and two Gram-positive bacteria (BS: *Bacillus subtilis* ATCC 6633 and LI: *Listeria innocua* CLIP 74915). The Petri plates were incubated at 37 °C for 24 hours. The inhibitory zone's diameter was measured in millimeters (mm). The antimicrobial tests were conducted in triplicate.²⁰

2. 14. Statistical Analysis

All of the experiments were performed in triplicate. The data were analyzed in Microsoft Excel and are presented as mean \pm standard deviation ($n = 3$). Graphpad Prism 7 for Windows was used to calculate the IC_{50} and EC_{50} values. The analysis of variance (ANOVA) technique was used to statistically analyze the data and determine the significance level. The XLSTAT software was utilized for this purpose.

3. Results and Discussion

3. 1. Phytochemical Screening

Phytochemical test results in our study indicate the presence of secondary metabolites including alkaloids, tannins, flavonoids, terpenoids and polyphenols, in the *Astragalus gombo* extract (Table 1), albeit in varying concentrations.

Table 1. Phytochemical composition of the aqueous extract of *A. gombo*

Phytochemical composition		Observation
polyphenols		(+)
alkaloids	Mayer	(–)
	Wagner	(+)
Flavonoids		(+)
Tannins		(+)
terpenoids		(+)
Saponins		(–)

The results of the phytochemical tests reveal the richness of the extract from various active constituents. The bioactive properties of these substances include antioxidant, anti-inflammatory, and antibacterial effects. Results of phytochemical screening are consistent with those found by Benferdia et al.²¹ Hence, the existence of each secondary metabolite in *A. gombo* provides us with an evidence to support this plant's traditional use as a remedy for a variety of diseases.

3. 2. Quantification of Phytochemical Compounds

Total phenolic, flavonoid and condensed tannic compounds were expressed using the following equations based on the calibration curve: $Y = 0.0153x + 0.265$, $R^2 = 0.8835$ for phenolic compounds and $Y = 0.0096x + 0.0521$, $R^2 = 0.9371$ for flavonoid compounds and $Y = 0.0031x + 0.0301$, $R^2 = 0.9977$ for condensed tannin compounds (Table 2).

Table 2. Total content of phenols, flavonoids, condensed tannins.

Compounds	<i>A. gombo</i>
Polyphenols	66.3 \pm 0.9
Flavonoids	34.3 \pm 1.4
Tannins	5.3 \pm 2.7

According to the results of the quantification of phytochemical compounds, the *A. gombo* plant contains high concentrations of flavonoid polyphenols and tannins. This may be due to the influence of climatic factors (high temperature, drought, exposure to sunlight and salinity), which stimulate the biosynthesis of these secondary metabolites.²² This proves the effectiveness of this plant and its high biological activity.

3. 3. HPLC Analysis

The HPLC results showed the presence of six compounds among nine reference compounds at the level of phenolic compounds on 65 peaks in the aqueous raw extract of *A. gombo*. The quercetin (9441.9 μ g/g) is the most abundant phenolic compound identified, while only trace amounts of other phenolic compounds including p-coumaric acid (113.1 μ g/g), caffeic acid (100.5 μ g/g), vanillic acid (63.5 μ g/g), vanillin (31.5 μ g/g), and rutin (12 μ g/g) were found in *A. gombo* (Table 3).

Table 3. Retention time and concentration of the phenolic compounds identified in the aqueous extract of *A. gombo*.

Retention time (min)	Compounds phenolic	Concentration (μ g/g extract)
5.29	Gallic acid	ND
13.39	Chlorogenic acid	ND
15.53	Vanillic acid	63.5
16.27	Caffeic acid	100.5
21.46	Vanillin	31.5
23.81	p-Coumaric acid	113.1
28.37	Rutin	12
34.79	Naringin	ND
45.05	Quercetin	9441.9

The qualitative analysis indicates the presence of quercetin, p-coumaric acid and caffeic acid in large amounts, suggesting that the plant has anti-inflammatory, antitumor and antioxidant effects,²³ and it has the ability to reduce the peroxidation of low-density lipoproteins (LDL) and the immune response.²⁴ This plant holds promise for applications in traditional medicine and drug development.

3. 4. Antioxidant Activity

The results of the DPPH assay and FRAP assay by the use of *Astragalus gombo* aqueous extract and different

standard antioxidants are summarized in Table 4. There are remarkable differences in the antioxidant capacity among the antioxidants tested; the antioxidant activity of *A. gombo* was much lower than that of the standard antioxidant with its IC₅₀ values for DPPH of 62.81±0.01 µg/mL, and the reducing power of FRAP was 19.37±0.04 µg/mL. However, ascorbic acid had the highest DPPH and reducing power activities with an IC₅₀ value of 18.79±0.05 µg/mL and 24.75±0.03 µg/mL, respectively. Additionally, statistical analysis demonstrated highly significant differences ($p < 0.001$) between the extract and the positive control (ascorbic acid). Both the DPPH and FRAP tests measure antioxidant capacity, but in different ways. The DPPH test focuses on the ability to neutralize a specific type of free radical, while the FRAP test evaluates the overall ability to reduce metal ions. Together, these tests provide a comprehensive view of the antioxidant capabilities of an *A. gombo*, showing both specific free radical neutralizing capacity and general reducing capacity.

Table 4. IC₅₀ in free-radical scavenging activity (DPPH) and Reducing Power Assay (FRAP) of the aqueous extract of *A. gombo*. a, b means with distinct letters in each column differ significantly ($p < 0.05$).

Extract/ standard	IC ₅₀ (µg/mL± SD) DPPH	EC ₅₀ (µg/mL± SD) FRAP
<i>A. gombo</i>	62.81±0.01 ^a	19.37±0.04 ^a
Ascorbic acid	18.79±0.05 ^b	24.75±0.03 ^b

The antioxidant activity findings were higher than those of ascorbic acid due to quercetin capacity to eliminate free radicals, as demonstrated by the HPLC analysis.²⁵

Moreover, P-coumaric acid and caffeic acid are phenolic compounds found in many plants, and they exhibit significant antioxidant properties due to their chemical structures, where both acids donate hydrogen atoms or electrons to neutralize free radicals, thereby preventing oxidative damage^{33,34}. Additionally, they can chelate transition metal ions such as iron, reducing their ability to catalyze the production of reactive oxygen species (ROS) through Fenton and Haber-Weiss reactions, thus limiting ROS generation.³⁵

3. 5. Hemolytic Activity

Weak hemolytic activity observed in general of crude extract of *A. gombo* was obtained at about 4.8–19.3% at 20–60 µg/mL, while SDS demonstrated the highest hemolytic activity when employed as a positive control (58.7–62.6%) and statistical analysis confirmed the significant difference ($p < 0.001$) between *A. gombo* and SDS (Figure 1).

The results of the hemolytic assay indicate that the extract exhibits a less significant hemolytic effect when in contact with human erythrocytes. This reduced hemolytic activity is attributed to the absence of saponins in the extract.²⁶ Clinical use of saponins is limited due to their hemolytic activity, which mediates toxicity in animals and humans. The mechanism of destruction of the erythrocyte membrane using saponins (hemolysis) is not yet fully elucidated,^{9,27} reported that saponin interacts with the sterols present in the membranes of erythrocytes and produces hemolytic reactions. This leads to rupture of the erythrocyte membrane, resulting in an increase in cell permeability and the loss of hemoglobin. Another mechanism involved in hemolysis has also been explored,²⁸ in which the

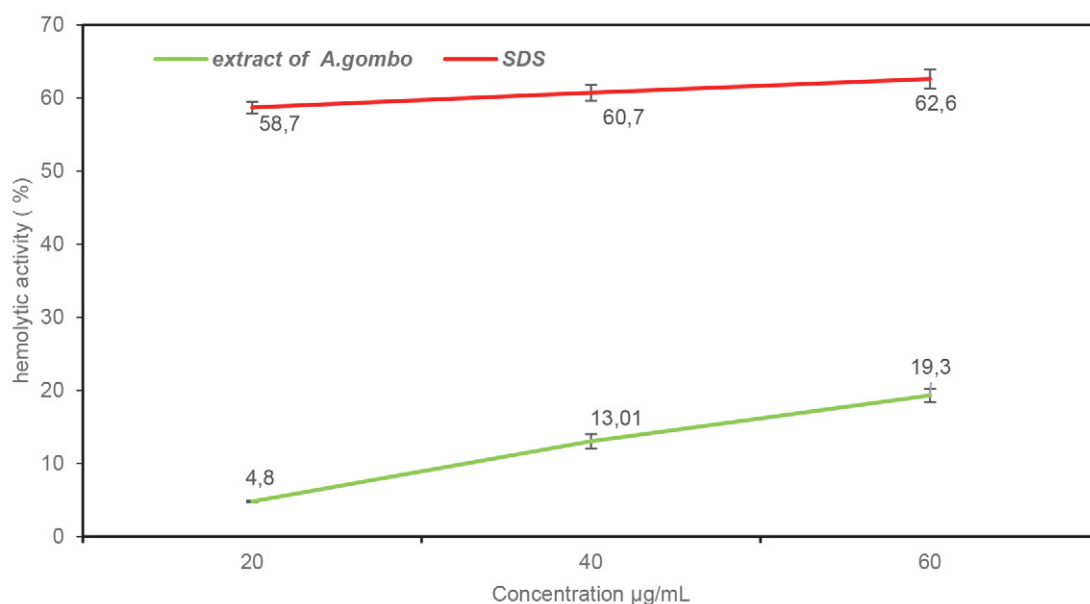


Figure 1. Hemolytic activity of *A. gombo* on red blood cells compared to 1% SDS.

extensive interaction between saponins and water channels, aquaporins, induces an increase in membrane permeability due to the entry of water molecules into the cells, causing the rupture of erythrocytes and the appearance of hemolysis.

3. 6. Anti-inflammatory Activity

The anti-inflammatory activity is very important ($IC_{50}=1615.81\pm2.8\text{ }\mu\text{g/mL}$). The percentage of inhibition of protein denaturation increased with increasing concentration (Figure 2). However, its anti-denaturation effects are generally lower compared to Aspegic.

Statistical analysis ($p < 0.001$) confirms a significant difference in anti-inflammatory activity between *A. gombo* and Aspegic.

Most biological proteins lose their efficacy when denatured. The ability of a substance to inhibit the denaturation of proteins implies its obvious potential for anti-inflammatory activity.

The findings show that the extract *A. gombo* has remarkable anti-inflammatory property. This activity may be attributed to the strong occurrence of polyphenolic compounds including alkaloids, flavonoids, tannins, steroids, and phenols.³³ The extract elements function as free radical inhibitors or scavengers by acting as primary oxidants and they are capable of controlling the production of autoantigens and inhibiting heat-induced albumin denaturation. Furthermore, p-coumaric acid, found abundantly in many plants, exhibits significant anti-inflammatory effects by inhibiting key enzymes and signaling pathways involved in

inflammation.^{34,36} It reduces the production of pro-inflammatory mediators like nitric oxide (NO), prostaglandins, and cytokines by downregulating the expression of inducible nitric oxide synthase (iNOS) and cyclooxygenase-2 (COX-2). Additionally, p-coumaric acid interferes with the activation of the nuclear factor-kappa B (NF- κ B) pathway, a critical regulator of inflammatory responses. By preventing NF- κ B activation, p-coumaric acid decreases the transcription of various inflammatory cytokines, thereby reducing overall inflammation in plant tissues.³⁶

Similarly, quercetin has well-known anti-inflammatory effects via multiple mechanisms. It inhibits the release of histamine and other inflammatory mediators from mast cells and basophils.³² Quercetin also downregulates the activity of COX-2 and lipoxygenase (LOX), leading to a reduction in the synthesis of pro-inflammatory prostaglandins and leukotrienes. Understanding these mechanisms highlights the importance of these compounds in plant defense and offers potential insights into their applications in medicinal contexts.²⁹

3. 7. Antibacterial Activity

The results presented in Table 5 clearly reveal a remarkable effect of the aqueous extract of *Astragalus gombo* leaves on the five strains studied. The extract exhibited notable antibacterial activity across all tested strains, with zones of inhibition varying from 8 to 11.3 mm. We also noted that in all the types of bacteria studied, the increase in the concentration of plant extract led to an increased zone of inhibition.

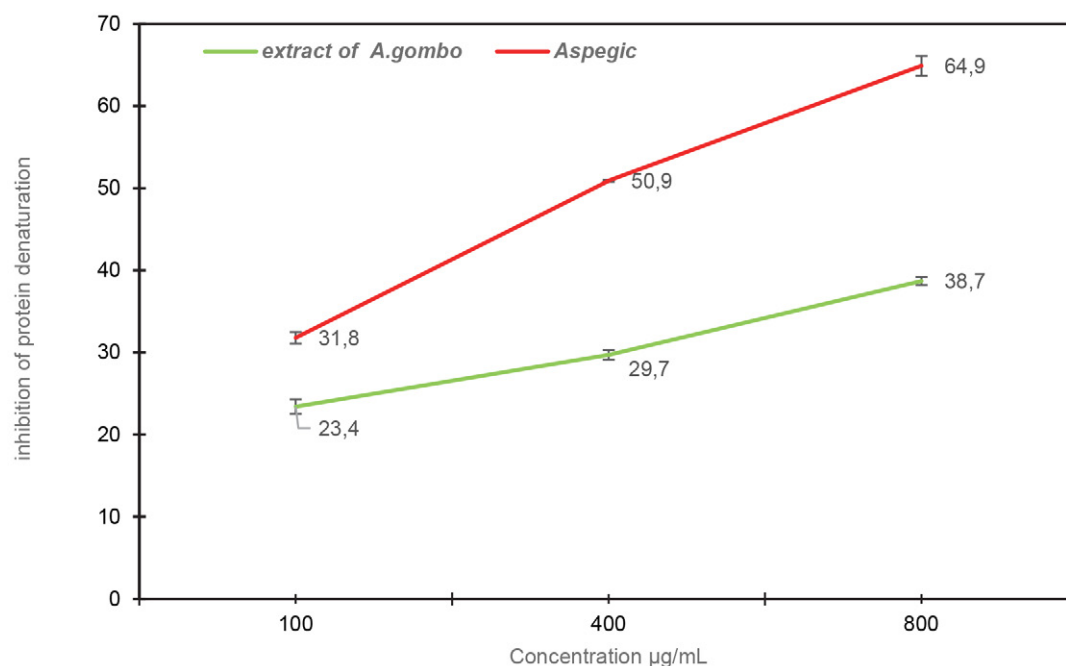


Figure 2. Anti-inflammatory activity of an aqueous extract of *A. gombo*.

Table 5. Result of the antibacterial activity of *A. gombo* extract on bacteria.

samples	Concentration ($\mu\text{g/mL}$)	Zone of inhibition (mm)				
		<i>Bacillus subtilis</i>	<i>Salmonella typhi</i>	<i>Listeria innocua</i>	<i>Escherichia coli</i>	<i>Pseudomonas aeruginosa</i>
<i>A. gombo</i>	1000	8 \pm 0.8	11.3 \pm 0.5	10 \pm 0.4	11 \pm 0.1	10.5 \pm 0.6
	750	8 \pm 0.5	10 \pm 0.3	10 \pm 0.2	10 \pm 0.1	9 \pm 0.3
	500	8 \pm 0.3	10 \pm 0.7	9.6 \pm 0.6	10 \pm 0.1	8 \pm 0.7
	250	8 \pm 0.6	9.66 \pm 0.8	8.7 \pm 0.1	9.5 \pm 0.1	8 \pm 0.9
DMSO	–	6	6	6	6	6
Erythromycin	15	33	22	22	22	23
Ofloxacin	5	23	25	29	29	30

According to the results of the antibacterial assay, the wide range of antibacterial activity can be explained by the presence of a variety of active secondary metabolites in the extract.³⁰ This inhibitory action could be due to tannins and flavonoids, which have long been used as antimicrobial agents. In this study, it was proven that tannins exhibit antibacterial activity against Gram+ and Gram-negative microorganisms.⁷ Tannic acid impedes bacterial adhesion to surfaces and inhibits the absorption of sugars and amino acids, thereby restricting bacterial growth.³¹ Also, the ability of tannins to penetrate the bacterial cell wall and into the inner membrane interferes with cell metabolism, consequently leading cell death. Tannic acid works by blocking the NorA efflux pump, which is believed to be the primary mechanism behind its antibacterial effects.

The activity of flavonoids is due to their ability to combine with extracellular and soluble proteins, as well as with bacterial cell walls.³² Furthermore, P-coumaric acid exhibits significant antibacterial activity by disrupting bacterial cell membranes and interfering with cellular functions. It disrupts membrane integrity, leading to leakage of cellular contents and eventual cell death.³⁷ Additionally, p-coumaric acid inhibits bacterial enzyme systems involved in cell wall synthesis and metabolic processes, thereby impairing bacterial growth and survival.

Similarly, caffeic acid, another widely occurring phenolic compound in plants, demonstrates potent antibacterial effects through multiple mechanisms.³⁴ It disrupts bacterial cell membranes, leading to increased membrane permeability and leakage of intracellular components. Caffeic acid also interferes with bacterial DNA replication and protein synthesis, thereby further inhibiting bacterial growth and proliferation. Moreover, it enhances the plant's immune response by activating defense-related genes and pathways, contributing to its overall antibacterial efficacy.³⁵ Additionally, quercetin also interferes with bacterial enzyme systems crucial for energy production and metabolic processes, leading to impaired bacterial growth and survival.³⁷

4. Conclusions

In this study, we familiarized ourselves with the *A. gombo* plant and characterized its phytochemical and bio-

logical activities. The plant is rich in secondary metabolites, contains high concentrations of polyphenols and flavonoids. As for biological activity, it shows strong antioxidant activity through analysis of DPPH and FRAP, which opens up opportunities for protection and treatment of problems and diseases caused by oxidative stress. With regard to anti-inflammatory activity, it has shown significant activity, which allows it to be used as a treatment for infection. In addition, hemolytic activity was low and safely usable without causing the lysis of red blood cells. The antibacterial activity was remarkable. The *Astragalus gombo* plant could be used for its proven biological efficacy at different levels, which opens up promising prospects. It encourages its application in the medical field to treat a range of illnesses.

Conflict of interest

Authors declare no conflict of interest.

5. References

1. R. A. Dar, M. Shah Nawaz, S. Rasool, P. H. Qazi, *J. Phytother. Pharmacol.* **2017**, *6*, 349–351. DOI:10.31254/phyto.2017.6608
2. N. Benchikha, I. Chelal, H. Debbiche, M. Messaoudi, S. Begaa, I. Larkem, D. G. Amara, A. Rebiai, J. Simal-Gandara, B. Sawicka, *Molecules* **2022**, *27*, 3744. DOI:10.3390/molecules27123744
3. I. Laib, A. B. Djahra, *Int. J. Secondary Metabolite* **2022**, *9*, 229–237. DOI:10.21448/ijsm.999518
4. F.K. Haraguchi, M.L. Pedrosa, H.D. Paula, R.C.d. Santos, M.E. Silva, *Rev. Nutr.* **2009**, *22*, 517–525. DOI:10.1590/S1415-52732009000400007
5. K. M. Watrous, J. H. Cane, *Am. Midl. Nat.* **2011**, *165*, 225–240. DOI:10.1674/0003-0031-165.2.225
6. R.A. Scherson, R. Vidal, M.J. Sanderson, *Am. J. Bot.* **2008**, *95*, 1030–1039. DOI:10.3732/ajb.0800017
7. G.S.S. Njatang, Z. Du, D. Gatsing, R.S. Mouokeu, Y. Liu, H.X. Zang, J. Gu, X. Luo, J. R. Kuai, *BMC Complement. Altern. Med.* **2017**, *17*. DOI:10.1186/s12906-017-1572-z
8. T. Chouana, G. Pierre, C. Vial, C. Gardarin, A. Wadouachi, D. Cailleu, D. Le Cerf, Z. Boual, M.D. Ould-El Hadj, P. Michaud,

- Carbohydr. Polym.* **2017**, *175*, 387–394. DOI:10.1016/j.carbpol.2017.08.003
9. T. Bahorun, B. Gressier, F. Troten, C. Brunet, T. Dine, M. Luyckx, J. Vasseur, M. Cazin, J. Cazin, M. Pinkas, *Arzneimittel-forschung* **1996**, *46*, 1086–1089. PMID:8955870
 10. A. Dasgupta, (Chapter 4) Antiinflammatory Herbal Supplements. In J. K. Actor, K. C. Smith, Perspectives in Translational Cell Biology, Translational Inflammation, Academic Press, United States, **2019**, pp. 69–91. DOI:10.1016/C2016-0-03242-4
 11. R. Murugan, T. Parimelazhagan, *J. King Saud Univ. Sci.* **2014**, *26*, 267–275. DOI:10.1016/j.jksus.2013.09.006
 12. H. Hamid, B. Moncef, B. Assia, H. Tazougart, B. Rachid, *Am. J. Innov. Res. Appl. Sci.* **2018**, *7*, 226–233. ID Article:EL-Haoud-ManuscriptRef.9-ajira061018
 13. K. Slinkard, V.L. Singleton, *American journal of enology and viticulture* **1977**, *28*, 49–55. DOI:10.5344/ajev.1974.28.1.49
 14. M. R. Ahn, S. Kumazawa, Y. Usui, J. Nakamura, M. Matsuka, F. Zhu, T. Nakayama, *Food Chem.* **2007**, *101*, 1383–1392. DOI:10.1016/j.foodchem.2006.03.045
 15. R.B. Broadhurst, W.T. Jones, *J. Sci. Food Agric.* **1978**, *29*, 788–794. DOI:10.1002/jsfa.2740290908
 16. A. Mansouri, G. Embarek, E. Kokkalou, P. Kefalas, *Food Chem.* **2005**, *89*, 411–420. DOI:10.1016/j.foodchem.2004.02.051
 17. M. Oyaizu, *Japanese J Nutr.* **1986**, *44*, 307–315. DOI:10.5264/eiyogakuzashi.44.307
 18. M.L. Tlili, C. Benine, *Ovidius Univ. Ann. Chem.* **2022**, *33*, 121–128. DOI:10.2478/auoc-2022-0018
 19. S. Dharmadeva, L.S. Galgamuwa, C. Prasadine, N. Kumarasinghe, *Ayu* **2018**, *39*, 239–242. DOI:10.4103/ayu.AYU_27_18
 20. I. Laib, A.B. Djahra, O. Boudebba, *J. Organomet. Chem.* **2023**, *986*, 122619. DOI:10.1016/j.jorganchem.2023.122619
 21. S. Benferdia, Z. Rahmani, A. Belfar, R. Cherbi, Z. Rahmani, A. Messaoudi, M. Saïdi, *Bulg. Chem. Commun.* **2021**, *53*, 307–312. DOI:10.34049/bcc.53.3.5351
 22. K. Zeghib, A.B. Djahra, S. Menai, M. Debouba, *Ukr. Biochem. J.* **2021**, *93*, 66–76. DOI:10.15407/ubj93.04.066
 23. L. Bellebcir, N. Abidli, M. Nasri, T. Khorchani, M. Mabrouk, N. Zouari, M. Hajji, *South Asian J. Exp. Biol.* **2022**, *12*, 94–107. DOI:10.38150/sajeb.12(1).p94-107
 24. L. Gao, R. Yue, J. Xu, Z. Liu, J. Chai, *J. Electroanal. Chem.* **2018**, *816*, 14–20. DOI:10.1016/j.jelechem.2018.03.024
 25. G. Joshi, R. Sultana, J. Tangpong, M.P. Cole, D.K. St Clair, M. Vore, S. Estus, D.A. Butterfield, *Free Radic. Res.* **2005**, *39*, 1147–1154. DOI:10.1080/10715760500143478
 26. S. Nouir, A. Dbeibia, R. Bouhaje, H. Haddad, A. Khélifa, L. Achour, M. Ghardallou, A. Zaïri, *Molecules* **2023**, *28*, 4019. DOI:10.3390/molecules28104019
 27. C. Gauthier, J. Legault, K. Girard-Lalancette, V. Mshvildadze, A. Pichette, *Bioorg. Med. Chem.* **2009**, *17*, 2002–2008. DOI:10.1016/j.bmc.2009.01.022
 28. A. Phuwajaroanpong, P. Chaniad, W. Plirat, A. Konyanee, A.W. Septama, C. Punsawad, *Adv. Pharmacol. Pharm. Sci.* **2023**, Article ID 6624040, 1–15. DOI:10.1155/2023/6624040
 29. A.W. Boots, L.C. Wilms, E.L. Swennen, J.C. Kleinjans, A. Bast, G.R. Haenen, *Nutrition* **2008**, *24*, 703–710. DOI:10.1016/j.nut.2008.03.023
 30. N.G. Baydar, G. Özkan, O. Sağdıç, *Food control* **2004**, *15*, 335–339. DOI:10.1016/S0956-7135(03)00083-5
 31. A. Pandey, P.S. Negi, *Nat. Prod. Res.* **2018**, *32*, 1189–1192. DOI:10.1080/14786419.2017.1323209
 32. R. Mogana, A. Adhikari, M. Tzar, R. Ramliza, C. Wiart, *BMC Complement. Med. Ther.* **2020**, *20*, 1–11. DOI:10.1186/s12906-020-2837-5
 33. E. Fernandes, S. Toste, A. Lima, J. L. Reis, S. D. S. Pinto, *J. Agric. Food Chem.* **2004**, *52*(3), 6820–6823. DOI: 10.1021/jf0402742
 34. V. Chobot, F. Hadacek, L.Kubicova Falta, M. Simek, *J. Agric. Food Chem.* **2009**, *57*(15), 7203–7208. DOI: 10.1021/jf9013984
 35. M. Radji, R.A. Agustama, B. Elya, B.C.R Tjampakasari, *Asian Pac. J. Trop. Biomed.* **2013**, *3*(8), 663–667. DOI:10.1016/S2221-1691(13)60133-1
 36. Z. Lou, H. Wang, S. Zhu, C. Ma, Z. Wang, *J. Food Sci.* **2011**, *76*(6), 398–403. DOI:10.1111/j.1750-3841.2011.02213.x
 37. A. Ganeshpurkar, A.K. Saluja, *Saudi Pharm. J.* **2017**, *25*(2), 149–164. DOI:10.1016/j.jsps.2016.04.025

Povzetek

Namen te študije je bil določiti vsebnost fitokemijskih snovi in biološko delovanje endemične vrste *Astragalus gombo*. Za identifikacijo sekundarnih metabolitov smo izvedli analizo HPLC. Ocenili smo antioksidativno (DPPH in FRAP), protivnetno, antihemolitično in antibakterijsko delovanje. Pri analizi HPLC smo dobili 65 vrhov in identificirali šest glavnih bioaktivnih spojin. Skupna koncentracija polifenolov, flavonoidov in kondenziranih taninov je znašala $66,3 \pm 0,9$ mg GA eq/g, $34,31 \pm 1,4$ mg Q eq/g in $5,3 \pm 2,7$ mg Ca eq/g. Kar zadeva antioksidativno aktivnost, je izvleček pokazal močno inhibitorno delovanje, in sicer $IC_{50} = 62,81 \pm 0,01$ µg/ml za DPPH in $IC_{50} = 19,37 \pm 0,04$ µg/ml za FRAP. Protivnetna aktivnost je bila ocenjena kot visoka ($1615,8 \pm 2,8$ µg/ml), antihemolitična aktivnost je bila šibka, antibakterijska aktivnost proti petim preučevanim sevom pa srednje močna. Ta študija je pokazala, da ima vodni izvleček *A. gombo* iz regije El Oued izjemno antioksidativno, protivnetno in antibakterijsko delovanje.



Except when otherwise noted, articles in this journal are published under the terms and conditions of the Creative Commons Attribution 4.0 International License

Scientific paper

Validation of High-Resolution Continuum Source Flame Atomic Absorption Spectrometry for Determination of Selected Toxic Metals in the Decontamination Process of Wastewater Discharged in Natural Receivers

Bame Sanah Senna,¹ Wellington Masamba,¹ Veronica Obuseng,² Tiberiu Frentiu,^{3,4} Bogdan Simion Angyus⁵ and Eniko Covaci^{3,4,*}

¹ Botswana International University of Science and Technology, Faculty of Science, Department of Chemical and Forensic Sciences, Plot 10071 Khurumela Ward, Private Bag 16, Palapye, Botswana

² University of Botswana, Faculty of Science, Department of Chemistry, Plot 4775 Notwane Road. Private Bag UB 022, Gaborone, Botswana

³ Babes-Bolyai University, Faculty of Chemistry and Chemical Engineering, Arany Janos 11, 400028 Cluj-Napoca, Romania

⁴ Babes-Bolyai University, Research Center for Advanced Analysis, Instrumentation and Chemometrics, Arany Janos 11, 400028 Cluj-Napoca, Romania

⁵ National Institute for Research and Development of Optoelectronics INOE 2000 INCĐ Bucharest, Research Institute for Analytical Instrumentation, Donath 67, 400293 Cluj-Napoca, Romania

* Corresponding author: E-mail: eniko.covaci@ubbcluj.ro

Received: 11-10-2023

Abstract

A new method based on high-resolution continuum source flame atomic absorption spectrometry (HR-CS FAAS) was validated for the determination of selected toxic metals in wastewater resulting from mining activity, compared to inductively coupled plasma optical emission spectrometry (ICP-OES) and line-source flame atomic absorption spectrometry (LS FAAS). The HR-CS FAAS method was characterized by detection limits (LODs) in the range ($\mu\text{g L}^{-1}$) 1(Mn)–30(Pb), better than ICP-OES for Cu, Fe, Ni, Co, Pb and Mn, and poorer for Cd, Zn and Cr. Dunnett's test showed that both methods were not affected by significant bias against certified values. The recovery in the HR-CS FAAS method was in the range of 98–103% with relative extended uncertainty of 9–18% and precision of 2–11%. Compared to LS FAAS, the HR-CS FAAS presented better LODs for Pb and Cr. The HR-CS FAAS method is suitable for determining selected toxic elements in filtered water samples without any chemical treatment.

Keywords: High-resolution continuum source flame atomic absorption spectrometry, inductively coupled plasma optical emission spectrometry, toxic metal, water analysis, method validation

1. Introduction

Over the years, chemical analysis, particularly in the determination and monitoring of environmentally significant elements, such as toxic metals (e.g., Pb, Cr and Cu, among many others) has necessitated the need for continued development of new and improved methods.^{1,2} Classically, line-source flame atomic absorption spectrometry (LS FAAS) has been one of the methods of choice for de-

termining such elements, even after introducing the high-resolution continuum source flame atomic absorption spectrometry (HR-CS FAAS) method.^{2,3} In order to make the AAS competitive, HR-CS FAAS was developed by Becker-Ross's team from Institut für Spektrochemie und Angewandte Spektroskopie (ISAS) (Berlin, Germany).² Several advantages are associated with HR-CS FAAS versus LS FAAS, which include: (i) improvement of detection in the far UV region (below 250 nm) through the use

of a xenon short-arc lamp; (ii) simultaneous elemental and background signal measurements that contribute to high signal-to-noise ratio; (iii) fast sequential multielemental determination and reduction of sample consumption and residue; (iv) determination of all elements by the use of the xenon short-arc lamp, including the simultaneous determination of a few elements, which have analytical lines that can be measured in the same spectral window that can be up to ± 1 nm, according to the wavelengths of the elements; (v) determination of trace elements using molecular absorption spectrometry at bands of some molecular radicals of elements; (vi) determination of anions, such as phosphate and nitrate, and non-metals, like halogens.^{1,3,4} The decision to use the xenon short-arc lamp and a high-resolution spectrometer instead of a typical xenon lamp was determined by the need for intense primary radiation and to obtain a high sensitivity for determination by HR-CS FAAS.^{3,5} Therefore, the HR-CS FAAS instrument has individual components specifically tailored to contribute to a highly effective and competitive method that can be on par with current analysis methods, usually based on inductively coupled plasma optical emission spectrometry (ICP-OES).² Some studies have presented the comparison between HR-CS FAAS and ICP-OES in determining hazardous metals in soil samples and report the new method as successful and comparable to the ICP-OES.^{5,6–10} Determination of toxic elements, such as Cd, Pb and Cr, in water samples requires highly sensitive methods, such as ICP-OES with or without preconcentration,^{11–13} inductively coupled plasma mass spectrometry (ICP-MS),^{14–16} or electrochemical methods based on potentiometry and voltammetry.^{17–19} Although methods based on ICP-OES and ICP-MS are highly sensitive and simultaneous with high speed of analysis, the instrumentation is costly and often difficult to access in routine (mostly under resourced) laboratories, despite the fact that both ICP-OES and ICP-MS are standardized for the determination of elements in water samples.^{20,21} Electrochemical methods are simpler than the spectrometric ones, but they are single elemental and affected by matrix, which require the use of standard addition calibration method for their compensation.¹⁷

The LS FAAS is the most accessible standardized method for metal determination used in laboratories that do not require highly skilled analytical chemists. The relatively new HR-CS FAAS instrumental concept still needs to be validated for multielement analyses because the current standards do not refer to determining elements based on this concept.²² Because HR-CS FAAS is rarely used in control laboratories versus HR GFAAS, it is interesting to check whether it can be used as an alternative to LS FAAS and ICP-OES to determine toxic metals in water/wastewater. The development and validation of analytical methods for multielemental determination in water samples based on relatively novel instrumental concepts are of broad scientific and social interest according to the water quality

framework directive of the European Union.²³ Generally, the metals have been outlined as environmentally hazardous by the World Health Organization even at trace concentrations, and this is exacerbated by their ubiquitousness, non-biodegradability, and tendency to biomagnify in the food chain.^{24–26} Some of these elements, such as Cd and Pb, are priority hazardous with high toxicity even at trace levels on humans, aquatic animals and plants, causing, among others, even cancer. On the other hand, Zn, Fe, Cu, Mn and Ni have been widely reported as micronutrients with biological importance to plant and animal life at trace levels. However, these metals could also become toxic if a certain concentration is exceeded.^{27–33} Therefore, this work aimed to validate a multielemental method based on HR-CS FAAS for the determination of Cu, Fe, Ni, Cd, Co, Zn, Mn, Pb and Cr in waters sampled from wastewater treatment plants following Au, Ag, Cu, Zn and Pb non-ferrous ores mining and processing by extraction and roasting for metals. The figures of merit, namely the limits of detection (LODs), linearity of calibration curves, combined uncertainty in the laboratory ($u_{c\text{ lab}}$), extended uncertainty in the laboratory (U_{lab}), and accuracy (recovery and precision), obtained in a performance study, were compared with those of ICP-OES method, in accordance with international regulations.^{34–38} Also, the characteristic concentrations experimentally determined were compared with the data from the ContrAA 300 software and with those for conventional LS FAAS. The direct determination of the mentioned elements in the original filtered water, without any chemical pretreatment, such as acid digestion, was investigated. This study presents analytical relevance because the method developed on HR-CS FAAS should be evaluated in accordance with international legislation in order to be used later in official quality control laboratories.

2. Experimental

2.1. Instrumentation

The ContrAA 300 high-resolution continuum source flame atomic absorption spectrometer manufactured by Analytik Jena AG (Jena, Germany) equipped with an air-acetylene flame was used for the multielemental determination in water. It is equipped with a compact high-resolution double monochromator (pre-prism monochromator and echelle monochromator), a linear charge-coupled device (CCD) as the detector and a xenon short-arc lamp that emits continuum radiation over a wide range of wavelength (185–900 nm) compared to specific hollow cathode lamps (HCLs). Thus, the fast-sequential determination of all elements is achievable using the Xe short-arc lamp, compared to the LS FAAS, which is a slow-sequential determination by selecting the corresponding single element HCL. The working conditions recommended by the manufacturer in order to obtain the best figures of merit for HR-CS FAAS ContrAA 300 spectrometer are outlined in Table 1.

Table 1. Optimum working conditions for the HR-CS FAAS ContrAA 300 spectrometer

Element	Wavelength (nm)	Wavelength range (nm)	Air (L h ⁻¹)	Acetylene (L h ⁻¹)	Burner Height (mm)
Cu	324.754	0.39	470	50	6
Fe	248.327	0.27	470	60	6
Ni	232.003	0.27	470	55	6
Cd	228.802	0.25	470	50	6
Co	240.725	0.28	470	50	6
Zn	213.857	0.23	470	50	6
Pb	217.001	0.25	470	65	6
Mn	279.482	0.33	470	80	6
Cr	357.869	0.40	400	100	8

Determinations by HR-CS FAAS were carried out at the principal analytical lines recommended by the instrument software, which ensures the best figures of merit. A LS FAAS spectrometer (PinAAcle 900T Perkin Elmer, Norwalk, USA), equipped with HCLs (Cu, Fe, Ni, Cd, Co, Zn, Mn and Cr) and electrodeless discharge lamps – EDLs (Cd, Pb), air-acetylene flame, high sensitivity nebulizer was used for comparison of LODs and characteristic concentration. The working conditions were the following: air flow rate 600 L h⁻¹, acetylene flow rate 150 L h⁻¹, slit 0.7 nm for Cd, Cr, Cu, Pb, Zn, and 0.2 nm for Co, Mn, Ni, HCLs current (mA) of (30)Co, (35)Cr, (15)Cu, (20)Mn, (25)Ni, (15)Zn, EDLs current (mA) of (230)Cd and (440)Pb. Measurements were carried out at the same wavelength as in the case of HR-CS FAAS, except for Pb, in which case 283.305 nm was used. Compared to the classical instrumentation with HCLs, in the case of HR-CS FAAS, the absorption spectrum is displayed over a range of between 0.23–0.40 nm (200 pixels), which increases with the element wavelength (Table 1). A number of 5 pixels (central pixel \pm 2) in the middle of the spectral window were attributed to the analytical line, while the rest, on both sides of the analytical line, were used for the continuum background signal correction. The net signal was obtained through the difference between the total signal at the analytical line and the background signal. Thus, in the case of the HR-CS FAAS method, the simultaneous correction of the background with the measurement of the analytical signal is possible, which contributes to a better repeatability of the measurements. The fine background absorption spectrum and interference of NO on Zn 213.856 nm was avoided using the least square background correction offered by the instrument software, using as reference spectrum a solution of 2% (v/v) HNO₃ as blank. An example of the absorption spectrum of Cu 324.754 nm recorded in the optimum operating conditions (Table 1) is presented in Supplementary Material, Fig. S1.

The simultaneous Spectro Ciros^{CCD} (Spectro, Kleve, Germany) ICP-OES with axial plasma viewing was used for comparison. This simultaneous multielemental analysis equipment features 22 CCD detectors and was designed to ensure the best sensitivity without spectral interference. The best signal-to-noise (SNR) strategy was selected for

measurements for an integration time of 48 s for the lines with the highest sensitivity. The background correction was achieved by the two-point model background strategy. The optimum operating conditions of the Spectro Ciros^{CCD} spectrometer are presented in Table 2.

Table 2. Operating conditions of the Spectro Ciros^{CCD} spectrometer

Parameter	Value
Plasma power (W)	1400
Radio frequency (MHz)	27.12
Outer Ar flow rate (L min ⁻¹)	12
Auxiliary Ar flow rate (L min ⁻¹)	0.6
Nebulizer Ar flow rate (L min ⁻¹)	1
3D torch position for axial viewing (mm)	x = -3.9, y = +3.6, z = +2.6 (for all elements)
Sample introduction (cross-flow nebulizer) (mL min ⁻¹)	2
Flushing time (s)	40
Delay time (s)	20
Elements wavelength (nm)	Cu 324.754; Fe 259.940; Ni 341.476; Cd 228.802; Co 237.862; Zn 213.857; Pb 220.351; Mn 260.569; Cr 267.716; Ca 422.673; Mg 285.213.

In the case of all three methods, the quantification of elements was achieved by external calibration using multi-elemental standards solution without appropriate sample matrix preparation. The concentrations of Na and K in the water samples as concomitants were determined by flame atomic emission spectrometry using the Sherwood Model 360 instrument (Cambridge, UK). Also, Ca and Mg determined by ICP-OES were considered as concomitant elements.

2. 2. Solutions, Reagents and Certified Reference Materials (CRMs)

Multielemental standard solution IV 1000 mg L⁻¹ from Merck (Darmstadt, Germany) was used to prepare

the standard solutions up to 5000 $\mu\text{g L}^{-1}$ for HR-CS FAAS/LS FAAS and 25000 $\mu\text{g L}^{-1}$ for ICP-OES by serial dilution with 2% (v/v) HNO_3 starting from the smallest concentration presented in Table 3, near the limit of quantification ($\text{LOQ} = 3.3 \times \text{LOD}$). These standards were used to establish the range of linearity of the calibration curves, and in which concentration range the proposed method could be used for the determination of selected elements in wastewaters. A 2% (v/v) HNO_3 solution was used as blank for background correction in the case of all three methods. Nitric acid 63% (m/m) for analysis was purchased from Merck (Darmstadt, Germany). Three water CRMs, namely TMDA-64.4 Lake Ontario water from Environment and Climate Change Canada (Burlington, ON, Canada), ERM[®]-CA713 wastewater and ERM[®]-CA615 groundwater from Institute for Reference Materials and Measurements (Geel, Belgium) were used to check the accuracy of the methods.

2. 3. Description of real test samples

Three real test water samples of 2 L each were collected using polyethylene bottles rinsed with ultrapure water. These were collected before and after decontamination of a plant treatment station of wastewater resulting from Au, Ag, Cu, Zn and Pb non-ferrous ores mining and processing by extraction and roasting for metals in the vicinity of Baia-Mare town, North-Western Romania, together with one sample from a natural receiver (river). This area is of particular interest because of the metal pollution that has previously been reported.^{39,40} The samples were homogenized, filtered (0.45 μm), acidified with 2% (v/v) HNO_3 and the concentrations of Cu, Fe, Ni, Cd, Co, Pb, Zn, Mn and Cr were determined by HR-CS FAAS and ICP-OES using external calibration, without any chemical preliminary pretreatment.

2. 4. Strategy for Validation of HR-CS FAAS Method

The HR-CS FAAS method was validated by evaluating the LODs, accuracy (recovery and precision), and linearity of calibration curves compared with ICP-OES. The sensitivities of the HR-CS FAAS and LS FAAS methods were compared by the characteristic concentration (0.0044 (1% Abs)/slope of the calibration curve ratio), an essential parameter for methods based on AAS. The values of the experimental characteristic concentrations, determined from the calibration curves for HR-CS FAAS, were compared with the data from the ContrAA 300 software. This comparison is useful, because the operator can check if the instrument operates under optimum conditions. Additionally, the LODs were evaluated, because the values of this figure of merit depend both on the sensitivity and stability of analytical signal. The LODs in water samples were evaluated based on instrumental LODs according to the 3σ criterion ($\text{LOD} = 3s_b/m$, where (s_b) is the standard deviation

of the blank signal ($n = 11$) and (m) is the slope of the calibration curve).⁴¹ Methods accuracy was checked by analyzing three CRMs by evaluating the mean recovery ($n = 3$ parallel measurements) and laboratory extended uncertainty ($U_{\text{lab}} = 2u_{\text{c lab}}$) of the found results and comparison with the certified values. The laboratory combined uncertainty ($u_{\text{c lab}} = \sqrt{\sum u_i^2}$) for each method was calculated based on individual uncertainties (u_i), namely uncertainty for the certified value ($u_{\text{CRM}} = U_{\text{CRM}}/2$), uncertainty of standards and sample preparation, calibration curve fitting and aliquots analysis. A relative value ($u_{\text{rel lab}}(\%)$) was calculated for both methods using equation (1).

$$u_{\text{rel lab}} = \frac{\sqrt{u_{\text{CRM}}^2 + u_{\text{ss}}^2 + u_{\text{sp}}^2 + u_{\text{cs}}^2 + u_{\text{meth}}^2}}{\sqrt{u_{\text{c lab}}^2}} \times 100 = u_{\text{c lab}} \times 100 \quad (1)$$

Where, u_{CRM} is the uncertainty from the certificate, u_{ss} is the uncertainty of stock solution concentration, u_{sp} is the uncertainty of sample preparation, u_{cs} is the uncertainty of calibration standards preparation, u_{meth} is the uncertainty of the method measurement, and $u_{\text{c lab}}$ is the laboratory combined uncertainty.

The precision was assessed through the relative standard deviation (RSD, %), based on $n = 3$ replicate measurements of real water test samples and $u_{\text{c lab}}$. In the case of real wastewater samples, the u_{CRM} (equation 1) was not considered in the calculation of $u_{\text{rel lab}}(\%)$ for RSD(%). The bias (Δm) between the found and certified values was discussed in accordance with the fulfillment of relationships ($\Delta m < U_{\text{CRM}}$ and $\Delta m < U_{\text{lab}}$) and Dunnett's statistical test ($p > 0.05$).⁴² The bias between HR-CS FAAS and ICP-OES methods was checked using Tukey's statistical test ($p > 0.05$), considering the mean concentration determined in CRMs and real test samples and $u_{\text{c lab}}$ for each method.⁴³

Calibration curve linearity was checked using Mandel's fitting test^{44,45}, which compares the residual standard deviation of the linear model ($S_{y/x,\text{lin}}$) with that of the non-linear quadratic model ($S_{y/x,\text{non}}$). The experimental Fischer-Snedecor (F_{exp}) was calculated with equation (2).

$$F_{\text{exp,Mandel}} = \frac{(n-2)S_{y/x,\text{lin}}^2 - (n-3)S_{y/x,\text{non}}^2}{S_{y/x,\text{non}}^2} \quad (2)$$

where, n is the number of calibration points between the lowest concentration used for the calibration curve, and the highest concentration over the linear range.

If $F_{\text{exp,Mandel}} < F_{\text{tab}}(95\%, 1, n-3)$, the null hypothesis is retained for a 95% confidence level, and the tested concentration range is considered linear.

Also, the variation coefficients on the linear range of the HR-CS FAAS, LS FAAS and ICP-OES (V_{ox}) were calculated³⁸:

$$V_{\text{ox}} = \frac{\sqrt{\frac{\sum_{i=1}^n (y_i - \hat{y}_i)^2}{n-2}}}{m \times \bar{c}} \times 100 \quad (3)$$

where (y_i) are the measured signals for elements in calibration standards, (\hat{y}_i) are the calculated signals for elements from the calibration curve equation, n is the number of calibration standards for HR-CS FAAS, LS FAAS and ICP-OES on the linear range, (m) is the slope of the calibration curve and (\bar{c}) is the mean concentration of elements in the calibration standards.

The fishbone diagram illustrating the individual uncertainties on $u_{rel\ lab}$ (%) for the determination of the metals in water CRMs by HR-CS FAAS and ICP-OES methods is presented in Supplementary Material, Fig. S2.

3. Results and Discussion

3. 1. Linearity of Calibration Curves, Characteristic Concentrations and LODs

Table 3 presents the figures of merit of HR-CS FAAS compared to ICP-OES, while Table 4 a comparison *versus* LS FAAS. According to Table 3, the HR-CS FAAS method ensured better LODs ($\mu\text{g L}^{-1}$) for Cu (2), Fe (4), Ni (3), Co (3) and Pb (30) compared to ICP-OES, in which case the LODs ($\mu\text{g L}^{-1}$) were Cu (12), Fe (29), Ni (15), Co (7) and Pb (45), due to the lower and less background noise in the method based on AAS compared to ICP-OES. In the case of three elements, poorer LODs were obtained by HR-CS FAAS ($\mu\text{g L}^{-1}$): Cd (3), Zn (11) and Cr (7), in comparison with Cd (1), Zn (1) and Cr (4) in ICP-OES. The poorer detection limits for Cd and Zn in HR-CS FAAS could be due to the lower energy of the Xe short-arc lamp in the UV region. Also, in the case of Zn, this was attributed to the background noise around the 213.856 nm analytical line due to the molecular absorption bands of NO, despite the background correction by the least square method being applied. A poorer LOD for Cr in HR-CS FAAS can be explained by lower atomization degree of Cr in an air-acety-

lene flame, in which case an acetylene- N_2O flame would be more appropriate. However, in the case of all elements, the LODs for HR-CS FAAS are lower than the pollutant loading limits of industrial and urban wastewater discharged into natural receivers, presented in Table 3.⁴⁶ The LODs in HR-CS FAAS are better for Pb and Cr, similar for Cu, Ni, Co and Mn, and poorer for Cd, Zn and Fe, compared to the LS FAAS method (Table 4). The characteristic concentration values, presented in Table 4, for the HR-CS FAAS method were in the range of 17–120 $\mu\text{g L}^{-1}$, while those for LS FAAS were 7–206 $\mu\text{g L}^{-1}$, which indicates that the sensitivity in HR-CS FAAS method is better for Pb and Cr, similar for Cu, Ni, Co and Mn, and poorer for Cd, Zn and Fe, compared to the LS FAAS method. The experimental values of the characteristic concentrations obtained for HR-CS FAAS method are similar with the values from the ContrAA software, except for Cr. This demonstrates that indeed, the HR-CS FAAS spectrometer was operated in optimum conditions. The highest characteristic concentration for Cr of 80 $\mu\text{g L}^{-1}$ compared to that from the software (47 $\mu\text{g L}^{-1}$) could be explained by the use of air-acetylene flame, and not that of N_2O -acetylene, recommended for Cr. Mandel's fitting test, which compares the residual standard deviation of the linear model ($S_{y/x,\text{lin}}$) with that of the nonlinear quadratic model ($S_{y/x,\text{non}}$), indicated a linear range for HR-CS FAAS method between 10–1000 $\mu\text{g L}^{-1}$ for Cu and Cd, 50–1000 $\mu\text{g L}^{-1}$ for Zn, 10–2000 $\mu\text{g L}^{-1}$ for Ni, 10–4000 $\mu\text{g L}^{-1}$ for Fe and Co, and 100–4000 $\mu\text{g L}^{-1}$ for Pb, for 95% confidence level, with determination coefficients in the range 0.9980–0.9999. These were similar to those obtained for LS FAAS method, but narrower than those for ICP-OES with up to 15000 $\mu\text{g L}^{-1}$ (Cu and Pb) and 20000 $\mu\text{g L}^{-1}$ for the rest of the elements, known for larger dynamic range compared to AAS based methods. Anyway, according to data presented in Table 3, the HR-CS FAAS method could be applied on the determination of lower concentration values for Cu, Fe and Co,

Table 3. Figures of merit of the HR-CS FAAS and ICP-OES methods for multielemental determination in wastewater

Element	Linear range ($\mu\text{g L}^{-1}$) and no. of standards in brackets		Determination coefficient (R^2)		$F_{\text{exp,Mandel}} < F_{\text{tab}(95\%,1,n-3)}$ ^a		Variation coefficient V_{ox} (%)		Limit of detection LOD ($\mu\text{g L}^{-1}$)		Pollutant loading limits ($\mu\text{g L}^{-1}$) ⁴⁶
	HR-CS FAAS	ICP-OES	HR-CS FAAS	ICP-OES	HR-CS FAAS	ICP-OES	HR-CS FAAS	ICP-OES	HR-CS FAAS	ICP-OES	
Cu	10–1000(7)	50–15000(10)	0.9999	0.9990	0.29<7.71	3.08<5.59	1	4	2	12	200
Fe	10–4000(10)	100–20000(10)	0.9998	0.9999	3.29<5.59	0.12<5.59	2	1	4	29	5000
Cd	10–1000(7)	5–20000(11)	0.9993	0.9999	3.61<7.71	0.03<5.32	2	2	3	1	200
Ni	10–2000(8)	50–20000(11)	0.9998	0.9990	1.75<6.61	0.63<5.32	2	4	3	15	500
Co	10–4000(10)	25–20000(11)	0.9994	0.9998	1.47<5.59	1.17<5.32	3	2	3	7	1000
Zn	50–1000(7)	5–20000(11)	0.9995	0.9998	4.89<7.71	0.04<5.32	2	2	11	1	500
Pb	100–4000(9)	150–15000(9)	0.9996	0.9992	2.64<5.99	0.02<5.99	2	2	30	45	200
Mn	5–1000(7)	5–20000(11)	0.9996	0.9999	0.32<7.71	3.14<5.32	2	3	1	1	1000
Cr	20–1000(7)	10–20000(11)	0.9980	0.9999	0.82<7.71	0.18<5.32	4	2	7	4	1000

^a The null hypothesis was retained when $F_{\text{exp,Mandel}} < F_{\text{tab}(95\%,1,n-3)}$.

Table 4. Figures of merit of LS FAAS and characteristic concentrations for HR-CS FAAS and LS FAAS methods for multielemental determination in wastewater

LS FAAS method					HR-CS FAAS method			
Element	Linear range ($\mu\text{g L}^{-1}$) and no. of standards in brackets	Determination coefficient (R^2)	$F_{\text{exp,Mandel}} < F_{\text{tab}(95\%,1,n-3)}$ ^a	Variation coefficient V_{ox} (%)	Limit of detection LOD ($\mu\text{g L}^{-1}$)	Characteristic concentration ($\mu\text{g L}^{-1}$) ^b	Characteristic concentration ($\mu\text{g L}^{-1}$) ^b	ContrAA software
						Experimental value	Experimental value	
Cu	10–1000(7)	0.9999	0.69<7.71	1	2	29	29	24
Fe	10–4000(6)	0.9992	0.49<10.13	3	2	39	65	63
Cd	10–1000(7)	0.9996	7.23<7.71	2	2	11	17	14
Ni	10–4000(6)	0.9998	8.22<10.13	1	3	57	67	57
Co	10–1000(7)	0.9996	0.01<7.71	2	3	47	56	40
Zn	20–1000(7)	0.9989	7.65<7.71	3	6	7	13	10
Pb	200–4000(6)	0.9999	9.92<10.13	1	58	206	120	117
Mn	5–1000(7)	0.9993	4.82<7.71	2	1	21	19	18
Cr	50–4000(6)	0.9963	4.15<10.13	6	17	194	80	47

^a The null hypothesis was retained when $F_{\text{exp,Mandel}} < F_{\text{tab}(95\%,1,n-3)}$.^b Experimental characteristic concentration = 0.0044 (1% absorbance)/slope of the calibration curve

compared to ICP-OES. Variation coefficients (V_{ox}) for the linear range were 1–4% for HR-CS FAAS, 1–6% for LS FAAS, and 1–4% for ICP-OES. The HR-CS FAAS method could be applied on elements concentration determination in wastewaters and in the monitoring of decontamination process on the linear ranges presented in Table 3. Therefore, the HR-CS FAAS method is suitable for monitoring wastewater from mining activities of non-ferrous metals at concentration levels below the pollutant loading limits of industrial wastewater discharged into natural receivers (values for pollutant loading limits in Table 3).

3. 2. Accuracy of HR-CS FAAS Method

The results obtained for the determination of selected metals in the CRMs are shown in Table 5. Data in Table 5 shows that there are no significant differences between found and certified values for all CRMs in the HR-CS FAAS and ICP-OES methods, as the bias (Δm) between the found and certified values is lower than the extended uncertainty found in the laboratory and that given in certificate for $k = 2$ and 95% confidence level. Dunnet's test indicated no significant differences between found and certified values for $p > 0.05$, with experimental values $p = 0.122$ – 0.999 for both methods. The statistical Tukey's test indicated no significant differences between the concentrations found by HR-CS FAAS and ICP-OES for $p > 0.05$ (experimental p -values = 0.064–0.891). For the HR-CS FAAS, the pooled recovery was in the range of 98–103% with relative extended uncertainty of 9–18%, compared to 96–109% and 9–18% for ICP-OES, respectively. The combined uncertainties presented in Supplementary Material, Fig. S3, indicate that the values obtained in the laboratory are higher than those of certified values, as a result of sig-

nificant contribution from aliquots analysis (weight 41%), followed by CRM uncertainty (weight 24%) and calibration curve fitting (weight 16%), from the $u_{\text{c lab}}$.

3. 3. Analysis of Real Water Samples

The results obtained for the determination of selected metals in several water samples by HR-CS FAAS and ICP-OES are presented in Table 6. The $u_{\text{rel lab}}$ (%), calculated based on combined uncertainty and the contribution of each analytical step are presented in Supplementary Material, Fig. S4. The concentration of Na and K in water samples determined by FAES and Ca and Mg by ICP-OES as multielement matrix are presented in Supplementary Material, Table S1. The HR-CS FAAS method precision used for water analysis without any chemical treatment was in the range of 2–11%, while for ICP-OES 3–11%. The main contribution of uncertainty was from aliquot analysis (weight of 37%). Tukey's test indicated the lack of bias between HR-CS FAAS and ICP-OES methods for $p > 0.05$ (experimental values 0.070–0.999), which also demonstrates the lack of non-spectral effects of Na, K, Mg and Ca on the signal of analytes in FAAS and ICP-OES at concentration levels in wastewater presented in Table S1. According to data presented in Table 6, the wastewater is treated efficiently in terms of Cu, Fe, Ni, Cd, Co and Pb, for which the concentrations in the decontaminated water were much below the pollutant loading limits. In the case of two elements (Cu and Cd), the concentrations in decontaminated water were below the LODs of HR-CS FAAS and ICP-OES. Unfortunately, the wastewater is not treated efficiently regarding Zn and Mn, as their concentrations are higher than the pollutant loading limits ($500 \mu\text{g L}^{-1}$ Zn and $1000 \mu\text{g L}^{-1}$ Mn). This also affected the river water, that had

Table 5. Concentration of selected metals and recovery obtained in water CRMs by HR-CS FAAS and ICP-OES

Element	Method	Certified reference material (CRM)									
		TMDA-64.4 ^a			ERM CA-713 ^a			ERM CA-615 ^a			Pooled
		Certified value ± U_{CRM}^a (µg L ⁻¹)	Found value ± U_{lab}^b (µg L ⁻¹)	Recovery ± U_{rel}^c (%)	Certified value ± U_{CRM} (µg L ⁻¹)	Found value ± U_{lab} (µg L ⁻¹)	Recovery ± U_{rel} (%)	Certified value ± U_{CRM} (µg L ⁻¹)	Found value ± U_{lab} (µg L ⁻¹)	Recovery ± U_{rel} (%)	Recovery ± U_{rel} (%)
Cu	HR-CS FAAS	251 ± 15	253 ± 28	101 ± 11	101 ± 7	107 ± 9	106 ± 8	-	-	-	103 ± 10
	ICP-OES		237 ± 38	94 ± 16		99 ± 14	98 ± 14		-	-	96 ± 15
Fe	HR-CS FAAS	291 ± 23	291 ± 28	100 ± 10	445 ± 27	436 ± 33	98 ± 8	5110 ± 260	5360 ± 440	105 ± 8	101 ± 9
	ICP-OES		287 ± 28	99 ± 10		446 ± 41	100 ± 9		5260 ± 460	103 ± 9	101 ± 9
Ni	HR-CS FAAS	246 ± 14	251 ± 31	102 ± 12	50.3 ± 1.4	49.8 ± 7.8	99 ± 16	25.3 ± 1.1	24.7 ± 6.0	98 ± 24	100 ± 8
	ICP-OES		240 ± 18	98 ± 8		51.6 ± 7.3	103 ± 14		<50 ^e		101 ± 11
Cd	HR-CS FAAS	256 ± 12	261 ± 36	102 ± 14	5.09 ± 0.20	<10 ^e		0.106 ± 0.011	< 3 ^f	-	102 ± 14
	ICP-OES		265 ± 26	104 ± 10		5.28 ± 1.17	104 ± 22		< 1 ^f	-	104 ± 17
Co	HR-CS FAAS	252 ± 19	254 ± 29	101 ± 11	-	-	-	-	-	-	101 ± 11
	ICP-OES		269 ± 38	107 ± 14					-	-	107 ± 14
Zn	HR-CS FAAS	329 ± 25	348 ± 58	106 ± 17	78 ^d	78 ± 12	100 ± 15	-	-	-	103 ± 16
	ICP-OES		352 ± 40	107 ± 11		86 ± 16	110 ± 19		-	-	109 ± 15
Pb	HR-CS FAAS	277 ± 20	269 ± 33	97 ± 12	49.7 ± 1.7	<100 ^e		7.1 ± 0.6	<30 ^f	-	98 ± 12
	ICP-OES		292 ± 37	105 ± 13		<150 ^e			< 45 ^f	-	104 ± 13
Mn	HR-CS FAAS	289 ± 21	279 ± 41	97 ± 15	95 ± 4	96 ± 12	101 ± 12	107 ± 5	107 ± 15	100 ± 14	99 ± 14
	ICP-OES		305 ± 56	106 ± 18		98 ± 13	103 ± 13		110 ± 18	103 ± 16	104 ± 16
Cr	HR-CS FAAS	274 ± 22	273 ± 41	100 ± 15	20.9 ± 1.3	22.0 ± 4.2	105 ± 19	-	-	-	102 ± 17
	ICP-OES		291 ± 39	106 ± 13		21.8 ± 4.7	104 ± 22			-	105 ± 18

^a U_{CRM} is absolute expanded uncertainty for certified concentration (k = 2; 95% confidence level)
^b U_{lab} is absolute expanded uncertainty in laboratory for found concentration (k = 2, n = 3 parallel measurements and 95% confidence level)
^c U_{rel} is relative expanded uncertainty in laboratory for found concentration (k = 2, n = 3 parallel measurements and 95% confidence level)
^d Indicative value; ^eValues corresponding to the lowest concentration of the linear range; ^fValues corresponding to LODs of the method

Table 6. Results for Cu, Fe, Ni, Cd, Co, Zn, Pb and Mn in real water samples determined by HR-CS FAAS and ICP-OES

Parameter	Methods	Wastewater before decontamination		Wastewater before decontamination		Decontaminated wastewater		River water	
		Mean concentration ± U_{lab}^a (µg L ⁻¹)	RSD ^b (%)	Mean concentration ± U_{lab} (µg L ⁻¹)	RSD ^b (%)	Mean concentration ± U_{lab} (µg L ⁻¹)	RSD ^b (%)	Mean concentration ± U_{lab} (µg L ⁻¹)	RSD ^b (%)
Cu	HR-CS FAAS	980 ± 40	2	950 ± 140	7	< 2 ^d	-	131 ± 24	9
	ICP-OES	1020 ± 97	5	1030 ± 160	8	< 12 ^d	-	134 ± 13	5
Fe	HR-CS FAAS	32000 ± 4300	7	35100 ± 2900	4	1540 ± 120	4	58 ± 10	9
	ICP-OES	33600 ± 2500	4	36800 ± 2800	4	1580 ± 140	4	<100 ^c	-
Ni	HR-CS FAAS	87 ± 12	7	87 ± 10	6	37 ± 6	8	< 3 ^d	-
	ICP-OES	83 ± 16	10	78 ± 17	11	<50 ^c	-	< 15 ^d	-
Cd	HR-CS FAAS	153 ± 13	4	166 ± 20	6	< 3 ^d	-	14 ± 3	11
	ICP-OES	161 ± 29	9	182 ± 29	8	< 1 ^d	-	14 ± 3	11
Co	HR-CS FAAS	105 ± 19	9	145 ± 19	7	47 ± 9	10	22 ± 5	11
	ICP-OES	113 ± 21	9	155 ± 29	9	43 ± 9	10	25 ± 5	10
Zn	HR-CS FAAS	39500 ± 3900	5	39400 ± 4900	6	1390 ± 220	8	6920 ± 800	6
	ICP-OES	41500 ± 2800	3	41600 ± 3400	4	1490 ± 150	5	7480 ± 890	6
Pb	HR-CS FAAS	141 ± 25	9	<100 ^c	-	<100 ^c	-	<100 ^c	-
	ICP-OES	<150 ^d	-	<150 ^c	-	<150 ^c	-	<150 ^c	-
Mn	HR-CS FAAS	21900 ± 2000	5	22300 ± 1600	4	5090 ± 620	6	3530 ± 220	3
	ICP-OES	23100 ± 1900	4	22900 ± 2040	5	5140 ± 720	7	3550 ± 460	6
Cr	HR-CS FAAS	< 7 ^d	-	< 7 ^d	-	< 7 ^d	-	< 7 ^d	-
	ICP-OES	< 4 ^d	-	< 4 ^d	-	< 4 ^d	-	< 4 ^d	-

^a U_{lab} is the absolute uncertainty in laboratory (k = 2, n = 3 parallel measurements and 95% confidence level)
^b RSD is the relative standard deviation in (%) obtained from the combined uncertainty in laboratory ($u_{c,lab}$)
^c Values corresponding to the lowest concentration of the linear range
^d Values corresponding to LODs of the method

in consequence, higher concentrations than the regulated values for metal pollutants. Chromium could not be determined, both in non-treated and decontaminated water, and river water, because the concentration values were below the LODs of both methods. The recovery and precision for Cr determinations in a spiked water sample with a concentration of $50 \mu\text{g L}^{-1}$ was $98 \pm 12\%$ (RSD 6%) for HR-CS FAAS and $103 \pm 13\%$ (RSD 6%) for ICP-OES.

4. Conclusions

The HR-CS FAAS method was validated for the determination of Cu, Fe, Ni, Cd, Co, Zn, Pb, Mn and Cr in wastewater resulting from mining activities of non-ferrous metals and those discharged into natural receivers in comparison with the ICP-OES method. It was demonstrated that like ICP-OES, the HR-CS FAAS method does not present systematic errors in the analysis of CRMs and real water samples. Furthermore, HR-CS FAAS ensured better LODs for Cu, Fe, Ni, Co, Pb and Mn, and poorer LODs for Cd, Zn and Cr compared to ICP-OES. The LODs for selected toxic elements obtained by HR-CS FAAS were much lower than the pollutant loading limits, and thus, they could be determined by the proposed method at concentrations below the regulated values. Compared to conventional LS FAAS, the HR-CS FAAS presented better LODs for Pb and Cr, similar for Cu, Cd, Ni, Co and Mn, and poorer for Fe and Zn, in agreement with their characteristic concentrations for the two instrumental concepts. The dynamic range was similar for FAAS methods equipped with line-sources and the continuum Xe short-arc lamp. Unfortunately, the HR-CS FAAS method presented a narrower dynamic range than ICP-OES. The major advantage of the HR-CS FAAS method *versus* the LS FAAS is the higher speed of analysis since it does not require lamp changing, while in comparison with ICP-OES, the better LODs for most elements.

Acknowledgements

This work was supported by a grant of Ministry of Research and Innovation, Romania, project CN-FIS-FDI-2022-0179, within PNCDI III.

Acknowledgement is also extended to Erasmus+ mobility grant funded through the European Union as well as the Botswana International University of Science and Technology for funding with the Initiation Grant Project code S00138.

5. References

1. B. Welz, *Anal. Bioanal. Chem.* **2005**, *381*, 69–71. DOI:10.1007/s00216-004-2891-8
2. H. Becker-Ross, S. Florek, U. Heitmann, *J. Anal. At. Spectrom.* **2005**, *15*, 137–141. DOI:10.1039/A903571K
3. B. Welz, H. Becker-Ross, S. Florek, U. Heitmann, High-resolution continuum source AAS: The better way to do atomic absorption spectrometry. Wiley-VCH Verlag GmbH & Co. KgaA: Weinheim, Germany. **2005**. DOI:10.1002/3527606513
4. B. Welz, S. Mores, E. Carasek, M. G. R. Vale, M. Okruss, H. Becker-Ross, *Appl. Spectrosc. Rev.* **2010**, *45*, 327–354. DOI:10.1080/05704928.2010.483669
5. H. Ciftci, C. Er, *Environ. Monit. Assess.* **2013**, *185*, 2745–2753. DOI:10.1007/s10661-012-2745-3
6. T. Frentiu, M. Ponta, R. Hategan, *Chem. Cent. J.* **2013**, *7*, article number 43. DOI:10.1186/1752-153X-7-43
7. M. D. Huang, H. Becker-Ross, S. Florek, U. Heitmann, M. Okruss, *Anal. Bioanal. Chem.* **2005**, *382*, 1877–1881. DOI:10.1007/s00216-005-3333-y
8. A. S. Ribeiro, M. A. Vieira, A. F. da Silva, D. L. Gallindo Borges, B. Welz, U. Heitmann, A. J. Curtius, *Spectrochim. Acta B: At. Spectrosc.* **2005**, *60*, 693–698. DOI:10.1016/j.sab.2005.01.002
9. M. D. Huang, H. Becker-Ross, S. Florek, U. Heitmann, M. Okruss, *Spectrochim. Acta B: At. Spectrosc.* **2008**, *63*, 566–570. DOI:10.1016/j.sab.2008.02.005
10. B. Welz, M. G. R. Vale, M. M. Silva, H. Becker-Ross, M.-D. Huang, S. Florek, U. Heitmann, *Spectrochim. Acta B: At. Spectrosc.* **2002**, *57*, 1043–1055. DOI:10.1016/S0584-8547(02)00031-9
11. R. S. da Cruz, J. S. Ribeiro, L. S. de Moura, R. B. Lopes, K. do Carmo Freitas Faial, K. Gul, S. Malik, P. S. Taube, *Water Air Soil Pollut.* **2022**, *233*, article number 247. DOI:10.1007/s11270-022-05726-2
12. A. M. Massadeh, A.W. O. El-Rjoob, S. A. Gharaibeh, *Water Air Soil Pollut.* **2020**, *231*, article number 243. DOI:10.1007/s11270-020-04555-5
13. L. Nyaba, P.N. Nomngongo, *Food Chem.* **2020**, *322*, 126749. DOI:10.1016/j.foodchem.2020.126749
14. X. L. Zhang, Y. Xu, T. Li, H. Li, Z. D. Yu, L. Song, J. Q. Xu, *J. Anal. At. Spectrom.* **2023**, *38*, 716–720. DOI:10.1039/D2JA00314G
15. C. Xu, M. He, B. B. Chen, B. He, *Talanta* **2022**, *245*, article number 123470. DOI:10.1016/j.talanta.2022.123470
16. N. Zhao, Y. W. Bian, X. Y. Dong, X. Gao, L. S. Zhao, *Water Sci. Technol.* **2021**, *84*, 1417–1427. DOI:10.2166/wst.2021.321
17. Q. Yang, B. Nagar, R. Alvarez-Diduk, M. Balsells, A. Farinelli, D. Bloisi, L. Proia, C. Espinosa, M. Ordeix, T. Knutz, E. De Vito-Francesco, R. Allabashi, A. Merkoci, *ACS EST Water* **2021**, *12*, 2470–2476. DOI:10.1021/acsestwater.1c00192
18. M. Caetano, M. M. C. dos Santos, N. Rosa, I. Carvalho, J. G. Rodriguez, M. J. Belzunze-Segarra, I. Menchaca, J. Larreta, M. R. Sanz, V. Millán-Gabet, J.-L. Gonzalez, I. Amouroux, S. Guesdon, F. Menet-Nedelec, B. White, F. Regan, M. Nolan, B. McHugh, P. Bersuder, T. Bolam, C. D. Robinson, G. R. Fones, H. Zhang, M. Schintu, N. Montero, B. Marras, *Mar. Pollut. Bull.* **2022**, *179*, article number 113715. DOI:10.1016/j.marpolbul.2022.113715
19. S. S. Shafqat, M. Rizwan, M. Batool, S. R. Shafqat, G. Mustafa-

- fa, T. Rasheed, M. N. Zafar, *Chemosphere* **2023**, 318, article number 137920. DOI:10.1016/j.chemosphere.2023.137920
- 20 ISO 11885:2007 Water quality — Determination of selected elements by inductively coupled plasma optical emission spectrometry (ICP-OES)
- 21 ISO 17294-2:2016 Water quality — Application of inductively coupled plasma mass spectrometry (ICP-MS) — Part 2: Determination of selected elements including uranium isotopes
- 22 ISO 8288:1986 Water quality — Determination of cobalt, nickel, copper, zinc, cadmium and lead — Flame atomic absorption spectrometric methods
- 23 DIRECTIVE 2000/60/EC OF THE EUROPEAN PARLIAMENT AND OF THE COUNCIL of 23 October 2000 establishing a framework for Community action in the field of water policy. *Off. J. Eur. Commun.* **2000**, 327, 1–72.
- 24 World Health Organization, Recommended health-based limits in occupational exposure to heavy metals. Report of a WHO study group. *World Health Organ. Tech. Rep. Ser.* **1980**, 647, 1–116.
- 25 Health risks of heavy metals from long-range transboundary air pollution, *World Health Organization Regional Office for Europe*, Germany, **2007**.
- 26 Guidelines for drinking-water quality. 3rd edition, Volume 1, Recommendations, World Health Organization, Geneva, **2004**.
- 27 J. Savory, M. R. Wills, *Clin. Chem.* **1992**, 38, 1565–1573.
- 28 A. Leskova, H. Javot, R. F. H. Giehl, *J. Exp. Bot.* **2002**, 73, 1751–1765. DOI:10.1093/jxb/erab483
- 29 Zs. Kolbert, A. Cuypers, N. Verbruggen, *J. Exp. Bot.* **2022**, 73, 1685–1687. DOI:10.1093/jxb/erac025
- 30 A. Shenkin, *Clin. Nutr.* **2006**, 25, 1–13. DOI:10.1016/j.clnu.2005.11.006
- 31 C. Camaschella, *Blood* **2019**, 133, 30–39. DOI:10.1182/blood-2018-05-815944
- 32 D. N. Srole, T. Ganz, *J. Cell Physiol.* **2021**, 236, 4888–4901. DOI:10.1002/jcp.30247
- 33 I. Blanco-Penedo, J. M. Cruz, M. Lopez-Alonso, M. Miranda, C. Castillo, J. Hernandez, J. L. Benedito, *Environ. Int.* **2006**, 32, 901–906. DOI:10.1016/j.envint.2006.05.012
- 34 V. Barwick (Ed.), Eurachem/CITAC Guide: Guide to Quality in Analytical Chemistry: An aid to Accreditation (3rd ed. 2016). ISBN 978-0-948926-32-7. (Available online at www.eurachem.org, accessed 05 February 2024))
- 35 ISO/IEC 17025:2018 General requirements for the competence of testing and calibration laboratories
- 36 Dr. Latimer, George W, Jr. (Ed.), Official Methods of Analysis of AOAC INTERNATIONAL (22), Oxford University Press, New York, **2023**. DOI:10.1093/9780197610145.001.0001
- 37 SR ISO 8466-1:2022 Water quality — Calibration and evaluation of analytical methods — Part 1: Linear calibration function
- 38 B. Magnusson, U. Ornemark (Eds.), Eurachem Guide: The fitness for purpose of analytical methods – A laboratory guide to method validation and related topics, 2nd ed., 2014, ISBN 978-91-87461-59-0. Available from www.eurachem.org. (Accessed 15 December 2021).
- 39 I. A. Petrean, V. Micle, I. M. Sur, M. Senila, *Sustainability* **2023**, 15, article number 1158. DOI:10.3390/su15021158
- 40 E. Cordos, R. Rautiu, C. Roman, M. Ponta, T. Frentiu, A. Sarkany, L. Fodorpataki, K. Macalik, C. McCormick, D. Weiss, *Eur. J. Miner. Process. Environ. Protect.* **2003**, 3, 324–335.
- 41 J. N. Miller, J. C. Miller, Statistics and chemometrics for analytical chemistry, 6th edition, Pearson Education Limited, Edinburgh Gate, England, **2010**.
- 42 C. W. Dunnett, *J. Am. Stat. Assoc.* **1955**, 50, 1096–1121. DOI:10.1080/01621459.1955.10501294
- 43 J.W. Tukey, *Biometrics* **1949**, 5, 99–114. DOI:10.2307/3001913
- 44 J. Mandel, The statistical analysis of experimental data, Dover Publications, New York, **1964**
- 45 J. M. Andrade, M. P. Gomez-Carracedo, *Anal. Methods* **2013**, 5, 1145–1149 DOI:10.1039/c2ay26400e
- 46 Regulation NTPA-001/2002 from 28.02.2002 (actualized) regarding the establishment of pollutant loading limits of industrial and urban wastewater when discharged into natural receivers (in Romanian) (<https://managerdemediu.ro/wp-content/uploads/2020/04/NTPA-001-din-2002-Normativul-privind-stabilirea-limitelor-de-%C3%AEnc%C4%83rcare-cu-polu-an%C5%A3i-a-apelor-uzate-industriale-%C5%9Fi-urbane-la-evacuarea-%C3%AEn-receptorii-naturali.pdf>, accessed 10 May 2023)

Povzetek

Nova metoda, ki temelji na plamenski atomski absorpcijski spektrometriji z visoko ločljivostjo (HR-CS FAAS), je bila validirana za določanje izbranih toksičnih kovin v odpadni vodi, ki je posledica rudarske dejavnosti. Zmogljivost metode smo primerjali z zmogljivostjo metod, ki temeljita na optični emisijski spektrometriji z induktivno sklopljeno plazmo (ICP-OES) in plamenski atomski absorpcijski spektrometriji z linijskim virom (LS FAAS). Za metodo HR-CS FAAS so bile meje zaznavnosti (LOD) v območju ($\mu\text{g L}^{-1}$) 1(Mn)–30(Pb) in boljše od ICP-OES za Cu, Fe, Ni, Co, Pb in Mn ter slabše za Cd, Zn in Cr. Dunnettov test je pokazal, da rezultati pridobljeni z eno ali drugo metodo ne odstopajo bistveno od certificiranih vrednosti. Izkoristek pri metodi HR-CS FAAS je bil v območju 98–103 % z relativno razširjeno negotovostjo 9–18 % in natančnostjo 2–11 %. V primerjavi z LS FAAS je imel HR-CS FAAS nižje LOD za Pb in Cr. Metoda HR-CS FAAS je primerna za določanje izbranih toksičnih elementov v vzorcih filtrirane vode brez kemične obdelave.



Except when otherwise noted, articles in this journal are published under the terms and conditions of the Creative Commons Attribution 4.0 International License

Synthetic Optimization and Antibacterial Activity of Novel Benzodioxepine-Biphenyl Amide Derivatives

Shao-Peng Yan,^{1,2,3} Zhi-Yu Zhu,^{1,2,3} Qi-Ke Jia,^{2,3} Rui-Ying Ji,^{1,2,3} Ya-Pin Wang,^{1,2,3} Dan He,^{1,2,3} Rong Wang^{1,2,3*} Xiao-Jun Xu⁴ and Yang Zhou^{1,2,3,5*}

¹ Cixi Biomedical Research Institute, Wenzhou Medical University, Ningbo, 315300, China

² Laboratory of Advanced Theranostic Materials and Technology, Ningbo Institute of Materials Technology and Engineering, Chinese Academy of Sciences, Ningbo, 315300, China

³ Ningbo Cixi Institute of Biomedical Engineering, Ningbo, 315300, China

⁴ College of Pharmaceutical Engineering and Biotechnology, Zhejiang Pharmaceutical University, Ningbo, 315500, China

⁵ Pingshan Translational Medicine Center, Shenzhen Bay Laboratory, Shenzhen, 518118 China

* Corresponding author: E-mail: rong.wang@nimte.ac.cn (R. Wang),
zhouyang876@nimte.ac.cn (Y. Zhou)

Received: 04-26-2024

Abstract

The biosynthesis of fatty acids is an important metabolic pathway in bacterial organisms. Previous studies have highlighted the synthesis of antimicrobial compounds anchored in the benzodioxepin scaffold and known for their pronounced antibacterial properties. Based on this fundamental knowledge, a series of eight innovative benzodioxepin-biphenyl amide derivatives were carefully designed and synthesized in the current research work. This was achieved through a sophisticated optimization of the synthetic methods. The scope of this study extends to a rigorous evaluation of the antibacterial properties and biocompatibility of the above-mentioned new derivatives. In particular, compound **E4** proved to be an extremely effective antimicrobial agent. In addition to a detailed elucidation of the crystalline architecture of compound **E4**, a thorough docking study was also carried out to investigate the interactions with the enzyme FabH.

Keywords: Benzodioxepine amide, biphenyl, Suzuki coupling, antibacterial activity, FabH inhibitor

1. Introduction

Fatty acid biosynthesis is an essential metabolic pathway that is crucial for the survival and growth of various organisms and exhibits remarkable biodiversity.^{1–3} This pathway is mainly facilitated by two enzyme systems: fatty acid synthase I (FAS I) and fatty acid synthase II (FAS II). FAS I, which is found primarily in mammals and yeasts, uses a multifunctional protein complex in which each step of synthesis is catalyzed by different domains within a single polypeptide. In contrast, FAS II, found in bacteria and plants, utilizes a series of independent, monofunctional enzymes, each responsible for specific steps of the process.^{4–6} Targeting these monofunctional enzymes in bacterial FAS II has proven to be a viable strategy for the development of new antimicrobial agents with lower toxicity to humans, highlighting the therapeutic potential of this approach. Among these enzymes, β -ketoacyl-ACP

synthase III (FabH) is increasingly recognized for its critical role in initiating fatty acid synthesis in bacteria, making it a priority target for antimicrobial drug development. As an essential β -ketoacyl-ACP synthase, FabH catalyzes the initiation of fatty acid synthesis through the use of acyl-CoA, setting the pace for subsequent elongation cycles. In contrast to its homologues FabF and FabB, which elongate the fatty acid chain using acyl-ACP, FabH exclusively utilizes acetyl-CoA, highlighting its unique substrate preference.^{7,8} Furthermore, FabH is ubiquitously present in a variety of clinically important pathogens, including Gram-positive and Gram-negative bacteria, chlamydiae, anaerobes, mycobacteria, and protozoa. In addition, the gene sequences and three-dimensional structures of FabH are conserved in these pathogens, whereas homologous proteins are absent in humans. Remarkably, the active site residues of FabH are consistent in both Gram-positive and

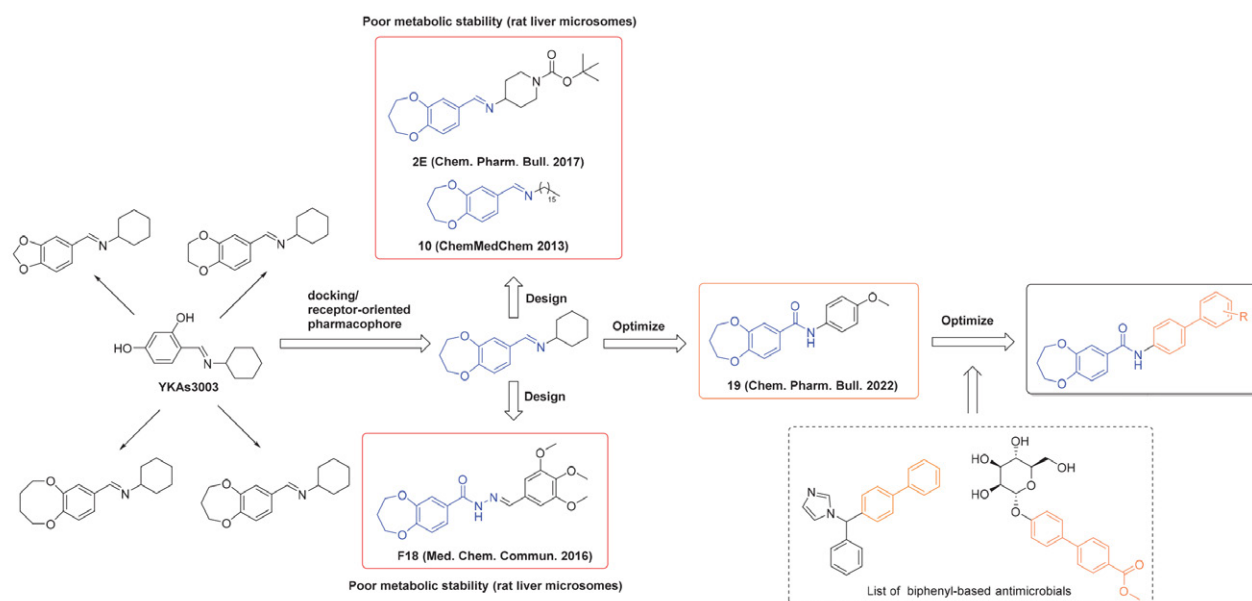
Gram-negative bacteria.^{9–12} All these features underscore its potential as a therapeutic target.

In preliminary studies, we have used the structural basis of YKAs3003 to develop a series of novel Schiff base derivatives. Using the CDOCKER computational platform, we found that derivatives with a benzodioxepin scaffold exhibited significant alignment (1.57282) and reduced binding energies (–28.4496 kcal/mol) compared to the pharmacophore model of the FabH enzyme, suggesting their potential as potent FabH inhibitors.^{13–15} We then investigated the antimicrobial activity of these Schiff bases and their hydrazone analogs. These compounds exhibited considerable activity against various Gram-positive and Gram-negative bacteria. Despite the recognized role of Schiff and hydrazone moieties as essential pharmacophores in numerous antimicrobial agents, including those targeting FabH, their susceptibility to hepatic metabolic degradation has limited further *in vivo* studies. To address the observed metabolic instability of Schiff and hydrazone groups in antimicrobial agents, our research has focused on the incorporation of more stable amide linkages. This modification has resulted in lead compounds with enhanced *in vitro* antibacterial activity, which is a promising direction for further antimicrobial exploration.¹⁶ The biphenyl motif, characterized by two benzene rings linked by a single bond, is a structural feature commonly observed in various antimicrobial compounds.^{17–19} Its inherent chemical stability and ability to form multiple interactions with bacterial targets are critical properties that influence our drug design. Compounds with the biphenyl structure are known to exert antimicrobial effects via multiple mechanisms, including disruption of cell walls or membranes and inhibition of protein and nucleic acid synthesis.^{20–25} Building on these findings, our current strategy

utilizes a combinatorial pharmacophore model in which the amide-modified benzodioxepin core is combined with the biphenyl scaffold. The details of this design approach are shown in Scheme 1. Using an optimized synthetic route, this study starts with the reaction of benzodioxepine with *p*-bromoaniline to synthesize the corresponding amide derivatives. This step is followed by a Suzuki–Miyaura coupling reaction with phenylboronic acid, which aims to determine the most favorable synthesis conditions.^{26,27} This methodological approach not only expands the substrate range but also improves the comprehensive exploration of the antimicrobial efficacy and target specificity of the derivatives. The results obtained provide a solid basis for the development of new benzodioxepin–biphenyl lead compounds specifically targeting the FabH enzyme.

2. Results and Discussion

In previous studies, the synthesis of benzodioxepine–biphenylamide derivatives was first carried out using a Suzuki coupling to produce an aminated biphenyl. This intermediate was then condensed with the carboxylic acid of benzodioxepine to obtain the desired amide derivatives. In this study, a critical re-evaluation of the synthetic sequence revealed an alternative approach in which the reaction begins with the coupling of the benzodioxepine carboxylic acid and *p*-bromoaniline to form the amide. This amide is then used in a Suzuki coupling with various phenylboronic acid derivatives. This revised methodology not only facilitated the purification of the final product, but also significantly reduced the occurrence of side reactions, increasing the overall purity of the benzodioxepine



Scheme 1. The design strategy of benzodioxepin–biphenyl compounds as FabH inhibitors.

Table 1. Optimization of the reaction conditions.^a

Entry	[Pd]	Amt of cat. (mol%)	Base	Solvent	T (°C)	Yield (%) ^b
1	Pd(PPh ₃) ₄	5	K ₂ CO ₃	1,4-dioxane	80	21
2	Pd(OAc) ₂	5	K ₂ CO ₃	1,4-dioxane	80	17
3	Pd(dba) ₂	5	K ₂ CO ₃	1,4-dioxane	80	45
4	Pd(dppf)Cl ₂ ·DCM	5	K ₂ CO ₃	1,4-dioxane	80	65
5	Pd/C	5	K ₂ CO ₃	1,4-dioxane	80	<5
6	Pd(dppf)Cl ₂ ·DCM	5	Na ₂ CO ₃	1,4-dioxane	80	81
7	Pd(dppf)Cl ₂ ·DCM	5	Cs ₂ CO ₃	1,4-dioxane	80	93
8	Pd(dppf)Cl ₂ ·DCM	5	AcOK	1,4-dioxane	80	72
9	Pd(dppf)Cl ₂ ·DCM	5	Et ₃ N	1,4-dioxane	80	54
10c	Pd(dppf)Cl ₂ ·DCM	5	Cs ₂ CO ₃	THF	65	69
11	Pd(dppf)Cl ₂ ·DCM	5	Cs ₂ CO ₃	EtOH	70	37
11	Pd(dppf)Cl ₂ ·DCM	5	Cs ₂ CO ₃	Toluene	90	37
12	Pd(dppf)Cl ₂ ·DCM	4	Cs ₂ CO ₃	1,4-dioxane	80	79
13	Pd(dppf)Cl ₂ ·DCM	6	Cs ₂ CO ₃	1,4-dioxane	80	94

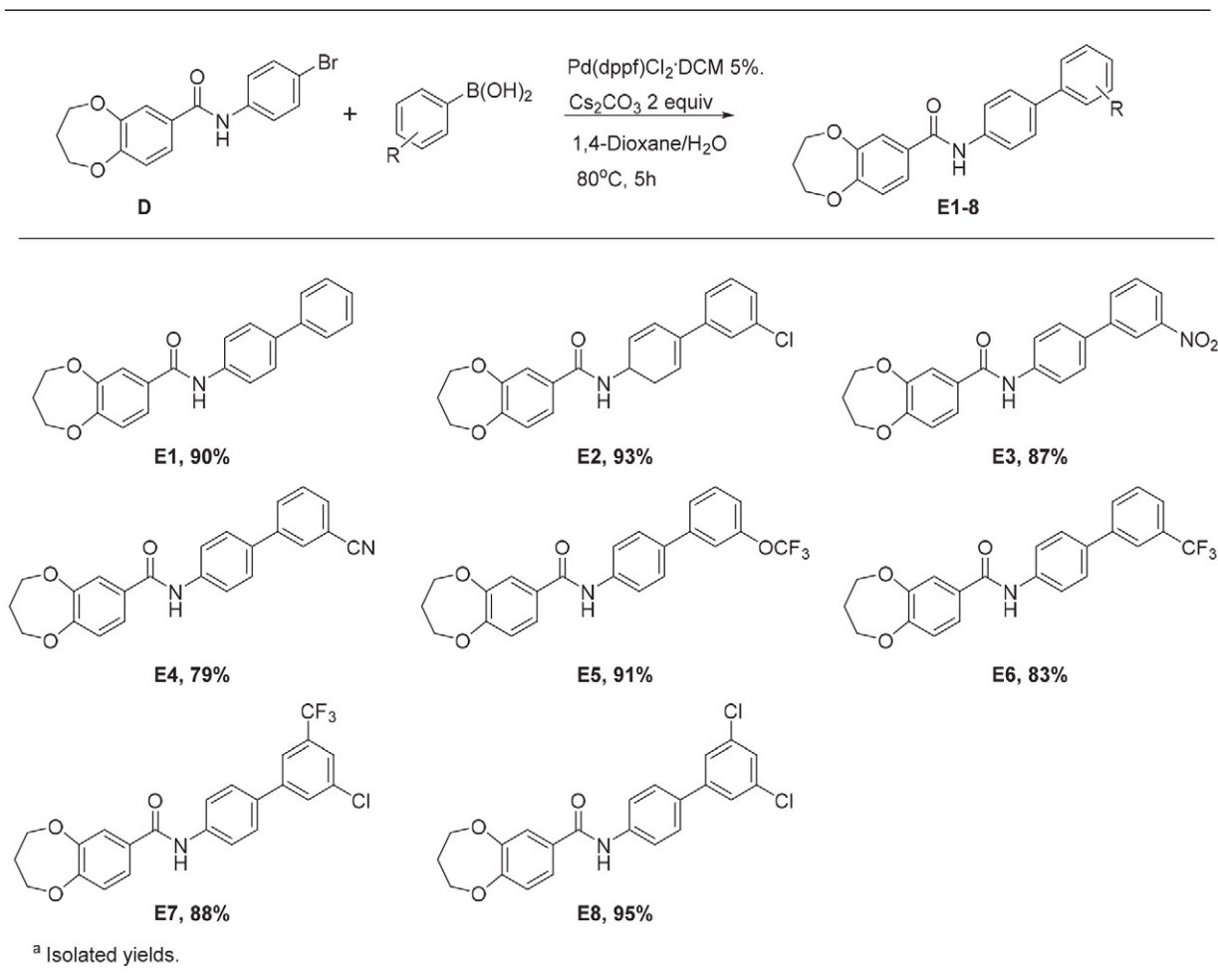
^a All reactions were carried out at a scale of 0.5 mmol of compound **D**. ^bGC yield.

biphenylamide derivatives. By strategically positioning the Suzuki coupling as the final step of the synthesis, process optimization led to a more efficient route to produce the desired compounds. Thus, we began our synthesis efforts with the preparation of *N*-(4-bromophenyl)-3,4-dihydro-2*H*-benzo[*b*][1,4]dioxepin-7-carboxamide (compound **D**). The synthetic pathway is shown in Figure 1, where we used compound **D** together with phenylboronic acid as substrates to optimize the conditions for Suzuki coupling.

In our study, shown in Table 1, we have investigated in detail the influence of various parameters on the Suzuki coupling reactions. Using a solvent system of 1,4-dioxane and water at a ratio of 20:1 and heating the mixture for five hours at a constant palladium catalyst concentration of 5 mol%, we first focused on evaluating the effects of different palladium catalysts on the reaction efficiency. As described in entries 1 through 5, a series of palladium catalysts were tested for their ability to facilitate the synthesis of benzodioxepine biphenyl compounds, herein referred to as compound **E**. In particular, Pd(dppf)Cl₂·DCM proved to be the most effective with a gas chromatographic yield of 65 %. The effects of different bases on the yield were then investigated, as documented in entries 4 and 6 to 9. When investigating the influence of base selection on the Suzuki coupling reactions, we found a positive correlation between the alkalinity of the inorganic bases and the resulting product yield. In particular, the replacement of potassium carbonate (K₂CO₃) with sodium carbonate (Na₂CO₃)

or cesium carbonate (Cs₂CO₃) led to a progressive improvement in yield, with Cs₂CO₃ producing the most significant increase. In contrast, the use of organic bases such as potassium acetate (AcOK) and triethylamine (Et₃N) was found to negatively affect the yield. Further investigations focused on the role of the solvent for the catalytic efficiency. Changing the solvent from 1,4-dioxane to toluene, THF or ethanol did not improve the yield. In addition, our analysis of the optimal catalyst concentration revealed that decreasing the Pd(dppf)Cl₂·DCM concentration from 5 mol% to 4 mol% significantly decreased the yield, while increasing the concentration to 6 mol% did not significantly increase the yield. Therefore, we determined that the optimal catalyst concentration was 5 mol%. After careful optimization of the Suzuki coupling reaction parameters, we established an effective protocol involving a catalyst concentration of 5 mol% Pd(dppf)Cl₂·DCM, the use of two equivalents of Cs₂CO₃, and a solvent system of 1,4-epoxycyclohexane and water in a volume ratio of 20:1. This mixture was refluxed at 80 °C for five hours. Under these optimized conditions, a comprehensive evaluation of the substrate scope was performed. The results presented in Table 2 show that substrates with a variety of substituent groups (E1-8) consistently gave products with isolated yields between 79% and 95%.

The investigation of the antimicrobial efficacy and biocompatibility of eight novel benzodioxepine-carbamide diphenyl derivatives is described, with the relevant results listed in Table 3. The octanol-water partition coeffi-

Table 2. Pd complex-catalyzed benzylic oxidation.^a

cient (AlogP) serves as an essential index for measuring the lipophilicity of active pharmaceutical ingredients and has a profound impact on their absorption, distribution, metabolism and excretion (ADME) properties. Optimal lipophilicity is crucial for facilitating the passage of drugs through cell membranes and thus improving their bio-availability. In this series, all compounds exhibited AlogP values below 7, which ensures a favorable lipid-water balance that supports adequate membrane permeability while mitigating the risks associated with excessive lipophilicity, such as insolubility and bioaccumulation. In addition, these derivatives exhibited minimal cytotoxicity to NIH-3T3 mouse fibroblast cells, with IC₅₀ values above 100 μM , opening promising prospects for subsequent in vivo efficacy studies. However, the study showed that the antimicrobial efficacy of the investigated compounds is significantly influenced by the nature of the substituents attached to the biphenyl group. This observation emphasizes the central role of chemical substituents in modulating biological activities and illustrates a complex relationship between molecular architecture and antimicrobial strength. In particular, the parent compound **E1** and its

chlorine-substituted derivative **E2** showed lower antimicrobial activity. This lower potency can be primarily attributed to the insufficient electronic effects required for optimal interaction with biological targets. In addition, the ability of chlorine to withdraw electrons was found to be relatively weak, resulting in less effective non-covalent interactions with the active sites of these targets. Our study also showed marked differences in the antimicrobial efficacy of biphenyl derivatives when modified with nitro (**E3**) and cyano (**E4**) substituents. The nitro group ($-NO_2$), known for its strong electron-withdrawing properties, is involved in conjugation processes that reduce the electron density around the biphenyl core. This reduction in electron density likely facilitates more effective interactions with biological targets and increases antimicrobial activity. In contrast, the cyano group ($-CN$) serves as a milder electron attractor. Its less pronounced effect preserves the electron density of the biphenyl backbone to a greater extent, potentially maintaining more balanced interactions with biological targets without compromising molecular stability too much. In addition, a comparative analysis of compounds containing trifluoromethoxy ($-OCF_3$) and trifluo-

Table 3. Antibacterial activity and cytotoxicity of synthetic compounds.

Comp.	Alog P	Minimum inhibitory concentrations (µg/mL)				Cytotoxicity IC ₅₀ (µM)
		Gram-negative		Gram-positive		
		<i>E. coli</i>	<i>P. aeruginosa</i>	<i>S. aureus</i>	<i>S. pneumoniae</i>	
E1	4.12	>100	>100	50	50	117.3±7.5
E2	4.68	50	>100	50	>100	158.9±11.8
E3	4.11	50	25	12.5	50	176.8±6.9
E4	4.16	6.25	12.5	12.5	25	124.6±8.4
E5	5.65	>100	25	50	50	161.4±5.2
E6	5.04	12.5	50	12.5	25	124.3±9.8
E7	5.60	12.5	25	25	12.5	139.5±8.1
E8	5.24	50	>100	50	>100	146.9±7.8

romethyl (–CF₃) groups showed considerable differences in their antimicrobial efficacy despite their structural similarities. In particular, the compounds with the OCF₃ group (E5) showed significantly lower activity than their CF₃-substituted counterparts (E6). This observation suggests that even subtle differences in the electronic properties of the substituent groups can have significant effects on the biological properties of the molecules, emphasizing the importance of precise molecular design for the development of effective antimicrobial agents.

The crystal structures of compound E4 were determined by X-ray diffraction analysis to better predict and

analyze the binding of E4 to the target in the future study. The crystal data shown in Table 4 and Figure 2 represent the perspective views of E4 with the atomic labeling system. The crystallographic data has been deposited at the Cambridge Crystallographic Data Center (CCDC, number 2348536).

To elucidate the binding pattern between the target protein and the small molecules, molecular docking was performed using the crystal structure of *E. coli* FabH (PDB entry code: 5BNM) as a receptor model. The computational analysis revealed that compound E4 with a binding energy of –37.4611 kcal/mol has an exceptional binding af-

Table 4. Crystal data and structure refinement for compound E4.

Compound	E4		
Empirical formula	C ₂₃ H ₁₈ N ₂ O ₃	Z	2
Temperature/K	223.00	D _{calcd} (Mg m ^{–3})	1.353
Crystal system	monoclinic	μ (mm ^{–1})	0.734
Space group	P2 ₁	F(000)	388.0
a (Å)	9.7698(10)	θ limits (°)	4.99 to 133.142
b (Å)	5.2535(5)	Reflections collected	5820
c (Å)	18.2571(18)	Independent reflections	2869 [R _{int} = 0.0472]
α (°)	90	Data/restraints/parameters	2869/1/254
β (°)	104.055(7)	GOF	0.959
γ (°)	90	R ₁ /wR ₂ [I > 2σG _s (I)]	0.0998/ 0.2098
Volume (Å ³)	909.00(16)	R ₁ /wR ₂ (all data)	0.1144/ 0.2187

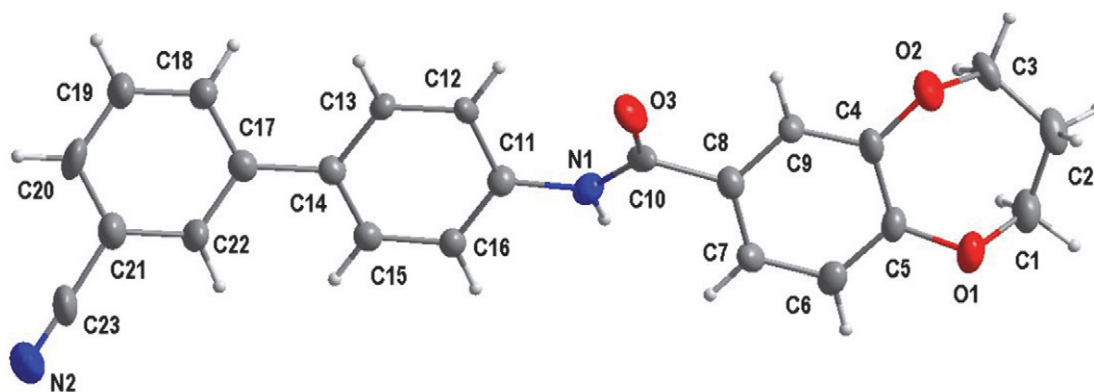


Figure 2. Crystal structure diagram of compound E4.

finity to the target protein FabH. Figure 3 shows the molecular docking visualization model of the target compound **E4** with FabH, where panel A shows the hydrogen bonding interactions between the compound and the amino acid residues, and panels B and C show the 3D and 2D interaction diagrams of compound **E4** with the amino acid residues. As shown in Figure 2, the amino acid residue ASN247 in the FabH protein forms a hydrogen bond with the carbonyl oxygen atom of the amide group of **E4** (O...H–N; 3.23 Å). In addition, the nitrile group on the biphenyl group forms a hydrogen bond with the amino acid residue CYS112 (N...H–O; 2.76 Å). In addition, the amino acid residue ASN can also form a π -donor hydrogen bond with the first benzene ring of the biphenyl. At the same time, the first benzene ring of the biphenyl is able to form π - σ forces with the MET207 residue of FabH, while the second benzene ring forms π - σ forces with residues ALA246 and VAL212 and π -sulfur interactions with CYS1112. These interactions emphasize the crucial role of the amide backbone and the nitrile-substituted biphenyl in target binding. In addition, other interactions between various residues of 5BNM, including AGR36, ILE156 and ALA212, such as alkyl and π -alkyl interactions, further facilitated the binding interaction between compound **E4** and FabH.

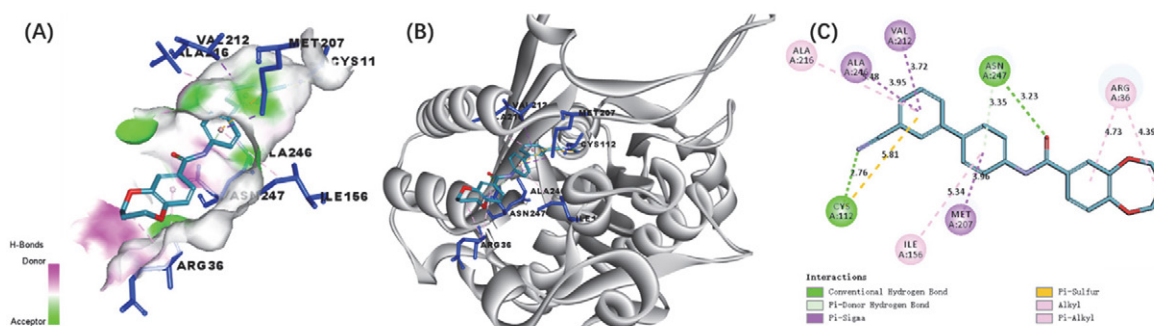


Figure 3. Molecular docking visualization model of the target compound **E4** with FabH: (A) the hydrogen bonds between compound **E4** and the amino acid residues, (B) and (C) the 3D and 2D interaction diagrams of compound **E4** with the amino acid residues of FabH.

3. Conclusion

In this study, we carefully optimized the experimental conditions to determine the optimal parameters for the Suzuki coupling of compound **D** with phenylboronic acid. After establishing these conditions, we expanded the substrate range, resulting in the synthesis of eight new benzodioxepine-carboxamide biphenyl derivatives. The antimicrobial activity of these derivatives was evaluated and showed different inhibitory effects against *Escherichia coli*, *Pseudomonas fluorescens*, *Bacillus subtilis* and *Staphylococcus aureus*. In particular, compound **E4** showed the strongest antibacterial activity. To further investigate the potential of **E4** as an inhibitor of the FabH enzyme, we obtained its crystal structure and performed molecular docking

studies with the FabH receptor model of *E. coli*. The computational analysis revealed a significant binding affinity of compound **E4** to the FabH target, interacting with several residues. These results not only highlight the potential antimicrobial mechanism of **E4**, but also provide the basis for future research to develop similar benzodioxepine-carboxamide biphenyl derivatives to explore efficient antimicrobial lead compounds.

4. Experimental Section

4. 1. Materials and Measurements

All chemicals used were purchased and used without further purification unless otherwise stated. Silica gel (Qingdao Haiyang Chemical) with a mesh size of 200–300 was used for column chromatography. Analytical thin-layer chromatography (TLC) was performed on Huanghai silica gel plates with HSGF 254. UV light (254 nm or 365 nm) was used to detect all compounds. Separation of compounds by column chromatography was performed using silica gel 60 (200–300 mesh ASTM, E. Merck). The amount of silica gel used was 50 to 100 times the weight applied to the column. ^1H and ^{13}C NMR data were recorded using a Bruker 400 MHz nuclear magnetic resonance spectrometer unless oth-

erwise stated. Chemical shifts are expressed in ppm (δ) using the residual solvent line as an internal standard. The splitting patterns are labeled s for singlet, d for doublet, t for triplet and m for multiplet. The ESI-MS spectra were recorded using a Mariner System 5304 mass spectrometer.

4. 2. Method for Preparing Compound D

The comprehensive synthesis of compounds **B** and **C**, including the respective yields, nuclear magnetic resonance (NMR) and mass spectrometry (MS) data, has already been documented in our research work. We therefore avoid redundant repetition of this information in this context. For the synthesis of the diazirinamide compounds, a dry 25 mL round bottom flask was equipped

with a magnetic stirrer. Compound **C** (97 mg, 0.5 mmol) was added to the flask along with the corresponding diazirinamine (0.5 mmol) and DMAP (1.1 equiv.) and then stirred in 2 mL dichloromethane at room temperature for 15 minutes. EDC·HCl (1.1 equiv.) was then added and stirred overnight. The resulting reaction mixture was diluted with 5 mL CH₂Cl₂ and filtered through a celite pad. The filtrate was further diluted with water (8 mL). After separation of the layers, the organic layer was washed with an aqueous saturated salt solution and then dried with Na₂SO₄. The organic layer was concentrated under reduced pressure, yielding the crude material, which was purified by column chromatography on silica gel. The structure elucidation of compound **D** was confirmed by ¹H NMR and ESI-HRMS.

***N*-(4-bromophenyl)-3,4-dihydro-2H-benzo[b][1,4]dioxepine-7-carboxamide (**D**)**

White solid, yield 81%. m.p. 138.8–139.0 °C. IR (cm⁻¹) ν 3324 (NH), 2973 (CH_{Ar}), 1655 (C=O), 1503 (C=C_{Ar}), 1323 (C-N), 1271, 1063 (=C-O-C). ¹H NMR (400 MHz, DMSO-*d*₆) δ : 7.73 (s, 1H), 7.56–7.49 (m, 2H), 7.49–7.42 (m, 3H), 7.43 (dd, *J* = 8.3, 2.3 Hz, 1H), 7.02 (d, *J* = 8.3 Hz, 1H), 4.29 (dt, *J* = 12.9, 5.8 Hz, 4H), 2.30–2.19 (m, 2H). ¹³C NMR (101 MHz, DMSO-*d*₆) δ 163.66, 153.07, 149.59, 135.89, 130.76, 128.22, 121.11, 120.54, 120.49, 119.59, 115.78, 69.26, 69.15, 29.91. ESI-HRMS *m/z*: 348.0222 [M+H]⁺, calcd for [C₁₆H₁₅BrNO₃]⁺: 348.0230.

4. 3. General method for preparing compound **E**

Under an inert nitrogen atmosphere, the synthesis procedure was initiated by adding the reactants one after the other to a three-necked flask: the intermediate **D** (50 mg, 0.14 mmol, 1.0 equiv.), a phenylboronic acid derivative (20.5 mg, 1.2 equiv.), Pd(dppf)Cl₂·DCM (12 mg, 5 mol%) and Cs₂CO₃ (94 mg, 2.0 equiv.), supplemented with a 2 mL aqueous solution of 1,4-dioxane (ratio 1:20 v/v). The mixture was then heated to 80 °C and kept under reflux conditions for 5 hours. After completion of the reaction and subsequent cooling to room temperature, the process was terminated by adding 10 mL of water. The reaction medium was then extracted three times in succession with dichloromethane and the organic layer was purified by washing with saturated sodium chloride solution. Concentration of the CH₂Cl₂ extract under reduced pressure by rotary evaporation yielded a crude product, which was subsequently purified by column chromatography to isolate the desired target compounds **E1–E8**.

***N*-([1,1'-biphenyl]-4-yl)-3,4-dihydro-2H-benzo[b][1,4]dioxepine-7-carboxamide (**E1**)**

White solid, yield 90%. m.p. 163.1–163.9 °C. IR (cm⁻¹) ν 3362 (NH), 2927 (CH_{Ar}), 1661 (C=O), 1500 (C=C_{Ar}),

1321 (C-N), 1278, 1048 (=C-O-C). ¹H NMR (400 MHz, CDCl₃) δ 8.96 (s, 1H), 8.44 (td, *J* = 8.1, 1.7 Hz, 1H), 7.60 (d, *J* = 8.4 Hz, 2H), 7.43 (d, *J* = 8.4 Hz, 2H), 7.16–7.02 (m, 2H), 7.01 (s, 2H), 6.89–6.81 (m, 2H), 6.67 (dd, *J* = 8.3, 2.2 Hz, 1H), 4.18 (dt, *J* = 17.1, 5.7 Hz, 4H), 2.15 (p, *J* = 5.7 Hz, 2H). ¹³C NMR (101 MHz, CDCl₃) δ 163.54, 152.95, 149.59, 139.25, 136.06, 136.03, 128.58, 127.54, 126.43, 125.87, 125.61, 121.08, 120.48, 119.53, 119.16, 69.25, 69.13, 29.93. ESI-HRMS *m/z*: 346.1433 [M+H]⁺, calcd for [C₂₂H₂₀NO₃]⁺: 346.1438.

***N*-(3'-chloro-[1,1'-biphenyl]-4-yl)-3,4-dihydro-2H-benzo[b][1,4]dioxepine-7-carboxamide (**E2**)**

White solid, yield 93%. m.p. 181.3–182.5 °C. IR (cm⁻¹) ν 3394 (NH), 2956 (CH_{Ar}), 1665 (C=O), 1532, 1497 (C=C_{Ar}), 1310 (C-N), 1271, 1046 (=C-O-C), 786 (C-Cl). ¹H NMR (400 MHz, CDCl₃) δ 7.77 (s, 1H), 7.74–7.68 (m, 2H), 7.61–7.54 (m, 3H), 7.51 (d, *J* = 2.3 Hz, 1H), 7.52–7.43 (m, 2H), 7.34 (s, 1H), 7.40–7.27 (m, 1H), 7.05 (d, *J* = 8.3 Hz, 1H), 4.36–4.26 (m, 4H), 2.26 (p, *J* = 5.8 Hz, 2H). ¹³C NMR (101 MHz, CDCl₃) δ 164.76, 154.27, 150.87, 142.34, 137.86, 135.78, 134.70, 130.03, 127.71, 127.12, 126.96, 124.99, 122.32, 121.78, 120.77, 120.40, 70.53, 70.40, 31.17. ESI-HRMS *m/z*: 402.0863 [M+Na]⁺, calcd for [C₂₂H₁₈ClNO₃Na]⁺: 402.0867.

***N*-(3'-nitro-[1,1'-biphenyl]-4-yl)-3,4-dihydro-2H-benzo[b][1,4]dioxepine-7-carboxamide (**E3**)**

Gray-yellow solid, yield 87%. m.p. 174.2–175.1 °C. IR (cm⁻¹) ν 3335 (NH), 2952 (CH_{Ar}), 1647 (C=O), 1518, 1497 (C=C_{Ar}), 1349 (Ar-NO₂), 1309 (C-N), 1268, 1047 (=C-O-C). ¹H NMR (400 MHz, CDCl₃) δ 8.45 (t, *J* = 2.1 Hz, 1H), 8.19 (dd, *J* = 7.7, 2.2 Hz, 1H), 7.92 (d, *J* = 7.7 Hz, 1H), 7.83–7.74 (m, 3H), 7.68–7.57 (m, 3H), 7.57–7.44 (m, 2H), 7.06 (d, *J* = 8.3 Hz, 1H), 4.31 (dt, *J* = 11.2, 5.7 Hz, 4H), 2.25 (p, *J* = 5.7 Hz, 2H). ¹³C NMR (101 MHz, CDCl₃) δ 164.78, 154.36, 150.89, 148.80, 138.50, 134.52, 132.70, 129.76, 129.56, 127.83, 122.33, 121.86, 121.82, 121.59, 120.78, 120.53, 70.54, 70.40, 31.14. ESI-HRMS *m/z*: 413.1103 [M+Na]⁺, calcd for [C₂₂H₁₈N₂O₅Na]⁺: 413.1113.

***N*-(3'-cyano-[1,1'-biphenyl]-4-yl)-3,4-dihydro-2H-benzo[b][1,4]dioxepine-7-carboxamide (**E4**)**

White solid, yield 79%. m.p. 169.5–170.1 °C. IR (cm⁻¹) ν 3331 (NH), 2965 (CH_{Ar}), 2227 (C≡N), 1646 (C=O), 1527, 1497 (C=C_{Ar}), 1306 (C-N), 1267, 1049 (=C-O-C). ¹H NMR (400 MHz, CDCl₃) δ 7.86 (d, *J* = 1.8 Hz, 1H), 7.84–7.78 (m, 2H), 7.75 (d, *J* = 8.5 Hz, 2H), 7.65–7.44 (m, 6H), 7.06 (d, *J* = 8.3 Hz, 1H), 4.31 (dt, *J* = 11.2, 5.7 Hz, 4H), 2.26 (p, *J* = 5.8 Hz, 2H). ¹³C NMR (101 MHz, CDCl₃) δ 164.83, 154.34, 150.87, 141.73, 138.39, 134.72, 131.17, 130.51, 130.36, 129.65, 129.58, 127.71, 122.35, 121.79, 120.80, 120.57, 118.87, 113.00, 70.53, 70.40, 31.15. ESI-HRMS *m/z*: 371.1392 [M+H]⁺, calcd for [C₂₃H₁₉N₂O₃]⁺: 371.1390.

***N*-(3'-(trifluoromethoxy)-[1,1'-biphenyl]-4-yl)-3,4-dihydro-2H-benzo[b][1,4]dioxepine-7-carboxamide (E5)**

Light yellow solid, yield 91%. m.p. 176.0–176.9 °C. IR (cm⁻¹) ν 3388 (NH), 2964 (CH_{Ar}), 1663 (C=O), 1533, 1498 (C=C_{Ar}), 1313 (C-N), 1181, 1177 (C-F), 1265, 1045 (=C-O-C). ¹H NMR (400 MHz, CDCl₃) δ 7.79 (s, 1H), 7.76–7.68 (m, 2H), 7.62–7.52 (m, 2H), 7.55–7.40 (m, 5H), 7.19 (ddt, *J* = 8.1, 2.3, 1.1 Hz, 1H), 7.05 (d, *J* = 8.3 Hz, 1H), 4.30 (dt, *J* = 11.3, 5.7 Hz, 4H), 2.25 (p, *J* = 5.8 Hz, 2H). ¹³C NMR (101 MHz, CDCl₃) δ 164.77, 154.29, 150.87, 149.75, 142.61, 137.98, 135.61, 130.11, 129.68, 127.75, 125.18, 122.32, 121.78, 120.77, 120.44, 119.39, 70.52, 70.39, 31.16. ESI-HRMS *m/z*: 452.1082 [M+Na]⁺, calcd for [C₂₃H₁₈F₃NO₄Na]⁺: 452.1086.

***N*-(3'-(trifluoromethyl)-[1,1'-biphenyl]-4-yl)-3,4-dihydro-2H-benzo[b][1,4]dioxepine-7-carboxamide (E6)**

White solid, yield 83%. m.p. 173.4–174.2 °C. IR (cm⁻¹) ν 3327 (NH), 2961 (CH_{Ar}), 1645 (C=O), 1526, 1498 (C=C_{Ar}), 1313 (C-N), 1158 (C-F), 1267, 1060 (=C-O-C). ¹H NMR (400 MHz, CDCl₃) δ 7.83 (s, 1H), 7.80–7.70 (m, 4H), 7.65–7.56 (m, 2H), 7.55 (t, *J* = 7.6 Hz, 2H), 7.52 (d, *J* = 2.3 Hz, 1H), 7.47 (dd, *J* = 8.3, 2.3 Hz, 1H), 7.05 (d, *J* = 8.3 Hz, 1H), 4.31 (dt, *J* = 10.5, 5.8 Hz, 4H), 2.26 (p, *J* = 5.7 Hz, 2H). ¹³C NMR (101 MHz, CDCl₃) δ 164.75, 154.30, 150.88, 141.28, 138.02, 135.70, 131.38, 130.12, 129.67, 129.28, 127.81, 123.80, 123.57, 122.32, 121.80, 120.76, 120.46, 70.53, 70.40, 31.16. ESI-HRMS *m/z*: 414.1318 [M+H]⁺, calcd for [C₂₃H₁₉F₃NO₃]⁺: 414.1312.

***N*-(3'-chloro-5'-(trifluoromethyl)-[1,1'-biphenyl]-4-yl)-3,4-dihydro-2H-benzo[b][1,4]dioxepine-7-carboxamide (E7)**

White solid, yield 88%. m.p. 143.8–144.2 °C. IR (cm⁻¹) ν 3330 (NH), 2964 (CH_{Ar}), 1652 (C=O), 1521, 1496 (C=C_{Ar}), 1336 (C-N), 1127 (C-F), 1260, 1060 (=C-O-C), 825 (C-Cl). ¹H NMR (400 MHz, CDCl₃) δ 7.83 (s, 1H), 7.79–7.72 (m, 3H), 7.70 (s, 1H), 7.58 (dd, *J* = 9.0, 2.1 Hz, 3H), 7.52 (d, *J* = 2.3 Hz, 1H), 7.47 (dd, *J* = 8.3, 2.3 Hz, 1H), 7.05 (d, *J* = 8.3 Hz, 1H), 4.31 (dt, *J* = 11.6, 5.7 Hz, 4H), 2.26 (p, *J* = 5.8 Hz, 2H). ¹³C NMR (101 MHz, CDCl₃) δ 163.96, 153.51, 150.03, 137.76, 134.51, 133.35, 131.64, 129.30, 128.68, 126.95, 123.10, 123.06, 121.50, 121.01, 120.98, 120.95, 119.94, 119.66, 69.68, 69.54, 30.29. ESI-HRMS *m/z*: 448.0933 [M+H]⁺, calcd for [C₂₃H₁₈ClF₃NO₃]⁺: 448.0922.

***N*-(3',5'-dichloro-[1,1'-biphenyl]-4-yl)-3,4-dihydro-2H-benzo[b][1,4]dioxepine-7-carboxamide (E8)**

White solid, yield 95%. m.p. 155.7–156.4 °C. IR (cm⁻¹) ν 3376 (NH), 2935 (CH_{Ar}), 1663 (C=O), 1536, 1502 (C=C_{Ar}), 1334 (C-N), 1127 (C-F), 1272, 1062 (=C-O-C), 795 (C-Cl). ¹H NMR (400 MHz, CDCl₃) δ 7.77 (s, 1H), 7.72 (d, *J* = 8.6 Hz, 2H), 7.58–7.51 (m, 2H), 7.54–7.44 (m, 3H), 7.45 (s, 1H), 7.32 (t, *J* = 1.9 Hz, 1H), 7.05 (d, *J* = 8.3 Hz, 1H), 4.31 (dt, *J* = 11.2, 5.7 Hz, 4H), 2.26 (p, *J* = 5.8 Hz,

2H). ¹³C NMR (101 MHz, CDCl₃) δ 164.79, 154.33, 150.87, 143.46, 138.40, 135.31, 134.38, 129.58, 127.71, 126.96, 125.30, 122.33, 121.79, 120.79, 120.43, 70.53, 70.39, 31.15. ESI-HRMS *m/z*: 414.0667 [M+H]⁺, calcd for [C₂₂H₁₈Cl₂NO₃]⁺: 414.0658.

4. 4. *In vitro* Bacterial Suppressive Assay

To evaluate the *in vitro* activity of the compounds, the tetrazolium reduction assay was performed with thiazolyl blue tetrazolium bromide (MTT) using the TTC double dilution method. Nutrient broth (NB) was used as the medium for bacterial growth. Seeding broth containing microbial spores was prepared in NB with 24-hour-old bacterial cultures on nutrient agar (Hi-media) and incubated at 37 °C. The bacterial suspension was then adjusted with sterile saline to a concentration of 1 × 10⁴ to 1 × 10⁵ colony forming units (CFU)/mL. The tested compounds and the reference drugs were serially diluted twice to obtain the desired concentrations of 100, 50, 12.5, 6.25, 3.13 and 1.56 µg/mL. The tubes were then incubated in BOD incubators at 37 °C for the bacterial strains. The minimum inhibitory concentrations (MIC) were determined based on visual observations after a 24-hour incubation period for the bacteria.

4. 5. Cytotoxicity Test

Cytotoxic *in vitro* activity was investigated using the MTT assay against NIH-3T3 mouse fibroblast cells. Cells were cultured in a 96-well plate at a density of 5 × 10³ cells per well, and different concentrations of the compounds were added to each well. After a 24-hour incubation at 37 °C under a 5% CO₂ atmosphere, cytotoxicity was assessed. In addition, 20 µL of MTT reagent (4 mg/mL) was added to each well 4 hours before the end of the incubation period. After four hours, the plate was centrifuged at 1200 rpm for 5 minutes, the supernatant was removed and 200 µL of DMSO was added to each well. The absorbance was then measured at a wavelength of 570 nm (OD₅₇₀ nm) using an ELISA microplate reader. Three replicate wells were used for each concentration and each test was performed three times so that the average IC₅₀ value could be calculated. The cytotoxicity of each compound was expressed as the concentration at which cell viability was reduced by 50% (IC₅₀).

4. 6. Experimental Protocol for Docking Study

In the molecular docking analysis, compound E4 was inserted into the three-dimensional X-ray structure of *E. coli* FabH (PDB: 5BNM) using the Discovery Studio Client (v19.1.0). The DS-CDOCKER protocol was used via the graphical user interface to facilitate this process. To generate accurate representations of the compounds in

three dimensions, Chem. 3D ultra 12.0 from Cambridge Soft Corporation, USA, which follows the Chemical Structure Drawing Standard, was used. To optimize the energy of the constructed structures, the MMFF94 force field was used, and the iterations were set to 5000 with a minimum RMS gradient of 0.10. For the comparative analysis, the crystal structures of the *E. coli* FabH (PDB: 5BNM) complex were taken from the RCSB Protein Data Bank (<http://www.rcsb.org/pdb/>). Prior to analysis, all water molecules and ligands bound to the protein were removed in order to focus exclusively on the interaction of interest. In addition, polar hydrogen atoms were added to the protein structures to ensure accurate representation of hydrogen bonding interactions.

Acknowledgments

This work was supported by the S&T Innovation 2025 Major Special Program of Ningbo (2020Z091), the Natural Science Foundation of China (22007090) and Shenzhen High-tech Zone Development Special Plan Pingshan District Innovation Platform Construction Project (29853MKCJ202300208), Natural Science Foundation of Ningbo (2019A610190), the Basic Public Welfare Research Program of Zhejiang Province (LGF21H180012).

Conflict of Interests

The authors do not report any conflicts of interest in this work.

Supplementary Data

CCDC 2348536 contains the additional crystallographic data for compound E4. These data are available free of charge at <http://www.ccdc.cam.ac.uk/contents/retrieving.html>, or from the Cambridge Crystallographic Data Center, 12 Union Road, Cambridge CB2 1EZ, UK; fax: (+44) 1223-336-033; or e-mail: deposit@ccdc.cam.ac.uk. The spectral data of the compounds can be found in the supporting information file.

5. References

1. D. C. C. Carla, C. M. Jose, *Molecules*. **2018**, *23*, 2583. DOI:10.3390/molecules23102583
2. A. N. Günenc, B. Graf, H. Stark, A. Chari. *Subcell Biochem.* **2022**, *99*, 1–33. DOI:10.1007/978-3-031-00793-4_1
3. C. Wu, B. Hong, S. S. Jiang, X. Luo, H. Lin, Y. Zhou, J. R. Wu, X. Q. Yue, H. S. Shi, R. N. Wu, *Biochem. Eng. J.* **2022**, *178*, 108306. DOI:10.1016/j.bej.2021.108306
4. J. W. Yao, C. O. Rock, *Biochim. Biophys. Acta BBA - Mol. Cell Biol. Lipids*. **2017**, *1862*, 1300–1309. DOI:10.1016/j.bbalip.2016.09.014
5. M. F. Currie, D. M. Persaud, N. K. Rana, A. J. Platt, J. Beld, K. L. Jaremko, *Sci. Rep.* **2020**, *10*, 17776. DOI:10.1038/s41598-020-74731-4
6. F. Asturias, J. Chadick, I. Cheung, H. Stark, A. Witkowski, A. Joshi, S. Smith. *Nat. Struct. Mol. Biol.* **2005**, *12*, 225–232. DOI:10.1038/nsmb899
7. O. S. Ostroumova, S. S. Efimova, *Antibiotics*. **2023**, *12*, 1716. DOI:10.3390/antibiotics12121716
8. N. Risa, P. Benjamin, N. Yosi, M. Taifo, *MedChemComm.* **2019**, *10*, 1517–1530. DOI:10.1039/C9MD00162J
9. X. Y. Lu, J. Tang, Z. Zhang, K. Ding, *Curr. Med. Chem.* **2015**, *22*, 651–667. DOI:10.2174/0929867322666141212115236
10. C. Davies, R. J. Heath, S. W. White, C. O. Rock, *Struct.* **2000**, *8*, 185–195. DOI:10.1016/S0969-2126(00)00094-0
11. X. Y. Qiu, A. E. Choudhry, C. A. Janson, M. Grooms, R. A. Daines, J. T. Lonsdale, S. S. Khandekar, *Protein Sci. Publ. Protein Soc.* **2005**, *14*, 2087–2094. DOI:10.1110/ps.051501605
12. W. C. Lee, M. C. Jeong, Y. Lee, C. Kwak, J. Y. Lee, Y. Kim, *Mol. Microbiol.* **2018**, *108*, 567–577. DOI:10.1111/mmi.13950
13. Y. Zhou, Q. R. Du, J. Sun, J. R. Li, F. Fang, D. D. Li, Y. Qian, H. B. Gong, J. Zhao, H. L. Zhu, *ChemMedChem.* **2013**, *8*, 433–441. DOI:10.1002/cmdc.201200587
14. Y. Zhou, Y. Luo, Y. S. Yang, L. Lu, H. L. Zhu, *MedChemComm.* **2016**, *7*, 1980–1987. DOI:10.1039/C6MD00263C
15. Y. Zhou, Y. S. Yang, X. D. Song, L. Lu, H. L. Zhu, *Chem. Pharm. Bull.* **2017**, *65*, 178–185. DOI:10.1248/cpb.c16-00772
16. H. Y. Chang, R. Y. Ji, Z. Y. Zhu, Y. P. Wang, S. P. Yan, D. He, Q. K. Jia, P. Huang, T. Cheng, R. Wang, Y. Zhou, *Eur. J. Med. Chem.* **2024**, *265*, 116064. DOI:10.1016/j.ejmech.2023.116064
17. Y. Gao, J. Yang, X. L. Yang, L. Zhang, J. Wang, Q. Li, D. M. Lin, M. Zhang, S. N. Xia, L. L. Xu, Q. Zhang, P. Hai, Y. H. Liu, S. Wang, L. P. Guo, *Fitoterapia.* **2021**, *152*, 104914. DOI:10.1016/j.fitote.2021.104914
18. C. G. Song, X. Wang, J. Yang, Y. Kuang, Y. X. Wang, S. X. Yang, J. C. Qin, L. P. Guo, *Chem. Biodivers.* **2021**, *18*, e2100079. DOI:10.1002/cbdv.202100079
19. X. Wang, H. Y. Fu, W. He, Y. T. Xiang, Z. C. Yang, Y. Kuang, S. X. Yang, *Curr. Issues Mol. Biol.* **2022**, *44*, 4087–4099. DOI:10.3390/cimb44090280
20. A. J. Tague, P. Putsathit, T. V. Riley, P. A. Keller, S. G. Pyne, *ACS Med. Chem. Lett.* **2021**, *12*, 413–419. DOI:10.1021/acsmmedchemlett.0c00611
21. S. Y. Ke, Z. L. Gao, Z. G. Zhang, F. Liu, S. H. Wen, Y. Y. Wang, D. Y. Huang, *J. Agric. Food Chem.* **2023**, *71*, 14505–14516. DOI:10.1021/acs.jafc.3c04307
22. A. Marta, R. Laura B, V. Albert, H. Sonia, A. Lidia, M. Mar, V. Henar, T. Carlos, R. Erney, H. Annabelle, N. Matthew, B. Isabel, C. Pablo, S. Steven A, A. Jose M, L. Maria L, *ACS Chem. Biol.* **2015**, *10*, 834–843. DOI:10.1021/cb500974d
23. Y. Guo, E. H. Hou, T. Y. Wen, X. T. Yan, M. Y. Han, L. P. Bai, X. G. Fu, J. F. Liu, S. S. Qin, *J. Med. Chem.* **2021**, *64*, 12903–12916. DOI:10.1021/acs.jmedchem.1c01073
24. X. N. Chen, W. Q. Lan, J. Xie, *Food Chem.* **2024**, *440*, 138198. DOI:10.1016/j.foodchem.2023.138198
25. Z. J. Jain, P. S. Gide, R. S. Kankate, *Arab. J. Chem.* **2017**, *10*, S2051–S2066. DOI:10.1016/j.arabjc.2013.07.035

26. H. Ibrar, C. Jawoeski, Y. Mirza A, *Adv. Synth. Catal.* **2016**, 358, 3320–3349. DOI:10.1002/adsc.201600354
27. Z. F. Han, J. S. Pinkner, B. Ford, R. Obermann, W. Nolan, S. A. Wildman, D. Hobbs, T. Ellenberger, C. K. Cusumano, S. J. Hultgren, J. W. Janetka, *J Med. Chem.* **2010**, 53, 4779–4792. DOI:10.1021/jm100438s

Povzetek

Biosinteza maščobnih kislin je pomembna presnovna pot v bakterijskih organizmih. Avtorji so v prejšnjih študijah že raziskovali protimikrobne spojine, zasidrane v ogrodju benzodioksepina, ki je znan po svojih izrazitih antibakterijskih lastnostih. Na podlagi teh znanj so avtorji zasnovali in sintetizirali serijo osmih inovativnih benzodioksepin-bifenil amidnih derivatov z optimizacijo sinteznih metod. Študija med drugim zajema tudi natančno oceno antibakterijskih lastnosti in biokompatibilnosti novih spojin. Predvsem spojina **E4** se je izkazala kot izjemno učinkovito protimikrobno sredstvo. Poleg podrobne analize kristalne strukture spojine **E4** je bila izvedena tudi temeljita študija sidranja, z namenom raziskati interakcije te spojine z encimom FabH.



Except when otherwise noted, articles in this journal are published under the terms and conditions of the Creative Commons Attribution 4.0 International License

Scientific paper

Extraction System for the Spectrophotometric Determination of Tungsten(VI) with 4-Nitrocatechol and Benzalkonium Chloride

Vidka V. Divarova,¹ Kirila T. Stojnova,² Ivelina D. Radkovska,¹ Antoaneta D. Saravanska,¹ Galya K. Toncheva,² Vassil B. Delchev³ and Kiril B. Gavazov^{1,*}

¹ Department of Chemical Sciences, Faculty of Pharmacy, Medical University of Plovdiv, 120 Buxton Bros Str., 4004 Plovdiv

² Department of General and Inorganic Chemistry with Methodology of Chemistry Education, Faculty of Chemistry, Plovdiv University "Paisii Hilendarski", 24 Tsar Assen Street, Plovdiv 4000, Bulgaria

³ Department of Physical Chemistry, Faculty of Chemistry, Plovdiv University "Paisii Hilendarski", 24 Tsar Assen Street, Plovdiv 4000, Bulgaria

* Corresponding author: E-mail: kiril.gavazov@mu-plovdiv.bg

Received: 06-03-2024

Abstract

A novel chromogenic system for the liquid-liquid extraction and determination of trace amounts of tungsten(VI) was investigated. The system comprises 4-nitrocatechol (4NC) as a chromogenic reagent, sulfuric acid as a complexing medium, and benzalkonium chloride (BAC) as a source of bulky cations (BA⁺), which readily form chloroform-extractable ion-association complexes. The impact of foreign ions and reagents was studied, and the optimal conditions for the sensitive, selective, and inexpensive determination of tungsten(VI) were identified. The limit of detection, linear working range, and molar absorptivity at λ_{\max} (422 nm) were determined to be 31 ng cm⁻³, 0.1–4.4 μ g cm⁻³, and 5.49×10^4 dm³ mol⁻¹ cm⁻¹, respectively. The composition of the extracted complex was 1:2:2 (W:4NC:BA). Two potential structures of its anionic component, [WO₂(4NC)₂]²⁻, were discussed based on optimizations at the B3LYP/CEP-4G theoretical level and comparison between theoretical and experimental spectra.

Keywords: Tungsten; liquid-liquid extraction; spectrophotometric determination; 4-nitrobenzene-1,2-diol; benzalkonium chloride; TD DFT calculations

1. Introduction

Tungsten is a third-row transition metal in Group 6 of the Periodic Table. It is distinguished by a number of unique properties, including the highest melting point of all metals, high hardness, high density, excellent corrosion resistance, low coefficient of thermal expansion, high thermal shock resistance, and good electrical conductivity. These properties render it a valuable component in modern technology and necessitate its inclusion in a wide variety of end products, including steels, superalloys, tungsten carbide tools, filament wires, armor-piercing projectiles and darts, nuclear shields, heavy electrical contact points, X-ray tubes, plasma-facing materials, welding rods, glass-to-metal seals, jewelry, pigments, catalysts, chemicals, and many others.^{1,2}

Tungsten is a rare element in the Earth's crust, occurring in 53 minerals.³ It is the heaviest element ($A_r = 183.84$)

with a known biological role.⁴ Unlike molybdenum, its closest analogue in the periodic table, which is essential for most organisms, tungsten is primarily used by bacteria and archaea. These organisms have developed specialized enzymes that utilize tungsten instead of molybdenum.^{5,6}

Tungsten is present in small amounts in food, water, and the atmosphere, but its potential to spread into the environment is increasing rapidly.⁴ Humans can be exposed to tungsten through inhalation, ingestion, dermal contact, and ocular contact. The recommended exposure limits established by the National Institute for Occupational Safety and Health are 5 mg m⁻³ for insoluble tungsten and 1 mg m⁻³ for soluble tungsten per 8-hour workday.⁷

The determination of tungsten, especially in trace amounts, is more challenging than that of other metals.^{8–10} There are problems associated with both the dissolution of

samples and the direct analysis of solids. Commonly employed techniques, such as atomic absorption spectrometry, inductively coupled plasma mass spectrometry, and inductively coupled plasma optical emission spectrometry, face limitations due to matrix effects and difficulties in results interpretation, alongside issues of low sensitivity and high operational costs. Consequently, spectrophotometric methods have become the preferred approach, as evidenced by the extensive literature on the subject.^{11–35} These methods are cost-effective and accessible to a wide range of laboratories. By selecting appropriate reagents and optimizing operational parameters, they can achieve sufficient sensitivity, selectivity, and efficiency, particularly when coupled with separation and preconcentration techniques.

The objective of this study was to examine a novel liquid-liquid extraction (LLE) system for the determination of W(VI), based on the complexation reaction of W(VI) with 4-nitrobenzene-1,2-diol (4-nitrocatechol, 4NC)^{36,37} in the presence of benzalkonium chloride (BAC). The system has been designed to overcome the primary limitations associated with this widely utilized and adaptable classical technique, namely the formation of stable emulsions, incomplete extraction, poor selectivity, long extraction time, and high organic solvent consumption.^{32,38}

4NC is a well-known compound^{37,39} that is included in the IUPAC list of the most important analytical reagents for spectrophotometric analysis.⁴⁰ It is classified as a non-hazardous substance according to Regulation (EC) No 1272/2008.⁴¹ BAC is a commercially available, cost-effective mixture of alkylbenzyltrimethylammonium chlorides with an average molecular weight of 360.^{42,43} It has been utilized in our laboratory as an ion-association reagent for LLE of molybdenum⁴⁴ and cobalt.⁴⁵ Initial studies have indicated that BAC is capable of forming a neutral, poorly water-soluble ternary complex with the anionic W(VI)–4NC species,^{36–37} which can be easily extracted from acidic media (pH *ca.* 1.0–1.2) in a small volume of chloroform.

2. Experimental Section

2.1. Chemicals and Instruments

The following chemicals were purchased and used as aqueous solutions: Na₂WO₄·2H₂O (ACS reagent, ≥99%, Merck, Schnelldorf, Germany), 4NC (>98%, Fluka AG, Buchs, Switzerland), BAC (>95.0%, Merck, Schnelldorf,

Germany), disodium ethylenediaminetetraacetate dihydrate, Na₂EDTA·2H₂O (ACS reagent, 99.0–101.0%, Merck, Schnelldorf, Germany), and sulfuric acid. Their solutions were prepared at concentrations of 2×10^{-4} mol dm⁻³ (W), 7.5×10^{-3} mol dm⁻³ (4NC), 2.5×10^{-3} mol dm⁻³ (BAC), 1.0×10^{-1} mol dm⁻³ (Na₂EDTA), and 2.5 mol dm⁻³ (H₂SO₄). Distilled water was used in the experiments. Chloroform (puriss. p.a., Honeywell, Riedel-de Haën) was repeatedly utilized following the process of redistillation.

Absorbance was measured on an Ultrospec 3300 pro UV/Vis spectrophotometer (Little Chalfont, UK) equipped with 10 mm quartz semi-micro cuvettes of 0.7 cm³ volume. The pH was checked with a WTW InoLab 720 pH meter (Weilheim, Germany). Chloroform was added to the separating funnels via a 1–5 cm³ bottle-top dispenser (Ceramus Classic, Hirschmann, Germany).

2.2. Optimization Procedure

The solutions of W(VI), H₂SO₄, 4NC, and BAC were combined in a separatory funnel, and the total volume was adjusted to 10 cm³ with water. Then, 3 cm³ of chloroform was added, and the mixture was shaken for a fixed period of time. A portion of the organic layer was poured into the cuvette, and the absorbance was measured against a similarly prepared blank.

2.3. Calculation of the Distribution Ratio

The distribution ratio (*D*) at the optimal conditions (Table 1) was calculated from Equation 1 using the absorbances obtained after single extraction (*A*₁) and triple extraction (*A*₃)^{44,46,47} at equal conditions. The final volume in both cases was 10 cm³, and the initial W(VI) concentration in the aqueous phase was 1.0×10^{-5} mol dm⁻³.

$$D = A_1 / (A_3 - A_1) \quad (1)$$

2.4. Recommended Procedure for the Determination of Tungsten(VI)

An aliquot of the analyzed solution, containing 1–44 µg W(VI), was placed in a 100 cm³ separatory funnel. The pH was adjusted to a range of 1.0–1.2 with 2.5 mol dm⁻³ H₂SO₄. If the analyzed solution was neutral, the requisite volume of acid was 0.6 cm³. Subsequently, 0.4 cm³ of a $7.5 \times$

Table 1. LLE-spectrophotometric optimization.^a

Parameter	Optimization range	Recommended value
Wavelength, nm	UV/Vis	422
Concentration of H ₂ SO ₄ , mol dm ⁻³	$(0.063\text{--}5.0) \times 10^{-1}$	1.5×10^{-1}
Concentration of 4NC, mol dm ⁻³	$(0.188\text{--}7.5) \times 10^{-4}$	3.0×10^{-4}
Concentration of BAC, mol dm ⁻³	$(0.125\text{--}3.0) \times 10^{-4}$	2.0×10^{-4}
Extraction time, sec	5–300	90

^a The volume of the aqueous phase was 10 cm³ and that of the chloroform was 3 cm³.

$10^{-3} \text{ mol dm}^{-3}$ 4NC solution and 0.8 cm^3 of a $2.5 \times 10^{-3} \text{ mol dm}^{-3}$ BAC solution were added. If necessary, a masking agent (1.6 cm^3 of a 0.1 mol dm^{-3} Na_2EDTA solution) was added prior to adjusting the volume of the aqueous phase to 10 cm^3 . Finally, 3 cm^3 of chloroform was dispensed and the mixture was shaken for 1.5 minutes. Following the separation of the phases, a portion of the chloroform extract was poured into the cuvette and the absorbance was measured at 422 nm against a blank. The concentration of W(VI) was calculated from a calibration plot.

2. 5. Procedure for Dissolving Steel

The steel was dissolved using a methodology that involved treatment with acids (sulfuric and nitric) followed by treatment with NaOH to dissolve the poorly soluble tungsten compounds.^{12,16,19,21,30,34} No separation of the matrix was necessary as the selectivity was sufficient, especially in the presence of Na_2EDTA as a masking agent.

A sample of the investigated steel (*ca.* 0.1 g) was treated with 20 cm^3 H_2SO_4 (1:4). Subsequently, approximately 2.5 cm^3 of concentrated HNO_3 was added dropwise. The excess HNO_3 was removed by heating the solution on a sand bath until white SO_3 vapor appeared. After cooling, the solution was alkalinized with 30 % NaOH until a stable residue was obtained. After a waiting period of 15–20 minutes, sulfuric acid (1:10) was added until the precipitate dissolved.^{12,16} The solution was then transferred to a 250 cm^3 volumetric flask and made up to the mark with water.

3. Theoretical Section

The ground-state equilibrium geometries of two possible structures of the anionic component, $[\text{WO}_2(4\text{NC})_2]^{2-}$, of the obtained complex were optimized at the B3LYP/CEP-4G theoretical level in the gas phase, with no symmetry or structural restrictions. The spin multiplicity and charge were set to 1 and -2 , respectively. Subsequent frequency calculations were performed to demonstrate that the optimized structures possess no imaginary frequencies, thereby confirming their stability as minima. Additionally, vertical excitation energies were computed to simulate their UV/Vis spectra. The calculations were performed using the GAUSSIAN 03 software. The ChemCraft program, v. 1.8 was employed for the visualization of the two structures.

4. Results and Discussion

4. 1. LLE-Spectrophotometric Optimization

A single-factor optimization was conducted at room temperature (approximately 22°C) to identify the optimal values for the following experimental parameters: sulfuric acid concentration (Fig. 1), 4NC concentration (Fig. 2,

series 1), BAC concentration (Fig. 2, series 2), and extraction time (Fig. 3). The absorption maximum (λ_{max}) was observed at 422 nm, a wavelength at which the absorbance of the blank was close to zero (Fig. 4). All subsequent LLE-spectrophotometric studies were conducted under the optimal conditions shown in Table 1.

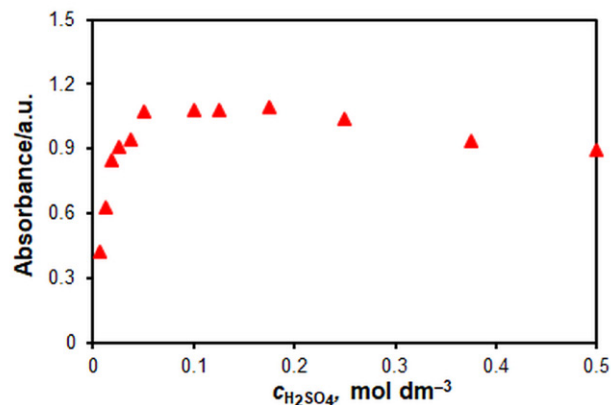


Figure 1. Effect of H_2SO_4 concentration: $c_W = 2 \times 10^{-5} \text{ mol dm}^{-3}$, $c_{4\text{NC}} = 7.5 \times 10^{-4} \text{ mol dm}^{-3}$, $c_{\text{BAC}} = 2.5 \times 10^{-4} \text{ mol dm}^{-3}$, $t_{\text{ex}} = 1.5 \text{ min}$, $\lambda = 422 \text{ nm}$.

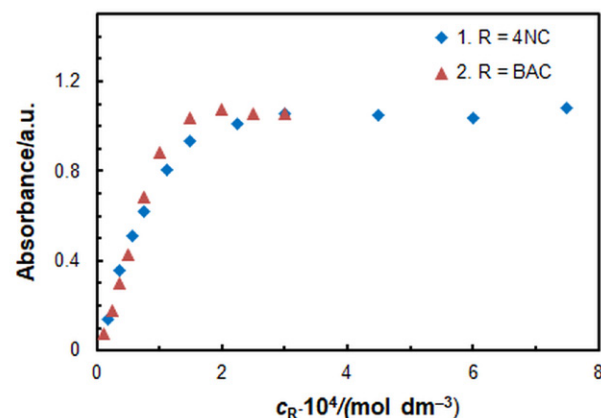


Figure 2. Effect of 4NC (1) and BAC (2) concentration: $c_W = 2 \times 10^{-5} \text{ mol dm}^{-3}$, $c_{\text{H}_2\text{SO}_4} = 1.5 \times 10^{-1} \text{ mol dm}^{-3}$, $t_{\text{ex}} = 1.5 \text{ min}$, $\lambda = 422 \text{ nm}$. 1: $c_{\text{BAC}} = 10^{-4} \text{ mol dm}^{-3}$; 2: $c_{4\text{NC}} = 3 \times 10^{-4} \text{ mol dm}^{-3}$.

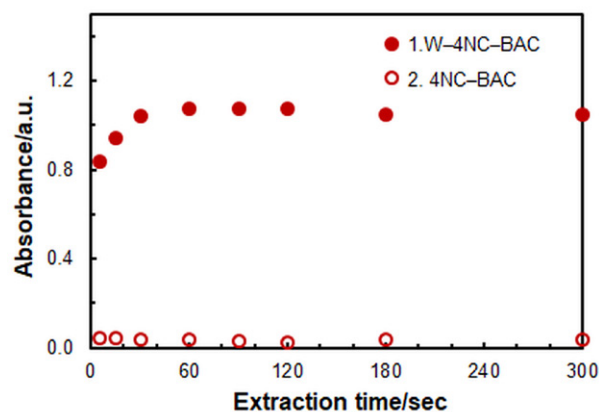


Figure 3. Effect of the extraction time: $c_W = 2 \times 10^{-5} \text{ mol dm}^{-3}$, $c_{4\text{NC}} = 3 \times 10^{-4} \text{ mol dm}^{-3}$, $c_{\text{BAC}} = 2 \times 10^{-4} \text{ mol dm}^{-3}$, $c_{\text{H}_2\text{SO}_4} = 1.5 \times 10^{-1} \text{ mol dm}^{-3}$, $\lambda = 422 \text{ nm}$.

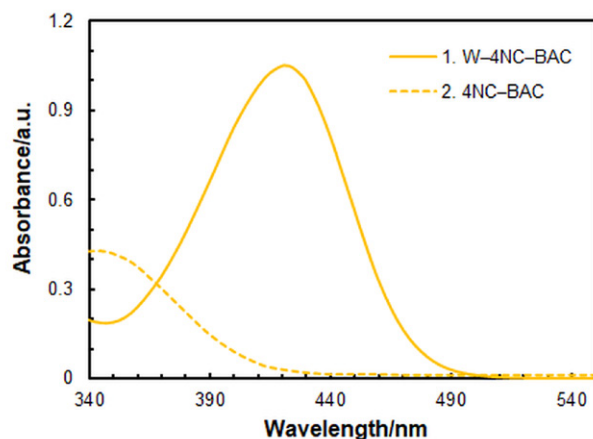
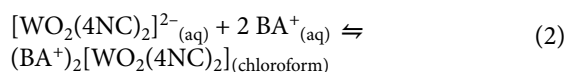


Figure 4. Absorption spectra of the ternary complex (1) and blank (2): $c_W = 2 \times 10^{-5} \text{ mol dm}^{-3}$, $c_{4NC} = 3 \times 10^{-4} \text{ mol dm}^{-3}$, $c_{BAC} = 2 \times 10^{-4} \text{ mol dm}^{-3}$, $c_{H_2SO_4} = 1.5 \times 10^{-1} \text{ mol dm}^{-3}$, $t_{ex} = 1.5 \text{ min}$.

4. 2. Composition, Formula and Chemical Equation

Two methods were employed to ascertain the molar ratios in the extracted ternary complex. These were the mobile equilibrium method⁴⁸ (Figure 5) and the straight-line method of Asmus⁴⁹ (Figure 6 a and b). The results are consistent with the conclusion that the complex has a composition of 1:2:2 (W:4NC:BAC). This composition is identical to that reported for complexes containing tetrazolium cations instead of benzalkonium cations (BA^+).¹⁶ Consequently, the anionic part of the complex can be represented by the formula $[WO_2(4NC)_2]^{2-}$.^{16,36} Its association with BA^+ and the subsequent chloroform extraction can be represented by Equation 2.



It is noteworthy that the behavior of Mo(VI) in such a system differs from that of W(VI), despite the widely recognized similarities in the chemistry of both elements^{5,36,50,51}. In fact, under analogous conditions, Mo(VI) is extracted as a 1:1:2-complex (Mo:4NC:BAC), whose established formula is $(BA^+)_2[MoO_2(OH)_2(4NC)]$.⁴⁴

4. 3. Distribution Ratio and Extraction Constant

Table 2 presents data for the distribution ratio (D) and the extraction constant (K_{ex}) characterizing Equation 2. Several methods based on the BAC saturation curve (Figure 2) were employed to ascertain this constant. These included the Harvey-Manning method,⁵² the Holme-Lanhmyhr method,⁵³ and the mobile equilibrium method.⁴⁸ The statistical identity of the values obtained indicates the absence of significant side processes. It is evident that the complex is suitable for analytical applications.

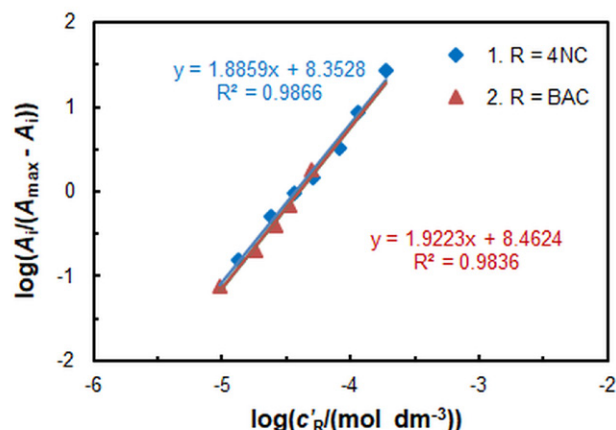


Figure 5. Determination of the 4NC : W (1) and BAC : W (2) molar ratios by the mobile equilibrium method. The resulting straight lines are based on the experimental points in Figure 2.

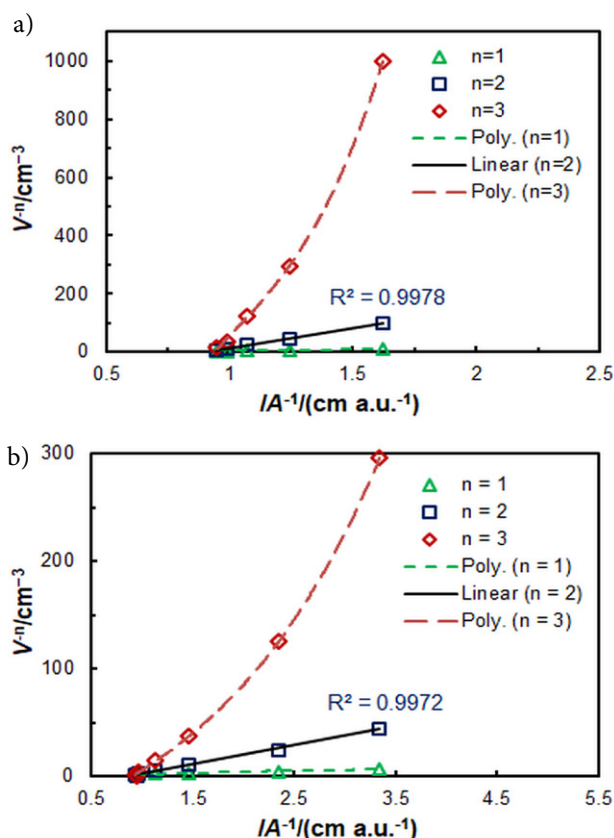


Figure 6. Determination of the 4NC : W (a) and BAC : W (b) molar ratios by the method of Asmus

Table 2. Extraction characteristics.

Characteristic	Value
Distribution ratio ($\log D$)	1.03 ± 0.15 ($n = 4$)
Extraction constant ($\log K_{ex}$)	8.76 ± 0.05^a ; 8.88 ± 0.14^b ; 8.80 ± 0.70^c

^a Harvey-Manning method; ^b Holme-Lanhmyhr method; ^c Mobile equilibrium method

4. 4. Ground-State Equilibrium Geometries and Spectral Comparison

It is postulated that the anionic component of the ternary complex is responsible for the spectral bands in the visible region. This is based on the fact that the benzalkonium ion (BA^+) is colorless and the complex is of the type of ionic associates.^{44,45,54} To verify this assumption, the anion $[\text{WO}_2(4\text{NC})_2]^{2-}$ was modeled using time-dependent density functional theory (TD DFT) calculations. Two isomers differing in the mutual arrangement of the NO_2 groups are theoretically possible.⁵⁵ Figure 7 illustrates their optimized ground state equilibrium geometries. The two structures, denoted as Str. 1 and Str. 2, possess octahedral symmetry, and differ slightly in bond lengths and valence angles. The aforementioned structures were employed to calculate vertical excitation energies with the time-dependent Hamiltonian, in order to simulate their theoretical absorption spectra.

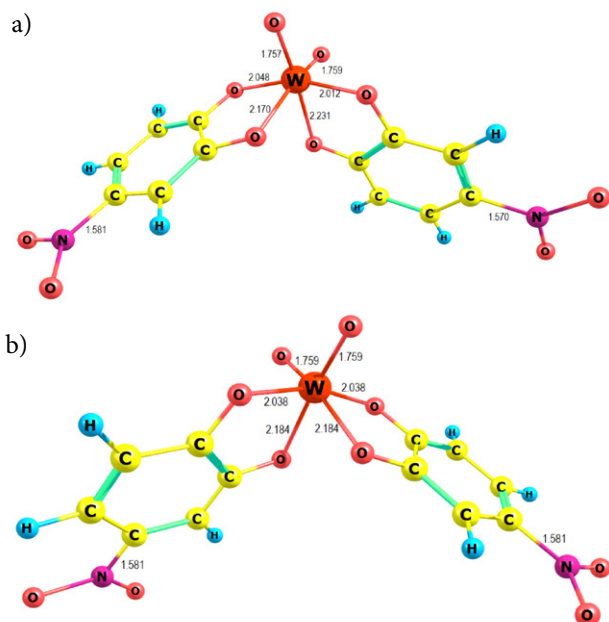


Figure 7. Optimized ground-state equilibrium geometries of the two $[\text{WO}_2(4\text{NC})_2]^{2-}$ isomers (a – Str. 1; b – Str. 2) found at the B3LYP/CEP-4G level

Figure 8 depicts the experimental spectrum of the ternary complex and the theoretical spectra of the two isomers at a scaling factor of 1. It can be concluded that the theoretical spectrum of Str. 1 is closer to the experimental spectrum. However, the presence of Str. 2 in the extract cannot be excluded. It seems that the presence of both structures would be very probable in case their energies are close.

4. 5. Energy Analysis

The frequency calculations demonstrated that the two structures in Figure 7 are real minima. Their energy

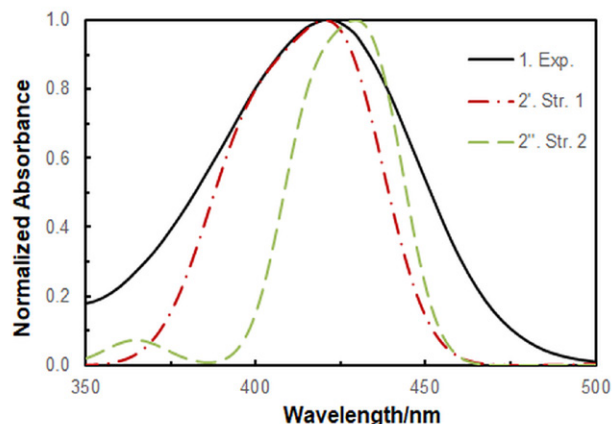


Figure 8. Comparison of the experimental spectrum (Exp.) with the two theoretical spectra (Str. 1 and Str. 2) found at the B3LYP/CEP-4G level and a scaling factor of 1

components are presented in Table 3. The Δ values were calculated as the difference between the energy components of Str. 1 and Str. 2, respectively. As can be observed, Str. 1 is slightly more stable than Str. 2. The transformation Str. 1 \rightarrow Str. 2 is an endothermic reaction accompanied by an increase in the Gibbs free energy. The transformation is also accompanied by an insignificant entropy change ($0.4 \text{ J mol}^{-1} \text{ K}^{-1}$).

Table 3. Energy Analysis.

Energy component, a. u.	Str. 1, a. u.	Str. 2, a. u.	Δ , kJ mol^{-1}
Electron energy, E	–317.379176	–317.374731	11.7
E_0^a	–317.208893	–317.204624	11.2
H^b	–317.183715	–317.179417	11.3
G^c	–317.265041	–317.260915	10.8

^a Sum of electronic and zero-point energies; ^b sum of electronic and thermal enthalpies; ^c sum of electronic and thermal free energies

4. 6. Impact of Foreign Ions and Masking Agents

The impact of foreign ions and masking agents is presented in Table 4. It is evident that large amounts of many ions do not affect the absorption of the resulting extract. The presence of at least a 5000-fold excess of Na_2EDTA , which is known as an excellent masking agent, is tolerable. If necessary, this agent can additionally raise the limiting tolerance ratios for some of the ions known to form complexes with 4NC.³⁷ Unfortunately, Na_2EDTA was unable to cope with interferences caused by Mo(VI) and Cr(VI) . Further studies demonstrated that the Cr(VI) interference problem can be readily solved through the use of ascorbic acid.

Table 4. Impact of foreign ions on the determination of 12 µg W(VI)

Foreign ion (FI)	Formula of the added salt	Amount of FI added/mg	FI : W(VI) mass ratio	Amount of W found/µg	E%
Acetate	CH ₃ COONa·3H ₂ O	12.0	1000 ^a	12.3	102
Al(III)	Al ₂ (SO ₄) ₃ ·18H ₂ O	12.0	1000 ^a	12.4	103
Br [−]	NaBr	0.12	10	12.0	100
Ca(II)	CaSO ₄ ·2H ₂ O	3.6	300 ^a	11.6	96.4
Cd(II)	CdSO ₄ ·8/3H ₂ O	9.0	750	12.1	101
Citrate	Na ₃ C ₆ H ₅ O ₇	0.6	50	11.5	96.2
Cl [−]	NaCl	0.9	75	12.0	99.7
Co(II)	CoSO ₄ ·7H ₂ O	0.6	50	12.4	103
Cr(III)	Cr ₂ (SO ₄) ₃	1.2	100	12.0	99.7
Cr(VI)	K ₂ CrO ₄	0.006	0.5	12.4	104
		0.24 ^b	20 ^b	12.2 ^b	101 ^b
Cu(II)	CuSO ₄ ·5H ₂ O	12.0	1000 ^a	11.6	97.1
EDTA ^{2−}	Na ₂ EDTA·2H ₂ O	60.0	5000 ^a	11.8	98.7
F [−]	NaF	0.6	50	11.7	97.6
Fe(II)	(NH ₄) ₂ Fe(SO ₄) ₂ ·6H ₂ O	0.24	20	11.9	99.2
Fe(III)	Fe ₂ (SO ₄) ₃	4.8	400	11.9	99.2
H ₂ PO ₄ [−]	KH ₂ PO ₄	12.0	1000 ^a	11.6	96.3
K ⁺	K ₂ SO ₄	12.0	1000 ^a	12.1	101
Li ⁺	Li ₂ SO ₄ ·H ₂ O	12.0	1000 ^a	12.5	104
Mg(II)	MgSO ₄ ·7H ₂ O	12.0	1000 ^a	12.1	101
Mn(II)	MnSO ₄ ·H ₂ O	0.6	50	11.9	99.0
Mo(VI)	(NH ₄) ₆ Mo ₇ O ₂₄ ·4H ₂ O	0.006	0.5	21	175
Ni(II)	NiSO ₄ ·7H ₂ O	12.0	1000 ^a	12.1	101
NO ₃ [−]	NaNO ₃	0.18	10	12.4	103
		6.0	500	1.03	8.6
Pb	Pb(CH ₃ COO) ₂ ·3H ₂ O	6.0	500 ^a	12.1	101
Re(VII)	NH ₄ ReO ₄	0.12	10	12.5	104
Tartrate	K ₂ NaC ₄ H ₄ O ₆	0.6	50	11.8	98.3
V(V)	NH ₄ VO ₃	0.024	2	12.1;	101
		0.36 ^b	30 ^b	12.1 ^b	101 ^b
		0.6 ^c	50 ^c	11.4 ^c	95.0 ^c
Zn(II)	ZnSO ₄ ·7H ₂ O	2.4	200	12.2	102

^a Higher FI-to-W(VI) ratios were not studied; ^b in the presence of 0.33 cm³ 0.2 mol dm^{−3} ascorbic acid; ^c in the presence of 1.6 cm³ 0.1 mol dm^{−3} Na₂EDTA

4. 7. Analytical Characteristics and Application

The relationship between absorbance and W(VI) concentration was linear up to 4.4 µg cm^{−3} W(VI) ($R^2 = 0.9999$, $n = 8$). The linear regression equation was $A = 0.2986\gamma + 0.0002$, where γ is the concentration in µg cm^{−3}. The standard deviation of the slope was 0.0013, while that of the intercept was 0.0031. Consequently, the intercept is statistically indistinguishable from zero. The molar absorption coefficient was 5.49×10^4 dm³ mol^{−1} cm^{−1}, and the Sandall's sensitivity was 3.35×10^{-3} µg cm^{−2}. The limit of detection (LOD) and limit of quantification (LOQ) were calculated in two ways: 1) as three and ten times the standard deviation of the blank divided by the slope; and 2) as three and ten times the standard deviation of the ordinate intercept divided by the slope. The results were virtually identical: LOD = 31 ng cm^{−3}, and LOQ = 104 ng cm^{−3}.

The proposed analytical procedure was then applied to the analysis of a reference standard steel (RSS) and sev-

eral artificial mixtures (AMs) that mimicked typical tungsten-containing alloys.¹ The results are presented in Table 5. The relative standard deviation (RSD) for these determinations was in the range of 0.94–2.25%.

It is important to note that the NaOH treatment in the RSS sample preparation stage (see above) was a critical step in obtaining reliable results. Failure to include this step may result in incomplete decomposition of the insoluble tungsten species. This is consistent with the data presented in Refs.^{9,56}

4. 8. Comparison with Other Methods Involving LLE

A comparison of the present method with other published methods for tungsten determination involving LLE is presented in Table 6. The present method exhibits excellent linearity and relatively high sensitivity. It is robust and reliable due to the wide optimum ranges of the parameters

Table 5. Determination of tungsten in a referent standard steel (RSS) and artificial mixtures (AM)

		Sample		Present method	
Description		W content/%	Other metal components/%	Tungsten found ^a /%	RSD/%
RSS	Referent standard steel ^b	1.57	17.55 (Cr), 9.61 (Ni), 1.04 (V), 0.99 (Nb), 0.13 (Ta), and the balance Fe	1.58	0.94
AM-1	chromium-tungsten shock resistant steel	2.00	1.0 (Cr), and the balance Fe	2.02	1.13
AM-2	9 % tungsten hot die steel	9.00	2.5 (Cr) and the balance Fe	8.89	1.57
AM-3	Stellite	10.0	25 (Cr), 2 (Ni), 0.5 (Mn), 0.1 (Mo), and the balance Co	10.2	2.25
AM-4	18 % tungsten general purpose high-speed cutting steel	18.0	4.5 (Cr), 1.25 (V), and the balance Fe	18.2	1.81
AM-5	12% cobalt super high-speed steel	21.0	12.0 (Co), 4.5 (Cr), 1.25 (V), and the balance Fe	21.3	1.97
AM-6	Tungsten-bearing super-alloys	50.0	50.0 (Cu)	49.2	1.83

^a Average of four replicate determinations; ^b Supplied by the Holding KCM 2000, Plovdiv, Bulgaria**Table 6.** Comparison with other LLE procedures for tungsten determination

Technique	Reagent(s)	Extraction solvent (ES)	Volume of ES/cm ³	Acidity	Working range/ $\mu\text{g cm}^{-3}$	λ , nm	$10^{-4}\epsilon/\text{dm}^3 \text{mol}^{-1} \text{cm}^{-1}$	Sample	Ref. (Year)
UV/Vis	EPH + NH ₄ SCN	Chloroform	10	4 mol dm ⁻³ HCl	1–15	404	1.74	Steel	¹³ (2002)
UV/Vis	HTB	Dichloromethane	10	0.2 mol dm ⁻³ HCl	0.44–2.8	415	6.45	Synthetic samples and reverberatory flue dust	¹⁴ (2004)
UV/Vis	4NC + MTT	Chloroform	10	pH 1.2–3.6	0.92–8.8	415	2.8	Steel and ferrotungsten	¹⁶ (2006)
UV/Vis	CHTB	Chloroform	10	0.16–0.32 mol dm ⁻³ HCl	0.5–3.0	420	4.05	Synthetic, technical, and natural samples	¹⁷ (2008)
UV/Vis	M2B	Toluene	5	pH 3	0.2–1.8	591	7.1	Steel	¹⁸ (2009)
UV/Vis	HCTP + HA	Chloroform	5	pH 4.2–5.4	0.5–16	465–475	2.4–2.6	Steel	¹⁹ (2013)
UV/Vis	CHPB	Chloroform	10	0.04–0.32 mol dm ⁻³ HCl	0.9–2.9	420	3.125	Synthetic and standard samples	²⁰ (2013)
UV/Vis	HCTP + DPG	Chloroform	5	pH 5–6	0.2–20	480	5.6	Steel, soil, and pea	^{22, 23} (2015, 2016)
UV/Vis	HTPD + HA	Chloroform	5	pH 3.5–5.5	0.04–3.8	461–490	2.0–2.8	Steel and soil	²⁴ (2016)
UV/Vis	DTMP + HA	Chloroform	5	pH 3.9–5.2	0.4–16	476–480	2.73–2.92	Steel, soil, and plant	²⁶ (2017)
UV/Vis	HPMPPB	Chloroform	10	0.1 mol dm ⁻³ HCl	0.36–2.0	420	9.936	Synthetic and industrial samples	²⁹ (2019)
UV/Vis	HBTP + HA	Chloroform	5	pH 4.1–5.6	0.2–16	470–482	2.6–3.9	Steel	³⁰ (2019)
UV/Vis	HMTB	Dichloromethane	10	0.1 mol dm ⁻³ HCl	0.35–1.5	418	8.28	Synthetic and technical samples	³¹ (2019)
AAS	HBPNA	n-Butanol	10	pH 2–3	1–10	255.1	3.4–4.2	Steel	⁵⁷ (2022)
UV/Vis	HTPD + HA	Chloroform	5	pH 4.5–5.5	0.04–3.8	490	2.0–2.8	Steel and soil	³³ (2022)
UV/Vis	DB-18-C-6 + NH ₄ SCN	Chloroform	10	2.5 mol dm ⁻³ HCl	1.8–183	415	1.6	Water samples and steel	^{21, 34} (2014, 2022)
UV/Vis	HTP + HA	Chloroform	5	pH 1.8–5.1	0.2–19	457–538	3.2–4.2	Soil	³⁵ (2023)
UV/Vis	4NC + BAC	Chloroform	3	0.05–0.20 mol dm ⁻³ H ₂ SO ₄	0.1–4.4	422	5.49	Synthetic samples and steel	This work

Abbreviations: 4NC, 4-nitrocatechol; BAC, benzalkonium chloride; CHPB, 6-chloro-3-hydroxy-2-phenyl-4-oxo-4H-1-benzopyran; CHTB, 6-chloro-3-hydroxy-2-(2'-thienyl)-4-oxo-4H-1-benzopyran; DB-18-C-6, dibenzo-18-C-6(2,3,11,12-dibenzo-1,4,7,10,13,16-hexaoxacyclooctadeca-2,11-diene); DPG, diphenylguanidine; DTMP, 2,6-dithiol-4-methylphenol; EPH, ethopropazine hydrochloride; HA, hydrophobic amines; HBPNA, 2-hydroxy-5-tert-butylphenol-4'-nitroazobenzene; HBTP, 2-hydroxy-5-bromothiophenol; HCTP, 2-hydroxy-5-chlorothiophenol; HMTB, 3-hydroxy-2-[2'-(5'-methylthienyl)]-4-oxo-4H-1-benzopyran; HPMPPB, 3-hydroxy-2-[1'-phenyl-3'-(p-methylphenyl)-4'-pyrazolyl]-4-oxo-4H-1-benzopyran; HTB, 3-hydroxy-2-(2'-thienyl)-4-oxo-4H-1-benzopyran; HTP, 2-hydroxy-5-halogenthiofenols; HTPD, o-hydroxythiophenol derivatives; M2B, methyl type 2B; MTT, 3-(4,5-dimethylthiazol-2-yl)-2,5-diphenyltetrazolium bromide.

and the high tolerable levels of most of the side ions studied. The reagents used are commercially available and do not require tedious syntheses. The determination is rapid, as the extraction time is short, and no stable emulsion is formed. Moreover, the volume of organic solvent utilized (3 cm³ per sample) is less than that of the other procedures listed in Table 6.

5. Conclusions

A novel liquid-liquid extraction system for W(VI) involving inexpensive commercially available reagents (4NC and BAC) was subjected to a comprehensive study. The optimal conditions for the formation and extraction of a ternary complex, (BA⁺)₂[WO₂(4NC)₂], were identified. The structure of its anionic component [WO₂(4NC)₂]²⁻, which is responsible for the spectral bands in the visible region, was elucidated through the use of theoretical calculations at the B3LYP/CEP-4G level. The complex is intensely colored, allowing for the determination of trace amounts of W(VI) in a simple and economical manner without the use of sophisticated instruments and expensive consumables. The developed method is sensitive, selective, rapid, and robust. Its reliability can be attributed to the high stability of the extracted complex, the low absorption of the blank, and the wide optimal ranges of the investigated parameters. The method has been successfully applied to the analysis of steel and artificial mixtures that closely resemble typical tungsten-containing alloys.

Acknowledgments

This research was funded by the Medical University of Plovdiv, grant number DPDP-4/2024. The theoretical research was carried out using the infrastructure purchased under the National Roadmap for RI, financially coordinated by the MES of the Republic of Bulgaria (grant No D01-325/01.12.2023).

6. References

1. K. K. Chatterjee, *Uses of Metals and Metallic Minerals*, New Age International (P) Ltd. Publishers, New Delhi, India, **2007**, pp. 264–271.
2. P. Morcos, A. Elwany, I. Karaman, R. Arróyave, *J. Mat. Sci.* **2022**, 57, 9769–9806. DOI:10.1007/s10853-022-07183-y
3. IMA Mineral List with Database of Mineral Properties – RRuff. <https://rruff.info/ima/> (Accessed: June 01, 2024)
4. K. K. Mann, R. Bakadlag, P. E. Leffler, in: G.F. Nordberg, M. Costa (Eds.): *Handbook on the Toxicology of Metals*. Vol. 2 (Fifth Edition), Academic Press, Cambridge, Massachusetts, USA, **2022**, pp. 869–883. DOI:10.1016/B978-0-12-822946-0.00031-3
5. A. Winiarska, D. Hege, Y. Gemmecker, J. Kryściak-Czerwenka, A. Seubert, J. Heider, M. Szaleniec, *ACS Catal.* **2022**, 12, 8707–8717. DOI:10.1021/acscatal.2c02147
6. C. S. Seelmann, M. Willstein, J. Heider, M. Boll, *Inorganics* **2020**, 8, 44. DOI:10.3390/inorganics8080044
7. The National Institute for Occupational Safety and Health (NIOSH). Tungsten. <https://www.cdc.gov/niosh/npg/npgd0645.html> (Accessed: June 01, 2024).
8. S. C. Srivastava, S. R. Bhaisare, D. N. Wagh, C. P. S. Iyer, *Bull. Mat. Sci.* **1996**, 19, 331–343. DOI:10.1007/BF02744670
9. J. J. Topping, *Talanta* **1978**, 25, 61–72. DOI:10.1016/0039-9140(78)80035-6
10. Y. He, J. Hu, W. Zou, H. Chen, X. Jiang, X. Hou, *Anal. Chim. Acta* **2023**, 1278, 341746. DOI:10.1016/j.aca.2023.341746
11. A. Aleksandrov, A. Dimitrov, A. Patcheva, M. Vrchlabsky, *Scripta Fac. Sci. Nat. Univ. Purk. Brun.* **1985**, 15, 497–504.
12. A. Dimitrov, A. Alexandrov, *Anal. Lab.* **1995**, 4, 172–179.
13. S. P. Masti, J. Seetharamappa, M.B. Melwanki, *Anal. Sci.* **2002**, 18, 913–915. DOI:10.2116/analsci.18.913
14. N. Agnihotri, J. R. Mehta, *Ann. Chim.* **2004**, 94, 341–345. DOI:10.1002/adic.200490039
15. L. P. Tsiganok, A. N. Vaculich, A. B. Vishnikin, E. G. Koltsova, *Talanta*, **2005**, 65, 267–270. DOI:10.1016/j.talanta.2004.05.012
16. V. Lekova, K. Gavazov, A. Dimitrov, *Chem. Pap.* **2006**, 60, 283–287. DOI:10.2478/s11696-006-0049-1
17. R. Agnihotri, N. Agnihotri, J. R. Mehta, *Bull. Chem. Soc. Jpn.* **2008**, 81, 116–119. DOI:10.1246/bcsj.81.116
18. L. Ngọc Thụ, L. Ngọc Thiêm, V. Anh Tuấn, *Tạp chí Hóa Học* **2009**, 47, 679–684.
19. A. Z. Zalov, N. A. Verdizade, *J. Anal. Chem.* **2013**, 68, 212–217. DOI:10.1134/S1061934813010152
20. J. Rohilla, R. Baweja, S. Kumar, *Arch. Appl. Sci. Res.* **2013**, 5, 81–89.
21. A. Saoud, N. Nasrallah, A. Amrane, A.M. Nabieva, B. Hama-da, M. Nabiev, *Desalin. Water Treat.* **2014**, 52, 4928–4934. DOI:10.1080/19443994.2013.809962
22. A. Z. Zalov, *J. Anal. Chem.* **2015**, 70, 1342–1345. DOI:10.1134/S106193481509018X
23. N. A. Verdizadeh, A. Z. Zalov, S. G. Aliyev, A. V. Hajieva, G. I. Amanullayeva, *Int. J. Chem. Stud.* **2016**, 4, 7–12.
24. G. I. Amanullayeva, A. Z. Zalov, *Int. J. Innov. Res. Sci. Eng. Technol.* **2016**, 3, 277–288.
25. B. Petković, R. Micić, R. Simonović, *Bull. Nat. Sci. Res.* **2016**, 6, 21–26. DOI:10.5937/univtho6-10437
26. K. A. Kuliev, G. S. Suleymanova, N. A. Novruzova, N. N. Efendiyeva, *J. Adv. Appl. Sci. Res.* **2017**, 1, 28–41.
27. Y. Bazal, M. Lešková, M. Rečlo, J. Šandrejová, A. Simon, M. Fizer, V. Sidey, *Spectrochim. Acta A Mol. Biomol. Spectrosc.* **2018**, 196, 398–405. DOI:10.1016/j.saa.2018.02.049
28. N. Hassan, Z. Al-Mallah, A. S. Amin, *Anal. Chem. Lett.* **2018**, 8, 297–310. DOI:10.1080/22297928.2018.1470940
29. N. Agnihotri, S. Akhtar, P. Rathi, N. Kaur, *Asian J. Chem.* **2019**, 31, 275–278. DOI:10.14233/ajchem.2019.21553
30. A. Z. Zalov, K. A. Kuliev, N. A. Akberov, U. B. Abasgulieva, U. S. Bakhshieva, *Chem. Probl.* **2019**, 1, 50–57. DOI:10.32737/2221-8688-2019-1-50-57

31. N. Kaur, N. Agnihotri, R. Agnihotri, *Vietnam J. Chem.* **2019**, *57*, 686–695. DOI:10.1002/vjch.201900069
32. H. M. Al-Saidi, M. A. Abdel-Fadeel, S. S. Alharthi, *J. Saudi Chem. Soc.* **2021**, *25*, 101301. DOI:10.1016/j.jscs.2021.101301
33. S. A. Mammadova, U. Abasqulieva, A. Zalov, N. Novruzova, *Chem. Probl.* **2022**, *2*, 164–174. DOI:10.32737/2221-8688-2022-2-164-174
34. A. Saoud, S. H. née Mesdour, A. Nabieva, B. Hamada, A. Amrane, M. Nabiev, *Int. J. Environ. Anal. Chem.* **2022**, *102*, 1814–1824. DOI:10.1080/03067319.2020.1743830
35. A. Z. Zalov, K. A. Kuliev, S. Q. Aliyev, R. A. İsmailova, S. S. Ahmed, *Azerbaijan J. Chem. News* **2023**, *5*, 19–29. DOI:10.32010/AJCN04022023-19
36. S. Natansohn, J. I. Krugler, J. E. Lester, M. S. Chagnon, R. S. Finocchiaro, *J. Phys. Chem.* **1980**, *84*, 2972–2980. DOI:10.1021/j100459a027
37. K. B. Gavazov, *Acta Chim. Slov.* **2012**, *59*, 1–17.
38. S. Mitra, in: J. D. Winefordner (Ed.) *Chemical analysis*. Vol. 162, John Wiley & Sons, New Jersey, USA, **2003**.
39. J.-P. Cornard, Rasmiwetti, J.-C. Merlin, *Chem. Phys.* **2005**, *309*, 239–249. DOI:10.1016/j.chemphys.2004.09.020
40. L. Sommer, G. Ackermann, D. T. Burns, S. B. Savvin, *Pure Appl. Chem.* **1990**, *62*, 2147–2166. DOI:10.1351/pac199062112147
41. Sigma-Aldrich safety data sheet. 4-Nitrocatechol, <https://www.sigmaaldrich.com/BG/en/sds/aldrich/n15553?user-Type=anonymous>, (Accessed: June 01, 2024)
42. R. C. Rowe, P. Sheskey, M. Quinn (Eds.) in: *Handbook of Pharmaceutical Excipients*, Pharmaceutical Press, London, UK, **2009**, pp. 56–58.
43. M. Y. Blazheyevskiy, O. V. Koval'ska, *Methods Objects Chem. Anal.* **2023**, *18*, 5–12. DOI:10.17721/moca.2023.5-12
44. V. V. Divarova, A. D. Saravanska, G. K. Toncheva, N. Milcheva, V. B. Delchev, K. B. Gavazov, *Molecules* **2022**, *27*, 1217. DOI:10.3390/molecules27041217
45. D. G. Hristov, N. P. Milcheva, K. B. Gavazov, *Acta Chim. Slov.* **2019**, *66*, 987–994. DOI:10.17344/acsi.2019.5244
46. K. Stojnova, P. Racheva, V. Divarova, P. Yanev, V. Lekova, *Acta Chim. Slov.* **2020**, *67*, 594–601. DOI:10.17344/acsi.2019.5612
47. K. Stojnova, P. Yanev, V. Lekova, *Acta Chim. Slov.* **2023**, *70*, 295–302. DOI:10.17344/acsi.2023.8197
48. Z. Zhiming, M. Dongsten, Y. Cunxiao, *J. Rare Earths* **1997**, *15*, 216–219.
49. E. Asmus, *Fresenius' J. Anal. Chem.* **1960**, *178*, 104–116. DOI:10.1007/BF00467200
50. J. R. Andreesen, K. Makdessi, *Ann. N. Y. Acad. Sci.* **2008**, *1125*, 215–229. DOI:10.1196/annals.1419.003
51. E. I. Stiefel, in: A. Sigel, H. Sigel (Eds.): *Metal Ions in Biological Systems*. Vol. 39, CRC Press, Boca Raton, USA, **2002**, pp. 1–29.
52. A. E. Harvey, D.L. Manning, *J. Am. Chem. Soc.* **1950**, *72*, 4488–4493. DOI:10.1021/ja01166a044
53. A. Holme, F. J. Langmyhr, *Anal. Chim. Acta* **1966**, *36*, 383–391. DOI:10.1016/0003-2670(66)80066-1
54. K. B. Gavazov, Liquid-liquid extraction of ion-association complexes, in: J. C. Taylor (Ed.) *Advances in Chemistry Research*, Vol. 50, Nova Science Publishers, New York, **2019**, pp. 203–238.
55. A. D. Saravanska, P. V. Racheva, V. V. Divarova, G. K. Toncheva, N. P. Milcheva, V. B. Delchev, K. B. Gavazov, *Russ. J. Inorg. Chem.* **2021**, *66*, 1880–1886. DOI:10.1134/S0036023621120147
56. C. M. Senger, K. F. Anschau, L. Baumann, A. L. H. Muller, P. A. Mello, E. I. Muller, *Microchem. J.* **2021**, *171*, 106781. DOI:10.1016/j.microc.2021.106781
57. A. M. Pashajanov, T. M. Ismailov, N. I. Ismayilov, M. M. Agamaliyeva, S. M. Bayramov, Z. A. Mamedova, *Azerb. Chem. J.* **2022**, *4*, 109–113. DOI:10.32737/0005-2531-2022-4-109-113

Povzetek

Raziskovali smo nov kromogeni sistem za ekstrakcijo tekoče-tekoče in določevanje sledov volframa(VI). Sistem sestavljajo 4-nitrokatehol (4NC) kot kromogeni reagent, žveplovo kislino kot kompleksirajoči medij in benzalkonijev klorid (BAC) kot vir velikih kationov (BA⁺), ki zlahka tvorijo ionske komplekse ki jih je možno ekstrahirati s kloroformom. Preučevali smo vpliv tujih ionov in reagentov in določili optimalne pogoje za občutljivo, selektivno in cenovno ugodno določanje volframa(VI). Meja detekcije, linearno področje analize in molarni absorpcijski koeficient pri λ_{\max} (422 nm) znašajo 31 ng cm⁻³, 0.1–4.4 µg cm⁻³ in 5.49×10^4 dm³ mol⁻¹ cm⁻¹. Sestava ekstrahiranega kompleksa je bila 1:2:2 (W:4NC:BA). Dve možni strukturi anionskega dela kompleksa, [WO₂(4NC)₂]²⁻, smo diskutirali na osnovi optimizacije z metodo B3LYP/CEP-4G in primerjave med izračunanimi ter izmerjenimi spektri.



Except when otherwise noted, articles in this journal are published under the terms and conditions of the Creative Commons Attribution 4.0 International License

Synthesis of (*E*)-3-{[2-Oxo-5-arylfuran-3(2*H*)-ylidene]methyl}-4*H*-1-benzopyran-4-ones, Crystal Structure, Quantum Chemical Substantiation

Ekaterina M. Arzyamova*, Olga A. Mazhukina and Alevtina Yu. Yegorova

Institute of Chemistry, N. G. Chernyshevsky Saratov National Research State University,
83 Ulitsa Astrakhanskaya, 410012 Saratov, Russia.

* Corresponding author: E-mail: katerina285@yandex.ru
Tel.: +7 9873122099

Received: 00-00-2024

Abstract

A directed method for the preparation of hybrid compounds based on furan-2(3*H*)-ones and chromen-4(4*H*)-one, (*E*)-3-{[2-oxo-5-arylfuran-3(2*H*)-ylidene]methyl}-4*H*-1-benzopyran-4-ones, the structure of which was confirmed by elemental analysis, IR, UV, NMR spectroscopy, and X-ray single crystal analysis, was developed. The molecular geometry of the synthesized compound (*E*)-3-((2-oxo-5-phenylfuran-3(2*H*)-ylidene)methyl)-4*H*-chromen-4-one (**3a**) was analyzed and compared with X-ray diffraction data, DFT calculations were performed using 6-311 G split-valence basis functions.

Keywords: Synthesis; hybrid structures; furan-2(3*H*)-ones; chromen-4(4*H*)-ones; crystal structure; DFT.

1. Introduction

Furan-2(3*H*)-one derivatives are among a large number of compounds with antinociceptive, anti-inflammatory, antiviral and antitumor activities.^{1–4} It is important to note nitrofurans derivatives with pronounced antibacterial activity.^{5–9} The 4*H*-chromen-4-one fragment is

part of the structure of compounds with anticancer, antibacterial, antiviral and other activities^{10–12} (Figure 1).

The main focus of this study is the synthesis of hybrid molecules based on furan-2(3*H*)-ones and 4-oxo-4*H*-chromen-3-carbaldehyde. Despite the large number of works on the synthesis of hybrid molecules based on

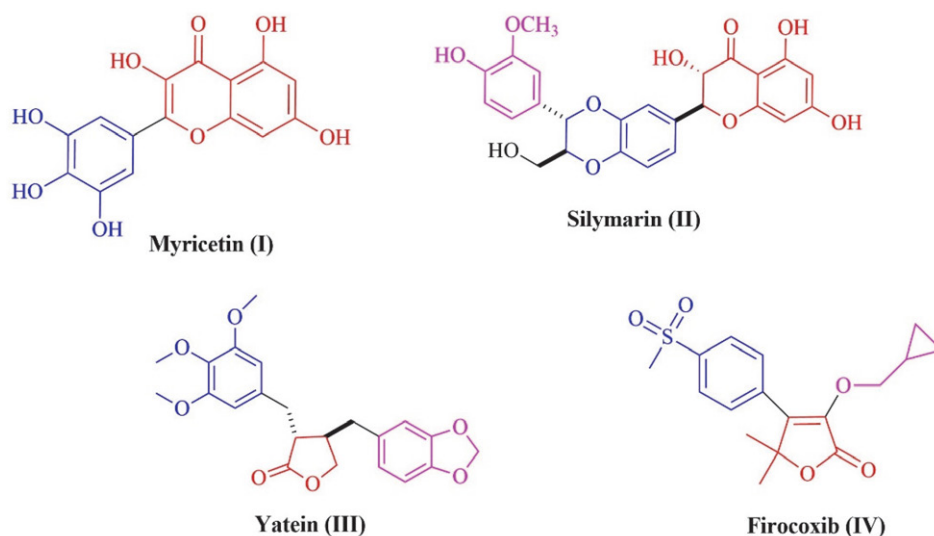
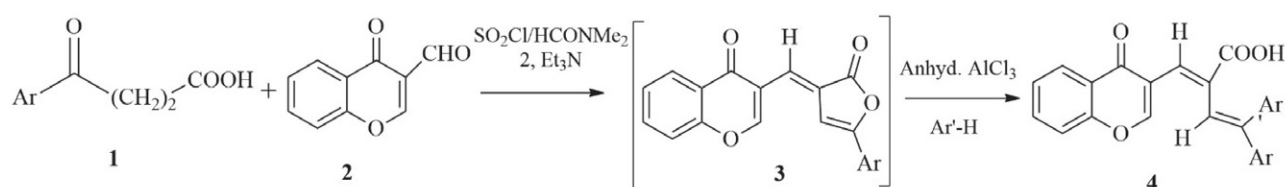


Figure 1. Examples of naturally occurring biologically active hybrid molecules

chromen-4-ones and furan-2-ones, systematic studies of directly coupled 4*H*-chromen-4-ones and furan-2(3*H*)-ones are very limited. The literature review showed that the construction of hybrid molecules is based on reactions with furan-2(5*H*)-one derivatives.^{13–17} The only example of the synthesis of hybrid structures based on 4*H*-chromen-4-ones and furan-2(3*H*)-ones, which are intermediates in the synthesis of 4,4-diaryl-1-(3-chromonyl)buta-1,3-dien-2-carboxylic acids **4**, was described by A. K. El-Ziaty *et al.*¹⁸ Condensation of 4-oxo-4*H*-chromen-3-carboxaldehyde **2** with 3-arylpropionic acids **1** under harsh conditions using thionyl chloride in *N,N*-dimethylformamide as a cyclodehydrating agent leads to the formation of the corresponding 5-aryl-3-chromonylmethylene-2(3*H*)-furanones **3** as a mixture of (*E*) and (*Z*) stereoisomers.¹⁸



Scheme 1. The synthetic route for compounds **4**

The main disadvantages of this method of synthesis are that it is a multistage, labor intensive process with a long duration, as well as the difficulty of separating products obtained in the form of an inseparable mixture of isomers with low yields. No convincing proof of the structures of the obtained compounds on the basis of the present spectral data was given. The methodology developed by the authors¹⁸ for the synthesis of 5-aryl-3-chromonylmethylene-2(3*H*)-furanones **3** is not reproducible.

Thus, the present work is devoted to finding optimal synthesis conditions and revealing the features of the spatial structure and configuration of hybrid structures: (*E*)-3-{[2-oxo-5-arylfuran-3(2*H*)-ylidene]methyl}-4*H*-1-benzopyran-4-ones.

2. Experimental

2.1. Materials

The reactions were carried out using Monowave 50 (Anton Paar, Austria) reactor. FTIR spectra were collected on an FSM-1201 Fourier spectrometer (Infraspek, St. Petersburg, Russia) in the range 4000–400 cm^{−1} with a spectral resolution of 4 cm^{−1}. Samples were mixed with ground KBr (FTIR grade, Sigma–Aldrich, Saint Louis, MO, USA) and pressed into pellets by removing water and air traces under reduced pressure. UV spectra of the studied solutions were recorded on a Shimadzu-1800 spectrophotometer in cuvettes with an optical layer thickness of 1 cm and a scanning step of 1 nm. Working solutions were prepared

according to the exact weight of the compounds and dissolved in chloroform, ethanol and DMSO ($c = 2 \cdot 10^{-5}$ M). ¹H (400 MHz) and ¹³C NMR (100 MHz), ¹H–¹³C gHSQC, ¹H–¹³C gHMBC, NOESY 2D, NOESY 1D spectra in DMSO-*d*₆ were recorded with a Varian (Agilent) 400 spectrometer (Agilent Technologies, Santa Clara, CA, USA), and the internal standard was TMS. Chemical shifts (δ) are reported in ppm. Elemental analysis was done on an Elemental Vario MICRO cube CHNS analyzer (Elementar Analysensysteme GmbH, Hanau, Germany). Melting points were determined on a Stuart[™] SMP10 melting point apparatus (Cole-Parmer, Beacon Road, Stone, Staffordshire, ST15 0SA, UK). The progress of the reaction and the purity of the synthesized compounds were monitored by TLC on ALUGRAM[®] SIL G UV254 plates (Mache-

rey-Nagel GmbH & Co. KG, Düren, Germany), with hexane–ethyl acetate–acetone (3:1:1) as the eluent.

2.2. Quantum Chemical Calculations

Quantum chemical calculations were performed using density functional theory (DFT) using the hybrid functional Lee–Yang–Parr three-parameter Becke B3LYP, split-valence basis set functions 6–311G, with the inclusion of p-orbitals of the hydrogen atom and d-orbitals for more heavy atoms as well as with the addition of polarization functions (B3LYP/6–311G++ (d,p)). For each of the possible isomers, a complete geometry optimization was carried out with a strict convergence criterion.¹⁹

2.3. Synthesis of the Compounds

General methodology for the preparation of hybrid structures 3a–f

Method A: A mixture of 3 mmol of the corresponding 5-arylfuran-2(3*H*)-ones **1a–f**, 3 mmol of 4-oxo-4*H*-chromen-3-carboxaldehyde **2** was refluxed in 10 mL of glacial acetic acid. The precipitated yellow crystals were filtered, washed with glacial acetic acid, recrystallized from benzene, and dried.

Method B: The 1 mmol of the corresponding 5-arylfuran-2(3*H*)-one **1a–f**, 1 mmol of 4-oxo-4*H*-chromene-3-carboxaldehyde **2** and 3.5 mL of glacial acetic acid are placed in a 10 mL borosilicate glass vial, placed in the vial with the reaction mixture with a magnetic stirrer. The vial is hermetically sealed with a silicone stopper and placed in a Monowave 50 reactor. The reaction is carried out at a temperature of 135 °C with a stirring speed of 600 rpm.

The precipitated yellow crystals were filtered, washed with glacial acetic acid, recrystallized from benzene, and dried.

(E)-3-((2-Oxo-5-phenylfuran-3(2H)-ylidene)methyl)-4H-chromen-4-one (3a).

Yellow crystals (benzene): *Method A* – 0.66 g, yield 70%; *Method B* – 0.25 g, yield 80%, mp 219–220 °C; FTIR (KBr) ν/cm^{-1} : 1759 (O=C=O), 1653 (C=O), 1613 (C=C); ^1H NMR (400 MHz, DMSO- d_6): δ 9.09 (s, 1H, C-H_{Chromone}), 8.15 (d, J = 8.0 Hz, 1H, Ar-H), 7.89–7.82 (m, 3H, Ar-H), 7.75 (d, J = 8.0 Hz, 1H, Ar-H), 7.59 (s, 1H, C-H_{Furanone}), 7.56–7.49 (m, 4H, Ar-H), 7.38 (s, 1H, =CH-); ^{13}C NMR (100 MHz, DMSO- d_6): δ 175.06 (C=O), 168.76 (O-C=O), 159.43 (C-H_{Chromone}), 156.19, 155.92, 155.86, 135.40, 131.18, 129.57, 128.12, 126.79, 126.09, 125.69, 125.37, 125.31, 125.27 (=CH-), 123.46, 119.79, 119.15, 102.35 (C-H_{Furanone}). Anal. calcd. for C₂₀H₁₂O₄: C, 75.94; H, 3.82. Found: C, 76.35; H, 4.14%.

(E)-3-((2-Oxo-5-(para-tolyl)furan-3(2H)-ylidene)methyl)-4H-chromen-4-one (3b).

Yellow crystals (benzene): *Method A* – 0.52 g, yield 52%; *Method B* – 0.22 g, yield 66%, mp 243–245 °C; FTIR (KBr) ν/cm^{-1} : 1760 (O=C=O), 1646 (C=O), 1615 (C=C); ^1H NMR (400 MHz, DMSO- d_6): δ 9.09 (s, 1H, C-H_{Chromone}), 8.15 (d, J = 8.0 Hz, 1H, Ar-H), 7.88 (t, J = 7.0 Hz, 1H, Ar-H), 7.77–7.72 (m, 3H, Ar-H), 7.58–7.53 (m, 2H, Ar-H and C-H_{Furanone}), 7.34 (d, J = 8.0 Hz, 3H, 2H Ar-H and =CH-), 2.36 (s, 3H, CH₃); ^{13}C NMR (100 MHz, DMSO- d_6): δ 175.09 (C=O), 168.86 (O-C=O), 159.24 (C-H_{Chromone}), 156.45, 155.92, 141.32, 135.40, 130.50, 130.19, 126.78, 126.09, 125.70, 125.39, 125.33, 124.57 (=CH-), 123.44, 123.39, 119.83, 119.16, 101.50 (C-H_{Furanone}), 21.58 (CH₃). Anal. calcd. for C₂₁H₁₄O₄: C, 76.35; H, 4.27. Found: C, 76.80; H, 4.41%.

(E)-3-((5-(4-Chlorophenyl)-2-oxofuran-3(2H)-ylidene)methyl)-4H-chromen-4-one (3c).

Yellow crystals (benzene): *Method A* – 0.58 g, yield 55%; *Method B* – 0.22 g, yield 63%, mp 284–285 °C; FTIR (KBr) ν/cm^{-1} : 1757 (O=C=O), 1649 (C=O), 1615 (C=C); ^1H NMR (400 MHz, DMSO- d_6): δ 9.10 (s, 1H, C-H_{Chromone}), 8.16 (d, J = 8.0 Hz, 1H, Ar-H), 7.90–7.83 (m, 3H, Ar-H), 7.77 (d, J = 8.2 Hz, 1H, Ar-H), 7.66 (s, 1H, C-H_{Furanone}), 7.66–7.59 (m, 2H, Ar-H), 7.56 (d, J = 7.0 Hz, 1H, Ar-H), 7.41 (s, 1H, =CH-); ^{13}C NMR (100 MHz, DMSO- d_6): δ 175.22 (C=O), 168.75 (O-C=O), 159.03 (C-H_{Chromone}), 157.37, 156.29, 155.13, 154.93, 135.53, 129.77, 127.52, 127.40, 126.78, 126.11, 126.02 (=CH-), 125.97, 125.09, 123.35, 119.25, 119.19, 103.09 (C-H_{Furanone}). Anal. calcd. for C₂₀H₁₁ClO₄: C, 68.49; H, 3.16; Cl, 10.11. Found: C, 68.54; H, 3.35; Cl, 10.20%.

(E)-3-((5-(4-Bromophenyl)-2-oxofuran-3(2H)-ylidene)methyl)-4H-chromen-4-one (3d).

Yellow crystals (benzene): *Method A* – 0.97 g, yield

82%; *Method B* – 0.36 g, yield 90%, mp 271–272 °C; FTIR (KBr) ν/cm^{-1} : 1755 (O=C=O), 1649 (C=O), 1614 (C=C); ^1H NMR (400 MHz, DMSO- d_6): δ 9.09 (s, 1H, C-H_{Chromone}), 8.16 (d, J = 8.0 Hz, 1H, Ar-H), 7.88 (t, J = 7.0 Hz, 1H, Ar-H), 7.79–7.74 (m, 5H, Ar-H), 7.67 (s, 1H, C-H_{Furanone}), 7.57 (t, J = 7.6 Hz, 1H, Ar-H), 7.42 (s, 1H, =CH-); ^{13}C NMR (100 MHz, DMSO- d_6): δ 175.24 (C=O), 168.40 (O-C=O), 157.07 (C-H_{Chromone}), 156.31, 155.91, 155.28, 154.45, 134.70, 132.66, 127.61, 127.54, 126.84, 126.10, 125.98 (=CH-), 124.52, 124.09, 123.46, 119.76, 119.18, 103.16 (C-H_{Furanone}). Anal. calcd. for C₂₀H₁₁BrO₄: C, 60.78; H, 2.81; Br, 20.22. Found: C, 60.54; H, 2.98; Br, 20.09%.

(E)-3-((5-(3,4-Dimethylphenyl)-2-oxofuran-3(2H)-ylidene)methyl)-4H-chromen-4-one (3e).

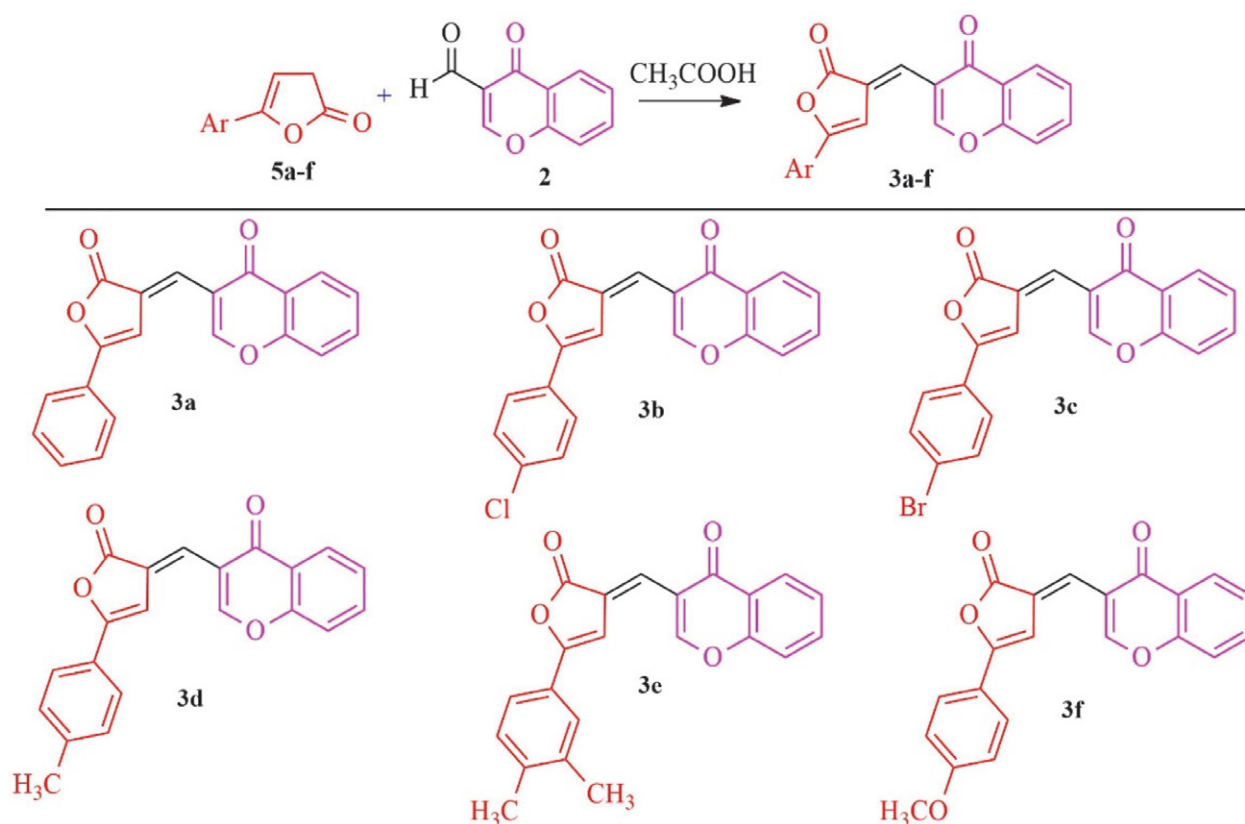
Yellow crystals (benzene): *Method A* – 0.59 g, yield 57%; *Method B* – 0.23 g, yield 68%, mp 232–233 °C; FTIR (KBr) ν/cm^{-1} : 1761 (O=C=O), 1651 (C=O), 1612 (C=C); ^1H NMR (400 MHz, DMSO- d_6): δ 9.08 (s, 1H, C-H_{Chromone}), 8.15 (d, J = 8.0 Hz, 1H, Ar-H), 7.87 (t, J = 7.0 Hz, 1H, Ar-H), 7.75 (d, J = 8.4 Hz, 1H, Ar-H), 7.62 (s, 1H, Ar-H), 7.56 (t, J = 8.1 Hz, 2H, Ar-H), 7.50 (s, 1H, C-H_{Furanone}), 7.34 (s, 1H, =CH-), 7.29 (d, J = 8.0 Hz, 1H, Ar-H), 2.27 (unresolved singlet, 6H, 2CH₃); ^{13}C NMR (100 MHz, DMSO- d_6): δ 175.09 (C=O), 168.90 (O-C=O), 159.16 (C-H_{Chromone}), 156.61, 155.92, 140.22, 137.65, 135.38, 130.65, 126.76, 126.58, 126.09, 125.68, 125.38, 124.34, 124.31 (=CH-), 123.31, 119.84, 119.15, 101.33 (C-H_{Furanone}), 19.96 (CH₃), 19.82 (CH₃). Anal. calcd. for C₂₂H₁₆O₄: C, 76.73; H, 4.68. Found: C, 76.97; H, 4.86%.

(E)-3-((5-(4-Methoxyphenyl)-2-oxofuran-3(2H)-ylidene)methyl)-4H-chromen-4-one (3f).

Yellow crystals (benzene): *Method A* – 0.51 g, yield 49%; *Method B* – 0.21 g, yield 60%, mp 241–242 °C; FTIR (KBr) ν/cm^{-1} : 1764 (O=C=O), 1653 (C=O), 1614 (C=C); ^1H NMR (400 MHz, DMSO- d_6): δ 9.06 (s, 1H, C-H_{Chromone}), 8.15 (d, J = 8.0 Hz, 1H, Ar-H), 7.87 (t, J = 8.7 Hz, 1H, Ar-H), 7.79–7.74 (m, 3H, Ar-H), 7.54 (t, J = 8.1 Hz, 1H, Ar-H), 7.44 (s, 1H, C-H_{Furanone}), 7.31 (s, 1H, =CH-), 7.09 (d, J = 8.8 Hz, 2H, Ar-H), 3.82 (s, 3H, OCH₃); ^{13}C NMR (100 MHz, DMSO- d_6): δ 175.11 (C=O), 168.97 (O-C=O), 158.89 (C-H_{Chromone}), 156.46, 155.93, 135.36, 130.23, 129.39, 127.59, 126.73, 126.25, 126.09, 125.44, 124.70, 123.42 (=CH-), 120.57, 119.91, 119.15, 115.17, 100.24 (C-H_{Furanone}), 55.94 (OCH₃). Anal. calcd. for C₂₁H₁₄O₅: C, 72.83; H, 4.07. Found: C, 72.99; H, 4.32%.

2. 4. Single Crystal X-ray Crystallography

The X-ray diffraction study of (E)-3-((2-oxo-5-phenylfuran-3(2H)-ylidene)methyl)-4H-chromen-4-one (**3a**) was performed on an Agilent New Xcalibur, Ruby diffractometer equipped with a CCD detector (MoK α radiation, λ = 0.71073 Å, graphite monochromator, ω -scan) at 295(2)



Scheme 2. Synthesis of hybrid structures: 3-{[2-oxo-5-aryl-5H-furan-3-ylidene]methyl}-4H-1-benzopyran-4-one **3**

Table 1. Crystallographic data and refinement parameters for the compound **3a**.

Crystal data	
Chemical formula	C ₂₀ H ₁₂ O ₄
<i>M_r</i>	316.30
T/K	295
Crystal system, space group	Monoclinic, <i>P</i> 2 ₁
<i>a</i> /Å	6.802(2)
<i>b</i> /Å	4.9703(16)
<i>c</i> /Å	22.217(9)
α /°	90
β /°	92.46(3)
γ /°	90
<i>V</i> /Å ³	750.4(4)
<i>Z</i>	2
<i>D_{calc}</i> / g cm ⁻³	1.400
μ /mm ⁻¹	0.10
<i>F</i> (000)	328
Reflections collected	2103
Independent reflections	2103
<i>I</i> ≥ 2 σ (<i>I</i>)	973
<i>R_{int}</i>	0.037
<i>R</i> [<i>I</i> ≥ 2 σ (<i>I</i>)]	0.051
<i>S</i>	0.85
<i>wR</i> (<i>I</i>)	0.116
No. of parameters	218
No. of restraints	1
$\Delta\rho_{\min}/\Delta\rho_{\max}$ (eÅ ⁻³)	−0.16/0.14

K. Absorption corrections were made using CrysAlis PRO program (Agilent Technologies) version 1.171.42.74a. Empirical corrections for absorption were made using spherical harmonics implemented in the SCALE3 ABSPACK program.²⁰ The structure was refined by full-matrix MNC on *F*² in the anisotropic approximation for all non-hydrogen atoms using the SHELXL program²¹ with the OLEX2 graphical interface.²² The hydrogen atoms of the aromatic rings are refined in a “riding” model. The other hydrogen atoms are included in the refinement independently in the isotropic approximation. The crystal refined as a two-component twin with component occupancies of 0.564(2) and 0.436(2), respectively. Component 2 rotated by −179.9940° around [0.00 0.00 1.00] (reciprocal) or [0.16 0.00 0.99] (direct).

3. Results and Discussion

As a result of the search for optimal conditions for the synthesis of arylmethylidene derivatives, we expanded the series and found the optimal method for the preparation of 3-{[2-oxo-5-aryl-5H-furan-3-ylidene]methyl}-4H-1-benzopyran-4-one (**3a–f**), based on the reaction of equimolar amounts of 5-aryl-2-oxo-5H-furan-3-ylidene (**5a–f**), obtained according to the method,²³ with 4-oxo-4H-chromene-3-carboxaldehyde (**2**) in glacial acetic acid without the use of a

catalyst (Scheme 2), with thermal activation of the reaction mixture and the use of a Monowave 50 closed-type reactor with various yields (Table 2). Considering the presence of three electrophilic centers in 3-formylchromone, several directions of reactions can be expected. Taking into account the structure of (*E*)-3-[[2-oxo-5-arylfuran-3(2*H*)-ylidene]methyl]-4*H*-1-benzopyran-4-ones **3a–f**, it is assumed that the initial enolization of the furanone ring in acetic acid occurs followed by the formation of a new C=C bond due to the involvement of the aldehyde group of substrate **2** in the reaction.

A comparison was made of two interaction methods: the conventional method of thermal heating under normal pressure conditions and in a closed vessel reactor (Monowave 50) at elevated pressure. The use of a sealed vessel reactor makes it possible to increase the efficiency of the process by increasing the temperature and pressure of the reaction, which will significantly reduce its time, which is unattainable under normal conditions of conventional heating at atmospheric pressure and the boiling point of the solvent. The parameters of the two modes are presented in Table 2.

It was shown that the reaction of 5-arylfuran-2 (3*H*)-ones **5a–f** with 3-formylchromone **2**, carried out both under conventional conditions and in a sealed vessel reactor, leads to (*E*)-3-[[2-oxo-5-arylfuran-3(2*H*)-ylidene]methyl]-4*H*-1-benzopyran-4-ones **3a–f**. It should be noted that the use of a reactor in a sealed vessels made it possible to increase the yield of products by 8–14%, as well as significantly increase the efficiency of interaction, which is reflected in a significant reduction in reaction time compared to conventional conditions (12 times) and compared to the literature data (20 times).¹⁸

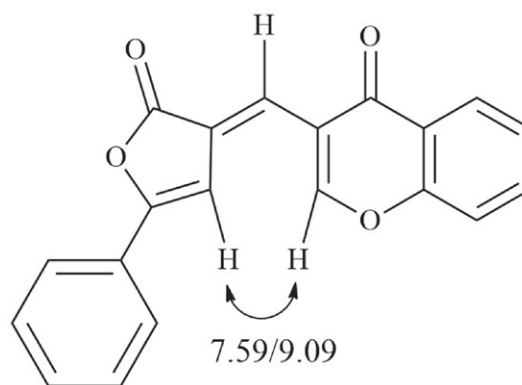
The structure of hybrid compounds **3a–f** was confirmed by IR, ¹H, ¹³C NMR, NOESY spectroscopy, and X-ray diffraction analysis using the example of (*E*)-3-((2-oxo-5-phenylfuran-3(2*H*)-ylidene)methyl)-4*H*-chromen-4-one **3a**. The IR spectra of the obtained compounds contain absorption bands of the lactam carbonyl group in the region of 1764–1755 cm^{−1}, as well as absorption bands of the carbonyl group of the 4*H*-chromen-4-one fragment at 1653–1646 cm^{−1}.

The key signals of (*E*)-3-[[2-oxo-5-arylfuran-3(2*H*)-ylidene]methyl]-4*H*-1-benzopyran-4-ones **3a–f** registered in DMSO-*d*₆ are the proton singlet chromen-4-one frag-

ment at 9.06–9.10 ppm, singlet of the vinyl proton of the furan-2-one fragment at 7.44–7.67 ppm and a singlet of the vinyl proton of the exocyclic bond at 7.31–7.42 ppm. In the low-field region of the ¹³C NMR spectra of compounds **3a–f**, signals of the lactone carbon atom were recorded at 168.40–168.97 ppm and the carbonyl carbon atom of the chromen-4-one fragment at 175.06–175.24 ppm.

Based on NMR spectroscopy, it was shown that the resulting compounds **3a–f** exist only in the form of *E*-isomers. Proof of this is the absence of duplication of signals in the ¹H NMR spectra, recorded in DMSO-*d*₆, as well as the presence in the NOESY 2D spectra of the example of compound **3a** of a cross-peak at 7.59/9.09 ppm, due to the NOE correlation of the proton at the C-4 position of furan-2-one fragment and the proton of the C-2 position of the chromen-4-one fragment (Figure 2), both in general form and upon selective excitation within the NOESY 1D method, which confirms their closeness and indicates in favor of the *E*-configuration. Additional confirmation is the absence of NOE correlation between the vinyl proton of the exocyclic bond and the vinyl proton of the furan-2-one fragment.

Figure 2. Key NOE correlation for (*E*)-3-((2-oxo-5-phenylfuran-



3(2*H*)-ylidene)methyl]-4*H*-chromen-4-one **3a**

The synthesized compounds **3a–f**, regardless of the reaction conditions, exist in a DMSO-*d*₆ solution only in the *E*-configuration. To identify the features of the spatial structure, reaction direction and configuration of the re-

Table 2. Optimal conditions for the synthesis of hybrid structures **3a–f**.

№	Reflux				Monowave 50			
	<i>T</i> , °C	<i>t</i> , min	<i>P</i> , bar	Yield, %	<i>T</i> , °C	<i>t</i> , min	<i>P</i> , bar	Yield, %
3a	118	180	1	70	135	15	4	80
3b	118	180	1	52	135	15	4	66
3c	118	60	1	55	135	5	4	63
3d	118	60	1	82	135	5	4	90
3e	118	180	1	57	135	15	4	68
3f	118	180	1	49	135	15	4	60

sulting hybrid structures **3a–f**, their theoretical study was carried out based on DFT calculations.¹⁹

It is known that M-base-catalyzed condensation reactions produce a chelate transition state, first proposed by Zimmerman, which has a chair conformation. This hypothesis perfectly explains the possibility of obtaining a stereoselective result. It is possible to unambiguously establish the direction of transformation only in the case of intramolecular transformations.

The intermolecular nature of reactions makes it impossible to unambiguously determine the location of the reacting substances. Under the proposed conditions, in the acid-catalyzed transformation, enolization occurs due to protonation of the carbonyl group of the furan-2-one moiety, which leads to the formation of a planar cyclic conjugated system. Subsequent attack by the activated carbonyl group on the chromenonaldehyde can occur from opposite sides relative to the ring plane and ultimately leads to the formation of four possible isomeric aldols **R1**, **R2** and **S1**, **S2** (Scheme 3).

According to the calculated molecular geometry data, the **R1** isomer is stabilized due to the formation of an intramolecular hydrogen bond, as a result of which the formation energy of this aldol is less important compared to other isomers (Figure 3).

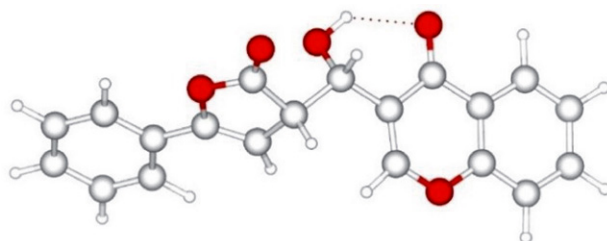
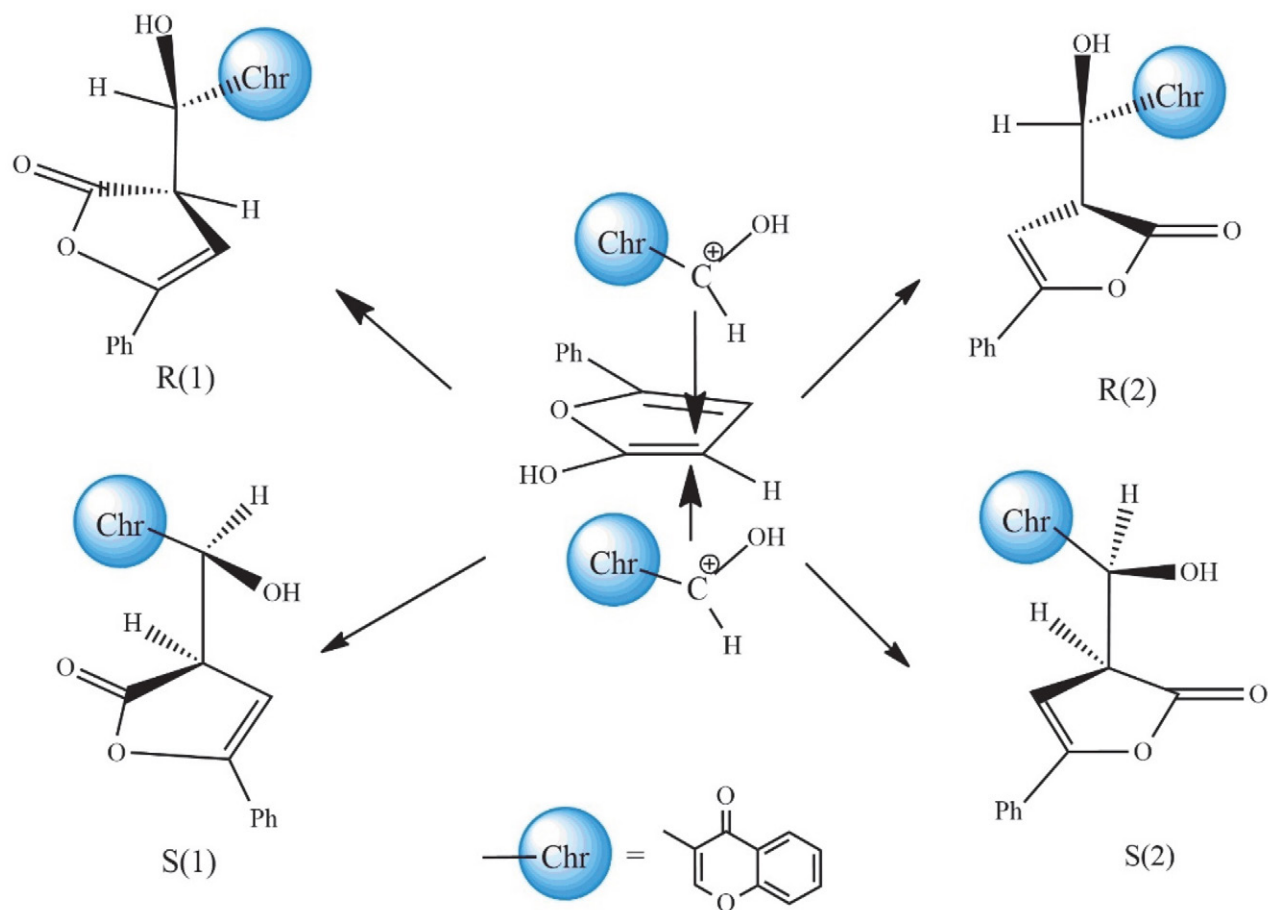


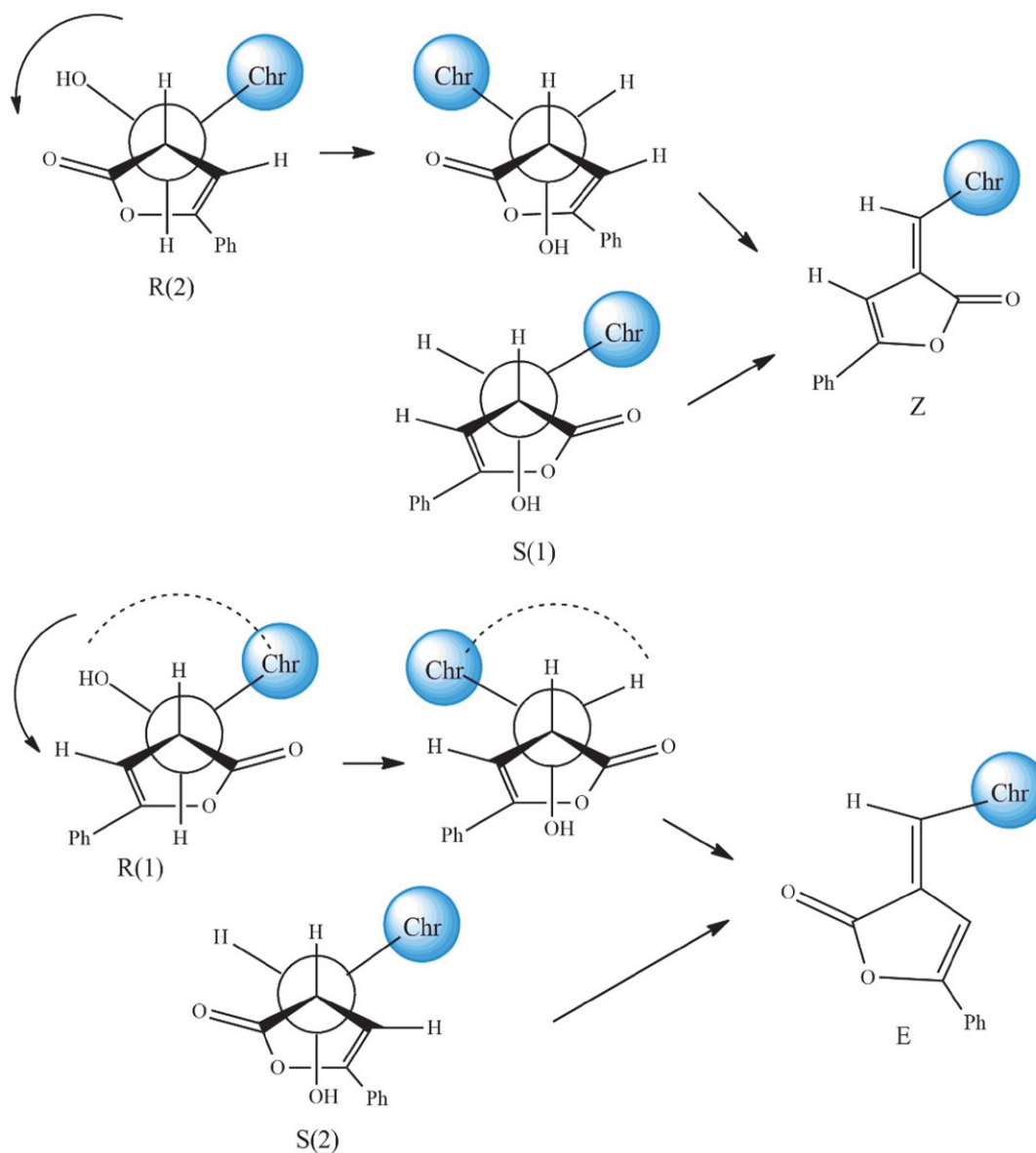
Figure 3. Optimized structure of compound **3a** (isomer **R1**)

The final product of the transformation in the process under study is 3-((2-oxo-5-phenylfuran-3(2*H*)-ylidene)methyl)-4*H*-chromen-4-one (**3a**), which can exist in the form of four geometric isomers **E1**, **E2**, **Z1**, **Z2** (Scheme 4).

This result is due to the different mutual arrangement of groups of atoms of the chromenone fragment due to its rotation around a single C–C bond within a fixed geometric configuration. According to calculated data, the probability of the formation of the **R1** isomer is higher; subsequent dehydration processes will lead to one of the *E* forms. According to NMR spectroscopy data (the presence of a corresponding cross-peak in the NOESY 2D and NOESY 1D spectra) and the results of X-ray diffraction studies, we have a single *E1* isomer as the final product of the reaction.



Scheme 3. Formation of possible isomeric aldols **R1**, **R2**, **S1**, **S2**



Scheme 4. Geometric isomers *E*1, *E*2, *Z*1, *Z*2 of 3-((2-oxo-5-phenylfuran-3(2*H*)-ylidene)methyl)-4*H*-chromen-4-one (**3a**)

A suitable crystal of compound **3a** was grown by slowly cooling a saturated solution in benzene. For X-ray diffraction analysis, a crystal with a size of $0.6 \times 0.1 \times 0.02$ mm³ was selected. The crystal structure of compound **3a** with atom labeling is shown in Figure 4. From this experiment, we were able to further confirm that the final compounds **3a–f** are in the *E*1 configuration. (*E*)-3-((2-oxo-5-phenylfuran-3(2*H*)-ylidene)methyl)-4*H*-chromen-4-one (**3a**) crystallizes in the non-centrosymmetric space group *P*2₁ with one molecule in the independent part of the unit cell.

The crystal packing for (*E*)-3-((2-oxo-5-phenylfuran-3(2*H*)-ylidene)methyl)-4*H*-chromen-4-one (**3a**) is shown in Figure 5, according to which the minimum

Table 3. Geometric parameters of (*E*)-3-((2-oxo-5-phenylfuran-3(2*H*)-ylidene)methyl)-4*H*-chromen-4-one (**3a**) according to X-ray diffraction results.

Angle	(°)	Bond lengths	(Å)
C11–C12–C16	117.2	C11–C12	1.44
C11–C12–C13	121.6	C12–C13	1.36
C3–C11–C12	131.6	C12–C16	1.44
C4–C3–C11	121.6	C3–C2	1.49
C12–C13–H13	118.4	C2–H2	0.93
C13–C12–C11–C3	14.7	C11–H11	0.93
C12–C11–C3–C2	7.4	C13–H13	0.93
H11–C11–C12–C16	9.3		
C11–C12–C13–H13	–6.6		
C4–C3–C11–C12	–174.1		

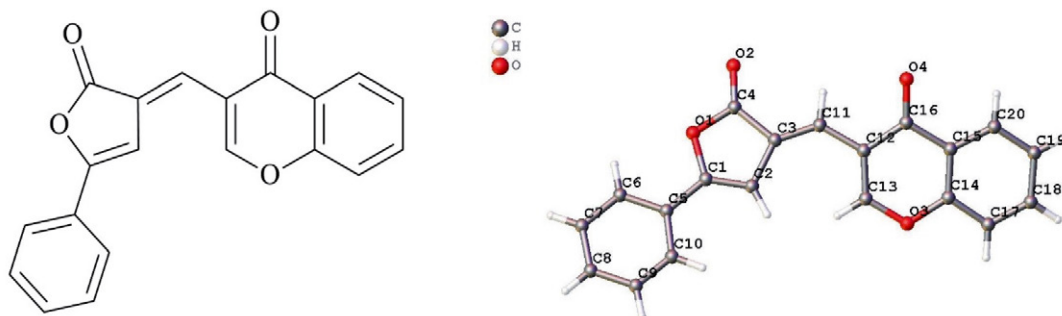


Figure 4. General view of compound **3a** in the representation of atoms by thermal ellipsoids ($p = 50\%$).

distance between two molecules oriented parallel to each other is 4.97 \AA , which indicates the absence of effective intermolecular interaction of the stacking type.

The phenyl substituent practically lies in the same plane with the furan-2(3*H*)-one ring, the angle between the C2–C1–O1–C4–C3 and C5–C6–C7–C8–C9–C10 planes is 6.8° . The chromenone fragment is rotated relative to the furan-2(3*H*)-one ring in such a way that the angle between the C2–C1–O1–C4–C3 and C17–C18–C19–C20–C15–C14 planes is 21.1° . The C5–C6–C7–C8–C9–C10 planes of the phenyl substituent and the C17–C18–C19–C20–C15–C14 planes of the chromenone ring are located at an angle of 28.8° .

We carried out a theoretical justification for the configurational features of the obtained series of compounds based on DFT calculations. For this purpose, the B3LYP functional and the 6–31G(d,p) basis set were used.

Using compound **3a** as an example, the geometry of all 4 possible configurations (*E1*, *E2*, *Z1*, *Z2*) was optimized (Table 4). The first parameter that demonstrates the correlation of the resulting structure with the *E1* form is the angle between the planes C14–C11–C10–O9–C5–C4–C3–C2–C7–C6–C5 of phenylmethylenefuranone and C15–C16–O17–C18–C21–C22–C23–C24–C19–C20 of chromenone fragments, which is 23.7° and corresponds to that in X-ray diffraction analysis (25.01°); the

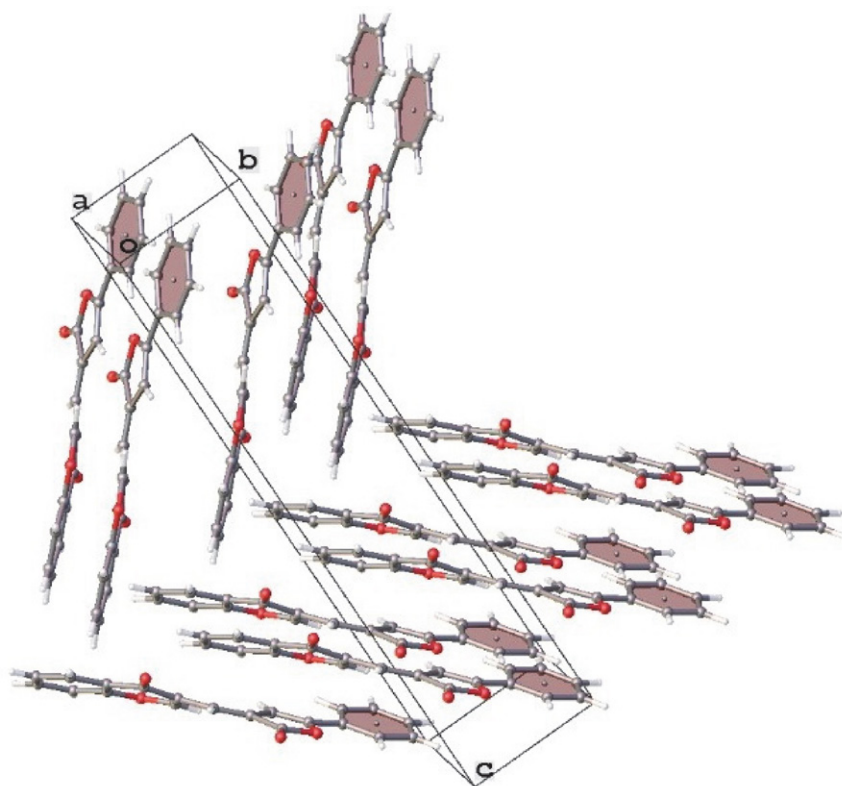


Figure 5. The packing diagram of compound **3a**

distance between the centers of the indicated planes of the structures under consideration is 7.43 Å and 7.45 Å, respectively. A confirming factor is also the close distance between the H33–H31 hydrogen atoms, equal to 2.18 Å in the *E1* structure with optimized geometry (Figure 6) and 2.11 Å, respectively, in the crystal of the resulting substance.

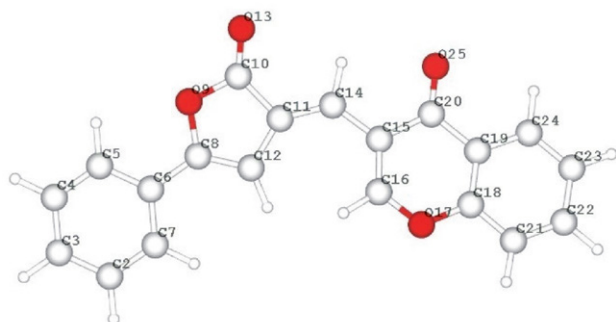


Figure 6. Optimized structure of compound 3a (*E1* isomer)

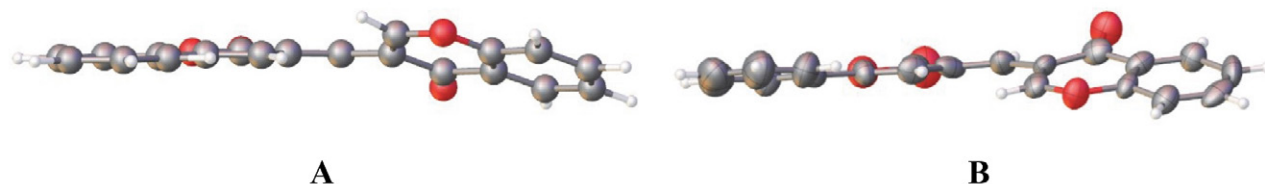


Figure 7. The location of the chromenone ring relative to the phenylmethylenefuranone ring in the optimized *E1* molecule (A) and in the crystal according to X-ray diffraction analysis (B)

When comparing the values of bond angles in the calculated model of configuration *E1* with the values obtained from X-ray diffraction studies, it can also be noted that they are almost identical. The values of the torsion angles differ, which is explained by the different rotation angle of the chromenone cycle plane relative to the phenylmethylenefuranium plane (Figure 7).

A comparative analysis of the experimentally obtained and theoretically calculated ^1H NMR spectra (Table 5) is also consistent with the above, with the exception of the shift of the vinyl proton of the furanone ring to a weaker field compared to that of the exocyclic fragment.

Table 5. Key signals of ^1H NMR spectra of optimized isomer structures *E1*, *E2*, *Z1*, *Z2* of compound 3a.

Key signals	Experiment	3a			
		Calculation			
		<i>E1</i>	<i>E2</i>	<i>Z1</i>	<i>Z2</i>
$\text{CH}_{\text{furanone}}$	7.59	7.25	8.89	7.19	7.09
$=\text{CH}-$	7.37	8.11	7.31	8.39	7.39
$\text{CH}_{\text{Chromone}}$	9.09	9.03	8.75	11.29	8.57

Table 4. Geometric parameters of the optimized structures of isomers *E1*, *E2*, *Z1*, *Z2* of compound 3a.

	Compound			
	3a (<i>E1</i>)	3a (<i>E2</i>)	3a (<i>Z1</i>)	3a (<i>Z2</i>)
Bond lengths (Å)				
C14–C15	1.45	1.45	1.45	1.46
C15–C16	1.36	1.37	1.37	1.35
C15–C20	1.48	1.48	1.49	1.48
C11–C12	1.44	1.44	1.44	1.44
C12–H31	1.08	1.07	1.08	1.08
C14–H32	1.09	1.09	1.09	1.09
C16–H33	1.08	1.08	1.08	1.08
Angle (°)				
C14–C15–C20	117.2	126.4	115.2	174.9
C14–C15–C16	123.9	115.6	125.9	119.2
C11–C14–C15	129.5	134.1	134.5	126.9
C10–C11–C14	119.8	117.2	129.7	125.9
C15–C16–H33	124.1	122.6	123.5	123.4
C16–C15–C14–C11	–22.2	179.98	0	139.22
C15–C14–C11–C12	–3.8	0.02	–0.004	172.9
H32–C14–C15–C20	–16.7	179.97	0	131.4
C14–C15–C16–H33	–1.5	–0.001	0	–2.5
C10–C11–C14–C15	177.7	–179.99	0	–11.8

If we consider the parameters of the theoretical model of the *E2* isomer (*Z1*, *Z2*), then almost all the lengths of the compared bonds will coincide with those for the experimentally obtained one from X-ray diffraction analysis data. However, the values of the bond and torsion angles will differ. In addition, based on these values of torsion angles for isomeric structures, we can conclude that *E2* is almost flat, and this configuration is stabilized due to an intramolecular hydrogen bond (O25–H31) 2.17 Å, which illustrates an even greater shift to the downfield region of the vinyl proton of furan-2-one ring.

Like the theoretical model *E2*, its isomer *Z1* is planar and stabilized by a hydrogen bond (O13–H33) of 2.01 Å, which contributes to a shift in the calculated spectrum to the region of 11.29 ppm vinyl proton of the chromenone ring.

In contrast to the latter, the model of isomer *Z2* has an even larger angle between the phenylmethylene-furanone and chromenone planes (C14–C11–C10–O9–C5–C4–C6–C3–C2–C7 and C15–C16–O17–C18–C21–C22–C23–C24–C19–C20) and amounts to 49.7°, due to repulsion between exocyclic oxygen atoms - oxygen of the furanone and chromenone rings.

Thus, a comparative analysis of data from theoretical calculations of geometry (distances, bond and torsion angles) and spectral data with data obtained from X-ray diffraction and spectral analyzes clearly shows the unambiguity of the formation of the *E1* stereoisomer. The obtained results of calculating the geometry and energy parameters of the intermediates of the condensation process (*R* and *S* adducts) make it possible to explain the further direction of the process of formation of stereoisomer *E*, as a product of dehydration of the most stable *R1* isomer.

We also discovered the ability of 3-{{[2-oxo-5-aryl-furan-3(2*H*)-ylidene]methyl}-4*H*-1-benzopyran-4-ones **3a–f** to exist only in one *E*-configuration by electron spectroscopy. For compounds **3a**, **3c**, **3f**, containing electron-donating and electron-withdrawing substituents and having different chromophores, electronic absorption spectra were recorded in various solvents ($c = 2 \cdot 10^{-5}$ M) and various pH values. Regardless of the polarity of the chosen solvent and the structure of the aromatic sub-

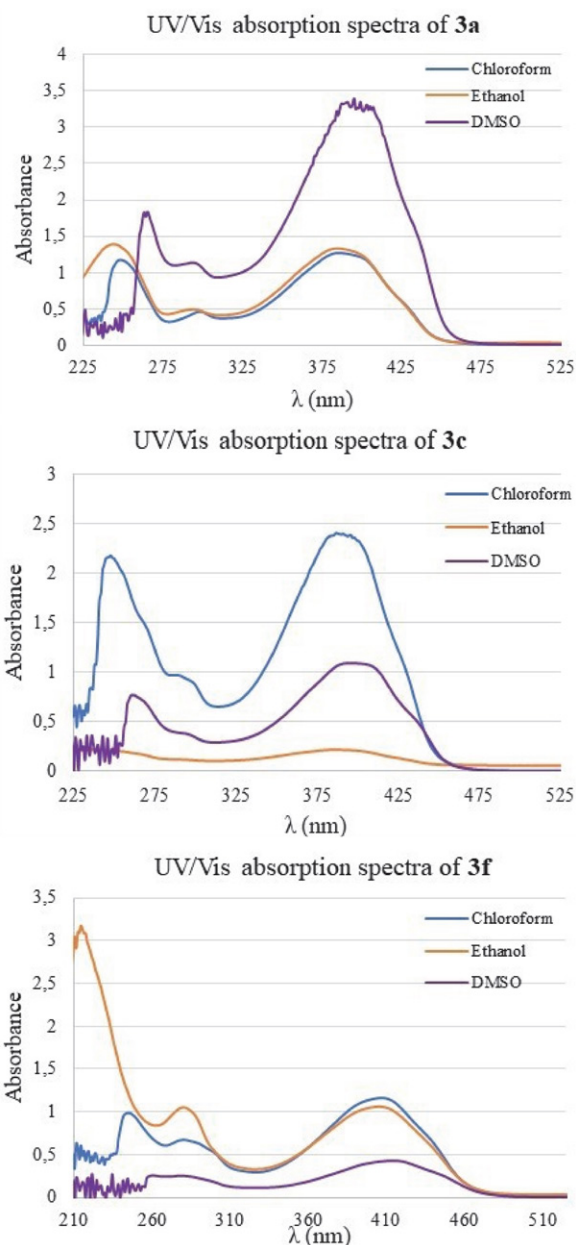


Figure 8. UV/Vis absorption spectra of **3a**, **3c**, **3f** in CHCl_3 , EtOH, DMSO

Table 6. Characteristics of 3-{{[2-oxo-5-aryl-furan-3(2*H*)-ylidene]methyl}-4*H*-1-benzopyran-4-ones **3a**, **3c**, **3f** in solvents of various polarities in neutral and acidic media.

№	λ_{max} , nm (A)					
	CHCl_3	$\text{CHCl}_3 + \text{CH}_3\text{COOH}$	EtOH	EtOH + CH_3COOH	DMSO	DMSO + CH_3COOH
3a	248 (1.18)	248 (1.22)	244 (1.39)	246 (1.60)	—	—
	298 (0.45)	298 (0.48)	294 (0.49)	294 (0.57)	294 (1.13)	294 (1.24)
	386 (1.24)	388 (1.27)	384 (1.33)	385 (1.58)	403 (3.30)	404 (3.40)
3c	248 (2.17)	248 (2.19)	241(0.21)	229 (1.41)	—	—
	288 (0.97)	288 (0.99)	298 (0.11)	299 (0.44)	296 (0.37)	295 (0.44)
	391 (2.39)	392 (2.40)	393 (0.21)	391 (0.68)	396 (1.09)	400 (1.18)
3f	246 (0.98)	246 (1.07)	215 (3.18)	231 (1.67)	—	—
	281 (0.66)	281 (0.72)	281 (1.05)	280 (1.07)	280 (0.24)	281 (0.25)
	408 (1.15)	409 (1.23)	406 (1.06)	407 (1.10)	416 (0.42)	414 (0.41)

stituent of the furan-2-one fragment, products **3a**, **3c**, **3f** show three bands in solution (chloroform, ethanol), corresponding to the $\pi \rightarrow \pi^*$ and $n \rightarrow \pi^*$ transitions at 215–248 nm, 281–298 nm and 384–408 nm, respectively. In a DMSO solution, two bands are observed (the first band is not detected due to the lower transmission limit of DMSO) at 280–296 nm and 396–416 nm. The first two absorption bands correspond to the furan-2-one and chromen-4-one fragments. The appearance of a new absorption band in the long-wavelength region is associated with the formation of a single conjugation system, including both fragments (Figure 8).

In DMSO, due to the high basicity and dielectric constant of this solvent, which is an effective electron donor, the interaction between this solvent and (*E*)-3-((2-oxo-5-phenylfuran-3(2*H*)-ylidene)methyl)-4*H*-chromen-4-one (**3a**) results in a significant hyperchromic band effect at 403 nm. When moving from the “parent” compound to (*E*)-3-((5-(4-chlorophenyl)-2-oxofuran-3(2*H*)-ylidene)methyl)-4*H*-chromen-4-one (**3c**) in the case of using an aprotic non-polar solvent (chloroform), there is no bathochromic shift of the band at 391 nm, but its hyperchromic effect is also observed, which is probably associated with nonspecific orientational, inductive and dispersive interactions of this solvent with the electron-withdrawing substituent (–Cl). Due to the introduction of an additional polar group (**3f**) containing a lone electron pair (–OCH₃ group), a bathochromic shift ($\lambda = 416$ nm) is observed relative to compounds **3a** and **3c**.

In the presence of catalytic amounts of glacial acetic acid in all of the above solvents, the position of the bands does not change, while the intensity of the band (hyperchromic effect) corresponding to the $n \rightarrow \pi^*$ transition slightly increases (Table 6).

4. Conclusions

In summary, hybrid compounds based on furan-2(3*H*)-ones and chromen-4(4*H*)-one: (*E*)-3-[[2-oxo-5-aryl-furan-3(2*H*)-ylidene]methyl]-4*H*-1-benzopyran-4-ones were prepared and structurally characterized. Using experimental and calculated data, they showed the probable path of transformations, the structure of the intermediates of the process and the final reaction products. The resulting hybrid compounds exist only in the *E*-configuration.

Supplementary Material

Copies of ¹H, ¹³C, NOESY NMR spectra of the products are presented in the supporting information.

CCDC–2350345 contains the supplementary crystallographic data for this paper. These data can be obtained free of charge at <http://www.ccdc.cam.ac.uk/const/retrieving.html> or from the Cambridge Crystallographic

Data Centre (CCDC), 12 Union Road, Cambridge CB2 1EZ, UK; fax: +44(0)1223-336033 or e-mail: deposit@ccdc.cam.ac.uk.

Acknowledgement

This research was funded by Foundation for Assistance to Small Innovative Enterprises (FASIE) (grant No. 18695GU/2023 to E. M. Arzyamova).

Conflict of interest

The authors declare no conflict of interest.

5. References

1. D. V. Lipina, E. I. Denisova, I. O. Devyatkin, E. A. Okoneshnikova, D. A. Shipilovskikh, R. R. Makhmudov, N. M. Igidov, S. A. Shipilovskikh, *Russ. J. Gen. Chem.* **2021**, *91*, 2469–2474. DOI10.1134/S1070363221120161
2. S. N. Igidov, D. V. Lipin, A. Yu. Turyshev, S. V. Chashchina, D. A. Shipilovskikh, O. V. Zvereva, K. A. Mitusova, P. S. Silaichev, N. M. Igidov, *Chim. Techn. Acta* **2023**, *10*, 1–8. DOI10.15826/chimtech.2023.10.1.02
3. E. M. Flefel, W. A. Tantawy, R. E. Abdel-Mageid, A. El-Galil E. Amr, R. Nadeem, *Res. Chem. Intermed.* **2014**, *40*, 1365–1381. DOI10.1007/s11164-013-1045-z
4. J. P. Rappai, V. Raman, P. A. Unnikrishnan, S. Prathapan, S. K. Thomas, C. S. Paulose, *Bioorg. Med. Chem. Lett.* **2009**, *19*, 764–765. DOI10.1016/j.bmcl.2008.12.030
5. M. M. Alam, D. P. Sarkar, A. Husain, A. Marella, M. Shaquiquz-zaman, M. Akhter, M. Shaharyar, O. Alam, F. Azam, *J. Serb. Chem. Soc.* **2011**, *76*, 1617–1626. DOI10.2298/JSC110131142A
6. T. Bhandu, T. Bhattacharyya, A. Gaurav, J. Akhter, M. Saini, V. K. Gupta, S. K. Srivastava, H. Sen, N. K. Navani, V. Gupta, D. Biswas, R. Chaudhry, R. Pathania, *J. Antimicrob. Chemother.* **2020**, *75*, 418–428. DOI10.1093/jac/dkz428
7. M. S. Mohamed, K. M. Elamin, R. Alenazy, E. M. Eltayib, M. T. Idriess, N. A. A. Alhudaib, T. Elsaman, M. A. Mohamed, *J. Chem.* **2023**, *2023*, 1–13. DOI10.1155/2023/1481595
8. S. Emami, N. Shahrokhira, A. Foroumadi, M. A. Faramarzi, N. Samadi, N. Soltani-Ghofrani, *Med. Chem. Res.* **2013**, *22*, 5940–5947. DOI10.1007/s00044-013-0581-9
9. A. Kamal, S. M. Ali Hussaini, S. Faazil, Y. Poornachandra, G. N. Reddy, C. G. Kumar, V. S. Rajput, C. Rani, R. Sharma, I. Ali Khan, N. J. Babu, *Bioorg. Med. Chem. Lett.* **2013**, *23*, 6842–6846. DOI10.1016/j.bmcl.2013.10.010
10. S. Jiang, S. Su, M. Chen, F. Peng, Q. Zhou, T. Liu, L. Liu, W. Xue, *J. Agric. Food Chem.* **2020**, *68*, 5641–5647. DOI10.1021/acs.jafc.0c01652
11. A. Kurt-Kızıldoğan, N. Akarsu, Ç. Otur, A. Kivrak, N. Aslan-Ertas, S. Arslan, D. Mutlu, M. Konus, C. Yılmaz, D. Cetin, T. Topal, N. Şahin, *Anticancer Agents Med. Chem.* **2022**, *22*, 362–370. DOI10.2174/1871520621666210311085748

12. F. Peng, T. Liu, Q. Wang, F. Liu, X. Cao, J. Yang, L. Liu, C. Xie, W. Xue, *J. Agric. Food Chem.* **2021**, *69*, 11085–11094. DOI10.1021/acs.jafc.1c03755
13. A. A. El-Tombary, Y. S. Abdel-Ghany, A. S. F. Belal, S. A. S. El-Dine, F. S. G. Soliman, *Med. Chem. Res.* **2011**, *20*, 865–876. DOI10.1007/s00044-010-9394-2
14. R. Zhang, G. Iskander, P. Da Silva, D. Chan, V. Vignevich, V. Nguyen, M. M. Bhadbhade, D. StC Black, N. Kumar, *Tetrahedron* **2011**, *67*, 3010–3016. DOI10.1016/j.tet.2011.02.014
15. Y. Isyaku, A. Uzairu, S. Uba, M. T. Ibrahim, A. B. Umar, *Bull. Nat. Res. Centre* **2020**, *44*, 1–11. DOI10.1186/s42269-020-00297-w
16. F. Hao, X. Wang, M. Mohammadnia, *Polycycl. Aromat. Compd.* **2022**, *42*, 4255–4269. DOI10.1080/10406638.2021.1887298
17. H. Shahbazi-Alavi, S. Khojasteh-Khosro, J. Safaei-Ghomi, S. H. Nazemzadeh, *J. Iran. Chem. Soc.* **2019**, *16*, 2433–2440. DOI10.1007/s13738-019-01711-5
18. A. K. El-Ziaty, W. S. I. Abou-Elmagd, S. K. Ramadan, A. I. Hashem, *Egypt. J. Chem.* **2016**, *59*, 637–646.
19. S. E. Denmark, B. R. Henke, *J. Am. Chem. Soc.* **1991**, *113*, 2177–2194. DOI10.1021/ja00006a042
20. OD Rigaku (2022). *CrysAlis PRO*. Rigaku Oxford Diffraction, Yarnton, Oxfordshire, England.
21. G. M. Sheldrick, *Acta Crystallogr.* **2015**, *C71*, 3–8. DOI10.1107/S2053229614024218
22. O. V. Dolomanov, L. J. Bourhis, R. J. Gildea, J. A. K. Howard, H. Puschmann, *J. Appl. Crystallogr.* **2009**, *42*, 339–341. DOI10.1107/S0021889808042726
23. V. A. Sedavkina, N. A. Morozova, A. Yu. Egorova, I. G. Ostroumov, *Chem. Heterocycl. Compd.* **1987**, *23*, 377–380. DOI10.1007/BF00546727

Povzetek

Razvili smo direktno metodo priprave hibridnih spojin (*E*)-3-[[2-okso-5-aryl-furan-3(2*H*)-iliden]metil]-4*H*-1-benzopirran-4-onov, ki temeljijo na furan-2(3*H*)-onu in kromen-4(4*H*)-onu. Strukture smo potrdili z elementno analizo, IR, UV in NMR spektroskopijo ter z rentgensko difrakcijo monokristala. Molekulska geometrija sintetizirane spojine (*E*)-3-((2-okso-5-fenil-furan-3(2*H*)-iliden)metil)-4*H*-kromen-4-ona (**3a**) smo analizirali z rentgensko difrakcijsko analizo ter rezultate primerjali z rezultati DFT izračunov, izvedenih s 6-311G bazno funkcijo z razcepljenimi valencami.



Except when otherwise noted, articles in this journal are published under the terms and conditions of the Creative Commons Attribution 4.0 International License

DRUŠTVENE VESTI IN DRUGE AKTIVNOSTI **SOCIETY NEWS, ANNOUNCEMENTS, ACTIVITIES**

Vsebina

Mednarodna kemijska olimpijada 2024	S77
Koledar važnejših znanstvenih srečanj s področja kemije in kemijske tehnologije	S79
Navodila za avtorje	S80

Contents

International Chemistry Olympiad 2024	S77
Scientific meetings – Chemistry and chemical engineering.....	S79
Instructions for authors	S80

Mednarodna kemijska olimpijada 2024

Andrej Godec, UL, FKKT

Slovenska šestčlanska ekipa se je vrnila iz Rijada v Savdski Arabiji, kjer je potekala 56. mednarodna kemijska olimpijada. Gre za dogodek najvišjega ranga, ki zahteva dobro teoretično in praktično znanje dijakov.

Letos so Slovenijo zastopali Matej Nastran, Luka Gašperlin (oba gimnazija Škofja Loka), Filip Zver (gimnazija Ljutomer) in Gabriel Žnidaršič (Gimnazija Vič Ljubljana). Ekipo sva vodila glavni mentor Andrej Godec in mentor Darko Dolenc, oba iz Fakultete za kemijo in kemijsko tehnologijo v Ljubljani.

Dijaki so v hudi konkurenci dosegli odličen uspeh: vsi štirje so dobili bronasto medaljo. Iskrene čestitke!

Na priloženi fotografiji smo z leve Darko, Matej, Gabriel, Filip, Luka in Andrej, nahajamo pa se pred stavbo Univerze kralja Sauda v Rijadu.

Mednarodna kemijska olimpijada obstaja od leta 1968. Na samem dogodku imajo dijaki priložnost, da - poleg doseganja čimboljših rezultatov v mednarodni konkurenci - srečajo podobne bistre glave iz celega sveta, in ohranijo stike še dolgo v bodočnost.

Priprave na olimpijado potekajo na Fakulteti za kemijo in kemijsko tehnologijo v Ljubljani. Štartamo običajno januarja z okrog 100 dijakov, do konca aprila pa po pripravah in testih izberemo štiri najboljše. Letos je dijake

pripravljala strokovna ekipa naše fakultete, ki so jo sestavljale dr. Berta Košmrlj, dr. Marta Počkaj, dr. Darko Dolenc, mag. Jernej Imperl in dr. Andrej Godec. Pri prevajanju nalog je pomagal tudi dr. Miha Lukšič.

Celotni ekipi se za opravljeno delo in požrtvovalnost najlepše zahvaljujemo.

Pri organizaciji udeležbe na olimpijadi plodno sodelujemo z Zvezo za tehnično kulturo Slovenije, in Slovenskim kemijskim društvom. Obema se iskreno zahvaljujemo za dragoceno pomoč.

Letošnje olimpijade se je udeležilo 333 dijakov iz 89 držav. Dijaki tekmujejo dva dni: najprej je na vrsti laboratorij, potem pa še teoretični test. Vsakič imajo na voljo 5 ur časa. Naloge so bile tudi letos zelo zahtevne; dve sta bili praktični, in devet teoretičnih.

Naloge zajemajo sicer vsa področja kemije, in ponekod presegajo fakultetni nivo. Povezava do dogodka je naslednja: IChO 2024, <https://www.icho2024.sa/en/Pages/default.aspx>.

Povejmo še, da lahko temperature v Savdski Arabiji v tem letnem času dosežejo 48 stopinj Celzija, kar je bila za nas, vajenih prijetnega vremena in zelene narave, prav posebna izkušnja.



KOLEDAR VAŽNEJŠIH ZNANSTVENIH SREČANJ S PODROČJA KEMIJE IN KEMIJSKE TEHNOLOGIJE

SCIENTIFIC MEETINGS – CHEMISTRY AND CHEMICAL ENGINEERING

2024

October 2024

- 6 – 10 INTERNATIONAL SYMPOSIUM ON CHROMATOGRAPHY (ISC2024)
Liverpool, United Kingdom
Information: <https://isc2024.org/>
- 7 – 11 4TH STEM-CPD SUMMER SCHOOL
Palermo, Italy
Information: <https://ectn.eu/summer-school/>
- 20 – 24 5TH EUROPEAN CONFERENCE OF PHYSICAL CHEMISTRY (ECPC25)
Antalya, Turkey
Information: <https://www.euchems.eu/divisions/physical-chemistry-2/conferences/>
- 20 – 25 6TH INTERNATIONAL SYMPOSIUM ON HALOGEN BONDING (ISXB6)
Srebreno, Croatia
Information: <https://isxb6.hkd.hr/>

November 2024

- 11 – 15 SOLUTIONS IN CHEMISTRY
Sveti Martin na Muri, Croatia
Information: <https://solutionsinchemistry.hkd.hr/>
- 13 – 15 20TH INTERNATIONAL CONFERENCE ON POLYSACCHARIDES AND GLYCOSCIENCE
(20TH ICPG)
Prague, Czech Republic
Information: <https://www.polysaccharides.csch.cz/>

December 2024

- 9 – 13 INTERNATIONAL N.I.C.E. CONFERENCE ON BIOINSPIRATION & BIOBASED
MATERIALS – WINTER 2024
Nice, France
Information: <https://www.nice-conference.com/winter-edition/>
- 15 – 17 1ST ANGLO ITALIAN CHEMICAL BIOLOGY BILATERAL MEETING (AICBBM-1)
Perugia, Italy
Information: <https://www.rsc.org/events/detail/78939/1st-anglo-italian-chemical-biology-bilateral-meeting-aicbbm-1>

Acta Chimica Slovenica

Author Guidelines

Submissions

Submission to ACSi is made with the implicit understanding that neither the manuscript nor the essence of its content has been published in whole or in part and that it is not being considered for publication elsewhere. All the listed authors should have agreed on the content and the corresponding (submitting) author is responsible for having ensured that this agreement has been reached. The acceptance of an article is based entirely on its scientific merit, as judged by peer review. There are no page charges for publishing articles in ACSi. The authors are asked to read the Author Guidelines carefully to gain an overview and assess if their manuscript is suitable for ACSi.

Additional information

- Citing spectral and analytical data
- Depositing X-ray data

Submission material

Typical submission consists of:

- full manuscript (PDF file, with title, authors, abstract, keywords, figures and tables embedded, and references)
- supplementary files
 - **Full manuscript** (original Word file)
 - **Statement of novelty** (Word file)
 - **List of suggested reviewers** (Word file)
 - **ZIP file containing graphics** (figures, illustrations, images, photographs)
 - **Graphical abstract** (single graphics file)
 - **Proposed cover picture** (optional, single graphics file)
 - **Appendices** (optional, Word files, graphics files)

Incomplete or not properly prepared submissions will be rejected.

Submission process

Before submission, authors should go through the checklist at the bottom of the page and prepare for submission.

Submission process consists of 5 steps.

Step 1: Starting the submission

- Choose one of the journal sections.
- Confirm all the requirements of the **checklist**.
- Additional plain text comments for the editor can be provided in the relevant text field.

Step 2: Upload submission

- Upload full manuscript in the form of a Word file (with title, authors, abstract, keywords, figures and tables embedded, and references).

Step 3: Enter metadata

- First name, last name, contact email and affiliation for all authors, in relevant order, must be provided. Corresponding author has to be selected. Full postal address and phone number of the corresponding author has to be provided.

- **Title and abstract** must be provided in plain text.
- Keywords must be provided (max. 6, separated by semicolons).
- Data about contributors and supporting agencies may be entered.
- **References** in plain text must be provided in the relevant text filed.

Step 4: Upload supplementary files

- Original Word file (original of the PDF uploaded in the step 2)
- **List of suggested reviewers** with at least five reviewers with two recent references from the field of submitted manuscript must be uploaded as a Word file. At the same time, authors should declare (i) that they have no conflict of interest with suggested reviewers and (ii) that suggested reviewers are experts in the field of the submitted manuscript.
- All **graphics** have to be uploaded in a single ZIP file. Graphics should be named Figure 1.jpg, Figure 2.eps, etc.
- **Graphical abstract image** must be uploaded separately
- **Proposed cover picture** (optional) should be uploaded separately.
- Any additional **appendices** (optional) to the paper may be uploaded. Appendices may be published as a supplementary material to the paper, if accepted.
- For each uploaded file the author is asked for additional metadata which may be provided. Depending of the type of the file please provide the relevant title (Statement of novelty, List of suggested reviewers, Figures, Graphical abstract, Proposed cover picture, Appendix).

Step 5: Confirmation

- Final confirmation is required.

Article Types

Feature Articles are contributions that are written on Editor's invitation. They should be clear and concise summaries of the author's most recent work written with the broad scope of ACSi in mind. They are intended to be general overviews of the authors' subfield of research but should be written in a way that engages and informs scientists in other areas. They should contain the following (see also general guidelines for article structure below): (1) an introduction that acquaints readers with the authors' research field and outlines the important questions for which answers are being sought; (2) interesting, novel, and recent contributions of the author(s) to the field; and (3) a summary that presents possible future directions. Manuscripts should normally not exceed 40 pages of one column format (font size 12, 33 lines per page). Generally, experts who have made an important contribution to a specific field in recent years will be invited by the Editor to contribute a **Feature Article**. Individuals may, however, send a proposal (of no more than one page) for a **Feature Article** to the Editor-in-Chief for consideration.

Scientific articles should report significant and innovative achievements in chemistry and related sciences and should exhibit a high level of originality. They should have the following structure:

1. Title (max. 150 characters),
2. Authors and affiliations,
3. Abstract (max. 1000 characters),
4. Keywords (max. 6),
5. Introduction,
6. Experimental,
7. Results and Discussion,
8. Conclusions,
9. Acknowledgements,
10. References.

The sections should be arranged in the sequence generally accepted for publications in the respective fields and should be successively numbered.

Short communications generally follow the same order of sections as Scientific articles, but should be short (max. 2500 words) and report a significant aspect of research work meriting separate publication. Editors may decide that a Scientific paper is categorized as a Short Communication if its length is short.

Technical articles report applications of an already described innovation. Typically, technical articles are not based on new experiments.

Preparation of Submissions

Text of the submitted articles must be prepared with Microsoft Word. Normal style set to single column, 1.5 line spacing, and 12 pt Times New Roman font is recommended. Line numbering (continuous, for the whole document) must be enabled to simplify the reviewing process. For any other format, please consult the editor. Articles should be written in English. Correct spelling and grammar are the sole responsibility of the author(s). Papers should be written in a concise and succinct manner. The authors shall respect the ISO 80000 standard [1], and IUPAC Green Book [2] rules on the names and symbols of quantities and units. The Système International d'Unités (SI) must be used for all dimensional quantities.

Graphics (figures, graphs, illustrations, digital images, photographs) should be inserted in the text where appropriate. The captions should be self-explanatory. Lettering should be readable (suggested 8 point Arial font) with equal size in all figures. Use common programs such as MS Excel or similar to prepare figures (graphs) and ChemDraw to prepare structures in their final size. Width of graphs in the manuscript should be 8 cm. Only in special cases (in case of numerous data, visibility issues) graphs can be 17 cm wide. All graphs in the manuscript should be inserted in relevant places and **aligned left**. The same graphs should be provided separately as images of appropriate resolution (see below) and submitted together in a ZIP file (Graphics ZIP). Please do not submit figures as a Word file. In **graphs**, only the graph area determined by both axes should be in the frame, while a frame around the whole graph should be omitted. The graph area should be white. The legend should be inside the graph area. The style of all graphs should be the same. **Figures and illustrations** should be of sufficient quality for the printed version, i.e. 300 dpi minimum. **Digital images and photographs** should be of high quality (minimum

250 dpi resolution). On submission, figures should be of good enough resolution to be assessed by the referees, ideally as JPEGs. High-resolution figures (in JPEG, TIFF, or EPS format) might be required if the paper is accepted for publication.

Tables should be prepared in the Word file of the paper as usual Word tables. The captions should appear above the table and should be self-explanatory.

References should be numbered and ordered sequentially as they appear in the text, likewise methods, tables, figure captions. When cited in the text, reference numbers should be superscripted, following punctuation marks. It is the sole responsibility of authors to cite articles that have been submitted to a journal or were in print at the time of submission to ACSi. Formatting of references to published work should follow the journal style; please also consult a recent issue:

1. J. W. Smith, A. G. White, *Acta Chim. Slov.* **2008**, *55*, 1055–1059.
2. M. F. Kemmere, T. F. Keurentjes, in: S. P. Nunes, K. V. Peinemann (Ed.): *Membrane Technology in the Chemical Industry*, Wiley-VCH, Weinheim, Germany, **2008**, pp. 229–255.
3. J. Levec, Arrangement and process for oxidizing an aqueous medium, US Patent Number 5,928,521, date of patent July 27, **1999**.
4. L. A. Bursill, J. M. Thomas, in: R. Sersale, C. Collola, R. Aiello (Eds.), *Recent Progress Report and Discussions: 5th International Zeolite Conference*, Naples, Italy, 1980, Gianini, Naples, **1981**, pp. 25–30.
5. J. Szegezdi, F. Csizmadia, Prediction of dissociation constant using microconstants, http://www.chemaxon.com/conf/Prediction_of_dissociation_constant_using_microconstants.pdf, (assessed: March 31, 2008)

Titles of journals should be abbreviated according to Chemical Abstracts Service Source Index (CASSI).

Special Notes

- Complete characterization, **including crystal structure**, should be given when the synthesis of new compounds in crystal form is reported.
- Numerical **data should be reported with the number of significant digits corresponding to the magnitude** of experimental uncertainty.
- **The SI system of units and IUPAC recommendations** for nomenclature, symbols and abbreviations should be followed closely. Additionally, the authors should follow the general guidelines when citing spectral and analytical data, and depositing crystallographic data.
- **Characters** should be correctly represented throughout the manuscript: for example, 1 (one) and l (ell), 0 (zero) and O (oh), x (ex), D7 (times sign), B0 (degree sign). Use Symbol font for all Greek letters and mathematical symbols.
- The rules and recommendations of the **IUBMB** and the **International Union of Pure and Applied Chemistry (IUPAC)** should be used for abbreviation of chemical names, nomenclature of chemical compounds, enzyme nomenclature, isotopic compounds, optically active isomers, and spectroscopic data.
- **A conflict of interest** occurs when an individual (author, reviewer, editor) or its organization is in-

volved in multiple interests, one of which could possibly corrupt the motivation for an act in the other. Financial relationships are the most easily identifiable conflicts of interest, while conflicts can occur also as personal relationships, academic competition, etc. **The Editors** will make effort to ensure that conflicts of interest will not compromise the evaluation process; potential editors and reviewers will be asked to exempt themselves from review process when such conflict of interest exists. When the manuscript is submitted for publication, **the authors** are expected to disclose any relationships that might pose potential conflict of interest with respect to results reported in that manuscript. In the Acknowledgement section the source of funding support should be mentioned. The statement of disclosure must be provided as Comments to Editor during the submission process.

- **Published statement of Informed Consent.** Research described in papers submitted to ACSi must adhere to the principles of the Declaration of Helsinki (<http://www.wma.net/e/policy/b3.htm>). These studies must be approved by an appropriate institutional review board or committee, and informed consent must be obtained from subjects. The Methods section of the paper must include: 1) a statement of protocol approval from an institutional review board or committee and 2), a statement that informed consent was obtained from the human subjects or their representatives.
- **Published Statement of Human and Animal Rights.** When reporting experiments on human subjects, authors should indicate whether the procedures followed were in accordance with the ethical standards of the responsible committee on human experimentation (institutional and national) and with the Helsinki Declaration of 1975, as revised in 2008. If doubt exists whether the research was conducted in accordance with the Helsinki Declaration, the authors must explain the rationale for their approach and demonstrate that the institutional review body explicitly approved the doubtful aspects of the study. When reporting experiments on animals, authors should indicate whether the institutional and national guide for the care and use of laboratory animals was followed.
- To avoid conflict of interest between authors and referees we expect that not more than one referee is from the same country as the corresponding author(s), however, not from the same institution.
- Contributions authored by **Slovenian scientists** are evaluated by non-Slovenian referees.
- Papers describing **microwave-assisted reactions** performed in domestic microwave ovens are not considered for publication in *Acta Chimica Slovenica*.
- *Manuscripts that are **not prepared and submitted** in accord with the instructions for authors are not considered for publication.*

Appendices

Authors are encouraged to make use of supporting information for publication, which is supplementary material (appendices) that is submitted at the same time as the manuscript. It is made available on the Journal's

web site and is linked to the article in the Journal's Web edition. The use of supporting information is particularly appropriate for presenting additional graphs, spectra, tables and discussion and is more likely to be of interest to specialists than to general readers. When preparing supporting information, authors should keep in mind that the supporting information files will not be edited by the editorial staff. In addition, the files should be not too large (upper limit 10 MB) and should be provided in common widely known file formats to be accessible to readers without difficulty. All files of supplementary materials are loaded separately during the submission process as supplementary files.

Proposed Cover Picture and Graphical Abstract Image

Graphical content: an ideally full-colour illustration of resolution 300 dpi from the manuscript must be proposed with the submission. Graphical abstract pictures are printed in size 6.5 x 4 cm (hence minimal resolution of 770 x 470 pixels). Cover picture is printed in size 11 x 9.5 cm (hence minimal resolution of 1300 x 1130 pixels)

Authors are encouraged to submit illustrations as candidates for the journal Cover Picture*. The illustration must be related to the subject matter of the paper. Usually both proposed cover picture and graphical abstract are the same, but authors may provide different pictures as well.

* The authors will be asked to contribute to the costs of the cover picture production.

Statement of novelty

Statement of novelty is provided in a Word file and submitted as a supplementary file in step 4 of submission process. Authors should in no more than 100 words emphasize the scientific novelty of the presented research. Do not repeat for this purpose the content of your abstract.

List of suggested reviewers

List of suggested reviewers is a Word file submitted as a supplementary file in step 4 of submission process. Authors should propose the names, full affiliation (department, institution, city and country) and e-mail addresses of five potential referees. Field of expertise and at least two references relevant to the scientific field of the submitted manuscript must be provided for each of the suggested reviewers. The referees should be knowledgeable about the subject but have no close connection with any of the authors. In addition, referees should be from institutions other than (and countries other than) those of any of the authors. Authors declare no conflict of interest with suggested reviewers. Authors declare that suggested reviewers are experts in the field of submitted manuscript.

How to Submit

Users registered in the role of author can start submission by choosing USER HOME link on the top of the page, then choosing the role of the Author and follow the relevant link for starting the submission process.

Prior to submission we strongly recommend that you familiarize yourself with the ACSi style by browsing the journal, particularly if you have not submitted to the ACSi before or recently.

Correspondence

All correspondence with the ACSi editor regarding the paper goes through this web site and emails. Emails are sent and recorded in the web site database. In the correspondence with the editorial office please provide ID number of your manuscript. All emails you receive from the system contain relevant links. **Please do not answer the emails directly but use the embedded links in the emails for carrying out relevant actions.** Alternatively, you can carry out all the actions and correspondence through the online system by logging in and selecting relevant options.

Proofs

Proofs will be dispatched via e-mail and corrections should be returned to the editor by e-mail as quickly as possible, normally within 48 hours of receipt. Typing errors should be corrected; other changes of contents will be treated as new submissions.

Submission Preparation Checklist

As part of the submission process, authors are required to check off their submission's compliance with all of the following items, and submissions may be returned to authors that do not adhere to these guidelines.

1. The submission has not been previously published, nor is it under consideration for publication in any other journal (or an explanation has been provided in Comments to the Editor).
2. All the listed authors have agreed on the content and the corresponding (submitting) author is responsible for having ensured that this agreement has been reached.
3. The submission files are in the correct format: manuscript is created in MS Word but will be **submitted in PDF** (for reviewers) as well as in original MS Word format (as a supplementary file for technical editing); diagrams and graphs are created in Excel and saved in one of the file formats: TIFF, EPS or JPG; illustrations are also saved in one of these formats. The preferred position of graphic files in a document is to embed them close to the place where they are mentioned in the text (See **Author guidelines** for details).
4. The manuscript has been examined for spelling and grammar (spell checked).
5. The **title** (maximum 150 characters) briefly explains the contents of the manuscript.
6. Full names (first and last) of all authors together with the affiliation address are provided. Name of author(s) denoted as the corresponding author(s), together with their e-mail address, full postal address and telephone/fax numbers are given.
7. The **abstract** states the objective and conclusions of the research concisely in no more than 150 words.
8. Keywords (minimum three, maximum six) are provided.
9. **Statement of novelty** (maximum 100 words) clearly explaining new findings reported in the manuscript should be prepared as a separate Word file.
10. The text adheres to the stylistic and bibliographic requirements outlined in the **Author guidelines**.
11. Text in normal style is set to single column, 1.5 line spacing, and 12 pt. Times New Roman font is

recommended. All tables, figures and illustrations have appropriate captions and are placed within the text at the appropriate points.

12. Mathematical and chemical equations are provided in separate lines and numbered (Arabic numbers) consecutively in parenthesis at the end of the line. All equation numbers are (if necessary) appropriately included in the text. Corresponding numbers are checked.
13. Tables, Figures, illustrations, are prepared in correct format and resolution (see **Author guidelines**).
14. The lettering used in the figures and graphs do not vary greatly in size. The recommended lettering size is 8 point Arial.
15. Separate files for each figure and illustration are prepared. The names (numbers) of the separate files are the same as they appear in the text. All the figure files are packed for uploading in a single ZIP file.
16. Authors have read **special notes** and have accordingly prepared their manuscript (if necessary).
17. References in the text and in the References are correctly cited. (see **Author guidelines**). All references mentioned in the Reference list are cited in the text, and vice versa.
18. Permission has been obtained for use of copyrighted material from other sources (including the Web).
19. The names, full affiliation (department, institution, city and country), e-mail addresses and references of five potential referees from institutions other than (and countries other than) those of any of the authors are prepared in the word file. At least two relevant references (important recent papers with high impact factor, head positions of departments, labs, research groups, etc.) for each suggested reviewer must be provided. Authors declare no conflict of interest with suggested reviewers. Authors declare that suggested reviewers are experts in the field of submitted manuscript.
20. Full-colour illustration or graph from the manuscript is proposed for graphical abstract.
21. **Appendices** (if appropriate) as supplementary material are prepared and will be submitted at the same time as the manuscript.

Privacy Statement

The names and email addresses entered in this journal site will be used exclusively for the stated purposes of this journal and will not be made available for any other purpose or to any other party.

ISSN: 1580-3155

Koristni naslovi

Slovensko kemijsko društvo
Slovenian Chemical Society



Slovensko kemijsko društvo

www.chem-soc.si

e-mail: chem.soc@ki.si



Wessex Institute of Technology

www.wessex.ac.uk



SETAC

www.setac.org



European Water Association

<http://www.ewa-online.eu/>



European Science Foundation

www.esf.org



European Federation of Chemical Engineering

<https://efce.info/>



IUPAC

INTERNATIONAL UNION OF
PURE AND APPLIED CHEMISTRY

International Union of Pure and Applied Chemistry

<https://iupac.org/>

Novice evropske zveze kemijskih društev EuChemS najdete na:

 **EuChemS**
European Chemical Society

Brussels News Updates

<http://www.euchems.eu/newsletters/>

Mini Spray Dryer S-300



+ Sušenje z uporabo organskih topil

V kombinaciji z aparatom Inert Loop S-395 Mini Spray Dryer S-300 ponuja varno delo z vzorci, ki vsebujejo organska topila. Nivo kisika in pretoka plina je zaradi varnosti kontinuirno spremljan.

+ Oddaljen dostop

Aplikacija na katerih koli mobilnih napravah ali računalnikih omogoča popolno kontrolo nad uporabniškim vmesnikom aparata.

+ Auto način

Omogoča programiranje aparata Mini Spray Dryer S-300 Advanced in avtomatski potek metode.

+ Prevečen zbiralni ciklon

Zmanjšuje izgubo vzorca med procesom.

+ SI enote

Vsi parametri, kot so npr. razpršilni in sušilni plin ter hitrost črpalke so na voljo v SI enotah in so avtomatsko regulirani.

+ Zaščita vzorca

Aparat omogoča tako monitoring izhodne temperature, kot tudi končne temperature produkta.

+ Programiranje metod

Programirajte sekvenco vzorcev za izvedbo enega vzorca za drugim, za kar največjo priročnost.

+ Poročila

Vsi eksperimenti se na aparatu Mini Spray Dryer S-300 beležijo in shranjujejo v pomnilnik. Na voljo so kot PDF poročilo ali kot .csv datoteka.

Donau Lab d.o.o.
Ljubljana Tbilisjska 85 SI-1000 Ljubljana
www.donaulab.si
office-si@donaulab.com

Tipične aplikacije:

Aktivne farmacevtske učinkovine, dostava zdravila, cepiva, zdravila za inhalacijo, nanotehnologija, keramika, UV absorberji, gorivne celice, baterije, sušenje, mikronizacija, enkapsulacija aditivov, kontrolirano sproščanje, nutracevtiki, funkcionalna hrana, arome, vitamini, proteini, probiotične bakterije, koncentri sokov, mleko v prahu, enkapsulacija bakterij in proteinov, transplantacija celic, kozmetika.



NATIONAL INSTITUTE OF CHEMISTRY

Hajdrihova 19,
1000 Ljubljana
Slovenia
www.ki.si



research
EXCELENCE

Basic and applied research in materials, life sciences, biotechnology, chemical engineering, structural and theoretical chemistry, analytical chemistry and environmental protection.

In line with EU research and innovation priorities: nanotechnology, genomics and biotechnology for health, sustainable development, climate change, energy efficiency and food quality and safety.

We expand knowledge and technology transfer to domestic and foreign chemical, automotive and nanobiotechnology industries.

We are aware of the power of youth, so we transfer our knowledge to younger generations and offer many opportunities for cooperation.



contact: mladi@ki.si

Razvoj in inovacije za globalno uspešnost

Znanje, kreativnost zaposlenih in inovacije so ključnega pomena v okolju, kjer nastajajo pametni premazi skupine KANSAI HELIOS. Z rešitvami, ki zadostijo široki paleti potreb, kontinuiranim razvojem ter s kakovostnimi izdelki, podjetje KANSAI HELIOS Slovenija predstavlja evropski center za inovacije in poslovni razvoj skupine Kansai Paint.



Part of



www.kansai-helios.si

 **KANSAI
HELIOS**
Designing Excellence

**PEKOČA
BOLEČINA?**

**TIŠČANJE
V ŽELODCU?**

**NADLEŽNA
ZGAGA?**



Nolpaza control vsebuje pantoprazol.



ZANESLJIVA ZMAGA
nad želodčno kislino.

www.nolpaza-control.si

 **KRKA** | 70^{let}

Pred uporabo natančno preberite navodilo!
O tveganju in neželenih učinkih se posvetujte z zdravnikom ali s farmacevtom.

ActaChimicaSlovenica

ActaChimicaSlovenica

This study introduces a series of innovative benzodioxepin-biphenyl amide derivatives, highlighting compound E4's potent antibacterial activity against major bacterial strains through enzyme FabH inhibition. It combines synthetic optimization with thorough biological evaluation, promising advances in antimicrobial therapies. See more details on p. 509



Year 2024, Vol. 71, No. 3

